

MAS NMR of Nuclei with Spin $S = 1/2$ in Polycrystalline Powders: Experiments and Numerical Simulations

Dissertation

zur Erlangung des Doktorgrades

der Fakultät für Biologie, Chemie und Geowissenschaften

der

Universität Bayreuth

vorgelegt von

Matthias Bechmann

(Diplom Physiker)

geboren in Staffelstein

Bayreuth, 2004

Vollständiger Abdruck der von der Fakultät für Biologie, Chemie und Geowissenschaften
der Universität Bayreuth zur Erlangung des akademischen Grades eines Doktors der
Naturwissenschaften angenommenen Dissertation.

Tag der Einreichung der Arbeit: 01. Dezember 2004

Tag des wissenschaftlichen Kolloquiums: 16. Juni 2005

Prüfungsausschuss:

Prof. Dr. B. Wrackmeyer (Vorsitzender)

P.D. Dr. A. Sebald (1. Gutachterin)

Prof. Dr. E. Rößler (2. Gutachter)

Prof. Dr. S. van Smaalen

Die vorliegende Arbeit wurde in der Zeit von Mai 1999 bis Oktober 2004 unter der Leitung von P.D. Dr. Angelika Sebald am Bayerischen Geoinstitut, Universität Bayreuth, angefertigt.

It is often stated that of all the theories proposed in this century, the silliest is quantum theory. In fact, some say that the only thing that quantum theory has going for it is that it is unquestionably correct.

— Michio Kaku “Hyperspace” (1995) —

Contents

1. Introduction	1
2. Theory of Nuclear Magnetic Resonance	3
2.1. Nuclear Magnetic Moments	3
2.1.1. Spins and the Magnetic Moment	5
2.1.2. Quantum-Mechanical Description	6
2.2. Nuclear Spin Interactions	10
2.2.1. Zeeman Interaction	11
2.2.2. Chemical Shielding	11
2.2.3. Direct Dipolar Coupling Interaction	12
2.2.4. Indirect Dipolar Coupling Interaction	13
2.2.5. High-Field Approximation and Rotating Frame of Reference	13
2.2.6. Representations of Nuclear Spin Interactions	14
2.2.6.1. Rotational Properties of Nuclear Spin Interactions	16
2.2.6.2. Spherical Representation of Interaction Hamiltonians	18
2.3. Time Dependence	20
2.3.1. Rotations in Spin Space	22
2.3.2. Rotations in Real Space	24
2.3.3. Solution to the Equation of Motion - Pulse Response	26
2.3.4. NMR Signal of Bulk Samples	28
3. Experimental and Numerical Methods	31
3.1. Nuclei with Spin $S = \frac{1}{2}$ under Magic Angle Spinning Conditions	31
3.1.1. Rotational-Resonance Recoupling	33
3.1.2. Double-Quantum Filtration and Rotational Resonance	35
3.2. Numerical Methods	37
3.2.1. Time Propagation	37
3.2.2. Powder Averaging	39
3.2.3. Computation	40
3.2.4. Extraction of Structural Parameters	40
3.2.4.1. Iterative Fitting	41
3.2.4.2. Calculation of Error Hyperplanes	41
3.2.5. Errors and Sensitivities of Fitted Parameter	42
4. Summary and Conclusions	45

5. Short Summary	51
6. Kurze Zusammenfassung	53
Bibliography	55
Appendix of Publications:	61
A. X-$\{^1\text{H}, ^{19}\text{F}\}$ Triple Resonance with a X-$\{^1\text{H}\}$ CP MAS Probe and Characterisation of a ^{29}Si-^{19}F Spin Pair	63
B. ^{13}C Chemical Shielding Tensor Orientations in the Phosphoenolpyruvate Moiety from ^{13}C Rotational-Resonance MAS NMR Lineshapes	77
C. Double-Quantum Filtered Rotational-Resonance MAS NMR in the Presence of Large Chemical Shielding Anisotropies	89
D. Double-Quantum Filtered MAS NMR in the Presence of Chemical Shielding Anisotropies and Direct Dipolar and J Coupling	103
E. Selectivity of Double-Quantum Filtered Rotational-Resonance Recoupling Experiments on Larger-than-Two-Spin Systems	121
F. MAS NMR with and without Double-Quantum Filtration at and near the $n = 0$ Rotational-Resonance Condition	133
G. Magnitudes and Orientations of ^{31}P Chemical-Shielding Tensors in Pt(II)-Phosphine Complexes and Other Four-Fold Coordinated Phosphorus Sites	145
H. Double-Quantum Filtered ^1H MAS NMR Spectra	153
Danksagung	161

Symbols and Abbreviations

Symbols

\mathcal{H}	classical Hamilton function
$\hat{\mathcal{H}}$	quantum mechanical Hamilton operator (Hamiltonian)
$\mathbb{1}_i$	unit matrix/tensor of dimension i
B_0	magnetic induction
A	vector object
\hat{S}	operators; here a spin vector operator
\mathbf{A}	tensor object
A	scalar physical variable or mathematical index
\hat{S}_z	quantum mechanical operator
$e_{x,y,z}$	Cartesian unit vector (base vector)
ω_{rot}	rotation frequency of the rotor (MAS frequency) in units of $[\frac{\text{rad}}{\text{s}}]$
ω_1^S	RF irradiation amplitude in units of $[\frac{\text{rad}}{\text{s}}]$
ω_{RF}	RF irradiation frequency in units of $[\frac{\text{rad}}{\text{s}}]$
ω_0^S	Larmor frequency of spin \hat{S} in units of $[\frac{\text{rad}}{\text{s}}]$

Abbreviations

NMR	Nuclear Magnetic Resonance
PAS	Principal Axes System
CAS	Crystal Axes System
AAS	Arbitrary Axes System
LAB	Laboratory Frame
MAS	Magic Angle Spinning

CP	Cross Polarisation
ZQ	Zero Quantum
SQ	Single Quantum
DQ	Double Quantum
DQF	Double-Quantum Filtration
R ²	Rotational Resonance
CTP	Coherence-Transfer Pathway

1. Introduction

Systems of nuclear spins possess unique properties that predestine them for the use in studies of molecular structural and dynamical properties. Nuclear spins are extremely well localised to dimensions of a few cubic femto meters (the nucleus) and tell about the magnetic field in their close environment with great sensitivity [1, 2]. Therefore nuclear spins can be regarded as sensors that can be used to examine the structure of molecules and matter in general. The interaction energy of a nucleus with its environment is extremely small [2, 3] (about $360 \frac{\text{mJ}}{\text{mol}}$, corresponding to ca. 14 mK), thus monitoring of a nuclear spin is virtually perturbation free. Despite the weakness of the interaction it is highly sensitive to its local environment. In addition, interactions of nuclear spins amongst each other are the key to further geometric information, such as internuclear distances. These interactions can be described by pairwise spin-spin interactions. For example, the magnetic direct dipolar coupling interaction between two spins is related to the distance between them [1, 4].

At first sight the determination of distances of the order of 100 pm to 1000 pm by means of radiofrequency irradiation with wavelengths of the order of 1 m seems to contradict the Heisenberg uncertainty principle [5, 6]. This is in contrast to the situation in scattering or microscopy experiments where the dimensions of the object of study and the irradiation wavelength have to be of the same order of magnitude [7]. This seeming contradiction to Heisenberg's uncertainty principle in nuclear magnetic resonance (NMR) experiments is easily resolved: in NMR spectroscopy the geometric information is derived from the inspection of the energy levels of nuclear spin systems [2]. This means that the accurate determination of e.g. internuclear distances are measurements of energy differences. In agreement with Heisenberg's uncertainty principle a measurement of an energy difference can be made arbitrarily precise by extending the time of measurement. Therefore, in NMR the accuracy of experimentally derived geometric information is solely restricted by the lifetime of the corresponding energy eigenstates.

The principal information content of a NMR spectrum of a crystalline sample is very high since it represents the magnitudes *and* orientations of all NMR interactions present in the spin system [1]. However, the weakness of the spin interactions, which keeps the nuclear spins quite immune to other influences, unfortunately bears a strong drawback. In NMR spectroscopy the signal to noise ratio is usually very low [2, 8] leading to severe detection problems. Therefore, relatively large numbers of spins in a sample are necessary to achieve an experimentally sufficient signal-to-noise ratio [1, 2] (about 10^{14} to 10^{15} spins on a modern high field NMR spectrometer). Accordingly, improvements of the signal-to-noise ratio in experimental NMR spectra as well as the extraction of structural and dynamical information from experimental NMR data, constitute important research areas

in contemporary NMR.

This work deals with investigations on solid state NMR techniques, suitable for the study of dipolar coupled spin $S = \frac{1}{2}$ systems in polycrystalline powders. The performance of several pulse sequences under various conditions as well as procedures for data analysis, based on numerically exact simulations, are the main focus here. In Chapter 2 the theoretical principles of nuclear magnetic resonance of nuclei with spin $S = \frac{1}{2}$ will be presented. In the following a description of the experimental and numerical methods used will be given in Chapter 3. Chapter 4 will give an overview as well as a discussion of the results obtained. Chapter 4 is thus a critical summary of the publications compiled in the Appendix following it.

2. Theory of Nuclear Magnetic Resonance

Nuclear magnetism can be understood as a macroscopic collective magnetic property of a set of atomic nuclei. Many atomic nuclei in their ground state have non-zero spin angular momentum \mathbf{S} and a magnetic moment $\boldsymbol{\mu}$, oriented parallel or antiparallel to \mathbf{S} . The order of magnitude of $\boldsymbol{\mu}$ is about $\approx 10^{-26} \frac{\text{J}}{\text{T}}$ (for $\mathbf{S} = \boldsymbol{\mu}/\gamma$ see Table 2.1 on page 5). It is these moments that give rise to nuclear magnetism. Generally there are three main categories of magnetism [2, 3, 7]. First there is diamagnetism, which is the effect of magnetic moments induced in matter when exposed to an external magnetic field; diamagnetism exists virtually in all forms matter. Second there is paramagnetism, which results from ordering effects occurring when permanent magnetic moments are placed in contact with a strong magnetic field which is the case e.g. for the nuclear paramagnetic moment used in NMR. And there is ferromagnetism which arises from an exchange interaction in matter itself and therefore is primarily independent of external magnetic fields. In nuclear magnetic resonance on diamagnetic samples at room temperature only the paramagnetism of the nuclei and the diamagnetism of the sample are of importance.

The phenomenon of nuclear magnetic resonance has been first observed by I.I. Rabi [9] in molecular beams. Afterwards F. Bloch [10] and E.M. Purcell [11] independently developed the method for its application to the solid state. The phenomenon is based on the resonant interaction of a radiofrequency field with the sample placed in a strong external magnetic field. In order to depict the way this resonance occurs several approaches exist. The two most common descriptions go back to the discoverers of nuclear magnetic resonance. Bloch is describing the phenomenon by the resonant interaction of a magnetic dipole oscillating in a strong magnetic field with a tuned coil surrounding the sample [12]. The induced current in the coil is changed [4, 13] when the resonance frequency is hit. Purcell's description [11, 14] uses a different picture where the absorption of energy quanta is leading to transitions between energy levels, which happens when the irradiation frequency matches the energy difference $\Delta E = \hbar\omega$ between two energy eigenstates of the nuclear magnetic moment. Both approaches account well for the magnetic resonance phenomenon in general, but in different ways are insufficient to explain the full range of effects occurring in NMR.

2.1. Nuclear Magnetic Moments

The basic property in magnetic resonance spectroscopy is the behaviour of a magnetic moment $\boldsymbol{\mu}$ in the presence of a strong magnetic field \mathbf{B}_0 . This is most easily described using Bloch's approach [14]. The magnetic moment $\boldsymbol{\mu}$ is, in a semi-classical description,

subjected to a torque \mathbf{N} when placed in a magnetic field \mathbf{B}_0

$$\mathbf{N} = \boldsymbol{\mu} \times \mathbf{B}_0 \quad (2.1)$$

This torque is equal to the change in angular momentum \mathbf{J} over time when a rotational motion is considered

$$\mathbf{N} = \frac{d}{dt} \mathbf{J} \quad (2.2)$$

Using the gyromagnetic ratio γ [7, 15] which defines the relative magnitude of magnetic moment $\boldsymbol{\mu}$ and angular momentum \mathbf{J}

$$\boldsymbol{\mu} = \gamma \mathbf{J} \quad (2.3)$$

the equation of motion of a magnetic moment in a magnetic field becomes

$$\frac{d}{dt} \boldsymbol{\mu} = \gamma \boldsymbol{\mu} \times \mathbf{B}_0 \quad (2.4)$$

Assuming the external magnetic field is pointing in the positive z -direction, $\mathbf{B}_0 = B_0 \mathbf{e}_z$, the equation of motion is solved by

$$\begin{aligned} \boldsymbol{\mu}(\mathbf{t}) &= \begin{bmatrix} \mu_x(t) \\ \mu_y(t) \\ \mu_z(t) \end{bmatrix} = \begin{bmatrix} \mu_x(0) \cos \omega_0 t - \mu_y(0) \sin \omega_0 t \\ \mu_y(0) \cos \omega_0 t + \mu_x(0) \sin \omega_0 t \\ \mu_z(0) \end{bmatrix} \\ &= \begin{bmatrix} \cos \omega_0 t & -\sin \omega_0 t & 0 \\ \sin \omega_0 t & \cos \omega_0 t & 0 \\ 0 & 0 & 1 \end{bmatrix} \begin{bmatrix} \mu_x(0) \\ \mu_y(0) \\ \mu_z(0) \end{bmatrix} \end{aligned} \quad (2.5)$$

This can be interpreted as a rotation applied to the initial magnetic moment $\boldsymbol{\mu}(0)$ which is oscillating with the so-called Larmor frequency

$$\omega_0 = -\gamma B_0 \quad (2.6)$$

around the direction of the external magnetic field at a constant angle θ . At equilibrium the energy

$$E = -\boldsymbol{\mu} B_0 \cos \theta \quad (2.7)$$

of the system has to be minimal and the magnetic moment will be aligned with the magnetic field \mathbf{B}_0 . However, in order to produce an observable effect an alternating magnetic moment is necessary. An additional (radiofrequency) field \mathbf{B}_1 that is applied perpendicular to the static magnetic field \mathbf{B}_0 causes an additional torque perpendicular to \mathbf{B}_0 (compare Eq. (2.1)). Because of the Larmor precession, this is just causing a quivering motion of the magnetic moment if $\mathbf{B}_0 \gg \mathbf{B}_1$. However, if the \mathbf{B}_1 is constantly perpendicular to \mathbf{B}_0 and $\boldsymbol{\mu}(\mathbf{t})$ and thus is rotating in the xy -plane at the Larmor frequency ω_0 , the magnetisation undergoes additional rotations around \mathbf{B}_1 and a resonance effect

occurs. This model is capable of describing the behaviour of an ensemble of isolated spins quite satisfactorily but is reaching its limits when also spin-spin interactions have to be taken into account.

It is not enough to introduce heuristic magnetic moments in the context of atomic nuclei. As has been shown by N. Bohr and H.J. van Leeuwen [16] the magnetisation at thermal equilibrium vanishes if it is described classically (i.e. no spin). Accordingly theory needs to take into account the multitude of spin interactions. This is achieved by the profound treatment of spin provided by quantum mechanics.

2.1.1. Spins and the Magnetic Moment

The concept of spin was first introduced by Uhlenbeck and Goudsmit [17] for the electron. Spin was later recognised to be an intrinsic property of all elementary particles including atomic nuclei.

An atomic nucleus contains neutrons and protons which are commonly referred to as nucleons [7]. A nucleon is characterised by three inherent properties: mass, charge and spin. Both neutron and proton have the spin $S = \frac{1}{2}$, but differ in their values of mass and charge [7] ($m_{\text{proton}} = 1.6726231 \cdot 10^{-27}$ kg, $m_{\text{neutron}} = 1.6749286 \cdot 10^{-27}$ kg, $q_{\text{proton}} = 1.60217733 \cdot 10^{-19}$ C, $q_{\text{neutron}} = 0$ C). The nucleus represents a combination of spins that according to the relative orientation of the proton and neutron spins either add or subtract to yield a net spin. The resulting magnetic moment is dependent on the ratio proton-to-neutron in the nucleus (protons and neutrons have different gyromagnetic ratios γ) as well as on its excitation state. Here only ground-state nuclei need to be considered which is generally true for NMR of samples at ambient conditions [2]: For example, the energy difference between the ground state and the excited state of a ^2H nucleus is $\approx 10^{11} \frac{\text{kJ}}{\text{mol}}$ which greatly exceeds any energies used in NMR experiments (see Chapter 1, Eq. (2.7)). There is no easy rule to tell which of the many possible combinations of protons and neutrons form the ground-state of a nucleus since this is dependent on the structure of the nucleus itself. Therefore, the ground-state spin is dealt with here as an empirical property of an isotope. The gyromagnetic ratio γ can be seen as a visualisation of the complex nuclear structure as it gives the ratio between the nuclear magnetic moment and the spin angular momentum. As can be seen in Table 2.1 on page 5 the value of γ can be either

Isotope	Natural Abundance [%]	Gyromagnetic ratio $\gamma/10^6$ [$\frac{\text{rad}}{\text{s}\cdot\text{T}}$]
^1H	~ 100	267.522
^{13}C	~ 1.1	67.283
^{29}Si	~ 4.7	-53.190
^{31}P	~ 100	108.394
^{119}Sn	~ 8.6	-100.317
^{19}F	~ 100	251.8148
^{195}Pt	~ 33.8	58.385

Table 2.1.: Gyromagnetic ratios [15] for some nuclei with spin $S = \frac{1}{2}$. The corresponding Larmor frequencies can be calculated using Eq. (2.6).

positive or negative, describing parallel or antiparallel orientations of spin and magnetic moment.

2.1.2. Quantum-Mechanical Description [5, 18]

Whereas in classical mechanics all information about the state of a physical system is fixed by a point in its phase space, in quantum mechanics the state of a system is represented by a so-called state vector $|\psi\rangle$, which is defined in a complex vector space. This vector space is called Hilbert space \mathfrak{H} . Following the developments of P.A.M. Dirac [19], $|\psi\rangle$ is referred to as a *ket* vector and $\langle\psi|$ as a *bra* vector. Both are defined in their own but dual Hilbert space and are defined as to contain all the information about the physical system.

Classical observables such as angular momentum \mathbf{J} are defined to be represented by linear operators, like the angular momentum operator $\hat{\mathbf{J}}$. These operators are defined in the Hilbert space of the corresponding physical system which is defined by the state vector $|\psi\rangle$.

In general an operator acting on a state vector is not keeping the state vector in its original form. However, there are particular kets of importance, known as eigenkets of an operator with the property

$$\begin{aligned}\hat{A}|a_1\rangle &= a_1|a_1\rangle \\ \hat{A}|a_2\rangle &= a_2|a_2\rangle \\ &\vdots \quad \vdots \quad \vdots\end{aligned}\tag{2.8}$$

where a_1, a_2, \dots are scalars and called eigenvalues of the operator \hat{A} . The physical state corresponding to an eigenket is called eigenstate. From this it is clear that the vector space over which an operator \hat{A} is defined is spanned by the N -dimensional basis of its eigenkets $|a_i\rangle$. Further it is postulated that all observables are represented by hermitian operators \hat{A}

$$\hat{A} \equiv \hat{A}^\dagger\tag{2.9}$$

and hence have purely real eigenstates. Eq. (2.9) also implies that the set of eigenkets $\{|a_i\rangle\}$ forms an orthonormal basis of the Hilbert space and therefore obeys

$$\langle a_i | a_j \rangle = \delta_{ij}\tag{2.10}$$

This is a reasonable postulate since we identified operators with the classical observables and therefore the value measured corresponds to the eigenvalues a_i which in turn have to be real. Using this, any arbitrary ket $|\psi\rangle$ can be linearly expanded as

$$\begin{aligned}|\psi\rangle &= \sum_i |a_i\rangle \langle a_i | \psi \rangle \\ &= \sum_i c_{a_i} |a_i\rangle\end{aligned}\tag{2.11}$$

in the basis of the eigenkets $|a_i\rangle$ of the operator \hat{A} , where c_{a_i} are in general complex scalars.

Looking at Eq. (2.11)

$$\hat{A}_{a_i} \equiv |a_i\rangle \langle a_i| \quad (2.12)$$

can be interpreted as a projection operator which, because of the completeness of the basis $|a_i\rangle$, fulfils

$$\sum_i |a_i\rangle \langle a_i| = \mathbb{1}_{\dim(\hat{A})} \quad (2.13)$$

\hat{A} is easiest represented as a matrix in the basis of its eigenstates.

$$\begin{aligned} \hat{A} &= \sum_i \sum_j |a_i\rangle \langle a_i | \hat{A} | a_j \rangle \langle a_j | \\ \hat{A}_{ij} &= a_j \langle a_i | a_j \rangle \delta_{ij} \end{aligned} \quad (2.14)$$

In general this is not the case and also off-diagonal elements of \hat{A} are non-zero.

The measurement of an observable \hat{A} of a system in state $|\psi\rangle$ puts the system into the state $|a_i\rangle$

$$\begin{aligned} \langle \psi | \hat{A} | \psi \rangle &= \sum_i \langle \psi | a_i \rangle \langle a_i | \hat{A} | a_j \rangle \langle a_j | \psi \rangle \\ &= a_i |\langle a_i | \psi \rangle|^2 \end{aligned} \quad (2.15)$$

yielding the eigenvalue a_i . Every following measurement on the same system will now yield the same eigenvalue since $|\psi\rangle$ (Eq. (2.11)) has been reduced to one eigenstate $|a_i\rangle$ of the operator \hat{A} (state reduction). The probability of measuring the eigenvalue a_i on a system in state $|\psi\rangle$ is given in accordance with Eq. (2.15) by

$$|\langle a_i | \psi \rangle|^2 = |c_i|^2 \quad (2.16)$$

The time evolution of a state $|\psi(t)\rangle$ is given by the time-dependent Schrödinger equation

$$i\hbar \frac{\partial}{\partial t} |\psi(t)\rangle = \hat{\mathcal{H}} |\psi(t)\rangle \quad (2.17)$$

where the Hamilton operator $\hat{\mathcal{H}}(\hat{\mathbf{p}}, \hat{\mathbf{q}})$ is derived from the classical Hamilton function $\mathcal{H}(\mathbf{p}, \mathbf{q})$ by replacing the canonical conjugate variables by operators (correspondence principle).

The equation of motion for a particle in a magnetic field \mathbf{B}_0 with a potential \mathbf{A} is

$$i\hbar \frac{\partial}{\partial t} |\psi(t)\rangle = \frac{1}{2m} \hat{\boldsymbol{\pi}}^2 |\psi(t)\rangle \quad (2.18)$$

$$\hat{\boldsymbol{\pi}} = \hat{\mathbf{p}} - e\hat{\mathbf{A}} \quad (2.19)$$

where $\hat{\boldsymbol{\pi}}$ is a generalised canonical momentum. While this equation is readily capable of describing the orbital angular momentum $\hat{\mathbf{L}}$, it does not yet involve the intrinsic spin $\hat{\mathbf{S}}$ of the nucleus. Motivated by Stern-Gerlach experiments which suggested the existence of operators that have two eigenstates, Pauli introduced the so-called Pauli spin matrices [20, 5]

$$\hat{\sigma}_x = \begin{pmatrix} 0 & 1 \\ 1 & 0 \end{pmatrix} \quad \hat{\sigma}_y = \begin{pmatrix} 0 & -i \\ i & 0 \end{pmatrix} \quad \hat{\sigma}_z = \begin{pmatrix} 1 & 0 \\ 0 & -1 \end{pmatrix} \quad (2.20)$$

that obey the following rules

$$[\hat{\sigma}_i; \hat{\sigma}_j]_- = i\epsilon_{ijk}\hat{\sigma}_k \quad (2.21)$$

$$[\hat{\sigma}_i; \hat{\sigma}_j]_+ = 2\delta_{ij}\mathbb{1}_2 \quad (2.22)$$

$$\hat{\sigma}_i^2 = \mathbb{1}_2 \quad (2.23)$$

Eq. (2.22), the anticommutator, is special for spins $S = \frac{1}{2}$ (fermions) and Eq. (2.21) is defining an angular momentum algebra. Pauli replaced the classical generalised momentum $\hat{\boldsymbol{\pi}}$ in Eq. (2.18) by $\hat{\boldsymbol{\sigma}}\hat{\boldsymbol{\pi}}$ using the Pauli spin matrices, yielding

$$i\hbar\frac{\partial}{\partial t}|\psi(t)\rangle = \frac{1}{2m}(\hat{\boldsymbol{\pi}}^2 - \hbar e(\hat{\boldsymbol{\sigma}}\mathbf{B}_0))|\psi(t)\rangle \quad (2.24)$$

$$i\hbar\frac{\partial}{\partial t}|\psi(t)\rangle = (\hat{\mathcal{H}}^\pi + \hat{\mathcal{H}}^S)|\psi(t)\rangle \quad (2.25)$$

Now the first term $\hat{\mathcal{H}}^\pi$ describes the classical generalised momentum $\hat{\boldsymbol{\pi}}$ of the particle, which will be neglected from now on since any orbiting motion of the nucleus itself shall be neglected. The second term is describing an angular momentum and can be written as

$$\begin{aligned} \hat{\mathcal{H}}^S &= -\frac{\hbar e}{2m}\hat{\boldsymbol{\sigma}}\mathbf{B}_0 \\ &= -\gamma_S\hat{\mathbf{S}}\mathbf{B}_0 \end{aligned} \quad (2.26)$$

where γ_S is the quantum-mechanical gyromagnetic ratio. It is important to mention that the quantum mechanical gyromagnetic ratio is not given exactly by $\frac{\hbar e}{2m}$ (see Section 2.1.1). Eq. (2.26) gives the key to the correspondence principle to convert the classical magnetic moment to the quantum mechanical operator

$$\boldsymbol{\mu} \rightarrow \gamma_S\hbar\hat{\mathbf{S}} \quad (2.27)$$

$\hat{\mathbf{S}}$ will from now on be referred to as spin operator which fulfils, together with its corresponding eigenstates $|S, m_S\rangle$, the following eigenequations

$$\hat{S}_z|S, m_S\rangle = \hbar m_S|S, m'_S\rangle\delta_{m_S m'_S} \quad S = \frac{1}{2}; -S \leq m_S \leq S \quad (2.28)$$

$$\hat{S}_x|S, m_S\rangle = \hbar m_S|S, m'_S\rangle\delta_{m_S m'_S \pm 1} \quad (2.29)$$

$$\hat{S}_y|S, m_S\rangle = -i\hbar m_S|S, m'_S\rangle\delta_{m_S m'_S \pm 1} \quad (2.30)$$

$$\hat{S}^2|S, m_S\rangle = \hbar^2 S(S+1)|S, m'_S\rangle\delta_{m_S m'_S} \quad (2.31)$$

where $|S, m_S\rangle$ are the two common eigenstates of both the squared spin operator $\hat{\mathbf{S}}^2$ and its z -component. $\hat{\mathbf{S}}^2$ and \hat{S}_z together form the complete set of compatible observables of a spin $S = \frac{1}{2}$. It follows that every possible orientation of spin $\hat{\mathbf{S}}$ must be representable by a linear superposition of the two eigenstates of $\hat{\mathbf{S}}^2$ and \hat{S}_z . The most general state of

a spin $S = \frac{1}{2}$, represented in the eigenbasis defined by Eq. (2.28), is

$$|\psi\rangle = c_{+\frac{1}{2}} \left| \frac{1}{2}, +\frac{1}{2} \right\rangle + c_{-\frac{1}{2}} \left| \frac{1}{2}, -\frac{1}{2} \right\rangle \quad (2.32)$$

where the phase factors $c_{\pm\frac{1}{2}}$ are related as

$$\frac{c_{+\frac{1}{2}}}{c_{-\frac{1}{2}}} = \frac{\cos \frac{\beta}{2}}{e^{i\alpha} \sin \frac{\beta}{2}} \quad (2.33)$$

and α and β are the azimuth and altitude of the spin orientation. Thus, Eq. (2.32) describes what is called a coherent superposition (coherence) of the eigenstates $|\frac{1}{2}, +\frac{1}{2}\rangle$ and $|\frac{1}{2}, -\frac{1}{2}\rangle$. For example, $|\alpha\rangle = \frac{1}{\sqrt{2}} |\frac{1}{2}, +\frac{1}{2}\rangle + \frac{1}{\sqrt{2}} |\frac{1}{2}, -\frac{1}{2}\rangle$ is describing a spin pointing in the positive x -direction.

The solution to the Schrödinger equation of a single spin in a magnetic field is

$$i\hbar \frac{\partial}{\partial t} |\psi\rangle = -\gamma \hat{S}_z B_0 |\psi\rangle \quad (2.34)$$

with

$$|\psi\rangle = e^{\frac{i}{\hbar} \gamma \hat{S}_z B_0 t} |S, m_S\rangle = e^{-\frac{i}{\hbar} \omega_0 \hat{S}_z t} |S, m_S\rangle \quad (2.35)$$

where $\mathbf{B}_0 = B_0 \mathbf{e}_z$ and $\omega_0 = -\gamma B_0$ (compare Eq. (2.6)).

This is as far as one can go with a single spin. When being concerned with more than one spin all degrees of freedom (eigenstates) of every spin need to be preserved and the common Hilbert space is constructed by combining the Hilbert spaces of the single spins by a tensorial product

$$\mathfrak{H} = \mathfrak{H}^{S_1} \oplus \mathfrak{H}^{S_2} \oplus \dots \quad (2.36)$$

where the dimension of the new Hilbert space is $(2S_1 + 1) \cdot (2S_2 + 1) \cdot \dots$ and the Hamiltonian for two uncoupled spins reads as

$$\hat{\mathcal{H}}^{S_1 S_2} = \omega_0^{S_1} \hat{S}_{1z} \oplus \mathbb{1}_2 + \mathbb{1}_2 \oplus \omega_0^{S_2} \hat{S}_{2z} \quad (2.37)$$

When combining the two Hilbert spaces of the spin operators $\hat{\mathbf{S}}_1$ and $\hat{\mathbf{S}}_2$

$$\hat{\mathbf{S}} = \hat{\mathbf{S}}_1 \oplus \mathbb{1}_2 + \mathbb{1}_2 \oplus \hat{\mathbf{S}}_2 \quad (2.38)$$

there exist two sets of mutually compatible observables and their respective eigenstates

$$\hat{\mathbf{S}}_1^2 |S_1 S_2; m_{S_1} m_{S_2}\rangle = \hbar^2 S_1 (S_1 + 1) |S_1 S_2; m_{S_1} m_{S_2}\rangle \quad (2.39)$$

$$\hat{S}_{1z} |S_1 S_2; m_{S_1} m_{S_2}\rangle = \hbar m_1 |S_1 S_2; m_{S_1} m_{S_2}\rangle \quad (2.40)$$

$$\hat{\mathbf{S}}_2^2 |S_1 S_2; m_{S_1} m_{S_2}\rangle = \hbar^2 S_2 (S_2 + 1) |S_1 S_2; m_{S_1} m_{S_2}\rangle \quad (2.41)$$

$$\hat{S}_{2z} |S_1 S_2; m_{S_1} m_{S_2}\rangle = \hbar m_2 |S_1 S_2; m_{S_1} m_{S_2}\rangle \quad (2.42)$$

and

$$\hat{S}_1^2 |S_1 S_2; S m_S\rangle = \hbar^2 S_1 (S_1 + 1) |S_1 S_2; S m_S\rangle \quad (2.43)$$

$$\hat{S}_2^2 |S_1 S_2; S m_S\rangle = \hbar^2 S_2 (S_2 + 1) |S_1 S_2; S m_S\rangle \quad (2.44)$$

$$\hat{S}^2 |S_1 S_2; S m_S\rangle = \hbar^2 S (S + 1) |S_1 S_2; S m_S\rangle \quad (2.45)$$

$$\hat{S}_z |S_1 S_2; S m_S\rangle = \hbar m |S_1 S_2; S m_S\rangle \quad (2.46)$$

for which

$$m_S = m_{S_1} + m_{S_2}$$

and

$$|S_1 - S_2| \leq S \leq S_1 + S_2$$

is true. The basekets of these two sets for two spins $S_1 = \frac{1}{2}$ and $S_2 = \frac{1}{2}$ are related by

$$|S_1 S_2; S = 1, m_S = 1\rangle = \left| S_1 S_2; \frac{1}{2}, \frac{1}{2} \right\rangle \quad (2.47)$$

$$|S_1 S_2; S = 1, m_S = 0\rangle = \frac{1}{\sqrt{2}} \left(\left| S_1 S_2; \frac{1}{2}, -\frac{1}{2} \right\rangle + \left| S_1 S_2; -\frac{1}{2}, \frac{1}{2} \right\rangle \right) \quad (2.48)$$

$$|S_1 S_2; S = 0, m_S = 0\rangle = \frac{1}{\sqrt{2}} \left(\left| S_1 S_2; \frac{1}{2}, -\frac{1}{2} \right\rangle - \left| S_1 S_2; -\frac{1}{2}, \frac{1}{2} \right\rangle \right) \quad (2.49)$$

$$|S_1 S_2; S = 1, m_S = -1\rangle = \left| S_1 S_2; -\frac{1}{2}, -\frac{1}{2} \right\rangle \quad (2.50)$$

Finally it is useful to make the distinction between cases where spins are indistinguishable, the so-called homonuclear case

$$[\hat{S}_{1i}, \hat{S}_{2j}] = i\hbar \epsilon_{ijk} \hat{S}_k; \quad (2.51)$$

and the case of distinguishable spins, the so-called heteronuclear case

$$[\hat{S}_{1i}, \hat{S}_{2j}] = 0 \quad (2.52)$$

Up to this point no interactions between spins have been considered and the Hamiltonian $\hat{\mathcal{H}}^S$ contains no structural information at all. In the following Section a closer look at the nuclear spin interactions will be taken.

2.2. Nuclear Spin Interactions [1, 2, 14, 21]

Since the spin has no classical analogue it is not immediately possible to apply a correspondence principle enabling the transition from the classical interaction described by the Hamilton function to the quantum mechanical Hamilton operator $\hat{\mathcal{H}}$. But Eq. (2.26) which describes a spin - magnetic field interaction suggests the conversion $\boldsymbol{\mu} \rightarrow \hbar\gamma\hat{\mathbf{S}}$ from the classical magnetic moment to the quantum mechanical spin term. Thus, in the following spin-interaction terms will be derived from classical magnetic interactions. From classical electrodynamics and especially from the Maxwell equations [4] it follows that every inter-

action of magnetic moments amongst themselves or with magnetic fields can be described by tensors of rank two mediating a two-body interaction.

The Hamilton operator $\hat{\mathcal{H}}$ used to describe a system of interacting spins under the influence of a strong external magnetic field \mathbf{B}_0 can be structured into different parts according to the nature of the interactions. First there are the interactions of a spin with magnetic fields applied to the sample which are described by so-called external Hamiltonians, and second there are the interactions of a spin with magnetic moments that are contained in the sample itself and these are described by so-called internal Hamiltonians.

Since the description of magnetic moments in the magnetic field leads to rotational motion (see Section 2.1) it is convenient to write Hamiltonians in dimensions of angular velocity ($[\hat{\mathcal{H}}] = [\frac{\text{rad}}{\text{s}}]$) after conversion from energy units by dividing the Hamiltonian $\hat{\mathcal{H}}$ by \hbar .

2.2.1. Zeeman Interaction

The only parameters the external Hamiltonian in Eq. (2.26) is dependent on are the gyromagnetic ratio γ_S and the spin quantum number S which are the same for all spins of the same isotope. The interaction of $\boldsymbol{\mu}$ with \mathbf{B}_0 is called the Zeeman interaction and its Hamilton function is (see Eq. (2.7))

$$\mathcal{H}^Z = -\boldsymbol{\mu}\mathbf{B}_0 \quad (2.53)$$

where the Hamilton operator becomes

$$\hat{\mathcal{H}}^Z = -\gamma_S \cdot \hat{\mathbf{S}} \cdot \mathbb{1}_3 \cdot \mathbf{B}_0 \quad (2.54)$$

and where the external magnetic field will always be assumed to be $\mathbf{B}_0 = B_0\mathbf{e}_z$. $\hat{\mathbf{S}} = \hat{S}_x\mathbf{e}_x + \hat{S}_y\mathbf{e}_y + \hat{S}_z\mathbf{e}_z$ is the spin operator of spin $S = \frac{1}{2}$ and $\mathbb{1}_3$, is a unit tensor of dimension 3 introduced to permit describing all interactions by tensors.

As pointed out in Section 2.1 nuclear magnetic moments in a magnetic field are rotating at the Larmor frequency $\omega_0/2\pi$ around the magnetic field $B_0\mathbf{e}_z$. Since the nucleons making up the nucleus do not only carry spin (magnetic moment) but also charge (protons) one also has to consider the interaction of a rotating charge distribution with the external magnetic field. For spin $S = \frac{1}{2}$ nuclei the charge distribution in the nucleus is spherical so any rotation of the nucleus cannot introduce additional magnetic effects. For nuclei with $S > \frac{1}{2}$ the charge distribution is generally not spherical and additional interactions are present (quadrupolar interaction).

2.2.2. Chemical Shielding

The magnetic field at the nucleus is equal to an external magnetic field \mathbf{B}_0 only for a naked atomic nucleus. In matter, \mathbf{B}_0 induces magnetic moments in the electron distribution surrounding the nuclei which leads to a local magnetic field \mathbf{B}^{loc} that can be written as

the sum of the external field \mathbf{B}_0 and the induced field \mathbf{B}^{CS}

$$\begin{aligned}\mathbf{B}^{\text{loc}} &= \mathbf{B}_0 + \mathbf{B}^{CS} \\ &= (1 + \mathbf{CS})\mathbf{B}_0\end{aligned}\quad (2.55)$$

The tensor \mathbf{CS} is describing the orientation dependent chemical shielding interaction of a spin $\hat{\mathbf{S}}$. This contribution is dependent on the electronic environment of the nuclear spin and by this carries information about chemical bonding and structure. In diamagnetic samples the magnitude of the chemical shielding interaction is about 10^{-4} to 10^{-9} of the Zeeman interaction. It is typically in the range of about 100 Hz to 100 kHz for both isotropic and anisotropic shielding effects ($\mathbf{CS}_{\text{iso}} \approx \mathbf{CS}_{\text{aniso}}$) [22]. It increases generally for isotopes of increasingly heavy elements. In introducing this chemical shielding interaction the spin Hamiltonian can be written as

$$\hat{\mathcal{H}} = \mathcal{H}^Z + \mathcal{H}^{CS} \quad (2.56)$$

$$\hat{\mathcal{H}} = -\gamma_S \hat{\mathbf{S}} (1 + \mathbf{CS}) \mathbf{B}_0 \quad (2.57)$$

with

$$\hat{\mathcal{H}}^{CS} = -\gamma_S \cdot \hat{\mathbf{S}} \cdot \mathbf{CS} \cdot \mathbf{B}_0 \quad (2.58)$$

being the chemical shielding term of the spin Hamiltonian.

2.2.3. Direct Dipolar Coupling Interaction

If two spins are spatially close to each other their nuclear magnetic moments exhibit a mutual dipolar magnetic interaction which is called direct dipolar coupling. Accordingly the Hamilton function of a pair of spins $\hat{\mathbf{S}}_1, \hat{\mathbf{S}}_2$ in spatial proximity to each other has a contribution independent of the external magnetic field

$$\mathcal{H}^{D_{12}} = \frac{\boldsymbol{\mu}_1 \boldsymbol{\mu}_2 - 3(\boldsymbol{\mu}_1 \mathbf{e}_{12})(\boldsymbol{\mu}_2 \mathbf{e}_{12})}{|\mathbf{r}_{12}|^3} \quad (2.59)$$

with $\mathbf{r}_{12} = \mathbf{r}_2 - \mathbf{r}_1 = |\mathbf{r}_{12}| \mathbf{e}_{12}$. Using the correspondence principle, this interaction can be described by a dipolar coupling tensor \mathbf{D}^{12} as

$$\hat{\mathcal{H}}^{D_{12}} = -b_{12} \left[\hat{\mathbf{S}}_1 \hat{\mathbf{S}}_2 - 3 \left(\hat{\mathbf{S}}_1 \mathbf{e}_{12} \right) \left(\hat{\mathbf{S}}_2 \mathbf{e}_{12} \right) \right] \quad (2.60)$$

$$\hat{\mathcal{H}}^{D_{12}} = -b_{12} \cdot \hat{\mathbf{S}}_1 \cdot \mathbf{D}^{12} \cdot \hat{\mathbf{S}}_2 \quad (2.61)$$

with the direct dipolar coupling constant

$$b_{12} = -\frac{\mu_0 \gamma_{S_1} \gamma_{S_2} \hbar}{4\pi |\mathbf{r}_{12}|^3} \quad (2.62)$$

in units of $\left[\frac{\text{rad}}{\text{s}}\right]$. $\mu_0 = 4\pi \cdot 10^7 \frac{\text{Vs}}{\text{Am}}$ is the vacuum permeability and $\mathbf{D}_{ij}^{12} = \delta_{ij} - 3\mathbf{e}_{1i}\mathbf{e}_{2j}$ the dipolar coupling tensor using the Kronecker δ_{ij} tensor. Typical values of $b_{12}/2\pi$ are given

in Table 2.2 on page 13

Distance [pm]	$b_{12}/2\pi$ [Hz] $\{^{13}\text{C}, ^{13}\text{C}\}$	$b_{12}/2\pi$ [Hz] $\{^{13}\text{C}, ^1\text{H}\}$	$b_{12}/2\pi$ [Hz] $\{^1\text{H}, ^1\text{H}\}$
140	-2767	-11001	-43772
200	-949	-3775	-15014
300	-281	-1119	-4449
400	-118	-472	-1877
550	-46	-182	-722

Table 2.2.: Some typical interatomic distances and the corresponding direct dipolar coupling constants $b_{12}/2\pi$ for $\{^{13}\text{C}, ^{13}\text{C}\}$, $\{^{13}\text{C}, ^1\text{H}\}$, $\{^1\text{H}, ^1\text{H}\}$ spin pairs.

2.2.4. Indirect Dipolar Coupling Interaction

Nuclear magnetic moments interact not only by means of the direct (through space) dipolar coupling. They are also influenced by dipolar interactions mediated by the electrons involved in the chemical bond between the two corresponding atoms. This coupling is called J coupling or indirect dipolar coupling

$$\mathcal{H}^{J_{12}} = \boldsymbol{\mu}_1 \mathbf{J}^{12} \boldsymbol{\mu}_2 \quad (2.63)$$

$$\hat{\mathcal{H}}^{J_{12}} = \gamma_{S_1} \gamma_{S_2} \hat{\mathbf{S}}_1 \cdot \mathbf{J}^{12} \cdot \hat{\mathbf{S}}_2 \quad (2.64)$$

Typical magnitudes of $\mathbf{J}_{\text{iso}}^{12}$ are about 1 Hz to 1 kHz [23, 24, 25, 26, 27, 28, 29]. The anisotropic part $\mathbf{J}_{\text{aniso}}^{12}$ has the same mathematical form as the direct dipolar coupling tensor \mathbf{D}^{12} . Therefore, it is generally difficult to distinguish contributions from $\mathbf{J}_{\text{aniso}}^{12}$ and \mathbf{D}^{12} . There are only few cases where $\mathbf{J}_{\text{aniso}}^{12}$ has been determined unambiguously, leading to values that are generally of the order of the corresponding isotropic J -coupling constant ($\mathbf{J}_{\text{iso}}^{12} \approx \mathbf{J}_{\text{aniso}}^{12}$) [23, 24, 25, 30, 26, 27, 28, 29].

2.2.5. High-Field Approximation and Rotating Frame of Reference

The Zeeman interaction of a spin \mathbf{S} with an external magnetic field is several orders of magnitude (compare Subsections 2.2.1 to 2.2.4) larger than the contribution of all other terms in the Hamiltonian. This makes it possible to apply a perturbation approach [5] which splits the Hamiltonian $\hat{\mathcal{H}}$ into a part $\hat{\mathcal{H}}_0$ which is commuting with the Zeeman interaction $\hat{\mathcal{H}}^Z$, and a perturbation part $\hat{\mathcal{H}}_1$ which does not commute with $\hat{\mathcal{H}}^Z$

$$\hat{\mathcal{H}} = \hat{\mathcal{H}}_0 + \hat{\mathcal{H}}_1 \quad (2.65)$$

Since $\hat{\mathcal{H}}_0$ and the Zeeman Hamiltonian $\hat{\mathcal{H}}^Z$ commute, they share a common set of eigenstates $|\alpha^Z\rangle = \exp(i\omega_0 \hat{S}_z t)$ (Eq. (2.35)) and the perturbation up to first order can be

written as

$$\hat{\mathcal{H}} = \hat{\mathcal{H}}^{(0)} + \hat{\mathcal{H}}^{(1)} + \dots \quad (2.66)$$

$$\hat{\mathcal{H}}^{(0)} = \hat{\mathcal{H}}_0 \quad (2.67)$$

$$\hat{\mathcal{H}}^{(1)} = e^{-i\omega_0 \hat{S}_z t} \hat{\mathcal{H}}_1 e^{i\omega_0 \hat{S}_z t} \quad (2.68)$$

The Larmor frequency $\omega_0 = -\gamma_S B_0$ in the first perturbation term depends linearly on the strength of the magnetic field. Hence the small first order perturbation terms are fluctuating rapidly if B_0 is large and can then safely be neglected. This high-field approximation is generally applicable for spin $S = \frac{1}{2}$ systems but sometimes needs to be reconsidered for spins with higher quantum numbers when quadrupolar interactions come into play.

The Hamiltonian within the limits of the high-field approximation $\hat{\mathcal{H}} = \hat{\mathcal{H}}_0$ is dominated by the Zeeman interaction. However, as can be seen from the spin-interaction Hamiltonians (Section 2.2.1 to 2.2.4) most of the information is contained not in the Zeeman term but in the remaining terms of the Hamiltonian. In order to access this information in a convenient way and without having to deal with the contributions of the Zeeman term it is common practise to apply a coordinate transformation to a suitable reference frame [21, 31]. Here this is accomplished by a transformation to a frame rotating at the Larmor frequency about the z -direction of the magnetic field. The Hamiltonian in the rotating frame $\hat{\mathcal{H}}_R$ is then

$$\hat{\mathcal{H}}_R = \hat{\mathcal{H}}_0 - \omega_0 \hat{S}_z \quad (2.69)$$

The contribution of the Zeeman interaction $\hat{\mathcal{H}}^Z = \omega_0 \hat{S}_z$ to the high-field Hamiltonian $\hat{\mathcal{H}}_0$ in the rotating frame is cancelled and $\hat{\mathcal{H}}_R$ just depends on the more informative spin interactions. The high-field approximation and the rotating frame of reference will be used from now on and the Hamiltonian $\hat{\mathcal{H}}_R$ will be referred to as $\hat{\mathcal{H}}$.

2.2.6. Representations of Nuclear Spin Interactions

All Hamiltonians in Eqs. (2.54), (2.58), (2.61), and (2.64) exhibit a common structure [32, 33]

$$\hat{\mathcal{H}}^\lambda = C^\lambda \mathbf{U} \cdot \mathbf{A}^\lambda \cdot \mathbf{V} \quad (2.70)$$

where λ is Z , CS , D or J for Zeeman, chemical shielding, direct dipolar coupling or indirect dipolar coupling interactions, respectively. \mathbf{A}^λ is the tensor corresponding to the interaction λ . \mathbf{U} , \mathbf{V} are either a spin operator $\hat{\mathbf{S}}_i$ or the external magnetic field $B_0 \mathbf{e}_z$, depending on the interaction λ . C^λ is a constant factor. Expanding the Hamiltonian in a Cartesian basis

$$\begin{aligned} \hat{\mathcal{H}}^\lambda &= C^\lambda \sum_u^3 \sum_v^3 \langle 1 | \mathbf{U} | u \rangle \langle u | \mathbf{A} | v \rangle \langle v | \mathbf{V} | 1 \rangle && \text{with } u, v \in \{x, y, z\} \\ &= C^\lambda \sum_u^3 \sum_v^3 \langle u | \mathbf{A} | v \rangle \langle v | \mathbf{V} | 1 \rangle \langle 1 | \mathbf{U} | u \rangle \end{aligned} \quad (2.71)$$

the Hamiltonian can be further simplified

$$\begin{aligned}\hat{\mathcal{H}}^\lambda &= C^\lambda \mathbf{A}^\lambda \circ \mathbf{X} \\ &= C^\lambda \sum_{u,v}^3 A_{uv} X_{vu}\end{aligned}\quad (2.72)$$

which is equal to the scalar product between the interaction tensor \mathbf{A}^λ and a tensor \mathbf{X} , where \mathbf{X} is defined as the dyadic product

$$\mathbf{X} = \mathbf{V} \bullet \mathbf{U} \quad (2.73)$$

$$X_{ij} = V_i U_j \quad (2.74)$$

such that a Cartesian tensor of rank 2 is directly obtained. The Hamiltonian is now a scalar product of two Cartesian second rank tensors.

Generally tensors are defined, in a rather unintuitive way, by the transformation behaviour of an object under rotation. The difficulty with Cartesian tensors such as \mathbf{X} is that they are reducible — that is, they can be decomposed into objects that transform differently under rotations. X_{ij} can be written as

$$\begin{aligned}U_i V_j &= \underbrace{\frac{1}{3} \text{Tr} \{ \mathbf{U} \bullet \mathbf{V} \} \delta_{ij}}_{\text{scalar}} + \underbrace{\frac{1}{2} (U_i V_j - U_j V_i)}_{\text{vector}} + \\ &\quad + \underbrace{\frac{1}{2} \left(U_i V_j + U_j V_i - \frac{2}{3} \text{Tr} \{ \mathbf{U} \bullet \mathbf{V} \} \delta_{ij} \right)}_{\text{matrix}}\end{aligned}\quad (2.75)$$

which corresponds to the irreducible decomposition of $U_i V_j$ with respect to the three dimensional rotation group $\text{SO}(3)$ [34]. The first summand, $\text{Tr} \{ \mathbf{U} \bullet \mathbf{V} \}$ is clearly a scalar product and therefore invariant under rotations. The second summand is an antisymmetric tensor which can be written as $\epsilon_{ijk} (\mathbf{U} \times \mathbf{V})_k$ and therefore behaves like a vector under rotations [5, 34]. The third summand is a symmetric tensor of rank 2 and therefore transforms like a matrix. For this reason it would be preferable to write the second rank tensors \mathbf{A}^λ and \mathbf{X} in terms of components that always transform equally under rotations (see Section 2.2.6.1). The antisymmetric component of \mathbf{X} is not commuting with the Zeeman interaction, leading to the suppression of all terms of rank 1 of \mathbf{X} and \mathbf{A}^λ in the high-field approximation.

\mathbf{A}^λ can be broken up in the same way as \mathbf{X} into rank 0 and rank 2 irreducible terms. Since the interaction tensors represented by \mathbf{A}^λ are describing the physical properties of the different interactions, it is convenient to define some parameters that reflect the shape of the interactions (isotropic, anisotropic) in a direct way [35]. In its principal axes system

(PAS) representation the interaction tensor can most easily be written as

$$\begin{aligned} \mathbf{A}^\lambda (\text{PAS}) &= \begin{pmatrix} \omega_{xx}^\lambda & 0 & 0 \\ 0 & \omega_{yy}^\lambda & 0 \\ 0 & 0 & \omega_{zz}^\lambda \end{pmatrix} \\ &= \omega_{\text{iso}}^\lambda \begin{pmatrix} 1 & 0 & 0 \\ 0 & 1 & 0 \\ 0 & 0 & 1 \end{pmatrix} + \omega_{\text{aniso}}^\lambda \begin{pmatrix} -\frac{1}{2}(\eta^\lambda + 1) & 0 & 0 \\ 0 & \frac{1}{2}(\eta^\lambda - 1) & 0 \\ 0 & 0 & 1 \end{pmatrix} \end{aligned} \quad (2.76)$$

where $\omega_{\text{iso}}^\lambda$, $\omega_{\text{aniso}}^\lambda$, and η^λ are defined as

$$\omega_{\text{iso}}^\lambda = \frac{1}{3} \text{Tr} \{ \mathbf{A}^\lambda \} \quad (\text{isotropic value}) \quad (2.77)$$

$$\omega_{\text{aniso}}^\lambda = \omega_{zz}^\lambda - \omega_{\text{iso}}^\lambda \quad (\text{anisotropy}) \quad (2.78)$$

$$\eta^\lambda = \frac{\omega_{yy}^\lambda - \omega_{xx}^\lambda}{\omega_{\text{aniso}}^\lambda} \quad (\text{asymmetry parameter}) \quad (2.79)$$

Together with the ordering of the eigenvalues of \mathbf{A}^λ according to [35]

$$\left| \omega_{zz}^\lambda - \omega_{\text{iso}}^\lambda \right| \geq \left| \omega_{xx}^\lambda - \omega_{\text{iso}}^\lambda \right| \geq \left| \omega_{yy}^\lambda - \omega_{\text{iso}}^\lambda \right| \quad (2.80)$$

the shape of the interaction tensors is now parameterised in a meaningful way.

2.2.6.1. Rotational Properties of Nuclear Spin Interactions

The rotation of a Cartesian tensor $\mathbf{A}(X, Y, Z)$ from the coordinate system $\{\mathbf{e}_X, \mathbf{e}_Y, \mathbf{e}_Z\}$ to the system with the basis $\{\mathbf{e}_x, \mathbf{e}_y, \mathbf{e}_z\}$ is generally described using the rotation matrix R

$$\mathbf{A}(x, y, z) = R \mathbf{A}(X, Y, Z) R^{-1} \quad (2.81)$$

The general form of these rotation operators is [34]

$$\hat{R}_{\mathbf{n}}(\varphi) = e^{-\frac{i}{\hbar} \varphi \mathbf{n} \cdot \hat{\mathbf{J}}} \quad (2.82)$$

Here $\hat{\mathbf{J}}$ is a generalised angular momentum operator that is the generator of rotation in its Hilbert space. Hence $\hat{\mathbf{J}} \rightarrow \hat{\mathbf{L}}$ is the orbital angular momentum operator for rotations in real space and $\hat{\mathbf{J}} \rightarrow \hat{\mathbf{S}}$ is the spin operator generating rotations in spin space. \mathbf{n} is a normal vector pointing along the rotation axis and φ is the rotation angle. Rotation operators are most conveniently used when describing rotations around the principal axes of the tensor. It is advantageous to make use of Euler's theorem [34], stating that every rotational transformation of a tensor can be uniquely defined by three successive rotations that generally do not commute. Using this theorem Eq. (2.81) can be written as

$$\begin{aligned} \mathbf{A}^\lambda(x, y, z) &= \hat{R}(\varphi) \mathbf{A}^\lambda(X, Y, Z) \hat{R}(\varphi)^\dagger \\ &= \hat{R}(\alpha, \beta, \gamma) \mathbf{A}^\lambda(X, Y, Z) \hat{R}(\alpha, \beta, \gamma)^\dagger \end{aligned} \quad (2.83)$$

with $\hat{R}(\alpha, \beta, \gamma)$ being either

$$\hat{R}_{z,y',Z}(\alpha, \beta, \gamma) = e^{-\frac{i}{\hbar}\hat{J}_z\gamma} e^{-\frac{i}{\hbar}\hat{J}_{y'}\beta} e^{-\frac{i}{\hbar}\hat{J}_z\alpha} \quad (2.84)$$

or

$$\hat{R}_{Z,Y,Z}(\alpha, \beta, \gamma) = e^{-\frac{i}{\hbar}\hat{J}_Z\alpha} e^{-\frac{i}{\hbar}\hat{J}_Y\beta} e^{-\frac{i}{\hbar}\hat{J}_Z\gamma} \quad (2.85)$$

depending on the definition of the rotation axes. $\hat{R}_{z,y',Z}(\alpha, \beta, \gamma)$ is describing the three rotations about the body-fixed axes $\{z, y', Z\}$ of the tensor, while $\hat{R}_{Z,Y,Z}(\alpha, \beta, \gamma)$ is describing the same rotation, but around the space-fixed axes $\{Z, Y, Z\}$.

So far the representation of the interaction tensors is Cartesian whereas the representation of the rotation operators (Eqs. (2.84), (2.85)) is not yet defined. \hat{R} and \hat{R}^\dagger are functions of the angular momentum operator $\hat{\mathbf{J}}$ and since we are concerned primarily with the rotation properties of the interaction tensors, it seems a good idea to represent \hat{R} and \hat{R}^\dagger in a basis most suitable for rotations. This basis is given by the eigenvectors of the angular momentum operator $\hat{\mathbf{J}}$ which in the case of orbital angular momentum $\hat{\mathbf{L}}$, is given by the spherical harmonic functions $Y_l^m(\theta, \varphi)$ [34]. The $Y_l^m(\theta, \varphi)$ form a complete orthogonal basis and therefore are suitable as a set of basis functions. Expanding e.g. the tensor \mathbf{A}^λ in this spherical basis it then transforms as a set of its $(2l + 1)$ components under the $(2l + 1)$ dimensional representation of the rotation group $\text{SO}(3)$ [34] as

$$\begin{aligned} A_l^{\lambda,m}(\text{AAS}) &= \hat{R}(\alpha^\lambda, \beta^\lambda, \gamma^\lambda) A_l^{\lambda,m}(\text{PAS}) \hat{R}^\dagger(\alpha^\lambda, \beta^\lambda, \gamma^\lambda) \\ &= \sum_{m'=-l}^l \mathcal{D}_{m'm}^l(\alpha^\lambda, \beta^\lambda, \gamma^\lambda) A_l^{\lambda,m'}(\text{PAS}) \end{aligned} \quad (2.86)$$

$\mathcal{D}_{m'm}^l(\alpha, \beta, \gamma)$ are the Wigner rotation matrix elements [34] and $A_l^{\lambda,m'}$ the tensor components of tensor \mathbf{A}^λ of rank l in its spherical representation. Using the fact that the eigenstates $|l, m\rangle$ of $\hat{\mathbf{L}}^2$ are also eigenstates of \hat{L}_Z , the Wigner matrix elements can be written as

$$\mathcal{D}_{mm'}^l(\alpha, \beta, \gamma) = \langle l, m' | e^{-\frac{i}{\hbar}\hat{L}_Z\alpha} e^{-\frac{i}{\hbar}\hat{L}_Y\beta} e^{-\frac{i}{\hbar}\hat{L}_Z\gamma} | l, m \rangle \quad (2.87)$$

$$\mathcal{D}_{mm'}^l(\alpha, \beta, \gamma) = e^{-i\alpha m'} d_{m'm}^l(\beta) e^{-i\gamma m} \quad (2.88)$$

where the $d_{m'm}^l(\beta) = \langle l, m' | e^{-\frac{i}{\hbar}\hat{L}_Y\beta} | l, m \rangle$ are the reduced Wigner rotation matrix elements [34] (see Table 2.3 on page 18). Spherical tensor components are defined, according to Racah [36], as objects \mathbb{T}_l^m which obey Eqs. (2.89) to (2.91)

$$[\hat{J}_z, \mathbb{T}_l^m]_- = q \mathbb{T}_l^m \quad (2.89)$$

$$[\hat{J}_\pm, \mathbb{T}_l^m]_- = \sqrt{(l \mp m)(l \pm m + 1)} \mathbb{T}_l^{m\pm 1} \quad (2.90)$$

$$[\mathbb{T}_l^m]^\dagger = (-1) \mathbb{T}_l^{-m} \quad (2.91)$$

where $\hat{\mathbf{J}}$ is an angular momentum operator fulfilling the commutation rule in Eq. (2.21).

	$m = -2$	$m = 0$	$m = 2$
$m' = -2$	$\cos^4 \beta/2$	$\sqrt{3/8} \sin^2 \beta$	$\sin^4 \beta/2$
$m' = -1$	$-1/2 \sin \beta (\cos \beta + 1)$	$\sqrt{3/2} \sin \beta \cos \beta$	$-1/2 \sin \beta (\cos \beta - 1)$
$m' = 0$	$\sqrt{3/8} \sin^2 \beta$	$1/2 (3 \cos^2 \beta - 1)$	$\sqrt{3/8} \sin^2 \beta$
$m' = 1$	$1/2 \sin \beta (\cos \beta - 1)$	$-\sqrt{3/2} \sin \beta \cos \beta$	$1/2 \sin \beta (\cos \beta + 1)$
$m' = 2$	$\sin^4 \beta/2$	$\sqrt{3/8} \sin^2 \beta$	$\cos^4 \beta/2$

Table 2.3.: Reduced Wigner matrix elements $d_{m'm}^2(\beta)$ [34]

Using this set of rules the spherical tensor components of \mathbf{X} are

$$\mathbf{X}_0^0 = \frac{1}{3} \mathbf{U} \mathbf{V} = \frac{1}{3} (U_+ V_- + U_- V_+ + U_z V_z) \quad (2.92)$$

$$\mathbf{X}_1^m = \frac{1}{i\sqrt{2}} (\mathbf{U} \times \mathbf{V})_m \quad (2.93)$$

$$\mathbf{X}_2^{\pm 2} = U_{\pm} V_{\pm} \quad (2.94)$$

$$\mathbf{X}_2^{\pm 1} = \frac{1}{\sqrt{2}} (U_{\pm} V_z + U_z V_{\pm 1}) \quad (2.95)$$

$$\mathbf{X}_2^0 = \frac{1}{\sqrt{6}} (U_+ V_- - 2U_z V_z + U_- V_+) \quad (2.96)$$

2.2.6.2. Spherical Representation of Interaction Hamiltonians

As demonstrated above, the representation of an interaction tensor is most straightforward in its principal axes system (PAS). The irreducible spherical components can be written as functions of the parameters defined in Eqs.(2.77) to (2.79) as

$$\mathbf{A}_0^{0,\lambda} (\text{PAS}) = -\sqrt{3} \omega_{\text{iso}}^{\lambda} \quad (2.97)$$

$$\mathbf{A}_2^{0,\lambda} (\text{PAS}) = \sqrt{\frac{3}{2}} \omega_{\text{aniso}}^{\lambda} \quad (2.98)$$

$$\mathbf{A}_2^{\pm 1,\lambda} (\text{PAS}) = 0 \quad (2.99)$$

$$\mathbf{A}_2^{\pm 2,\lambda} (\text{PAS}) = -\frac{1}{2} \eta^{\lambda} \omega_{\text{aniso}}^{\lambda} \quad (2.100)$$

However, the Hamiltonian is usually dependent on multiple spin interactions represented by interaction tensors which in general do not share a common principal axes system. This makes it necessary to rotate tensors from their PAS to several general axes systems (AAS) by using sets of Euler angles $\Omega_{\text{PA}}^{\lambda} = \{\alpha_{\text{PA}}^{\lambda}, \beta_{\text{PA}}^{\lambda}, \gamma_{\text{PA}}^{\lambda}\}$ [34]

$$\mathbf{A}_2^{0,\lambda} (\text{AAS}) = -\sqrt{3} \omega_{\text{iso}}^{\lambda} \quad (2.101)$$

$$\mathbf{A}_2^{m,\lambda} (\text{AAS}) = \sqrt{\frac{3}{2}} \omega_{\text{aniso}}^{\lambda} \mathcal{D}_{0m}^2 (\Omega_{\text{PA}}^{\lambda}) - \frac{1}{2} \eta^{\lambda} \omega_{\text{aniso}}^{\lambda} \mathcal{D}_{-2m}^2 \left[\left(\Omega_{\text{PA}}^{\lambda} \right) + \mathcal{D}_{2m}^2 \left(\Omega_{\text{PA}}^{\lambda} \right) \right] \quad (2.102)$$

The tensor \mathbf{X} represents the magnetic field $B_0 \mathbf{e}_z$ (see Eq. (2.72)) and thus relates the tensor directly to the laboratory frame (LAB). This makes it reasonable to use LAB as

the final and common axes system and the Hamiltonian can then be written as

$$\begin{aligned}
\hat{\mathcal{H}}(\text{LAB}) &= \sum_{\lambda} C^{\lambda} \mathbf{A}^{\lambda}(\text{LAB}) \circ \mathbf{X}^{\lambda}(\text{LAB}) \quad \text{where } \lambda \in \{Z_i, CS_i, D_{ij}, J_{ij}\} \\
&= \sum_{\lambda} C^{\lambda} \sum_{l=0}^2 \sum_{m=-l}^l (-1)^m \mathbf{A}_l^{m,\lambda}(\text{LAB}) \mathbf{X}_l^{-m,\lambda}(\text{LAB}) \\
&= \sum_{\lambda} -C^{\lambda} \sqrt{3} \omega_{\text{iso}}^{\lambda} \mathbf{X}_0^0 + C^{\lambda} \sum_m (-1)^m \mathbf{A}_2^{m,\lambda}(\text{LAB}) \mathbf{X}_2^{-m} \quad (2.103)
\end{aligned}$$

However, in solid state NMR usually several axes systems are involved (molecular axes system, crystal axes system, etc.) making it necessary to express tensors in these various axes systems. Generally transformations will start with the respective PAS of the tensor and end in the laboratory frame LAB

$$\mathbf{A}^{\lambda}(\text{PAS}) \xrightarrow[\{\alpha_{\text{PL}}^{\lambda}, \beta_{\text{PL}}^{\lambda}, \gamma_{\text{PL}}^{\lambda}\}]{\Omega_{\text{PL}}^{\lambda}} \mathbf{A}^{\lambda}(\text{LAB}) \quad (2.104)$$

A direct rotation to LAB is not always desirable nor is it always possible. Often it is better to have interaction-dependent rotations $\Omega_{\text{PA}}^{\lambda}$ to a common system (AAS) that is related to the LAB by a unique set of angles Ω_{AL}

$$\mathbf{A}^{\lambda}(\text{PAS}) \xrightarrow[\{\alpha_{\text{PA}}^{\lambda}, \beta_{\text{PA}}^{\lambda}, \gamma_{\text{PA}}^{\lambda}\}]{\Omega_{\text{PA}}^{\lambda}} \mathbf{A}^{\lambda}(\text{AAS}) \xrightarrow[\{\alpha_{\text{AL}}, \beta_{\text{AL}}, \gamma_{\text{AL}}\}]{\Omega_{\text{AL}}} \mathbf{A}^{\lambda}(\text{LAB}) \quad (2.105)$$

For example, the direct dipolar coupling tensor \mathbf{D} is directly related to the internuclear distance between two interacting spins and therefore connects directly to a molecule- or crystal-fixed axes system. This, in turn makes it often convenient to express the chemical shielding tensor in relation to the PAS of \mathbf{D} .

A look at \mathbf{X} in Eqs. (2.92) to (2.96) shows that only terms with \mathbf{X}_l^0 commute with the Zeeman interaction and the Hamiltonian is

$$\hat{\mathcal{H}}^{\lambda} = -C^{\lambda} \sqrt{3} \omega_{\text{iso}}^{\lambda} \mathbf{X}_0^0 + C^{\lambda} \mathbf{A}_2^{0,\lambda}(\text{AAS}) \mathbf{X}_2^0 \quad (2.106)$$

where the two components of \mathbf{X} for the chemical shielding are (where $U \rightarrow \hat{S}$, $V \rightarrow B_0 \mathbf{e}_z$, and $\lambda = CS_i$)

$$\mathbf{X}_0^0 = -\frac{1}{\sqrt{3}} B_0 \hat{S}_z \quad (2.107)$$

$$\mathbf{X}_2^0 = \sqrt{\frac{2}{3}} B_0 \hat{S}_z \quad (2.108)$$

For the direct and the indirect dipolar coupling (where $U \rightarrow \hat{S}_1$, $V \rightarrow \hat{S}_2$, and $\lambda = D_{ij}$ or J_{ij}) the \mathbf{X}_l^0 terms become

$$\mathbf{X}_0^0 = -\frac{1}{\sqrt{3}} \left(\hat{S}_{1z} \hat{S}_{2z} + \frac{1}{2} (\hat{S}_{1+} \hat{S}_{2-} + \hat{S}_{1-} \hat{S}_{2+}) \right) \quad (2.109)$$

$$\mathbf{X}_2^0 = \frac{1}{\sqrt{6}} \left(2 \hat{S}_{1z} \hat{S}_{2z} - \frac{1}{2} (\hat{S}_{1+} \hat{S}_{2-} + \hat{S}_{1-} \hat{S}_{2+}) \right) \quad (2.110)$$

The general structure of the Hamiltonians can now be written as

$$\hat{\mathcal{H}}^{CS_i} = \omega^{CS_i} \left(\omega_{\text{iso}}^{CS_i}, \omega_{\text{aniso}}^{CS_i}, \eta^{CS_i}, \alpha_{\text{PL}}^{CS_i}, \beta_{\text{PL}}^{CS_i}, \gamma_{\text{PL}}^{CS_i} \right) \hat{S}_{iz} \quad (2.111)$$

$$\hat{\mathcal{H}}^{D_{ij}} = \omega^{D_{ij}} \left(b^{D_{ij}}, \alpha_{\text{PL}}^{D_{ij}}, \beta_{\text{PL}}^{D_{ij}}, \gamma_{\text{PL}}^{D_{ij}} \right) \left[2\hat{S}_{iz}\hat{S}_{jz} - \frac{1}{2} \left(\hat{S}_{i+}\hat{S}_{j-} + \hat{S}_{i-}\hat{S}_{j+} \right) \right] \quad (2.112)$$

$$\hat{\mathcal{H}}^{J_{ij}^{\text{iso}}} = \omega^{J_{ij}^{\text{iso}}} \left[2\hat{S}_{iz}\hat{S}_{jz} + \frac{1}{2} \left(\hat{S}_{i+}\hat{S}_{j-} + \hat{S}_{i-}\hat{S}_{j+} \right) \right] \quad (2.113)$$

$$\hat{\mathcal{H}}^{J_{ij}^{\text{aniso}}} = \omega^{J_{ij}^{\text{aniso}}} \left(\omega_{\text{aniso}}^{J_{ij}}, \eta^{J_{ij}} \alpha_{\text{PL}}^{J_{ij}}, \beta_{\text{PL}}^{J_{ij}}, \gamma_{\text{PL}}^{J_{ij}} \right) \left[2\hat{S}_{iz}\hat{S}_{jz} - \frac{1}{2} \left(\hat{S}_{i+}\hat{S}_{j-} + \hat{S}_{i-}\hat{S}_{j+} \right) \right] \quad (2.114)$$

For heteronuclear coupling interactions in addition the commutation relation Eq. (2.52) is valid and the Hamiltonian for these spin-spin couplings can be further simplified to

$$\hat{\mathcal{H}}^{D_{ij}} = \omega^{D_{ij}} \left(b^{D_{ij}}, \alpha_{\text{PL}}^{D_{ij}}, \beta_{\text{PL}}^{D_{ij}}, \gamma_{\text{PL}}^{D_{ij}} \right) 2\hat{S}_{iz}\hat{S}_{jz} \quad (2.115)$$

$$\hat{\mathcal{H}}^{J_{ij}^{\text{iso}}} = \omega^{J_{ij}^{\text{iso}}} \hat{S}_{iz}\hat{S}_{jz} \quad (2.116)$$

$$\hat{\mathcal{H}}^{J_{ij}^{\text{aniso}}} = \omega^{J_{ij}^{\text{aniso}}} \left(\omega_{\text{aniso}}^{J_{ij}}, \eta^{J_{ij}} \alpha_{\text{PL}}^{J_{ij}}, \beta_{\text{PL}}^{J_{ij}}, \gamma_{\text{PL}}^{J_{ij}} \right) 2\hat{S}_{iz}\hat{S}_{jz} \quad (2.117)$$

In NMR the term ‘‘heteronuclear’’ is used as a description of two spins that have a substantial chemical shielding difference (different resonance frequencies) compared to the magnitude of internuclear (dipolar) couplings. Sometimes even spin systems composed of identical isotopes can be described sufficiently well by the simpler heteronuclear coupling Hamiltonians.

2.3. Time Dependence

So far the Hamilton operator in the Schrödinger equation of motion

$$i\frac{\partial}{\partial t} |\psi\rangle = \hat{\mathcal{H}} |\psi\rangle \quad (2.118)$$

is time-independent and the corresponding state vector $|\psi\rangle$ is stationary. However, in order to access the information described by the Hamiltonian it is necessary to interact with the spins which renders the Hamiltonian time-dependent. Here a quite unique property of the Hamiltonian of NMR comes into play. The weakness of the NMR interactions makes it possible to easily inflict perturbations on the system that tailor the system in a way that is impossible in many other spectroscopic techniques. The tools to manipulate the Hamiltonian externally are generally of two categories, inherent in the general structure of the Hamiltonian in Eq. (2.72). The perturbations to the interaction tensors \mathbf{A}^λ are generally of spatial character, while the spin part \mathbf{X} is modified by electromagnetic interactions with the magnetic moment.

The description of time dependence in quantum mechanics is dealt with by means of time-evolution operators \hat{U} [5]. It is in the same way that angular momentum operator $\hat{\mathbf{J}}$ is the generator of rotation that the Hamilton operator $\hat{\mathcal{H}}$ is the generator of time evolution (see Eq. (2.35)). The expectation value of a general operator \hat{O} (observable) is according

to Eq. (2.15)

$$\langle \hat{O} \rangle = \langle \psi | \hat{O} | \psi \rangle \quad (2.119)$$

where time evolution of the expectation value is described by the unitary time-evolution operator $\hat{U}^\dagger = \hat{U}^{-1}$

$$\langle \hat{O} \rangle = \langle \psi | \hat{U}^\dagger \hat{O} \hat{U} | \psi \rangle \quad (2.120)$$

This equation can be interpreted in two ways. The operator \hat{U} can either be seen as acting on the state vector

$$|\psi\rangle \rightarrow \hat{U} |\psi\rangle \quad (2.121)$$

and therefore describing the time dependence of the state ket ($|\psi(t)\rangle = \hat{U} |\psi(t_0)\rangle$) while the operator stays time-independent. Or, analogous to the case of rotations, it can be seen as describing the time evolution of the operator

$$\hat{O} \rightarrow \hat{U}^\dagger \hat{O} \hat{U} \quad (2.122)$$

where the time evolution is described by the change of $\hat{O}(t) = \hat{U}^\dagger \hat{O}(t_0) \hat{U}$ and the state vector stays constant. The first way to look at time evolution resembles the way it is dealt with in the Schrödinger equation and therefore is called the Schrödinger picture. The second approach is called Heisenberg picture [5].

The time-evolution operator in its most general form is

$$\begin{aligned} \hat{U}(t, t_0) &= \hat{T} \exp \left(-i \int_{t_0}^t dt' \hat{\mathcal{H}}(t') \right) \\ &= \lim_{\delta t \rightarrow 0} e^{-i\hat{\mathcal{H}}(t)\delta t} e^{-i\hat{\mathcal{H}}(t-\delta t)\delta t} \dots e^{-i\hat{\mathcal{H}}(t-n\delta t)\delta t} \dots e^{-i\hat{\mathcal{H}}(t_0)\delta t} \end{aligned} \quad (2.123)$$

which is a short form of writing the von Neumann time series [6] and where \hat{T} is the Dyson time ordering operator [37]. It is possible to greatly simplify the operator $\hat{U}(t, t_0)$ if certain characteristics of the Hamilton operator apply:

- If the Hamiltonian $\hat{\mathcal{H}}$ is not explicitly time-dependent ($\frac{\partial}{\partial t} \hat{\mathcal{H}} = 0$) then $\hat{U}(t, t_0)$ is

$$\hat{U}(t, t_0) = \exp \left(-i\hat{\mathcal{H}}(t - t_0) \right) \quad (2.124)$$

This is the case for all the Hamiltonians so far (see Eq. (2.103)).

- If the Hamilton operator $\hat{\mathcal{H}}(t)$ is time-dependent but is commuting with itself at different times t and t'

$$\left[\hat{\mathcal{H}}(t), \hat{\mathcal{H}}(t') \right] = 0 \quad \forall t, t' \quad (2.125)$$

then time ordering becomes redundant and the time-evolution operator becomes

$$\hat{U}(t, t_0) = \lim_{\delta t \rightarrow 0} \exp \left(-i \sum_{n=0}^{\infty} \hat{\mathcal{H}}(t - n\delta t) \right) = \exp \left(-i \int_{t_0}^t \hat{\mathcal{H}}(t') dt' \right) \quad (2.126)$$

A Hamilton operator such as the one in Eq. (2.126) is called inhomogeneous, while non-commuting Hamiltonians are referred to as homogeneous following the classification of Maricq and Waugh [38].

2.3.1. Rotations in Spin Space

A classical coherent radiofrequency (RF) field oscillating along the x -direction in LAB is described by [4]

$$\mathbf{B}_1(t) = 2B_1 \cos(\omega_{\text{RF}}t - \phi) \mathbf{e}_x \quad (2.127)$$

and the corresponding RF Hamilton operator $\hat{\mathcal{H}}^{\text{RF}}(t)$ can be constructed in the same way as for the Zeeman interaction (Eq. (2.53)) by using the correspondence principle (Eq. (2.27))

$$\hat{\mathcal{H}}^{\text{RF}}(t) = -2B_1 \cos(\omega_{\text{RF}}t - \phi) \gamma_S \hat{S}_x \quad (2.128)$$

Using the fact that every linearly polarised RF field can be decomposed into the sum of two circularly polarised fields rotating in opposite directions, the Hamiltonian can be written as

$$\hat{\mathcal{H}}^{\text{RF}}(t) = -B_1 \gamma_S \hat{S} \left[\underbrace{\cos(\omega_{\text{RF}}t - \phi) \mathbf{e}_x + \sin(\omega_{\text{RF}}t - \phi) \mathbf{e}_y}_{\text{counterclockwise}} + \right. \quad (2.129)$$

$$\left. + \underbrace{\cos(\omega_{\text{RF}}t - \phi) \mathbf{e}_x - \sin(\omega_{\text{RF}}t - \phi) \mathbf{e}_y}_{\text{clockwise}} \right] \quad (2.130)$$

According to the description of rotations in Eq. (2.83) it is possible to describe a spin rotating in the xy -plane with the frequency ω_{RF} in clockwise direction by

$$\hat{\mathcal{H}}^{\text{RF}}(t) = -B_1 \gamma_S e^{i\omega_{\text{RF}} \hat{S}_z t} \hat{S}_x e^{-i\omega_{\text{RF}} \hat{S}_z t} \quad (2.131)$$

and in the counterclockwise direction by replacing ω_{RF} with $-\omega_{\text{RF}}$. Representing Eq. (2.131) in the rotating frame leads to

$$\begin{aligned} \hat{\mathcal{H}}_{\text{R}}^{\text{RF}}(t) &= -B_1 \gamma_S e^{-i\omega_0 \hat{S}_z t} e^{i\omega_{\text{RF}} \hat{S}_z t} \hat{S}_x e^{-i\omega_{\text{RF}} \hat{S}_z t} e^{i\omega_0 \hat{S}_z t} \\ &= -B_1 \gamma_S e^{-i(\omega_0 - \omega_{\text{RF}}) \hat{S}_z t} \hat{S}_x e^{i(\omega_0 - \omega_{\text{RF}}) \hat{S}_z t} \end{aligned} \quad (2.132)$$

If $\omega_0 = \omega_{\text{RF}}$ (on-resonant irradiation) $\hat{\mathcal{H}}_{\text{R}}^{\text{RF}}(t)$ becomes time-independent

$$\begin{aligned} \hat{\mathcal{H}}_{\text{R}}^{\text{RF}} &= -B_1 \gamma_S \hat{S}_x \\ &= \omega_1^S \hat{S}_x \end{aligned} \quad (2.133)$$

for the clockwise rotation. Here the amplitude of the RF irradiation field has been defined as $\omega_1^S = -B_1\gamma_S$. For the counterclockwise component the time dependence does not disappear but leads to fast oscillations with twice the Larmor frequency ω_0 and therefore can be neglected (compare Section 2.2.5).

The amplitudes of RF irradiation fields $\omega_1^S = -B_1\gamma_S$ generally can vary over a broad range. In typical NMR experiments this can be of the order of 1 kHz to 100 kHz and therefore is generally much smaller than the Zeeman interaction. Compared to the spin interactions, $\hat{\mathcal{H}}_R^{\text{RF}}$ can be often regarded as dominant so that a perturbation approach truncates the Hamiltonian during the RF irradiation to $\hat{\mathcal{H}} = \hat{\mathcal{H}}_R^{\text{RF}}$. This Hamiltonian is time-independent and the corresponding time-evolution operator can easily be calculated using Eq. (2.124) to be

$$\hat{U}(t) = e^{-i\omega_1\hat{S}_x t} \quad (2.134)$$

This operator describes also rotations around the positive x -axis by an angle $\beta = \omega_1 t$ when considering Eq. (2.82). The time evolution of a single spin in the pure eigenstate $|\frac{1}{2}, \frac{1}{2}\rangle$ is therefore

$$\begin{aligned} |\psi(t)\rangle &= e^{-i\omega_1\hat{S}_x t} \left| \frac{1}{2}, \frac{1}{2} \right\rangle = \\ &= \left(\sum_{n=0}^{\infty} \frac{(-i\omega_1\hat{S}_x t)^{2n}}{n!} + \sum_{n=0}^{\infty} \frac{(-i\omega_1\hat{S}_x t)^{2n-1}}{n!} \right) \left| \frac{1}{2}, +\frac{1}{2} \right\rangle \\ &= \cos\left(\frac{\omega_1 t}{2}\right) \left| \frac{1}{2}, +\frac{1}{2} \right\rangle - i \sin\left(\frac{\omega_1 t}{2}\right) \left| \frac{1}{2}, -\frac{1}{2} \right\rangle \end{aligned} \quad (2.135)$$

and corresponds to a spin rotating in the yz -plane as can be seen by inspection of Eq. (2.33). The RF field therefore transforms the system from a pure eigenstate $|S, m_s\rangle$ into a coherent superposition state (coherence). The expectation values of the spin operators $\hat{S}_x, \hat{S}_y, \hat{S}_z$ are no longer time independent but become

$$\begin{aligned} \langle \hat{S}_x(t) \rangle &= \left\langle \frac{1}{2}, +\frac{1}{2} \right| e^{-i\omega_1\hat{S}_x t} \hat{S}_x e^{i\omega_1\hat{S}_x t} \left| \frac{1}{2}, +\frac{1}{2} \right\rangle \\ &= 0 \end{aligned} \quad (2.136)$$

$$\langle \hat{S}_y(t) \rangle = \sin \omega_1 t \quad (2.137)$$

$$\langle \hat{S}_z(t) \rangle = \cos \omega_1 t \quad (2.138)$$

For example, choosing a finite duration of the RF irradiation (pulse) such that the rotation angle is 90° ($\beta = \omega_1 t = \frac{\pi}{2}$) the spin system is prepared to have a spin pointing into the $-y$ -direction.

For weaker RF amplitudes the approximation used above is no longer valid. The time evolution of the spin system under the influence of the complete Hamiltonian is leading to a complex time dependence of the system state vector. Especially for larger spin systems the number of eigenstates increases by $(2S + 1)$ for each spin and therefore a plethora of coherences can be created [1].

2.3.2. Rotations in Real Space

The spin operators \mathbf{X} are not affected by a spatial rotation of the spin system. This can be seen from the fact that the orbital angular momentum operator $\hat{\mathbf{L}}$ is commuting with any sort of spin operator. However, rotations in real space are affecting the interaction tensors \mathbf{A}^λ . In this context rotations can be understood in a less abstract way as a physical rotation of a spin system in real space and not just as a transformation between two reference frames. This kind of rotation can originate, for example, from the mobility of the spin system within the specimen as seen from a microscopic point of view. But also macroscopic rotation of the specimen itself containing the spin system is possible [21, 31].

To describe rotations in real space one can think of a rotor, represented by its rotor axis system (RAS), which is rotated around its z -axis. Then the spin system, and therefore also the PAS of its interaction tensors \mathbf{A}^λ are fixed and oriented to RAS by sets of Euler angles $\Omega_{\text{PR}} = \{\alpha_{\text{PR}}^\lambda, \beta_{\text{PR}}^\lambda, \gamma_{\text{PR}}^\lambda\}$. Finally the rotor itself is described in LAB by a set of Euler angles $\Omega_{\text{RL}} = \{\omega_{\text{rot}}t, \beta_{\text{RL}}, 0\}$. Here the time-dependent angle $\omega_{\text{rot}}t$ is replacing the angle α_{RL} , describing the rotation around the z -axis of the rotor. β_{RL} is the angle between the z -axis of RAS and the z -axis of LAB and therefore represents the inclination of the rotor with respect to the magnetic field $B_0\mathbf{e}_z$. The third Euler angle γ_{RL} has been defined to be zero and therefore restricts the rotor axis to orientations in the xz -plane of LAB. This is possible since LAB is actually just defined by the direction of the vector $\mathbf{B}_0 = B_0\mathbf{e}_z$ and the orientation of a vector with respect to RAS is uniquely defined by a set of two angles. The Hamilton operator can therefore be written as

$$\begin{aligned} \hat{\mathcal{H}}(\text{LAB}) &= \sum_{\lambda} C^\lambda \sum_l^2 \sum_{m=-l}^l (-1)^m A_l^{\lambda,m}(\text{LAB}) \\ &\times \sum_{m'=-l}^l \mathcal{D}_{m',-m}^l(\omega_{\text{rot}}t, \beta_{\text{RL}}, 0) \sum_{m''=-l}^l \mathcal{D}_{m'',m'}^l(\Omega_{\text{PR}}^\lambda) X_l^{m''}(\text{PAS}) \end{aligned} \quad (2.139)$$

The time dependence of the spin interactions in Eqs. (2.111) to (2.114) is periodic. That can be taken advantage of by expanding $\hat{\mathcal{H}}(t)$ in a Fourier series

$$\omega^\lambda(t, \Omega_{\text{PR}}) = \sum_{m'=-2}^2 \omega_{(m')}^\lambda e^{im'\omega_{\text{rot}}t} \quad (2.140)$$

where the complex Fourier components have the symmetry $\omega_{(-m')}^\lambda = i\omega_{(m')}^\lambda$ and obey

$$\omega_m^\lambda = \omega_{\text{iso}}^\lambda \delta_{0m'} + \omega_{\text{aniso}}^\lambda \left\{ \mathcal{D}_{0,m'}^2(\Omega_{\text{PR}}^\lambda) - \frac{\eta^\lambda}{\sqrt{6}} \left[\mathcal{D}_{-2,m'}^2(\Omega_{\text{PR}}^\lambda) + \mathcal{D}_{2,m'}^2(\Omega_{\text{PR}}^\lambda) \right] \right\} d_{m',0}^2(\beta_{\text{RL}}) \quad (2.141)$$

Here it is important to distinguish between cases of homogeneous and inhomogeneous Hamiltonians (see Eq. (2.126)). The calculation of the time-evolution operator (Eq.

(2.126)) makes it necessary to evaluate

$$\begin{aligned} \int_{t_0}^t \hat{\mathcal{H}}(t') dt' &= \int_{t_0}^t \omega^\lambda(t) + \dots dt' = \int_{t_0}^t \sum_{m'=-2}^2 \omega_{(m')}^\lambda e^{im'\omega_{\text{rot}}t'} + \dots dt' \\ &= \sum_{m'=-2}^2 \frac{\omega_{(m')}^\lambda}{im'\omega_{\text{rot}}} [\cos(m'\omega_{\text{rot}}t') + i \sin(m'\omega_{\text{rot}}t')] \Big|_{t_0}^t \end{aligned} \quad (2.142)$$

Eq. (2.142) shows that if the the rotation frequency ω_{rot} is much larger than the anisotropy of the spin interaction $\omega_{\text{aniso}}^\lambda$, the Hamiltonian only depends on time-independent terms where $m' = 0$. Eq. (2.141) then reduces to

$$\omega_m^\lambda = \omega_{\text{iso}}^\lambda + \omega_{\text{aniso}}^\lambda \left\{ \mathcal{D}_{0,0}^2(\Omega_{\text{PR}}^\lambda) - \frac{\eta^\lambda}{\sqrt{6}} [\mathcal{D}_{-2,0}^2(\Omega_{\text{PR}}^\lambda) + \mathcal{D}_{2,0}^2(\Omega_{\text{PR}}^\lambda)] \right\} d_{0,0}^2(\beta_{\text{RL}}) \quad (2.143)$$

A closer look at the reduced Wigner matrix element

$$d_{0,0}^2(\beta_{\text{RL}}) = \frac{1}{2} (3 \cos^2 \beta_{\text{RL}} - 1) \quad (2.144)$$

shows that the matrix element exactly vanishes for rotation angles

$$\beta_{\text{RL}} = \theta_{\text{MAS}} = \arccos\left(\frac{1}{\sqrt{3}}\right) \quad (2.145)$$

A rotation about an axis inclined at an angle $\arccos\left(\frac{1}{\sqrt{3}}\right)$ to the magnetic field $B_0 \mathbf{e}_z$ cancels all anisotropic parts in Eq. (2.143) and this is why θ_{MAS} is called the magic angle. However, if the Hamiltonian $\hat{\mathcal{H}}(t)$ does not commute with itself at different times (e.g. for Hamiltonians describing homonuclear coupled spin pairs) $d_{m',0}^2(\beta_{\text{RL}})$ contains terms with $m' \neq 0$. This means even fast spinning keeps anisotropic parts in the time-evolution operator. The same, incomplete averaging effect occurs also for an inhomogeneous Hamiltonian if the rotation speed does not exceed the anisotropies ($\omega_{\text{rot}} \not\gg \omega_{\text{aniso}}^\lambda$).

From Section 2.3.1 and 2.3.2 it can be concluded that real space and spin space manipulation of the Hamiltonian does not affect all terms of the Hamiltonian in the same way. Especially the behaviour under rotations that is characteristic for the different spin interactions provides a valuable tool to discriminate one type of interaction from another [39, 40, 41] (see Table 2.4 on page 25).

Interaction	Space rank l	Space components m	Spin rank λ	Spin components μ
Isotropic chemical shielding	0	{0}	1	{-1, 0, 1}
Chemical shielding anisotropy	2	{-2, -1, 1, 2}	1	{-1, 0, 1}
Isotropic J -coupling	0	{0}	0	{0}
Anisotropic J -coupling	2	{-2, -1, 1, 2}	2	{-2, -1, 1, 2}
Direct dipolar coupling	2	{-2, -1, 1, 2}	2	{-2, -1, 0, 1, 2}

Table 2.4.: Spin rank λ and space rank l of the spin interaction Hamiltonians, describing their different behaviour under rotations [41].

2.3.3. Solution to the Equation of Motion - Pulse Response

The expectation value $\langle \hat{O} \rangle$ of a general spin operator \hat{O} can easily be written by using the correspondence principle (Eqs. (2.27) and (2.15))

$$\begin{aligned} \langle \hat{O}(t) \rangle &= \sum_{ij} \langle o_i | \hat{O} | o_j \rangle \langle o_j | \psi(t) \rangle \langle \psi(t) | o_i \rangle \\ &= \sum_{ij} \hat{O}_{ij} \hat{\rho}_{ji} \\ &= \text{Tr} \{ \hat{O} \hat{\rho}(t) \} \end{aligned} \quad (2.146)$$

where the density operator

$$\hat{\rho}(t) = |\psi(t)\rangle \langle \psi(t)| \quad (2.147)$$

obeys the fundamental Liouville von Neumann equation [42, 5]

$$\frac{d}{dt} \hat{\rho}(t) = \frac{1}{i} [\hat{\rho}(t); \hat{\mathcal{H}}(t)] \quad (2.148)$$

Here it is important to note that Eq. (2.146) is independent of the representation used. For example, for a two spin system either of the two basis systems in Eqs. (2.47) to (2.50) can be used.

Eq. (2.148) is equivalent to the Schrödinger equation but implements the convenient formalism of probabilities from the definition of the expectation values (see Eq. (2.15)). Here the time dependence $\hat{\rho}(t)$ and hence the formal solution of Eq. (2.148) is

$$\hat{\rho}(t) = \hat{U}(t, t_0) \hat{\rho}(t_0) \hat{U}^\dagger(t, t_0) \quad (2.149)$$

This must not be confused with the time evolution in the Heisenberg picture. $\hat{\rho}(t)$ is built of state vectors $|\psi(t)\rangle$ and Eq. (2.149) therefore describes a time evolution in the Schrödinger picture. For a time-independent Hamiltonian $\hat{\mathcal{H}}$, $\hat{\rho}(t)$ is

$$\hat{\rho}(t) = e^{-i\hat{\mathcal{H}}t} \hat{\rho}(t_0) e^{i\hat{\mathcal{H}}t} \quad (2.150)$$

$$\hat{\rho}(t_0) \xrightarrow{\hat{\mathcal{H}}t} \hat{\rho}(t) \quad (2.151)$$

Comparing this to Eq. (2.83) the similarities to rotations become obvious. In the Hamiltonian eigenbasis $|S, m_s\rangle$ the exponential operators $e^{-i\hat{\mathcal{H}}t}$ are diagonal and the density matrix becomes

$$\begin{aligned} \langle S, m_S | \hat{\rho}(t) | S, m'_S \rangle &= e^{-i\sum_\lambda \omega_{m_S}^\lambda t} \langle S, m_S | \hat{\rho}(t_0) | S, m'_S \rangle e^{i\sum_\lambda \omega_{m'_S}^\lambda t} \\ &= e^{-i\sum_\lambda \omega_{m_S m'_S}^\lambda t} \langle S, m_S | \hat{\rho}(t_0) | S, m'_S \rangle \end{aligned} \quad (2.152)$$

Then $\hat{\rho}(t)$ describes the evolution of the density matrix $\hat{\rho}(t_0)$ under the influence of a static Hamiltonian. The $\sum_\lambda \omega_{m_S m'_S}^\lambda$ are the energy differences between the spin states $|S, m_S\rangle$ and $|S, m'_S\rangle$ and the diagonal elements of $\hat{\rho}(t)$ are therefore stationary and correspond to

the population of the respective spin state while the off-diagonal elements are oscillating. It is convenient to classify the matrix elements with respect to the coherence they are representing [1, 21]. This is done by defining the coherence-order parameter p as the difference in magnetic spin-quantum number

$$p = m_S - m'_S \quad (2.153)$$

and naming the matrix elements after the value of p as zero-quantum (ZQ) coherences, single-quantum (SQ) coherences, and so forth. The parameter p makes it possible to write the density matrix as the sum of terms containing only coherences of one kind

$$\hat{\rho}(t) = \sum_{p=-2S}^{2S} \hat{\rho}^p(t) \quad (2.154)$$

$$\hat{\rho}^p(t) = \sum_{m_S, m'_S} \langle S, m_S | \hat{\rho}(t) | S, m'_S \rangle | S, m_S \rangle \langle S, m'_S |, \forall m_S - m'_S = p \quad (2.155)$$

where $S = \sum_i S_i$ is the sum of the spin quantum numbers of the spin system (compare Eqs. (2.43) to (2.46)). Picking up the rotational transformation of the density matrix (Eq. (2.150)) it is useful to represent the density matrix in terms of irreducible tensor elements $\mathbb{T}_l^{m,(i)}$

$$\hat{\rho}(t) = \sum_{i,l,m} b_l^{m,(i)}(t) \mathbb{T}_l^{m,(i)} \quad p = m = -, -l, -l+1, \dots, l \quad (2.156)$$

where the magnetic quantum number m can be identified with the coherence order p and the index (i) distinguishes different operators with the same transformation properties. The $b_l^{m,(i)}(t)$ represent the coherence amplitude. For example, for a single spin $S = \frac{1}{2}$ the density matrix is described by the three tensor components [34]

$$\mathbb{T}_1^{\pm 1,(1)} = \frac{\hat{S}_{1x} \pm i\hat{S}_{1y}}{\sqrt{2}} \quad (2.157)$$

$$\mathbb{T}_1^{0,(1)} = \hat{S}_{1z} \quad (2.158)$$

$$\mathbb{T}_0^{0,(1)} = \mathbb{1}_2 \quad (2.159)$$

and represent the $p = \pm 1, 0$ SQ, ZQ coherences, respectively. For a two spin-system $S_1, S_2 = \frac{1}{2}$ the $\mathbb{T}_l^{m,(i)}$ resemble the $\mathbb{X}_l^{m,(i)}$ of the spin tensors defined in Eqs. (2.92) to (2.96).

- Generally the tensor elements transform under the influence of a static Hamiltonian without RF irradiation as

$$\mathbb{T}_l^{m,(i)} \xrightarrow{\mathcal{H}t} \sum_{i'l'} b_{l'}^{m,(i')}(t) \mathbb{T}_{l'}^{m,(i')} \quad (2.160)$$

This is changing the rank of the tensor components, but is not changing the coherence order p . Therefore coherences are conserved under free evolution without RF

irradiation.

$$\hat{\rho}^p \xrightarrow{\hat{S}_z \phi} \hat{\rho}^p e^{-ip\phi} \quad (2.161)$$

- Under the influence of a hard pulse, corresponding to a rotation in three-dimensional space, the tensor elements transform as

$$\mathbb{T}_l^{m,(i)} \xrightarrow{\sum_i \beta \hat{S}_{iy}} \sum_{m'} d_{mm'}^l(\beta) \mathbb{T}_l^{m,(i)} \quad , p = m \quad (2.162)$$

Thus, as already seen in Section 2.3.1, the RF pulse transforms coherences without affecting the rank l of the tensor elements.

RF fields create coherences which renders the density matrix time dependent. It is the time dependence of the density matrix elements that is characteristic for the spin system and its spin states. However, for a coherence to be detectable it is necessary to find an observable $\langle \hat{O} \rangle$ that makes the coherence accessible to experiment.

2.3.4. NMR Signal of Bulk Samples

The most general quantum mechanical state a spin system can be in is the linear superposition of all its eigenstates [5]. For a single spin $S = \frac{1}{2}$ this is according to Eq. (2.32)

$$|\psi\rangle = c_{+\frac{1}{2}} \left| \frac{1}{2}, +\frac{1}{2} \right\rangle + c_{-\frac{1}{2}} \left| \frac{1}{2}, -\frac{1}{2} \right\rangle \quad (2.163)$$

This is sufficient to describe an isolated spin system. In a macroscopic solid sample the size of the spin system is generally very large, which makes the number of possible eigenstates immense. However, macroscopic samples can generally be regarded as being a set of independent spin systems i each one described by its own state vector $|\psi^{(i)}\rangle$. Reasons for this are:

- The r^{-3} dependence of the direct dipolar coupling renders it rather short ranged.
- The pathway of the J couplings via the bonding electrons leads to a natural limit of molecular size at least in liquid-state NMR
- The limited abundance of some NMR “active” nuclei.

The macroscopic magnetic properties of the sample are therefore not derived from the quantum mechanical expectation value (Eq. 2.146) but by an ensemble average over all quantum mechanical spin-system states [5, 42]. This is done by defining weighting factors w_i that represent the normalised population density $\sum_i w_i = 1$ of the spin-system state

$|\psi^{(i)}\rangle$. The ensemble average of the observable \hat{O} is then

$$\begin{aligned} [\hat{O}] &= \sum_i w_i \langle \psi^{(i)} | \hat{O} | \psi^{(i)} \rangle \\ &= \sum_i w_i \langle \hat{O} \rangle^{(i)} \\ &= \text{Tr} \{ \hat{\rho} \hat{O} \} \end{aligned} \quad (2.164)$$

and the density matrix becomes

$$\hat{\rho} = \sum_i w_i |\psi^{(i)}\rangle \langle \psi^{(i)}| \quad (2.165)$$

Statistical mechanics now help to connect the quantum mechanical probabilities in the density operator with the Boltzmann description of a system at thermal equilibrium [42]. The probability P_k of finding the macroscopic system in the energy state E_k compares to the quantum mechanical probability as

$$P_k = \frac{e^{-\frac{E_k}{k_B T}}}{Z} = w_k |\psi^{(k)}\rangle \langle \psi^{(k)}| \quad \text{with } Z = \sum_k e^{-\frac{E_k}{k_B T}} \quad (2.166)$$

This simplifies for high temperatures ($\frac{1}{k_B T} \ll 1$) to

$$P_k = w_k |\psi^{(k)}\rangle \langle \psi^{(k)}| \approx 1 - \frac{\hat{\mathcal{H}}_k}{k_B T} \quad (2.167)$$

Since $\hat{\mathcal{H}}$ is dominated by the Zeeman interaction, the high-field approximation (Section 2.2.5) leaves

$$\hat{\mathcal{H}} \approx \omega_0 \hat{S}_z = \omega_0 m_k \quad (2.168)$$

The population difference for a system of isolated spin $S = \frac{1}{2}$ systems is given by [2]

$$P_{-\frac{1}{2}} - P_{+\frac{1}{2}} = \frac{\omega_0}{k_B T} \approx 10^{-4} - 10^{-5} \quad (2.169)$$

leaving only a very small fraction of spins in the sample that contribute to the macroscopic net magnetisation

$$M_z = \sum_i^{\text{Spins}} \gamma_{S_i} [\hat{S}_{iz}] \quad (2.170)$$

Similarly for the magnetisation after a non selective $\frac{\pi}{2}$ -pulse M_y becomes

$$M_y = - \sum_i^{\text{Spins}} \gamma_{S_i} [\hat{S}_{iy}] \quad (2.171)$$

After the pulse the magnetisation M_y is evolving under the influence of the time-evolution operator dominated by the Zeeman term ($\hat{U} = e^{-i\omega_0 \hat{S}_z}$), leading to a free precession in

the xy -plane [1, 21]. Placing the specimen in a coil that is oriented e.g. along the x -axis induces an alternating current, the NMR signal

$$\begin{aligned}\bar{s}(t) &= \bar{s}_x(t) - i\bar{s}_y(t) \\ &= \text{Tr} \left\{ \hat{\rho}(t) \hat{S}_- \right\} \quad \text{with } \hat{S}_- = \hat{S}_x - i\hat{S}_y\end{aligned}\tag{2.172}$$

The signal $\bar{s}(t)$ is described in the complex plane. This is necessary in order to identify the sense of the rotation in the xy -plane which is not possible by just measuring the magnetic field in one dimension [21, 43].

An important property of the NMR signal is that the coherence state has only limited life time [2, 14]. The NMR signal is decaying with time and is referred to as free induction decay (FID).

The free precession and the NMR signal are determined by the Hamiltonian which is a function of the frequencies ω^λ (see Eqs. (2.111) to (2.114)). In order to visualise the contributions of the different spin interactions λ , it is instructive to transform the time-domain NMR signal to the frequency domain by a Fourier transformation (FT) [1, 44]. By applying FT to the FID the familiar NMR spectrum is obtained.

3. Experimental and Numerical Methods

In order to obtain information about a spin system it needs to be manipulated so that the resulting state vector (density matrix) is creating a spectrum containing the wanted information. However, the resulting spectrum often is not only dependent on the wanted information but also contains additional contributions, possibly making interpretation difficult or impossible. Several ways to handling this situation exist [45]: One is to develop selective pulse sequences [35, 41] including two- and multi-dimensional FT-NMR experiments [1, 46, 47]. Another approach is to evaluate experimental spectra by numerical means using iterative fitting approaches. This makes it possible to handle a fair amount of parameters and is less demanding on the selectivity of the experiment. However, it makes it necessary to simulate spectra numerically exactly.

Here the latter approach is followed. First the experiments used in this work are briefly described. Secondly, the numerical methods used are briefly explained.

3.1. Nuclei with Spin $S = \frac{1}{2}$ under Magic Angle Spinning Conditions

In reality it is often difficult, if not impossible, to grow single crystals suitable for NMR purposes. Polycrystalline samples are often much easier to prepare, therefore making NMR applicable to a much broader range of solid samples. All aspects of this work deal with polycrystalline powder samples.

The NMR spectrum $\bar{s}(t)$ of spins in polycrystalline powders consists generally of broad lines (see Figure 3.1a). The resonance frequency of a spin (see Eqs. (2.111) to (2.114)) is generally orientation dependent. Spectra of static powdered samples are consequently a superposition of the resonances of individual single crystallites. The lineshape of this kind of spectrum is determined by the spin-system parameters of the respective Hamiltonian. However, the orientational information of the spin-interaction tensors is generally averaged by the random orientations of the crystallites in a powder, leaving only information about the interaction tensor magnitudes. Only in the presence of dipolar couplings in multi-spin systems the orientation of the interaction tensors with respect to each other can be obtained from NMR spectra of polycrystalline powders.

Because of the broad lines in NMR spectra of static powders the resonances of different spins are likely to overlap. This makes it difficult to interpret the spectra or makes it even impossible to identify the number of spins contributing to the spectrum. A common way to cope with this situation is the use of magic angle spinning (MAS) [48, 49]. MAS implies that the sample is physically spun around an axis which is inclined at the magic angle θ_{MAS} (see Eq. (2.145)) with respect to the external magnetic field \mathbf{B}_0 .

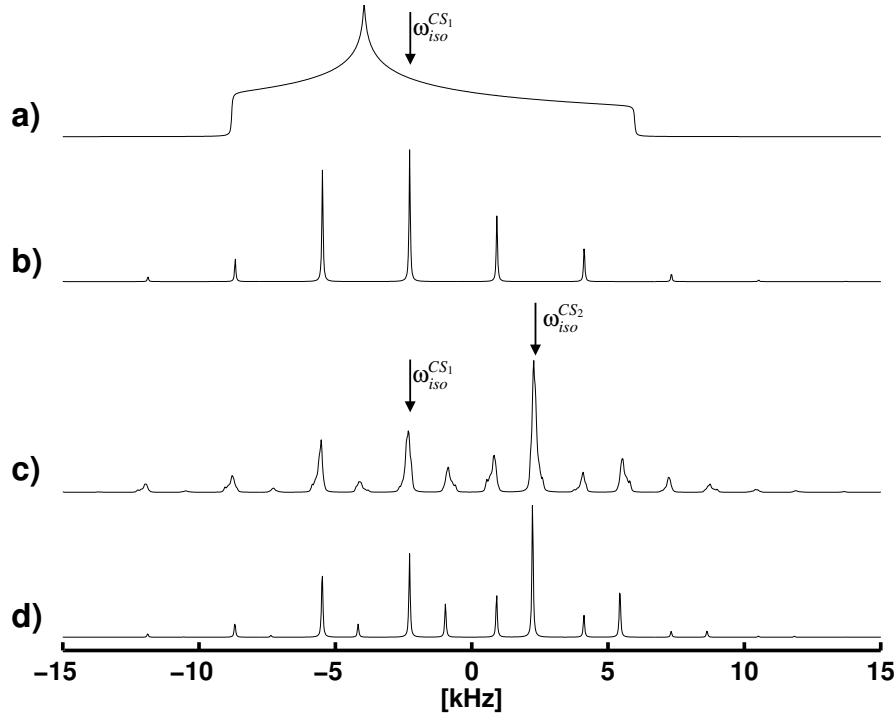


Figure 3.1.: Calculated spectra of a sample of a polycrystalline powder with the isotropic chemical shieldings ω_{iso}^{CS} marked by arrows: a) Static spectrum of an isolated spin $S_1 = \frac{1}{2}$ ($\omega_{\text{iso}}^{CS_1}/2\pi = -2250$ Hz, $\omega_{\text{aniso}}^{CS_1}/2\pi = 8303$ Hz, $\eta^{CS_1} = 0.6$). b) Same spin but under MAS with $\omega_{\text{rot}}/2\pi = 3.2$ kHz. c) Spin from a) coupled to a second spin $S_2 = \frac{1}{2}$ with $\omega_{\text{iso}}^{CS_2}/2\pi = 2250$ Hz, $\omega_{\text{aniso}}^{CS_2}/2\pi = -6190$ Hz, $\eta^{CS_2} = 0.5$ ($\omega_{\text{rot}}/2\pi = 3.2$ kHz) by a strong homonuclear dipolar coupling ($b_{12}/2\pi \approx \Delta\omega_{\text{iso}}^{CS_{1,2}}/2\pi = 4$ kHz). d) Homonuclear spin pair ($\omega_{\text{rot}}/2\pi = 3.2$ kHz) with weak dipolar coupling ($\Delta\omega_{\text{iso}}^{CS_{12}}/2\pi \gg b_{12}/2\pi = 1$ kHz) and CSA parameters as in c).

For a single spin under MAS the Hamiltonian is inhomogeneous and the signal $s(t)$ is given by

$$s(t) = e^{-i\phi^{CS}(t)} \quad (3.1)$$

$$\phi^{CS}(t) = \omega_{\text{iso}}^{CS} t + \sum_{m' \neq 0} \frac{\omega_{(m')}^{CS}}{im'\omega_{\text{rot}}} [\cos(m'\omega_{\text{rot}}t') + i \sin(m'\omega_{\text{rot}}t')] \Big|_{t_0}^t \quad (3.2)$$

Spinning speeds ω_{rot} exceeding $\omega_{\text{aniso}}^{CS}$ result in a signal $s(t) = e^{-i\omega_{\text{iso}}^{CS}t}$ and the FID becomes independent of the crystallite orientation. The spectrum consists of a single peak at the isotropic shielding frequency ω_{iso}^{CS} . When considering spinning speeds smaller than the size of the anisotropic contributions in Eq. (3.2), the averaging as described in Section 2.3.2 is incomplete and the orientation dependence of the Fourier components $\omega_{(m')}^{CS}$ becomes visible. However, due to the periodic modulation by the sample rotation the magnetisation is refocused after each completed revolution of the rotor and consequently the signal obeys

$$\bar{s}(n\tau_{\text{rot}}) = e^{-in\omega_{\text{iso}}^{CS}\tau_{\text{rot}}} \quad (3.3)$$

For a polycrystalline powder this results in a spectrum consisting of narrow peaks separated by $\omega_{\text{rot}} = \frac{1}{\tau_{\text{rot}}}$ around the resonance of the isotropic shielding, the so-called MAS sideband pattern [50, 51, 52] (compare Figure 3.1b–d)). The spectrum obtained contains information about the magnitude of the CSA $\{\omega_{\text{iso}}^{CS}, \omega_{\text{aniso}}^{CS}, \eta^{CS}\}$ while the orientational information of the CSA tensor is averaged by the random orientation distribution of the powder.

For spinning speeds slower than any anisotropic interaction ($\omega_{\text{rot}} < \omega_{\text{aniso}}^{\lambda}$) the envelope of the MAS sideband pattern resembles the static powder line shape. If not an isolated spin is considered but, for example, a pair of coupled homonuclear spins (Figure 3.1c) the Hamiltonian is generally homogeneous. For this kind of spin system a MAS sideband pattern is also obtained. However, the sidebands are no longer narrow lines but show broadenings and splittings, which are an effect of the incomplete averaging of an homogeneous Hamiltonian [38] by MAS. Now not only the magnitudes of the spin interactions but also their relative orientations are encoded in the spectrum. Only spinning speeds substantially exceeding the dipolar coupling reduce the spectrum to narrow lines. The homogeneous character of the homonuclear Hamiltonian is strongly dependent on the relative size of the dipolar coupling interactions (\mathbf{D}, \mathbf{J}) compared to the difference in isotropic shieldings of the two spins. If $\Delta\omega_{\text{iso}}^{CS_{1,2}} \gg b_{12}, \omega^{J_{12}}$, the chemical shielding has a truncating effect on the Hamiltonian which leads to narrow MAS sidebands. This is sometimes called a weak coupling regime [1].

It is generally impossible to analytically describe the spin dynamics of a homonuclear spin system under MAS. The Hamiltonian is generally homogeneous and only in the weak coupling regime with small CSA interactions low-order theoretical approximations are reproducing experimental NMR spectra in a reasonable manner [53, 54, 55, 56, 30]. Here mostly cases with large CSA and sizable dipolar coupling interactions are considered.

Generally the advantages of the MAS experiment are an increase in resolution, especially when more than one spin species is involved. In addition MAS also increases the sensitivity of the experiment in that the intensity of the static powder spectrum is condensed into more or less narrow spinning sidebands, hence improving the signal-to-noise ratio in a MAS spectrum.

For these two reasons MAS is used for all experiments exploited here.

3.1.1. Rotational-Resonance Recoupling

The averaging or at least scaling of NMR interactions by MAS can be a desirable effect when, for example, one is only concerned about isotropic chemical shielding information or CSA magnitudes of isolated spins. However, the Hamiltonian of a spin system normally carries information that gives much more insight into molecular structure such as the direct dipolar coupling which relates directly to internuclear distances, or the chemical shielding anisotropy that allows to answer structural questions that can not be answered by the determination of internuclear distances alone.

One way to reintroduce (“recouple”) those interactions that are normally averaged by MAS while mostly keeping the advantages of MAS for homonuclear spin systems is the

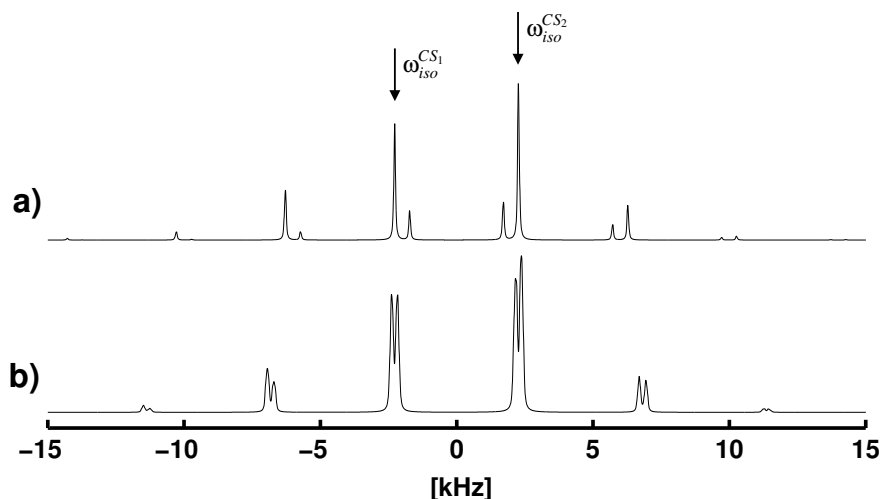


Figure 3.2.: Calculated MAS spectra of a spin pair with parameters equivalent to those in Figure 3.1d): a) away from a R^2 condition with $\omega_{\text{rot}}/2\pi = 4$ kHz; b) at the $n = 1$ R^2 condition with $\omega_{\text{rot}}/2\pi = 4.5$ kHz.

rotational-resonance (R^2) experiment [57]. This resonance effect has been discussed theoretically using various approximation methods [30, 53, 54, 55, 56, 58, 59, 60, 61]. The rotational-resonance effect occurs whenever the difference in isotropic chemical shieldings $\Delta\omega_{\text{iso}}^{CS_{1,2}}$ is equal or very similar to a small integer multiple of the MAS frequency ω_{rot} . When

$$\Delta\omega_{\text{iso}}^{CS_{1,2}} = n\omega_{\text{rot}} \quad , \quad n = 1, 2, \dots \quad (3.4)$$

the dipolar couplings b_{12} and $\omega_{\text{aniso}}^{J_{12}}$ are reintroduced into the spectrum. The mechanical rotation of the rotor is interfering with the precessional motion of the spin coherences resulting in a recoupling effect opposed to the averaging by MAS.

A special situation arises if the difference in chemical shielding between two dipolar coupled spins is zero, or nearly zero

$$\Delta\omega_{\text{iso}}^{CS_{1,2}} \simeq 0 \quad (3.5)$$

This is leading to a recoupling effect which is virtually independent of the spinning speed and is called the $n = 0$ R^2 condition. It requires the two CSA tensors to be different, either in magnitude or orientation. This condition is no longer an experimental parameter but is dictated by the spin system. A $n = 0$ R^2 condition occurs e.g. for two CSA tensors related by a C_2 axis of symmetry or a mirror plane.

The effect of R^2 on the spectrum is that the recoupled dipolar interaction is causing an increase in line broadening and lineshape distortions (see Figure 3.2). These lineshape effects encode structural information.

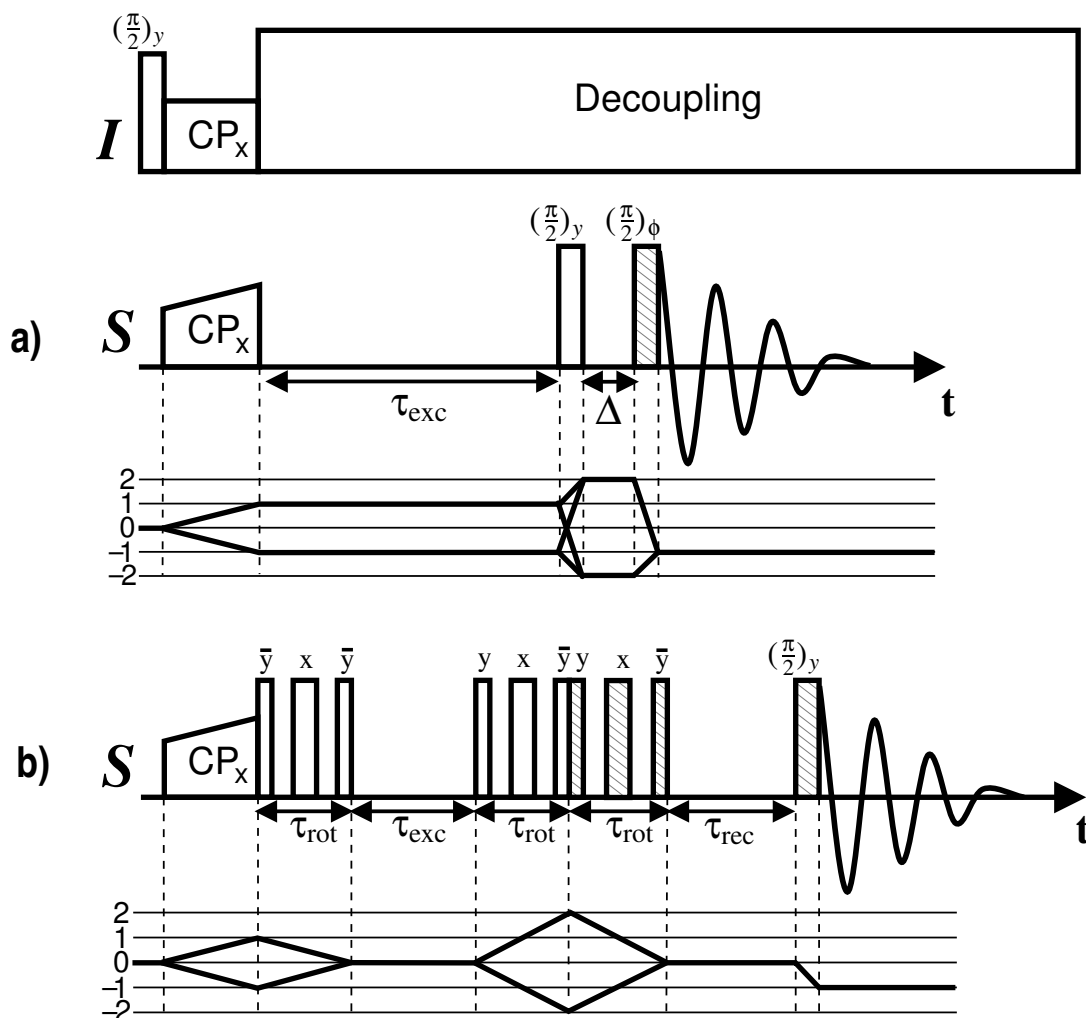


Figure 3.3.: Pulse sequences suitable for R^2 -DQF together with the respective coherence transfer pathways (CTP) [1]. Cross polarisation (CP) from the I -spin species to the S -spin species is included as well as decoupling in the I -spin channel. Double-quantum filtration is accomplished by phase cycling the hashed pulses. a) R^2 -DQF $_{\beta,\gamma}$ experiment [66]. b) R^2 -DQF $_{\beta}$ experiment [63].

3.1.2. Double-Quantum Filtration and Rotational Resonance

The presence of resonances from isolated spins in addition to those stemming from e.g. a R^2 recoupled spin pair often makes it awkward to interpret the resulting spectra. Commonly this scenario arises when dealing with spins that do not have 100% natural abundance, leading to samples containing a variety of isotopomers. A way to remove spectral contributions originating from isolated spins is double-quantum filtration (DQF). DQF suppresses the SQ coherences stemming from uncoupled spins and leaves the signature of DQ coherences unique to the dipolar coupled spins. Here DQF has been implemented by the use of suitable phase cycling techniques [1]. There are many possibilities to achieve DQF under R^2 conditions [62, 1, 63, 64, 65]. A basic and straightforward way to do so is the R^2 -DQF $_{\beta,\gamma}$ pulse sequence [66] (see Figure 3.3a)) It corresponds to the COSY-DQF [46, 67, 68] experiment as known in liquid state NMR. During this pulse sequence the initially excited SQ

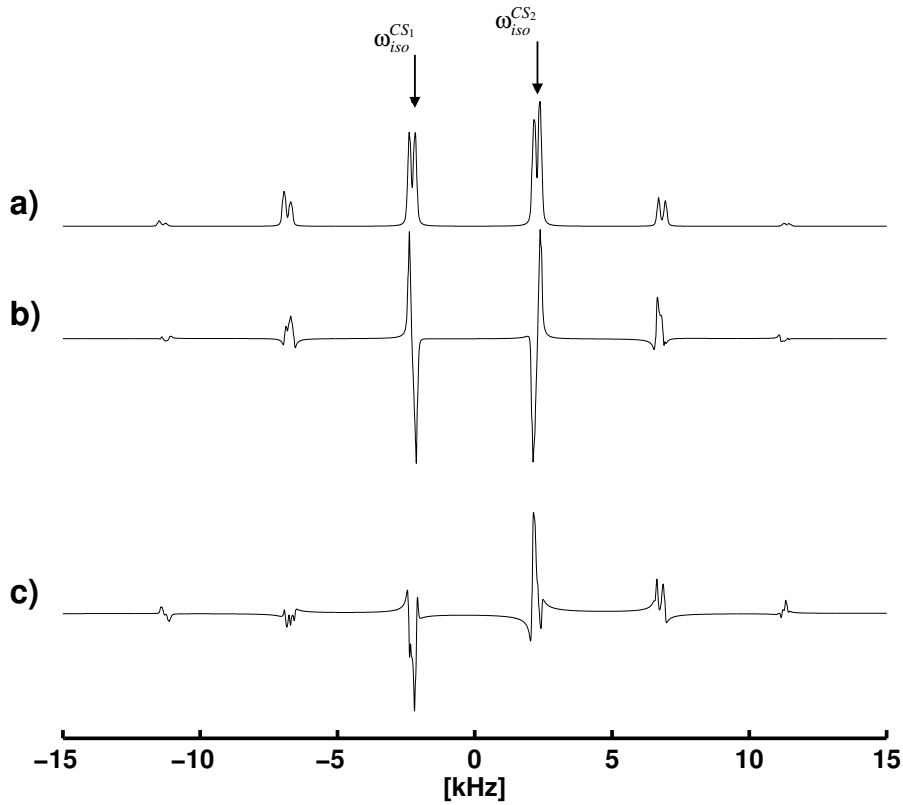


Figure 3.4.: Simulated R^2 MAS spectra of a two-spin system (same parameters as in Figure 3.1d)). Isotropic chemical shielding is marked by arrows. a) $n = 1$, R^2 MAS without DQF; b) $n = 1$ R^2 , R^2 -DQF $_{\beta,\gamma}$; c) $n = 1$ R^2 , R^2 -DQF $_{\beta}$.

coherences are evolving freely during an evolution interval τ_{exc} . Afterwards DQ coherences are excited by a single $\frac{\pi}{2}$ -pulse and are allowed to evolve during a short interval Δ . A final $\frac{\pi}{2}$ -pulse reconverts DQ coherences to detectable SQ coherences and the FID is recorded. The excitation time τ_{exc} has to be optimised depending on the spin system in order to achieve optimum DQF efficiency. Spectra of this kind of experiment show characteristic anti-phase lineshapes (see Figure 3.4b).

The R^2 -DQF $_{\beta}$ pulse sequence (see Figure 3.3b)) deploys a three-pulse module $((\frac{\pi}{4})_y - \tau - (\frac{\pi}{2})_x - \tau - (\frac{\pi}{4})_y)$ to first invert the magnetisation of one of the two resonating spins. Afterwards the ZQ coherences evolve during an excitation time that is a multiple of the rotation period ($\tau_{\text{exc}} = \tau_{\text{rot}}$). A similar three-pulse block is then used to excite DQ that are afterwards reconverted by an identical three-pulse sequence to ZQ coherence. Afterwards a reconversion interval $\tau_{\text{rec}} = \tau_{\text{exc}}$ is used to refocus the ZQ coherences to the inverted initial state. This is converted to SQ coherences by a non selective $\frac{\pi}{2}$ -pulse to be detected as FID. The resulting spectrum (see Figure 3.4c)) displays the final inverted spin state.

A common characteristic of MQ-filtration processes is that the amount of detected signal is generally less than is obtained for the same experiment without the filter. The so-called DQF efficiency (ratio between the signal amplitude in the filtered and the unfiltered experiment) refers to this fact. Theoretically for the R^2 -DQF $_{\beta,\gamma}$ experiment a maximum possible DQF efficiency of 50% is predicted [66]. This value is based on the assumption

that the spin system is determined by isotropic chemical shielding and dipolar couplings only.

Then the Hamiltonian describing the effect of the pulse sequence on a single crystallite is dependent on the Euler angles $\beta_{\text{CR}}, \gamma_{\text{CR}}$ [62]. It is possible to reduce this dependence of the Hamiltonian to β_{CR} only. Theoretically it should then be possible to reach $\approx 73\%$ of DQF efficiency. The $\text{R}^2\text{-DQF}_\beta$ pulse sequence [63] (see Figure 3.3c)) belongs to this category of so-called γ_{CR} -encoded [62] pulse sequence.

3.2. Numerical Methods

The Hamilton operator $\hat{\mathcal{H}}(t)$ necessary for describing the spin systems in this work generally depends on all spin interactions of the spin system and the numerical description has to be based on the spin Hamiltonians as defined in Eqs. (2.111) to (2.114). All the information accessible by experiment is stored in the spectra in a more or less complex way as spectral intensities and resonance splittings and broadenings. The spin dynamics can generally not be described in an analytical way and it is generally not sufficient to use an approximated description of the spin dynamics. It is assumed that a reproduction of the experimental lineshape by simulation [69, 70, 71, 72] is only possible with the parameter values $p_0(i)$ encoded in the experimental spectrum. Hence numerically exact simulations are needed.

Such simulations may be rather time consuming. Fortunately some of the experiments chosen display properties that allow for numerical procedures that help to greatly speed up these numerically exact simulations. Quite often it is the successful exploitation of such procedures that render the experiment feasible for the use in an iterative fitting approach. A second aspect of this numerical approach is the possibility to interpret the spin-system parameters obtained regarding their accuracy and sensitivity.

3.2.1. Time Propagation

The time signal $\bar{s}(t)$ of the NMR experiments used can always be calculated using Eq. (2.123) where the time propagation operator $\hat{U}(t, t_0)$ is calculated in a chronological way. Its numerical implementation assumes that the Hamiltonian of a n -spin system in its $(2S + 1)^n$ -dimensional matrix representation is constant during a sufficiently short time interval δt and that the actual time integration can then be broken up according to Eq. (2.124) into a product of matrix exponentials

$$\hat{U}(t, t_0) = \hat{U}(t, t - n\delta t) \hat{U}(t - \delta t, t - 2\delta t) \cdot \dots \cdot \hat{U}(t_0 + \delta t, t_0) \quad (3.6)$$

$$\hat{U}(t, t - \delta t) = e^{\hat{\mathcal{H}}(t)\delta t} \quad (3.7)$$

Efficient ways of calculating these matrix exponentials have been discussed in the literature [73]. This computation is called direct integration or direct method for calculating the time propagator. It has the general advantage to be applicable independently of the properties of the spin system or the pulse sequence. However, the direct method is a computationally

slow way of calculating time evolution [74]. The direct method may, however, serve as a reference for speed and accuracy when comparing with more advanced numerical methods described in the following.

For rotating powdered samples it is often possible to take advantage of the symmetric time dependence of the Hamiltonian induced by the physical sample rotation

$$\hat{\mathcal{H}}(t) = \hat{\mathcal{H}}(t + n\tau_{\text{rot}}) \quad (3.8)$$

and consequently the time propagators obey

$$\hat{U}(t + \delta t, t) = \hat{U}(t + \tau_{\text{rot}} + \delta t, t + \tau_{\text{rot}}) \quad (3.9)$$

Therefore, propagators have to be calculated only once and can be reused at integer multiple of rotation periods τ_{rot} later on. This implies that the pulse sequence used fulfils the same periodicity. The reuse of propagators obviously can be used to speed up simulations.

The rotational symmetry of the Hamiltonian under MAS can be exploited further. In the situation where the detection operators Q and equilibrium density matrix $\hat{\rho}(0)$ display excitation-detection symmetry [75]

$$\hat{\rho}(0) = \frac{1}{2} (\hat{Q} + \hat{Q}^\dagger) \quad (3.10)$$

it is possible to use the so-called COMPUTE algorithm [76, 77, 78]. This algorithm is based on the fact that a periodic function is readily described by one period. Therefore, a time propagation over only one rotation period is sufficient to simulate the complete final spectrum. Depending on the ratio of the duration τ_{rot} to the length of the actual FID to be simulated this leads to gains in calculation speeds of up to two orders of magnitude [79]. Excitation-detection symmetry is generally given in standard MAS and R² experiments. For experiments involving RF pulses apart from an initial CP transfer or single $\frac{\pi}{2}$ -pulse, this symmetry is not usually given for the entire duration of the experiment. Here only for the simulation of time evolution during the detection of the FID (τ_{FID}) the COMPUTE algorithm can be exploited while the preparation of the spin-system magnetisation under the influence of RF pulses (τ_{p}) has to be calculated using the direct method [80].

$$\hat{U}(t, t_0) = \hat{U}_{\text{COMPUTE}}(t_0 + \tau_{\text{p}} + \tau_{\text{FID}}, t_0 + \tau_{\text{p}}) \hat{U}_{\text{direct}}(t_0 + \tau_{\text{p}}, t_0) \quad (3.11)$$

Depending on the ratio of τ_{p} to τ_{FID} this combination of calculation methods still may provide one order of magnitude of gain in calculation time.

3.2.2. Powder Averaging

The numerically exact simulation of powder NMR spectra makes it generally necessary to calculate the sum of signals $\bar{s}(t)$ originating from all n single crystallites in the specimen

$$\bar{s}(t) = \sum_{i=1}^n s\left(t; \Omega_{\text{CR}}^{(i)}\right) \quad (3.12)$$

Assuming a completely random orientation distribution and a large number of crystallites, this average signal $\bar{s}(t)$ corresponds to an integral over the Euler angles $\Omega_{\text{CR}} = \{\alpha_{\text{CR}}, \beta_{\text{CR}}, \gamma_{\text{CR}}\}$

$$\bar{s}(t) = \int_0^{2\pi} d\alpha_{\text{CR}} \int_0^{\pi} d\beta_{\text{CR}} \sin \beta_{\text{CR}} \int_0^{2\pi} d\gamma_{\text{CR}} s(t; \Omega_{\text{CR}}) \quad (3.13)$$

This integral can not be solved analytically. This makes it necessary to numerically mimic the powder average. In order to minimise the computation time, it is desirable to keep the number of sets Ω_{CR} as small as possible. The goal is to have a distribution of orientations for which every crystallite contributes equally to the final signal. This can be achieved by using a uniform distribution of orientations for which only the total number has to be optimised to reproduce the experimental powder signal. To date there are no analytical solutions describing a uniform distribution of sets of two or three Euler angles. Numerical approaches to simulate such uniform distributions exist [81, 82, 83]. Such sets Ω_{CR} can be pre-calculated and stored so they only need to be read from a database during the actual simulation of the NMR experiment.

In the context of rotation operators the Euler angle γ_{CR} of the set Ω_{CR} is connected to a rotation around the z -axis of RAS (Eq. (2.85)) which is identical to the rotation axis of the MAS sample holder. The signal from crystallites only differing by their orientation γ_{CR} is therefore related by a time shift $t_\gamma = \frac{\gamma_{\text{CR}}}{\omega_{\text{rot}}}$ of the signal and the Hamiltonian and $\hat{U}(t, t_0)$ obey

$$\hat{\mathcal{H}}(t; \gamma_{\text{CR}}) = \hat{\mathcal{H}}(t + t_\gamma; 0) \quad (3.14)$$

$$\hat{U}(t, t_0; \gamma_{\text{CR}}) = \hat{U}(t + t_\gamma, t_0 + t_\gamma; 0) \quad (3.15)$$

For MAS and R^2 experiments this time shift (γ_{CR} -average) can be calculated analytically yielding the partially averaged signal $\bar{s}^{\gamma_{\text{CR}}}\left(t; \alpha_{\text{CR}}^{(i)}, \beta_{\text{CR}}^{(i)}\right)$ and the numerical powder average is then calculated according to

$$\bar{s}(t) = \sum_{i=1}^N \bar{s}^{\gamma_{\text{CR}}}\left(t; \alpha_{\text{CR}}^{(i)}, \beta_{\text{CR}}^{(i)}\right) w_i \quad , \quad \text{with} \quad \sum_{i=1}^N w_i = 1 \quad (3.16)$$

Analytical γ_{CR} -averaging is not always possible or may be tedious to calculate [77, 84] for example, when the periodicity of the experiment is modified by RF pulses. For the R^2 -DQF $_{\beta}$, R^2 -DQF $_{\beta\gamma}$, and $C7_2^1$ experiments the average over γ_{CR} is better calculated numerically, normally using 15 to 30 angles. This explicit calculation slows down the

simulation by a factor equivalent to the number of γ_{CR} -angles necessary for the powder average.

For the powder average over the Euler angles $\{\alpha_{\text{CR}}^{(i)}, \beta_{\text{CR}}^{(i)}\}$ in Eq. (3.16) the number of sets N is usually in the range of 100 to 700 crystallite orientations. This range can be expected to be suitable for the simulation of MAS experiments, whereas simulation of static or off-magic angle spinning (OMAS) spectra require larger sets $\{\alpha_{\text{CR}}^{(i)}, \beta_{\text{CR}}^{(i)}\}$.

3.2.3. Computation

Another possibility to speed up the calculation of powder NMR spectra is to split serial calculations in order to execute them on different computers (CPUs) in parallel [85, 86, 87]. The runtime of a parallel program can be characterised by two parameters: the size of input data (n_{in}) and the number of processes (n_{proc}) working on the data. The speedup $S(n_{\text{in}}, n_{\text{proc}})$ of a parallel execution over a serial execution can be defined as

$$S(n_{\text{in}}, n_{\text{proc}}) = \frac{T_{\sigma}(n_{\text{in}})}{T_{\pi}(n_{\text{in}}, n_{\text{proc}})} \quad (3.17)$$

where $T_{\sigma}(n_{\text{in}})$ and $T_{\pi}(n_{\text{in}}, n_{\text{proc}})$ are the serial and parallel runtime of the calculation, respectively. Ideally a linear speedup $S(n_{\text{in}}, n_{\text{proc}}) = n_{\text{proc}}$ is achieved. In a more real description the speedup is reduced by an overhead due to programming the parallelisation and the time used for interprocess communication

$$0 < S(n_{\text{in}}, n_{\text{proc}}) \leq n_{\text{proc}} \quad (3.18)$$

This overhead is generally independent of the actual time of execution of the process and can be bigger than the actual serial computation ($T_{\sigma}(n_{\text{in}}) < T_{\pi}(n_{\text{in}}, n_{\text{proc}})$).

Two-spin and three-spin simulations using the COMPUTE algorithm together with γ_{CR} -averaging (γ -COMPUTE) on contemporary hardware (CPUs with core frequency exceeding 600 MHz) are prone to this slowdown. When considering small spin systems (≤ 3) parallelisation is useful for the simulation of all experiments except where γ -COMPUTE is exploitable. The most obvious candidate for serial calculation in the simulation of NMR spectra of powder samples is the calculation of the powder average itself. Another candidate for parallelisation is the calculation of the time propagators (Eq. (3.6)).

3.2.4. Extraction of Structural Parameters

The degree of agreement (quality) of a simulated spectrum S_{sim} with an experimental spectrum S_{exp} is denoted as

$$\chi^2 = \frac{1}{N} \sum_i [S_{\text{exp}}(\omega_i) - S_{\text{sim}}(\omega_i)]^2 \quad (3.19)$$

where N is the number of data points in the spectrum and χ^2 is the chi-squared error. Experimental and simulated spectra are normalised as

$$\sum_{i=1}^N S_{\text{exp}}(\omega_i) = \sum_{i=1}^N S_{\text{sim}}(\omega_i) = 1 \quad (3.20)$$

in order to make it possible to compare spectra recorded at different experimental conditions (ω_{rot} , τ_{exc} , etc.). Otherwise a normalisation

$$\max(S_{\text{exp}}(\omega_i)) = \max(S_{\text{sim}}(\omega_i)) = 1 \quad (3.21)$$

is used.

Before starting to extract parameters from experimental spectra it is important to optimise some of the purely numerical parameters, for example, the number of powder angles Ω_{CR} , or the number of short time intervals δt during time evolution. Only if small variations of these parameters do not show significant effects on the line shape of the simulated spectra the next step is the actual extraction of the parameters from an experimental spectrum. The procedure of determining spin-system parameters usually involves the use of multiple experimental spectra/conditions, depending on the properties of the spin system.

3.2.4.1. Iterative Fitting

One way to determine the best-fit set of spin-system parameters $\{p_0(1), \dots, p_0(n)\}$ is the continuous variation of parameters while aiming to minimise the $\chi^2(p(1), \dots, p(n))$ -error difference between S_{exp} and S_{sim} as defined in Eq. (3.19). This iterative fitting approach is implemented here exploiting the MINUIT [88] minimisation package. It provides different strategies to minimise a function $\chi^2(p(1), \dots, p(n))$ dependent on a set of n parameters $p(i)$. The characteristics of these strategies have been compared in [89].

Fitting programmes require more hands-on guidance the higher the number of parameters n varied are. This is due to various reasons: The final best-fit minimum is not necessarily found by the fit when the initially guessed starting parameters are too different from the best-fit set $\{p_0(1), \dots, p_0(n)\}$ (global minimum). The danger of local minima has to be monitored carefully. Additionally, special attention has to be paid to parameters that are highly correlated and such ones that display strongly differing overall sensitivity (effect on χ^2). Hence, it is usually good practise to combine iterative fitting with calculations of low dimensional error hyperplanes as described in the following.

3.2.4.2. Calculation of Error Hyperplanes

It is possible to calculate the full n -dimensional χ^2 -error plane by varying all parameters over their full range of possible/reasonable values. This approach has the advantage that the global minimum $\chi_0^2(p_0(1), \dots, p_0(n))$ is definitely found as opposed to the fitting approach where careful additional checks are necessary in order to ensure that no local minimum was found. However, calculation of error hyperplanes is becoming more awkward the larger the number n of parameters $p(i)$ becomes that need to be varied since the number

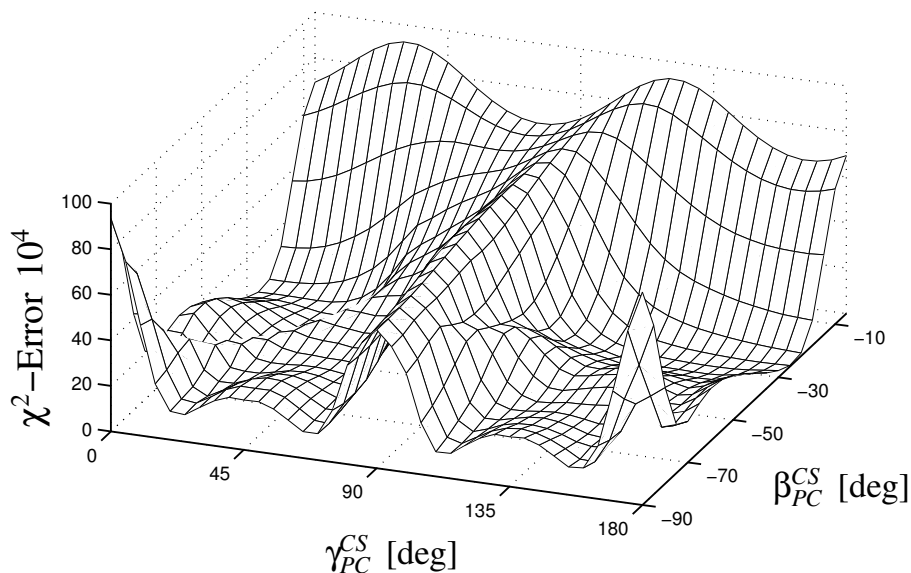


Figure 3.5.: Two dimensional $\chi^2(p(1), p(2))$ -error hyperplane visualised as a surface plot, showing multiple minima.

of calculation steps is growing exponentially with n . The number of calculations can be minimised for orientational parameters $\Omega_{PC}^\lambda = \{\alpha_{PC}^\lambda, \beta_{PC}^\lambda, \gamma_{PC}^\lambda\}$ by taking advantage of the sets Ω_{CR} as developed for powder averaging schemes. These sets Ω_{CR} are optimised to cover the range of these parameters more uniformly than e.g. a Cartesian grid of the same number of coordinate points would do.

The interpretation of the error plane can only be visualised completely for dimensions smaller than four. However, visualisation of the plane is desirable since it is a common situation that there exist multiple equally good minima that are indistinguishable by an NMR experiment. Some such minima are related by symmetry operations, especially when a variation of Euler angles $\Omega_{PC}^\lambda = \{\alpha_{PC}^\lambda, \beta_{PC}^\lambda, \gamma_{PC}^\lambda\}$ is describing physically identical situations. A graphical evaluation helps greatly to determine possible correlations between parameters. Here the maximum of simultaneously varied parameters has been four.

3.2.5. Errors and Sensitivities of Fitted Parameter

Once the global minimum $\chi_0^2(p_0(1), \dots, p_0(n))$ of $\chi^2(p(1), \dots, p(n))$ is determined it is useful to have a measure for the quality of the best-fit parameters $p_0(i)$. This so-called error of the best-fit values should provide limits within which the parameters are assumed to be reproducible. Usually this task is accomplished by calculating the standard deviation of the parameters. However, a concise error calculation based on error propagation is not easily possible due to the complex dependence of the signal (spectrum) on the spin parameters and therefore a more heuristic error estimation is used here. The uncertainty of a determined parameter $p_0(i)$ is said to be equal to half the width of an one-dimensional error scan of this parameter at twice the minimum error $\chi_0^2(p_0(1), \dots, p_0(n))$ (see Figure 3.6).

An second aspect which is focusing not directly on the accuracy of the parameter but

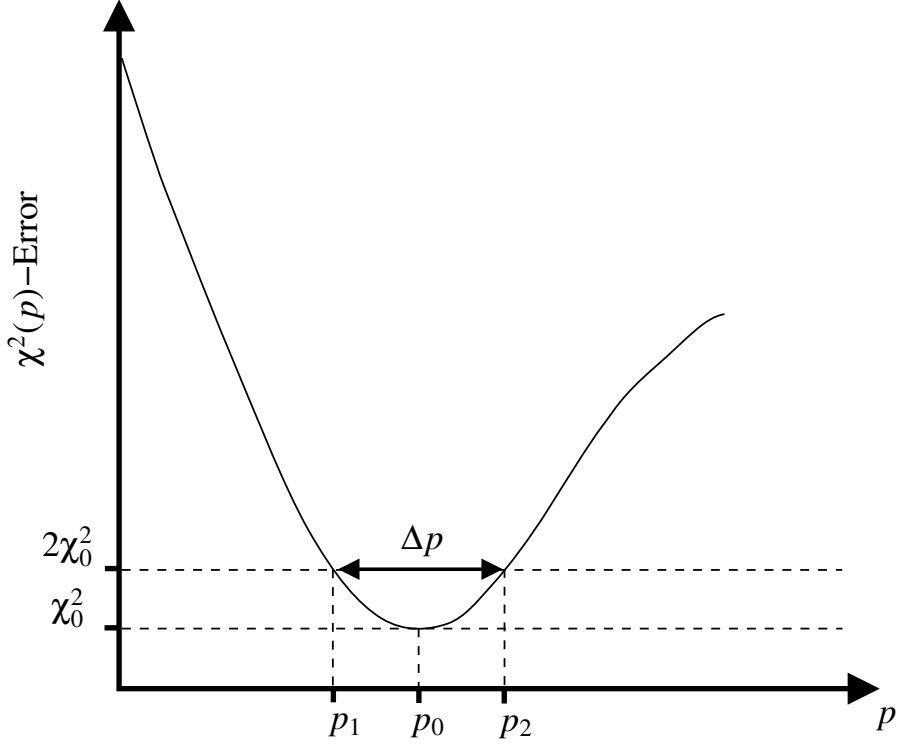


Figure 3.6.: One dimensional $\chi^2(p)$ -error scan of a parameter p . For a converged fit p_0 is the best-fit value of p and χ_0^2 the best-fit $\chi^2(p)$ -error. The confidence in the accuracy of p_0 is estimated by defining $\Delta p = \frac{p_2 - p_1}{2}$ as the error of the value p_0 .

on the sensitivity with which a parameter $p(i)$ is encoded in the spectrum. Knowledge about this helps to tailor experimental conditions so that optimum sensitivity is provided for all the spin-system parameters. Alternatively, it can be used to tune experiments to discriminate for or against some parameter and to justify a reduction of the dimension of the error plane to be fitted/calculated. In this work, two approaches have been used. A statistics-based way is possible by calculating Cramér-Rao lower bounds $c(p(i))$ [90, 91] and defining true reliability $r(p(i))$ as

$$r(p(i)) = \frac{p(i)}{c(p(i))} \quad (3.22)$$

Cramer-Rao bounds are based on the calculation of the covariance matrix and therefore, describe the behaviour of the parameters $p(i)$ under the influence of variations. This approach to parametrise the sensitivity of parameter encoding is rather calculation intensive and complex if the number of parameters rises. A second definition of sensitivity is based on the one-dimensional error scans shown in Figure 3.6. The sensitivity of a parameter $p(i)$ is defined to be the integral

$$r(p(i)) = \int_{p_a(i)}^{p_b(i)} \chi^2(p(i)) \quad (3.23)$$

where the integration limits are chosen suitably (e.g. $0^\circ - 360^\circ$ for $p(i) = \alpha_{\text{PC}}^{\text{CS}}$). In com-

bination with the definition of the accuracy $\Delta p(i)$ of the parameter $p(i)$ this provides a fast and intuitive estimation of parameter sensitivity. One-dimensional χ^2 -scans are not only useful to examine the parameters sensitively encoded in an experimental NMR spectrum (e.g. to set up an iterative fit) but also serve for the purpose of predicting/choosing suitable experimental conditions for a given purpose.

4. Summary and Conclusions

The objective of this work is the examination of one-dimensional magic angle spinning (MAS) nuclear magnetic resonance (NMR) spectra. These spectra serve as a source of spin-system parameters which are related to structural and conformational parameters. It is to show that all spin-system parameters can be derived in a robust and reliable manner. Further on it is investigated how experimental conditions can be optimised in order to determine parameters in a stepwise fashion and get best accuracy for the derived data.

This work is dealing with dipolar coupled spin $S = \frac{1}{2}$ systems in polycrystalline powdered samples. MAS is used in order to increase spectral resolution and achieve gain in signal-to-noise ratio. However, MAS also causes a substantial down scaling of the information content about the anisotropic interactions of a spin system. A technique to remedy this drawback, while keeping the advantages of MAS, is the use of pulse sequences that reintroduce (“recouple”) anisotropic dipolar coupling interactions.

To access the spin-system parameters encoded in the lineshapes of MAS NMR spectra an iterative fitting approach is applied. These procedures make numerically exact simulations mandatory and involve accurate calculations of the complete spin-system dynamics. As a consequence all spin-system parameters sensitively encoded in the spectral lineshapes can principally be extracted. Computation of numerically exact simulations can be quite demanding on hardware (CPU speed). The algorithmic implementation of the spin dynamics has significant impact on the time required to simulate a spectrum. Optimisation and clever design of such algorithms is crucial especially when considering the need for repeated simulations in the process of iterative fitting. Usually spin-system size and the complexity of the pulse sequence are the principal factors determining the computation time of a spectrum. The numerical strategy adopted here is applied to one- to four-spin systems where the limiting factor is less the size of the spin system but rather the spin-system characteristics themselves. Spin systems composed of one to four spins have been chosen such that a representative range of spin-system parameters is covered. In the following the results presented in Appendix A to H are summarised. The contribution of coauthors is noted at the end of every of the following paragraphs.

Appendix A: ^{29}Si MAS NMR spectra of R_3SiF ($\text{R} = 9\text{-anthryl}$) yield the magnitudes and orientations of the ^{29}Si CSA tensor and the heteronuclear direct and indirect dipolar coupling constants $b_{ij}(^{29}\text{Si}\text{-}^{19}\text{F})$ and $^1J_{\text{iso}}(^{29}\text{Si},^{19}\text{F})$, respectively. Heteronuclear $^{29}\text{Si}\text{-}\{^1\text{H}, ^{19}\text{F}\}$ double decoupling is useful to selectively determine the ^{29}Si CSA tensor magnitudes. Based on the parameters of this $^{29}\text{Si}\text{-}^{19}\text{F}$ spin pair, the optimum choice of experimental parameters ($\omega_{\text{rot}}, \omega_0$) can be predicted when aiming at the complete determination of all spin-system parameters.

The X- $\{^1\text{H}, ^{19}\text{F}\}$ double decoupling MAS NMR probe head has been designed and built by Klaus Hain. Claire Marichal helped with fitting some of the experimental ^{29}Si spectra.

Appendix B: MAS NMR spectra of two-spin systems generally only provide orientational information relative to the symmetric dipolar coupling tensor and leave an ambiguity regarding the orientation around the symmetry axis of the dipolar tensor. However, absolute orientations are accessible for larger-than-two spin systems. The fully ^{13}C labelled three-spin system in triammonium phosphoenolpyruvate (PEP) monohydrate is providing this kind of condition and absolute ^{13}C CSA-tensor orientations are obtained. Additionally, these relate to the orientation of the carboxylic group in the PEP moiety yielding information, which could not be derived from internuclear ^{13}C - ^{13}C distance information alone. The usually large number of unknown parameters in homonuclear three-spin systems make it desirable to determine them by stepwise procedures. These procedures rely on the combination of the partial selectivity of different R^2 conditions and the scaling of the chemical shielding interaction as a function of the magnetic field strength (ω_0) relative to the dipolar couplings ($b_{ij}({}^{13}\text{C}-{}^{13}\text{C})$).

Stephan Dusold measured all the experimental spectra of $(\text{NH}_4)_3(\text{PEP}) \cdot \text{H}_2\text{O}$. W.A. Shuttleworth, D.L. Jakeman, D.J. Mitchell and J.N.S. Evans prepared the fully ^{13}C -enriched sample of $(\text{NH}_4)_3(\text{PEP}) \cdot \text{H}_2\text{O}$.

Appendix C: Two pulse sequences ($\text{R}^2\text{-DQF}_{\beta,\gamma}$, $\text{R}^2\text{-DQF}_{\beta}$) combining R^2 and double-quantum filtration (DQF) are examined. They are tested for their DQF efficiency and their ability to encode spin parameters sensitively in the spectral lineshapes. An emphasis is placed on spin systems with large CSA magnitudes as compared to the direct dipolar couplings constants (b_{ij}) (as is even sometimes found in ^{13}C spin systems of organic compounds). For such spin systems the non- γ_{CR} -encoded pulse sequence $\text{R}^2\text{-DQF}_{\beta,\gamma}$ is performing better in terms of efficiency, while for the γ_{CR} -encoded pulse sequence $\text{R}^2\text{-DQF}_{\beta}$ a slightly more sensitive encoding of the spin-system parameters in the spectral lineshapes is found.

Xavier Helluy measured some of the experimental spectra and carried out all numerical simulations of the sodium pyruvate ^{13}C two-spin system. He also implemented the combined COMPUTE- and direct-method time propagation as a parallelised routine.

Appendix D: The $\text{R}^2\text{-DQF}_{\beta,\gamma}$ sequence is applied to a spin system characterised by large CSA magnitudes. Both, direct and indirect, dipolar coupling interactions are present and are of the same order of magnitude and are considerably smaller than the CSA magnitude. This situation is given for the ^{119}Sn spin pair in $(\text{chex}_3\text{Sn})_2\text{S}$. $\text{R}^2\text{-DQF}_{\beta,\gamma}$ experiments on this kind of spin system show that high DQF efficiencies are not only possible for spinning speeds (ω_{rot}) matching a R^2 condition. This is due to the isotropic J -coupling (${}^2J_{\text{iso}}(\text{Sn}^{119}, \text{Sn}^{119})$) interaction which is unaffected by MAS.

Xavier Helluy measured some initial experimental spectra. Claire Marichal measured some of the experimental spectra.

Appendix E: The selectivity of the R^2 effect in larger-than-two spin systems is examined when additionally applying DQF. The ^{13}C three-spin system in sodium pyruvate serves as a model making different R^2 conditions accessible. Selectivity is found for certain R^2 conditions resulting in virtual two-spin spectra. The selectivity of certain R^2 conditions is a feature of the respective spin system.

Xavier Helluy measured some of the experimental spectra.

Appendix F: The narrowbandedness of the $n = 0$ R^2 condition, for which $\Delta\omega_{\text{iso}}^{CS_{1,2}} = 0$ has to be fulfilled, is investigated with and without DQF. The resulting lineshapes are examined regarding their information content. Different values for the isotropic shielding difference $\Delta\omega_{\text{iso}}^{CS_{1,2}}$ are used to examine the region around the resonance condition on a purely numerical basis. These simulations employed the known spin-system parameters of the ^{31}P spin pair in $\text{Na}_4\text{P}_2\text{O}_7 \cdot 10\text{H}_2\text{O}$. Without DQF the lineshapes of the resulting spectra display good sensitivities to all spin-system parameters up to $\Delta\omega_{\text{iso}}^{CS_{1,2}} \approx 400$ Hz. Additional DQF extends further the range of $\Delta\omega_{\text{iso}}^{CS_{1,2}}$ for which parameters can be extracted sensitively from the resulting spectral lineshapes. However, the DQF efficiency is decaying drastically when $\Delta\omega_{\text{iso}}^{CS_{1,2}} \geq 400$ Hz.

Appendix G: The ^{31}P spin pairs in two Pt(II)-bis(phosphine) dithiolate complexes serve as test platforms for the numerical results found regarding the $n \approx 0$ R^2 condition (Appendix F). For one of the two complexes $\Delta\omega_{\text{iso}}^{CS_{1,2}} = 0$ ppm for its two isotropic ^{31}P shielding values and the $n = 0$ R^2 condition is fulfilled. The other complex displays a shielding difference $\Delta\omega_{\text{iso}}^{CS_{1,2}} = 0.5$ ppm and represents a $n \approx 0$ R^2 situation. Both cases allow the determination of all spin-system parameters with good precision from a selection of suitable R^2 and R^2 -DQF $_{\beta,\gamma}$ spectra where good efficiencies are obtained for DQF. Further, the ^{31}P CSA-tensor orientations point to a general trend for P atoms in a four-fold coordination, according to which always one direction of the CSA principal axes is perpendicular to a local pseudo-mirror plane.

Stephan Dusold carried out some initial simulations and iterative fitting of the ^{31}P and ^{195}Pt MAS NMR spectra of the two Pt(II) - Phosphine Complexes. Franz Geipel and Dieter Sellmann provided the samples of the two Pt(II) Phosphine Complexes.

Appendix H: A different set of spin-system parameters is characteristic for the ^1H spins of the two olefinic protons in solid maleic acid where the ^1H CSA magnitudes are small as compared to $b_{ij}(^1\text{H}-^1\text{H})$. Several samples are prepared with different degrees of deuteration. These serve the purpose to examine the various degrees of isolation of the olefinic ^1H spin pairs from each other and the concomitant effects on ^1H R^2 -DQF $_{\beta,\gamma}$ lineshapes.

Hans Förster measured some of the experimental ^1H R^2 -DQF $_{\beta,\gamma}$ spectra. Heidi Maisel prepared all the samples of crystalline maleic acid.

A combination R^2 and DQF proved to build robust and reliable experiments making all spin-system parameters accessible to an iterative fitting approach in a usually stepwise

manner. The numerical simulations used in this approach additionally can serve for optimising existing pulse sequences. This usually results in better experimental spectra due to a better prediction of optimum experimental setup parameters. Such pre-experiment simulations are especially useful when large CSA interactions are present in dipolar coupled spin systems, a scenario not amenable to a complete theoretical description. Numerically exact simulations can also be regarded as an additional way of designing new pulse sequences. However, there is a certain lack of insight in the physical mechanisms of a pulse sequence when obtained by numerical methods only.

Spin-system parameters determined by NMR relate to structure. This NMR information can serve as reference data used in the development of new structure investigation approaches such as *ab initio* calculations. *Ab initio* calculations are already quite capable of calculating structures of (bio)molecules containing only light elements. However, there are still problems handling ionic structures and heavy elements which by themselves often do not put difficulties to NMR.

A spectral lineshape fitting approach also bears some caveats. Spectral lineshapes encode all spin-system parameters in a way accessible to lineshape fitting only if originating from well-crystallised samples. Non-crystalline (rigid) samples display a dispersion of the chemical shieldings which manifests itself as broadenings in the spectral lineshapes. These inhomogeneous broadenings tend to blur the meaningful lineshape features that are essential to a lineshape-fitting approach aiming at the determination of all spin system parameters. Furthermore, the presence of dynamic disorder in a sample is adding complexity to a numerically exact simulation of spin dynamics. Samples in this work have been chosen such that spectral lineshapes are not affected by any dynamical disorder.

NMR is not always the only technique to obtain a desired structural information. However, there are unique properties to NMR that often render it the preferred method. NMR provides the possibility to selectively investigate only parts of a molecule, for instance by isotopic labelling. The spectra of such isolated spin systems only contain information specific to this system making it possible to neglect parts of the sample. Another characteristic of NMR is the existence of a plethora of different experiments tailored to investigate specific aspects of the spin dynamics. NMR experiments, therefore can give answers to specific questions as well as it may be possible to determine all spin parameters in a single experiment. All this together promotes NMR as a tool to investigate primarily local structure. The examination of large structures by NMR is confined by the relative weakness of long range direct dipolar couplings and therefore the lack of long range internuclear distance information. Extended structures therefore can be determined by NMR only by combining piecewise information. This makes NMR in a sense complementary to x-ray diffraction which can handle extended crystalline structures well, but in turn x-ray has difficulties in resolving the location of light elements such as hydrogen atoms, or describing dynamically disordered groups in molecules.

For the future it would be useful to improve further the techniques of NMR that give complete and accurate information about local structure. This includes dipolar recoupling experiments of improved selectivity like R^2 -DQF. But when aiming for the ability

to handle larger dipolar coupled spin systems it would also be advantageous to exploit pulse sequences that completely suppress the influence of CSA interactions while maintaining/recoupling the information about dipolar interactions. Further it is important to vary the information content of the spectra, a task for which e.g. OMAS experiments could be used.

5. Short Summary

The objective of this work is the examination of one-dimensional magic angle spinning (MAS) nuclear magnetic resonance (NMR) spectra. These spectra serve as a source of spin-system parameters which are related to structural and conformational parameters. It is to show that all spin-system parameters can be derived in a robust and reliable manner. Further on it is investigated how experimental conditions can be optimised in order to determine parameters in a stepwise fashion and get best accuracy for the derived data.

This work is dealing with dipolar coupled spin $S = \frac{1}{2}$ systems in polycrystalline powdered samples. MAS is used in order to increase spectral resolution and achieve gain in signal-to-noise ratio. However, MAS also causes a substantial down scaling of the information content about the anisotropic interactions of a spin system. A technique to remedy this drawback, while keeping the advantages of MAS, is the use of pulse sequences that reintroduce (“recouple”) anisotropic dipolar coupling interactions.

To access the spin-system parameters encoded in the lineshapes of MAS NMR spectra an iterative fitting approach is applied. These procedures make numerically exact simulations mandatory and involve accurate calculations of the complete spin-system dynamics. As a consequence all spin-system parameters sensitively encoded in the spectral lineshapes can principally be extracted. Computation of numerically exact simulations can be quite demanding on hardware (CPU speed). The algorithmic implementation of the spin dynamics has significant impact on the time required to simulate a spectrum. Optimisation and clever design of such algorithms is crucial especially when considering the need for repeated simulations in the process of iterative fitting. Usually spin-system size and the complexity of the pulse sequence are the principal factors determining the computation time of a spectrum. The numerical strategy adopted here is applied to one- to four-spin systems where the limiting factor is less the size of the spin system but rather the spin-system characteristics themselves. Spin systems composed of one to four spins have been chosen such that a representative range of spin-system parameters is covered.

A combination R² and DQF proved to build robust and reliable experiments making all spin-system parameters accessible to an iterative fitting approach in a usually stepwise manner. The numerical simulations used in this approach additionally can serve for optimising existing pulse sequences. This usually results in better experimental spectra due to a better prediction of optimum experimental setup parameters. Such pre-experiment simulations are especially useful when large CSA interactions are present in dipolar coupled spin systems, a scenario not amenable to a complete theoretical description. Numerically exact simulations can also be regarded as an additional way of designing new pulse sequences. However, there is a certain lack of insight in the physical mechanisms of a pulse sequence when obtained by numerical methods only.

For the future it would be useful to improve further the techniques of NMR that give complete and accurate information about local structure. This includes dipolar recoupling experiments of improved selectivity like R²-DQF. But when aiming for the ability to handle larger dipolar coupled spin systems it would also be advantageous to exploit pulse sequences that completely suppress the influence of CSA interactions while maintaining/recoupling the information about dipolar interactions. Further it is important to vary the information content of the spectra, a task for which e.g. OMAS experiments could be used.

6. Kurze Zusammenfassung

Das Ziel dieser Arbeit ist es eindimensionale „magic angle spinning“ (MAS) magnetische Kernresonanz (NMR) Spektren zu untersuchen. Derartige Spektren dienen als Quelle für Spinsystem Parameter welche wiederum Aussagen über Struktur und Konformation erlauben. Es wird gezeigt, dass sich alle Spinsystem Parameter auf reproduzierbare und präzise Art und Weise bestimmen lassen. Des Weiteren wird untersucht wie die experimentellen Bedingungen gewählt werden können um Spinsystem Parameter schrittweise und auch mit bestmöglicher Genauigkeit zu bestimmen.

Die Arbeit behandelt dipolar gekoppelte Spin $S = \frac{1}{2}$ Systeme in polykristallinen, Pulvern. MAS wird verwendet um sowohl die spektrale Auflösung zu erhöhen als auch um das Signal-zu-Rausch Verhältnis zu verbessern. Außerdem führt MAS auch zu einem stark reduzierten Informationsgehalt über die anisotropen Wechselwirkungen eines Spinsystems. Eine Methode um diese Eigenschaft von MAS zu unterdrücken, während die Vorteile erhalten bleiben, ist die Verwendung von Pulssequenzen die die anisotrope dipolare Wechselwirkung wieder einführen.

Um die Spinsystem Parameter, die in den Linienformen der MAS NMR Spektren kodiert sind, zu bestimmen wird die Methode einer iterativer Anpassung experimenteller Spektren („Fitten“) angewandt. Dieses Vorgehen bedingt die Verwendung numerische exakter Simulationen und setzt eine präzise Berechnung der gesamten Spinsystem Dynamik voraus. Als Konsequenz lassen sich daher prinzipiell alle Spinsystem Parameter bestimmen die sensitiv in den spektralen Linien kodiert sind. Die computergestützte Berechnung numerisch exakter Simulationen stellt bisweilen hohe Anforderungen an Hardware (CPU Geschwindigkeit). Die Implementierung der Algorithmen zur Berechnung der Spindynamik hat entscheidenden Einfluss auf die Dauer der Simulation eines Spektrums. Eine clevere Wahl und Optimierung solcher Algorithmen ist entscheidend besonders in Anbetracht wiederholter Simulation im Verlauf des Fittens. Generell sind die Größe des Spinsystems und die Komplexität der verwendeten Pulssequenzen die bestimmenden Zeitfaktoren für die Dauer der Simulation eines Spektrums. Die numerische Strategie die hier verwendet wird, wird auf Systeme bestehend aus zwei bis vier Spins angewandt wobei der limitierende Faktor weniger die Größe des Spinsystems als die jeweilige Charakteristik der Spinsysteme selbst ist. Spinsysteme wurden hier so gewählt, dass eine repräsentative Bandbreite von Spinsystem Parametern abgedeckt ist.

Die Kombination von R^2 und DQF ergab reproduzierbare und präzise Experimente die alle Spinsystem Parameter bestimmbar machen. Dabei können die Spinsystem Parameter meist schrittweise mittels der Strategie des iterativen Fittens bestimmt werden. Die numerische Simulationen die in diesem Rahmen verwendet werden lassen sich auch benutzen um bereits existierende Pulssequenzen zu optimieren. Ein solches Vorgehen ermög-

licht verbesserte experimentelle Spektren, da die optimalen Parameter des experimentelle Aufbaus besser vorhergesagt werden können. Derartige vor-experimentelle Simulationen sind dann besonders nützlich wenn große CSA-Wechselwirkungen in dipolar gekoppelten Spinsystemen auftreten, einem Szenario für das die Theorie keine analytische Komplettlösung bietet. Des weiteren können numerisch exakte Simulationen auch benutzt werden um neue Pulssequenzen zu entwickeln. Allerdings existiert bei einer auf rein numerischem Weg entwickelten Pulssequenz immer ein gewisses Defizit im Bezug auf das physikalische Verständnis für die Methode.

Für die Zukunft wäre es nützlich NMR-Methoden für die komplette und genaue Bestimmung lokaler Strukturen zu verbessern. Das beinhaltet Experimente, die bei der Wiedereinführung der dipolaren Wechselwirkung eine sehr gute Selektivität aufweisen wie z.B. R^2 -DQF. Für die Untersuchung größere dipolar gekoppelte Spinsysteme wäre es außerdem vorteilhaft Pulssequenzen verwenden zu können die den Einfluss der CSA-Wechselwirkung ganz unterdrücken während die Information über die dipolaren Kopplungen erhalten bleibt. Des Weiteren wäre es wichtig den Informationsgehalt der NMR-Spektren optimal variieren zu können, eine Forderung die z.B. durch OMAS Experiment erfüllt werden kann.

Bibliography

- [1] R. R. ERNST, G. BODENHAUSEN and A. WOKAUN, *Principles of Nuclear Magnetic Resonance in One and Two Dimensions*, Clarendon Press, Oxford, 1987.
- [2] A. ABRAGAM, *The Principles of Nuclear Magnetism*, Clarendon Press, Oxford, 1978.
- [3] N. W. ASHCROFT and N. D. MERMIN, *Solid State Physics*, Thomson Learning, London, 1976.
- [4] J. D. JACKSON, *Classical Electrodynamics*, John Willey & Sons, New York, 1999.
- [5] J. J. SAKURAI, *Modern Quantum Mechanics*, Addison-Wesley Publishing Company, Reading, MA, 1994.
- [6] W. NOLTING, *Grundkurs: Theoretische Physik 5 (Quantenmechanik)*, Verlag Zimmermann-Neufang, Ulmen, 1993.
- [7] H. VOGEL, *Gerthsen Physik*, Springer-Verlag, Berlin, 1995.
- [8] D. I. HOULT and R. E. RICHARDS, *J. Magn. Reson.* **24**, 71 (1976).
- [9] I. RABI, S. MILLMAN, P. KUSCH and J. ZACHARIAS, *Phys. Rev. Let.* **55**, 526 (1939).
- [10] F. BLOCH, *Phys. Rev.* **70**, 460 (1946).
- [11] E. M. PURCELL, H. C. TORREY and R. V. POUND, *Phys. Rev.* **69**, 37 (1946).
- [12] F. BLOCH, W. W. HANSEN and M. PACKARD, *Phys. Rev.* **69**, 127 (1946).
- [13] F. BLOCH, W. W. HANSEN and M. PACKARD, *Phys. Rev.* **70**, 474 (1946).
- [14] C. P. SLICHTER, *Principles of Magnetic Resonance*, Springer-Verlag, Berlin, 1996.
- [15] D. R. LIDE, *CRC Handbook of Chemistry and Physics*, CRC Press, New York, 2003.
- [16] J. H. VAN VLECK, *The Theory of Electric and Magnetic Susceptibilities*, Oxford University Press, London, 1932.
- [17] G. UHLENBECK and S. GOUDSMIT, *Nature* **117**, 264 (1926).
- [18] L. I. SCHIFF, *Quantum Mechanics*, McGraw-Hill, New York, 1968.
- [19] P. M. DIRAC, *The Principles of Quantum Mechanics*, Clarendon Press, Oxford, 1982.

- [20] D. J. S. ROBINSON, *A Course in the Theory of Groups*, Springer Verlag, Berlin, 1996.
- [21] M. H. LEVITT, *Spin Dynamics*, John Wiley, Chichester, 2001.
- [22] M. T. DUNCAN, *A Compilation of Chemical Shift Anisotropies*, Farragut Press, Chicago, 1990.
- [23] A. NOLLE, *Z. Physik B: Condens. Matter* **34**, 175 (1979).
- [24] J. JOKISAARI, K. RÄISÄNEN, J. KUONANOJA, P. PYYKKÖ and L. LAJUNEN, *Molec. Phys.* **39**, 715 (1980).
- [25] C. MARICHAL and A. SEBALD, *Chem. Phys. Lett.* **286**, 298 (1998).
- [26] P. PYYKKÖ and L. WIESENFELD, *Molec. Phys.* **43**, 557 (1981).
- [27] R. E. J. SEARS, Q. Z. GUO and H. J. MACKEY, *J. Chem. Phys.* **80**, 5448 (1984).
- [28] P. N. TUTUNJIAN and J. S. WAUGH, *J. Magn. Reson.* **49**, 155 (1982).
- [29] J. VAARA, J. JOKISAARI, R. WASYLISHEN and D. BRYCE, *Prog. Nucl. Magn. Reson. Spectrosc.* **41**, 233 (2002).
- [30] T. NAKAI and C. A. MCDOWELL, *J. Chem. Phys.* **96**, 3452 (1992).
- [31] I. I. RABI, N. F. RAMSEY and J. SCHWINGER, *Rev. Mod. Phys.* **26**, 167 (1954).
- [32] S. A. SMITH, W. E. PALKE and J. T. GERIG, *Concepts Magn. Reson.* **4**, 107 (1992).
- [33] S. A. SMITH, W. E. PALKE and J. T. GERIG, *Concepts Magn. Reson.* **4**, 181 (1992).
- [34] W. J. THOMPSON, *Angular Momentum*, Wiley, New York, 1994.
- [35] U. HAEBERLEN, High Resolution NMR in Solids, in *Adv. Magn. Reson., Suppl. 1*, Ed.: J. S. WAUGH, Academic Press, New York, 1976.
- [36] G. RACAH, *Phys. Rev.* **62**, 186 (1942).
- [37] F. J. DYSON, *Phys. Rev.* **75**, 486 (1949).
- [38] M. M. MARICQ and J. S. WAUGH, *J. Chem. Phys.* **70**, 3300 (1979).
- [39] A. BRINKMANN, M. EDÉN and M. H. LEVITT, *J. Chem. Phys.* **112**, 8539 (2000).
- [40] M. HOHWY and N. C. NIELSEN, *J. Chem. Phys.* **106**, 7571 (1997).
- [41] M. H. LEVITT, Symmetry-Based Pulse Sequences in Magic Angle Spinning Solid-State NMR, in *Encycl. Nucl. Magn. Reson.*, volume 9, pp. 165–196, John Wiley & Sons, Chichester, 2002.
- [42] W. NOLTING, *Grundkurs: Theoretische Physik 6 (Statistische Physik)*, Verlag Zimmermann-Neufang, Ulmen, 1993.

- [43] M. H. LEVITT, *J. Magn. Reson.* **126**, 164 (1997).
- [44] R. R. ERNST and W. A. ANDERSON, *Rev. Sci. Instrum.* **37**, 93 (1966).
- [45] E. FUKUSHIMA and S. B. W. ROEDER, *Experimental Pulse NMR - A Nuts and Bolts Approach*, Addison-Wesley, London, 1981.
- [46] J. JEENER, *Ampère Summer School, Basko Polje, Jugoslavia* (1971), unpublished.
- [47] R. R. ERNST, Multidimensional Spectroscopy: Concepts, in *Encycl. Nucl. Magn. Reson.*, volume 5, pp. 3122–3133, John Wiley & Sons, Chichester, 1996.
- [48] E. R. ANDREW, A. BRADBURY and R. G. EADES, *Nature* **183**, 1802 (1959).
- [49] I. J. LOWE, *Phys. Rev. Lett.* **2**, 285 (1959).
- [50] M. H. LEVITT, *J. Magn. Reson.* **82**, 427 (1989).
- [51] T. GULLION and M. S. CONRADI, *J. Magn. Reson.* **86**, 39 (1990).
- [52] S. C. SHEKAR, *Magn. Reson. Chem.* **36**, 496 (1998).
- [53] A. E. BENNETT, R. G. GRIFFIN and S. VEGA, Recoupling of Homo- and Heteronuclear Dipolar Interactions in Rotating Solids, volume 33 of *NMR Basic Principles and Progress*, pp. 3, Springer-Verlag, Berlin, 1994.
- [54] M. H. LEVITT, D. P. RALEIGH, F. CREUZET and R. G. GRIFFIN, *J. Chem. Phys.* **92**, 6347 (1990).
- [55] A. SCHMIDT and S. VEGA, *J. Chem. Phys.* **96**, 2655 (1992).
- [56] T. NAKAI and C. A. MCDOWELL, *Molec. Phys.* **77**, 569 (1992).
- [57] E. R. ANDREW, A. BRADBURY, R. G. EADES and V. T. WYNN, *Phys. Lett.* **4**, 99 (1963).
- [58] Z. H. GAN and D. M. GRANT, *Molec. Phys.* **67**, 1419 (1989).
- [59] E. KUNDLA and E. LIPPMAA, *J. Chem. Phys.* **102**, 1569 (1995).
- [60] E. KUNDLA, I. HEINMAA, H. KOOSKORA and E. LIPPMAA, *J. Magn. Reson.* **129**, 53 (1997).
- [61] A. KUBO and C. A. MCDOWELL, *J. Chem. Phys.* **92**, 7156 (1990).
- [62] S. DUSOLD and A. SEBALD, Dipolar Recoupling under Magic-Angle Spinning Conditions, volume 41 of *Ann. Rep. NMR Spectrosc.*, pp. 185 – 264, Academic Press Inc., San Diego, CA, 2000.
- [63] T. KARLSSON, M. EDÉN, H. LUTHMAN and M. H. LEVITT, *J. Magn. Reson.* **145**, 95 (2000).
- [64] A. BAX, R. FREEMAN and S. KEMPESELL, *J. Am. Chem. Soc.* **102**, 4849 (1980).

- [65] R. CHALLONER and A. SEBALD, *J. Magn. Reson. A* **122**, 85 (1996).
- [66] N. C. NIELSEN, F. CREUZET, R. G. GRIFFIN and M. H. LEVITT, *J. Chem. Phys.* **96**, 5668 (1992).
- [67] A. BAX and R. FREEMAN, *J. Magn. Reson.* **44**, 452 (1981).
- [68] M. RANCE, O. W. SORENSEN, G. BODENHAUSEN, G. WAGNER, R. R. ERNST and B. WUETHRICH, *Biochem. Biophys. Res. Commun.* **117**, 479 (1983).
- [69] M. EDÉN, *Concepts Magn. Reson.* **17A**, 117 (2003).
- [70] M. EDÉN, *Concepts Magn. Reson.* **18A**, 1 (2003).
- [71] M. EDÉN, *Concepts Magn. Reson.* **18A**, 24 (2003).
- [72] P. HODGKINSON and L. EMSLEY, *Prog. Nucl. Magn. Reson. Spectrosc.* **36**, 201 (2000).
- [73] C. MOLER and C. VAN LOAN, *SIAM Rev.* **45**, 3 (2003).
- [74] W. PRESS, B. FLANNERY, S. TEUKOLSKY and W. VETTERLING, *Numerical recipes in C*, Cambridge University Press, Cambridge, 1992.
- [75] M. H. LEVITT and M. EDÉN, *Molec. Phys.* **95**, 879 (1998).
- [76] M. EDÉN, Y. K. LEE and M. H. LEVITT, *J. Magn. Reson. A* **120**, 56 (1996).
- [77] T. CHARPENTIER and C. FERMON, *J. Magn. Reson.* **109**, 3116 (1998).
- [78] M. HOHWY, H. BILDSOE, H. J. JAKOBSEN and N. NIELSEN, *J. Magn. Reson.* **136**, 6 (1999).
- [79] S. DUSOLD, *Numerische Simulationen Experimenteller MAS-NMR-Spektren*, PhD thesis, Universität Bayreuth, 1999.
- [80] X. HELLUY, *Application de la Résonance Magnétique Nucléaire des Spins 1/2 aux Solides Cristallines: Mobilité Moléculaire et Études Structurales*, PhD thesis, École National Supérieure Agronomique de Rennes, 2001.
- [81] M. BAK and N. C. NIELSEN, *J. Magn. Reson.* **125**, 132 (1997).
- [82] M. EDÉN and M. H. LEVITT, *J. Magn. Reson.* **132**, 220 (1998).
- [83] S. K. ZAREMBA, *Ann. Mat. Pura Appl.* **4-73**, 293 (1966).
- [84] T. CHARPENTIER, C. FERMON and J. VIRLET, *J. Magn. Reson.* **132**, 181 (1998).
- [85] P. S. PACHECO, *Parallell Programming with MPI*, Morgan Kaufmann Publishers Inc., San Francisco, CA, 1997.
- [86] A. GEIST, A. GEGUELIN, J. DONGARRA, W. JIANG, R. MANCHEK and V. S. SUNDERAM, *PVM: Parallel Virtual Machine*, MIT Press, Cambridge, MA, 1994.

- [87] G. A. GEIST, J. A. KOHL and P. M. PAPADOPULOS, *Calculateurs Paralleles* **8** (1996).
- [88] F. JAMES, *MINUIT – Users Guide, Program Library D506*, CERN, Geneva, 1998.
- [89] E. CHONG and S. ZAK, *An Introduction to Optimisation*, Wiley, New York, 1996.
- [90] P. HODGINSON and L. EMSLEY, *J. Chem. Phys.* **107**, 4808 (1997).
- [91] A. C. OLIVIERI, *J. Magn. Reson. A* **123**, 207 (1979).

Appendix of Publications:

A. X- $\{^1\text{H}, ^{19}\text{F}\}$ Triple Resonance with a X- $\{^1\text{H}\}$ CP MAS Probe and Characterisation of a ^{29}Si - ^{19}F Spin Pair

M. Bechmann, K. Hain, C. Marichal, and A. Sebald, *Solid State Nuclear Magnetic Resonance*, **23**, 50–61 (2003).

doi:10.1016/S0926-2040(02)00014-0

©2002 Elsevier Science.

All rights are reserved by Elsevier Science. The article is reproduced with the rights granted to the author.

X- $\{^1\text{H}, ^{19}\text{F}\}$ triple resonance with a X- $\{^1\text{H}\}$ CP MAS probe and characterisation of a ^{29}Si – ^{19}F spin pair

Matthias Bechmann,^a Klaus Hain,^b Claire Marichal,^c and Angelika Sebald^{a,*}

^a Bayerisches Geoinstitut, Universität Bayreuth, 95440 Bayreuth, Germany

^b Wissenschaftliche Elektronikwerkstatt, Universität Bayreuth, 95440 Bayreuth, Germany

^c Laboratoire de Matériaux Minéraux, 3 rue Alfred Werner, F-68093 Mulhouse Cedex, France

Received March 28, 2002; revised June 10, 2002

Abstract

An economic approach for implementing X- $\{^1\text{H}, ^{19}\text{F}\}$ double-decoupling MAS NMR experiments with a conventional X- $\{^1\text{H}\}$ dual-channel CP MAS probe is demonstrated. The parameters characterising the isolated ^{29}Si – ^{19}F spin pair in an organosilicon compound R_3SiF (R = 9-anthryl) are determined. In addition, we discuss the optimum choice of experimental parameters for determining all ^{29}Si – ^{19}F spin-pair parameters from straightforward ^{29}Si MAS NMR spectra with only ^1H decoupling applied during acquisition.

© 2002 Elsevier Science (USA). All rights reserved.

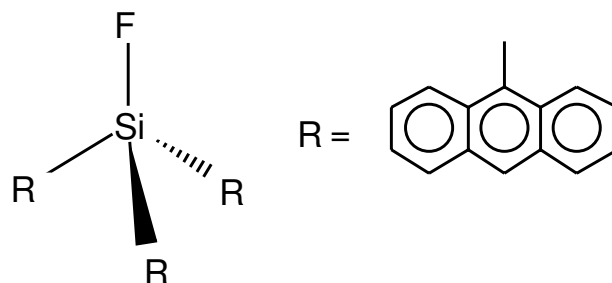
Keywords: $\{^1\text{H}, ^{19}\text{F}\}$ double-decoupling MAS NMR; ^{29}Si – ^{19}F spin pair

1. Introduction

The simultaneous presence of hydrogen and fluorine fairly commonly occurs in many materials, ranging from organic polymers and polymer blends, organometallic compounds, to inorganic materials and minerals. From the point of view of solid-

*Corresponding author. Fax: 49-921-55-3769.

E-mail address: angelika.sebald@uni-bayreuth.de (A. Sebald).



Scheme 1. Schematic illustration of the molecular structure of R_3SiF , **1**, with $R = 9$ -anthryl.

state NMR it is thus desirable to have available experimental options enabling simultaneous $\{^1H, ^{19}F\}$ decoupling while observing a third isotope X, coupled to 1H and ^{19}F . Of course, this task can be accomplished by a dedicated triple-channel X- $\{^1H, ^{19}F\}$ probe. Here we will present an economic alternative which permits X- $\{^1H, ^{19}F\}$ triple-resonance experiments on a conventional X- $\{^1H\}$ double-resonance MAS NMR probe. The experimental set-up will be demonstrated by ^{29}Si - $\{^1H, ^{19}F\}$ MAS NMR spectra of an organosilicon compound R_3SiF ($R = 9$ -anthryl, see Scheme 1), **1**. In addition, we will consider the isolated ^{29}Si - ^{19}F spin pair in **1** under conventional ^{29}Si MAS NMR conditions, with only 1H decoupling applied during acquisition. We will focus on the choice of the most suitable range of MAS frequencies when aiming to determine all ^{29}Si - ^{19}F spin-pair parameters from straightforward ^{29}Si MAS NMR spectra with only 1H decoupling applied during acquisition.

2. Experimental

2.1. Sample

The synthesis and single-crystal X-ray diffraction structure of R_3SiF ($R = 9$ -anthryl), **1**, are described in Ref. [1]. Our sample of **1** was donated by K. Tamao, Kyoto. The purity of the sample was checked by solution-state NMR and powder X-ray diffraction.

2.2. NMR experiments

^{29}Si MAS NMR experiments were carried out at room temperature on Bruker MSL 100, MSL 300, and DSX 600 NMR spectrometers. The corresponding ^{29}Si Larmor frequencies are $\omega_0/2\pi = 19.9, 59.6,$ and 119.2 MHz, respectively. Standard 4 mm double-bearing Bruker CP MAS probes were used for ^{29}Si MAS NMR

experiments on the MSL 300 and DSX 600 spectrometers, while ^{29}Si MAS NMR experiments on the MSL 100 spectrometer employed a modified (see Section 3) 7 mm double-bearing Bruker CP MAS probe. MAS frequencies $\omega_r/2\pi$ were generally in the range 0.8–12.0 kHz and were actively controlled to within ± 2 Hz. All ^{29}Si MAS spectra of **1** were obtained with $^1\text{H} \rightarrow ^{29}\text{Si}$ cross polarization (CP). Optimum $^1\text{H} \rightarrow ^{29}\text{Si}$ CP parameters for **1** are realised with a recycle delay of 30 s and a CP contact time of 12 ms. ^1H $\pi/2$ pulse durations were in the range 4.0–7.3 μs . $^1\text{H} \rightarrow ^{29}\text{Si}$ CP MAS experiments on **1** with $\{^1\text{H}, ^{19}\text{F}\}$ double decoupling during acquisition simultaneously employed c.w. decoupling amplitudes in both channels in the range 34–63 kHz.

2.3. Numerical simulations

Shielding notation is used, the signs of frequencies have been defined elsewhere [2]. For the interactions $\lambda = \text{CS}$ (chemical shielding), $\lambda = D$ (direct dipolar coupling), and $\lambda = J$ (indirect dipolar (J) coupling) the isotropic part ω_{iso}^λ , the anisotropy ω_{aniso}^λ , and the asymmetry parameter η^λ relate to the principal elements of the interaction tensor ω^λ as follows [3]: $\omega_{iso}^\lambda = (\omega_{xx}^\lambda + \omega_{yy}^\lambda + \omega_{zz}^\lambda)/3$, $\omega_{aniso}^\lambda = \omega_{zz}^\lambda - \omega_{iso}^\lambda$, and $\eta^\lambda = (\omega_{yy}^\lambda - \omega_{xx}^\lambda)/\omega_{aniso}^\lambda$ with $|\omega_{zz}^\lambda - \omega_{iso}^\lambda| \geq |\omega_{xx}^\lambda - \omega_{iso}^\lambda| \geq |\omega_{yy}^\lambda - \omega_{iso}^\lambda|$. For indirect dipolar coupling $\omega_{iso}^J = \pi J_{iso}$, and for direct dipolar coupling $\eta^D = \omega_{iso}^D = 0$ and $\omega_{aniso}^{D_{ij}} = b_{ij} = -\mu_0 \gamma_i \gamma_j \hbar / (4\pi r_{ij}^3)$, where γ_i , γ_j denote gyromagnetic ratios and r_{ij} is the internuclear distance between spins S_i , S_j . The Euler angles $\Omega_{IJ} = \{\alpha_{IJ}, \beta_{IJ}, \gamma_{IJ}\}$ [4] relate axis system I to axis system J , where I, J denote P (principal axis system, PAS) and C (crystal axis system, CAS). For simulations of MAS NMR spectra of the isolated two-spin system (S_i , S_j) with $S_i = ^{29}\text{Si}$, $S_j = ^{19}\text{F}$, the PAS of the corresponding dipolar coupling tensor $\omega^{D_{ij}}$ has been taken as the CAS, $\Omega_{PC}^{D_{ij}} = \{0, 0, 0\}$. The numerical simulations are based on the γ -COMPUTE approach [5] and use the REPULSION scheme [6] for powder averaging. Calculations of n -dimensional error maps employed routines of the MATLAB program package [7], minimisation routines from the MINUIT program package [8] served for purposes of iterative fitting.

3. Results and discussion

First, we will briefly describe an economic approach permitting $\{^1\text{H}, ^{19}\text{F}\}$ double-decoupling MAS NMR experiments with a conventional X- $\{^1\text{H}\}$ dual-channel MAS NMR probe. Since technical details of the experimental set-up are strongly dependent on the probe and spectrometer hardware used, only a general outline will be given. The second part will be devoted to the characterisation of the ^{29}Si - ^{19}F spin pair in **1**, the choice of the experimental parameters for this purpose and its impact on the accuracy of the extracted data.

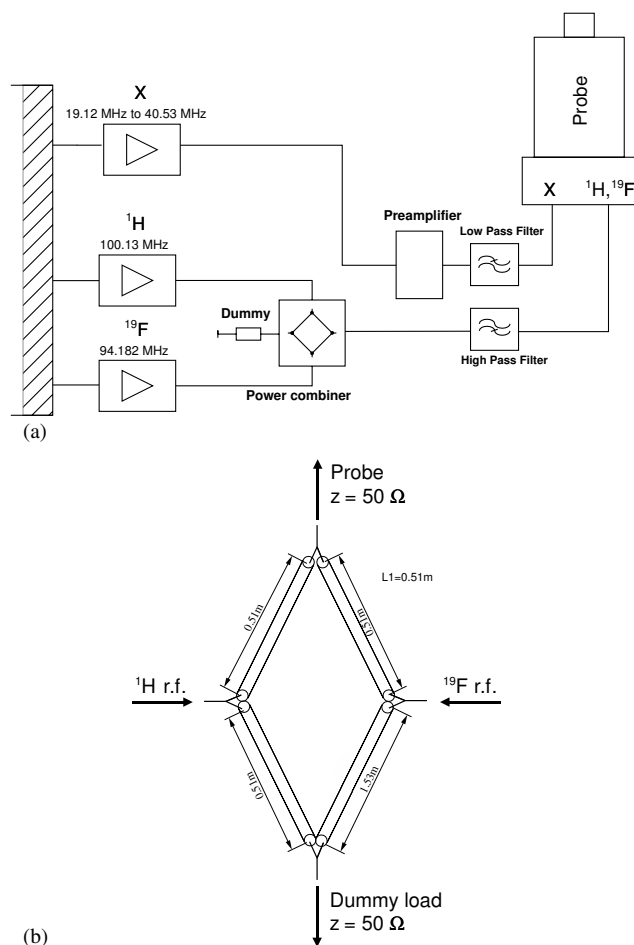


Fig. 1. Experimental set-up for X- $\{^1\text{H}, ^{19}\text{F}\}$ double-decoupling MAS NMR experiments: (a) overview, (b) the power combiner with dimensions appropriate for the Larmor frequencies $\omega_0/2\pi = 100.1$ MHz (^1H) and $\omega_0/2\pi = 94.2$ MHz (^{19}F).

Fig. 1(a) illustrates the general spectrometer set-up for X- $\{^1\text{H}, ^{19}\text{F}\}$ double-decoupling MAS NMR experiments with three high-power rf transmitters. The output from the two transmitters tuned at the ^1H and ^{19}F Larmor frequencies is fed via a power combiner (see Fig. 1(b)) into the probe channel which previously was tuned solely at the ^1H Larmor frequency, but is now tuned to accommodate both frequencies. Suitable high-pass filters for the two high-frequency channels, as well as a low-pass filter in the X-channel are required. These filters need to be able to handle powers of at least 500 W, a minimum damping requirement for the high-pass filters being > 40 dB, while at least 60 dB are necessary for the X-channel low-pass filter.

The X-observe channel of the probe remains tuneable to different X Larmor frequencies, but dedicated low-pass filters for each individual X Larmor frequency may be necessary. With regard to the tuning of the probe itself, an additional ^{19}F -frequency reject filter in the probe-tuning circuit, apart from the usual ^1H -frequency reject filter, is required. The capacitors for these reject filters have to be rated for high-voltage handling. How this is best implemented in a given case depends on the construction of the probe at hand. A practical solution should include an option for tuning the probe channel at the ^{19}F frequency, in addition to a common matching at the ($^1\text{H} + ^{19}\text{F}$) frequencies.

In our experimental set-up the ^1H and ^{19}F Larmor frequencies are taken from two tube amplifiers, the output of which is fed into the power combiner. This device follows a simple approach of combining cables of suitable $\lambda/4$ lengths (0.51 m at 94.2 MHz, see Fig. 1(b)) with in- and output resistances of $50\ \Omega$. This results in a forward-power damping of ca. 3.4 dB and an attenuation between the two transmitters of ca. 35 dB. The dummy load is the single most expensive part of this set-up, it has to be rated at $50\ \Omega$ and needs to be able to handle c.w. power exceeding 100 W. However, such a dummy load is an item which is available in most solid-state NMR laboratories anyway. In principle, this type of power combiner can be used in the same spirits at higher Larmor frequencies as long as the two combined frequencies do not differ from each other by more than 10 percent. When used at higher frequencies, cable material other than the type RG59/U cable used here will be needed [9].

Fig. 2 shows a practical example, ^{29}Si MAS NMR spectra of **1** obtained at $\omega_0/2\pi = 19.9$ MHz and $\omega_r/2\pi = 2450$ Hz. The bottom trace represents a ^{29}Si MAS NMR spectrum of **1** with only ^1H decoupling applied during the acquisition. The splitting originates from $|^1J_{\text{iso}}(^{29}\text{Si}, ^{19}\text{F})| = 274$ Hz, while the origin of the spinning sidebands is predominantly due to the presence of heteronuclear ^{29}Si – ^{19}F dipolar coupling: the internuclear ^{29}Si – ^{19}F distance of 161.5 pm in **1** [1] corresponds to a dipolar coupling constant $b_{ij} = 5167$ Hz which, at a MAS frequency $\omega_r/2\pi = 2450$ Hz, is not completely averaged out. The middle trace shows a ^{29}Si MAS NMR spectrum of **1** obtained under identical conditions, except that now on-resonance $\{^1\text{H}, ^{19}\text{F}\}$ double decoupling was applied during acquisition. Accordingly, spinning sidebands and splitting from ^{29}Si – ^{19}F dipolar and J coupling vanish, only a single sharp ^{29}Si resonance remains. The top trace illustrates the effects of off-resonance ^{19}F decoupling in the $\{^1\text{H}, ^{19}\text{F}\}$ double-decoupling mode. Here the ^{19}F transmitter frequency was set 6 kHz away from the ^{19}F resonance of **1**. This point refers to a slightly inconvenient aspect of our experimental set-up as we cannot directly observe ^{19}F under ^1H decoupling conditions. This, however, would be necessary in order to determine directly the correct ^{19}F transmitter frequency for proper on-resonance decoupling conditions with simultaneous irradiation at the ^1H Larmor frequency. Since the ^1H and ^{19}F Larmor frequencies are very similar, considerable Bloch–Siegert shifts will occur [10] in the $\{^1\text{H}, ^{19}\text{F}\}$ double-decoupling mode. With our set-up, the correct settings of the ^1H and ^{19}F transmitter frequencies have to be

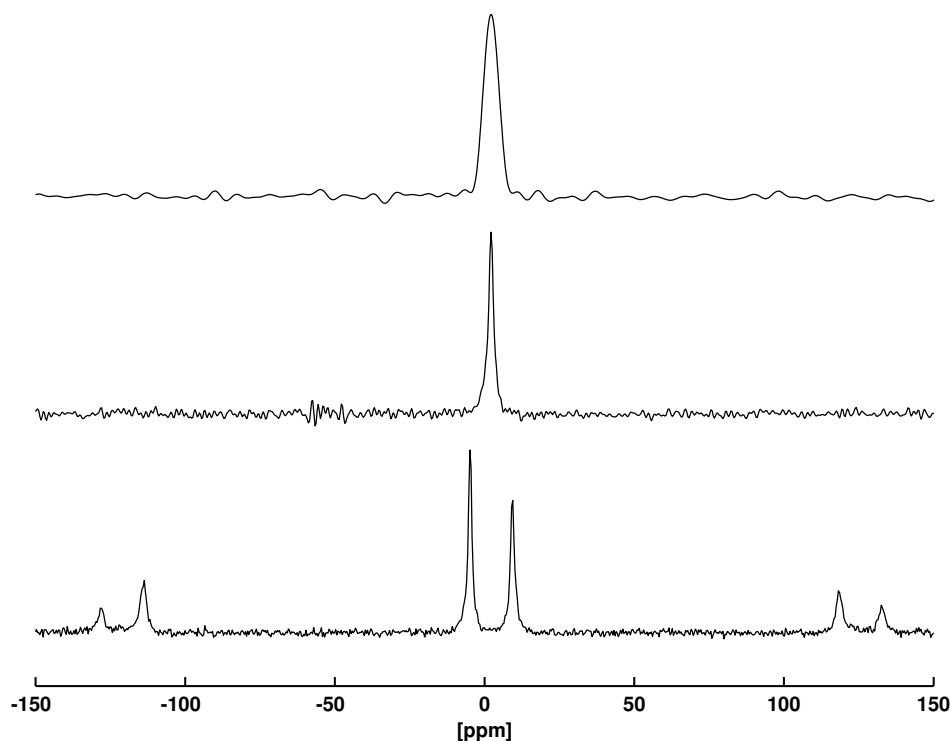


Fig. 2. Experimental ^{29}Si MAS NMR spectra of **1** ($\omega_0/2\pi = 19.9$ MHz, $\omega_r/2\pi = 2449$ Hz). Bottom trace: only ^1H decoupling applied during acquisition; the splitting is due to $^1J_{\text{iso}}(^{29}\text{Si}, ^{19}\text{F})$ and the spinning sideband amplitudes under these conditions mainly reflect the magnitude of the ^{29}Si – ^{19}F heteronuclear dipolar coupling constant. Middle trace: simultaneous $\{^1\text{H}, ^{19}\text{F}\}$ on-resonance decoupling applied during acquisition; the observation of a single ^{29}Si resonance is consistent with the findings of single-crystal X-ray diffraction on **1** (1). Top trace: simultaneous $\{^1\text{H}, ^{19}\text{F}\}$ decoupling applied during acquisition with the ^{19}F transmitter frequency set off resonance by 6.0 kHz.

optimised indirectly via the observation of the X-spin spectrum recorded with different ^1H and ^{19}F transmitter settings.

Another, more general comment seems in place. There can be distinct advantages in implementing double-decoupling MAS NMR experiments at low magnetic field strengths (though not necessarily quite as low as $B_0 = 2.3$ T as we used here): at lower magnetic field strengths ^{19}F chemical shielding dispersion and chemical shielding anisotropies are less likely to influence negatively the decoupling efficiency.

Double-decoupling MAS NMR experiments can be very useful for obtaining good spectral resolution, for identifying the number of resonances/crystallographic sites of the X nucleus, and for determining the chemical shielding tensor components of the X-spin resonance(s), undisturbed by further interactions such as residual

heteronuclear dipolar and/or J coupling. For example, the ^{29}Si chemical shielding tensor of **1** is found to be axially symmetric with a small ^{29}Si chemical shielding anisotropy (csa), $\omega_{\text{aniso}}^{\text{CS}} = 23 \pm 2$ ppm. Given the nearly axially symmetric C_3SiF moiety in solid **1** [1], the direction of the unique (here: most shielded) ^{29}Si chemical shielding tensor component is likely to be oriented along the Si–F bond direction.

While ^{29}Si $\{^1\text{H}, ^{19}\text{F}\}$ double-decoupling MAS experiments are helpful in characterising the ^{29}Si chemical shielding tensor components, information regarding the orientation of the chemical shielding tensor is generally destroyed in this experiment. For a heteronuclear spin pair ^{29}Si – ^{19}F such as in **1**, characterised by a fairly small ^{29}Si csa and a substantial magnitude of the ^{29}Si – ^{19}F dipolar coupling constant ($b_{ij} = 5167$ Hz), the spinning-sideband amplitudes in straightforward ^{29}Si MAS NMR spectra at slow-spinning conditions with only ^1H decoupling applied during acquisition, reflect both magnitude and relative orientation of the ^{29}Si chemical shielding tensor and the ^{29}Si – ^{19}F dipolar coupling tensor. By means of numerically exact simulations, complete calculations of error maps and iterative fitting, these parameters of the ^{29}Si – ^{19}F spin pair can be extracted from straightforward experimental ^{29}Si MAS NMR spectra. An example, comparing experimental and best-fit simulated ^{29}Si MAS spectra of **1** is shown in Fig. 3. For **1**, it

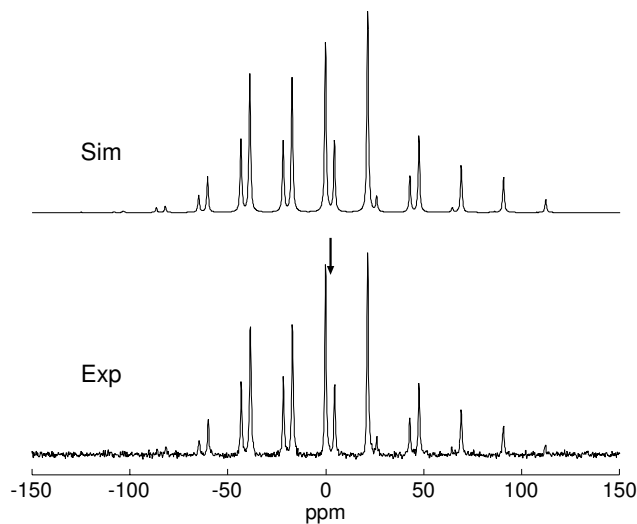


Fig. 3. ^{29}Si MAS NMR spectra of **1** ($\omega_0/2\pi = 59.6$ MHz, $\omega_r/2\pi = 1286$ Hz, only ^1H decoupling applied during acquisition). Top: simulated spectrum, based on best-fit values (the isotropic ^{29}Si chemical shielding value of solid **1** is 2.4 ppm relative to the ^{29}Si resonance of SiMe_4 at 0 ppm; the direction of the unique (most shielded) component of the axially symmetric ^{29}Si chemical shielding tensor with $\omega_{\text{aniso}}^{\text{CS}} = 23 \pm 2$ ppm is collinear with the direction of the unique component of the ^{29}Si – ^{19}F dipolar coupling tensor, $\beta_{\text{PC}}^{\text{CS}} = 0$; $^1J_{\text{iso}}(^{29}\text{Si}, ^{19}\text{F}) = +274$ Hz). Bottom: experimental spectrum; the arrow indicates the center band.

comes as no surprise that indeed the most shielded, unique component of the axially symmetric ^{29}Si chemical shielding tensor is found to be oriented along the Si–F bond direction. For a simple heteronuclear ^{29}Si – ^{19}F spin pair the relative contributions of csa and dipolar coupling interactions to the spinning-sideband amplitudes are

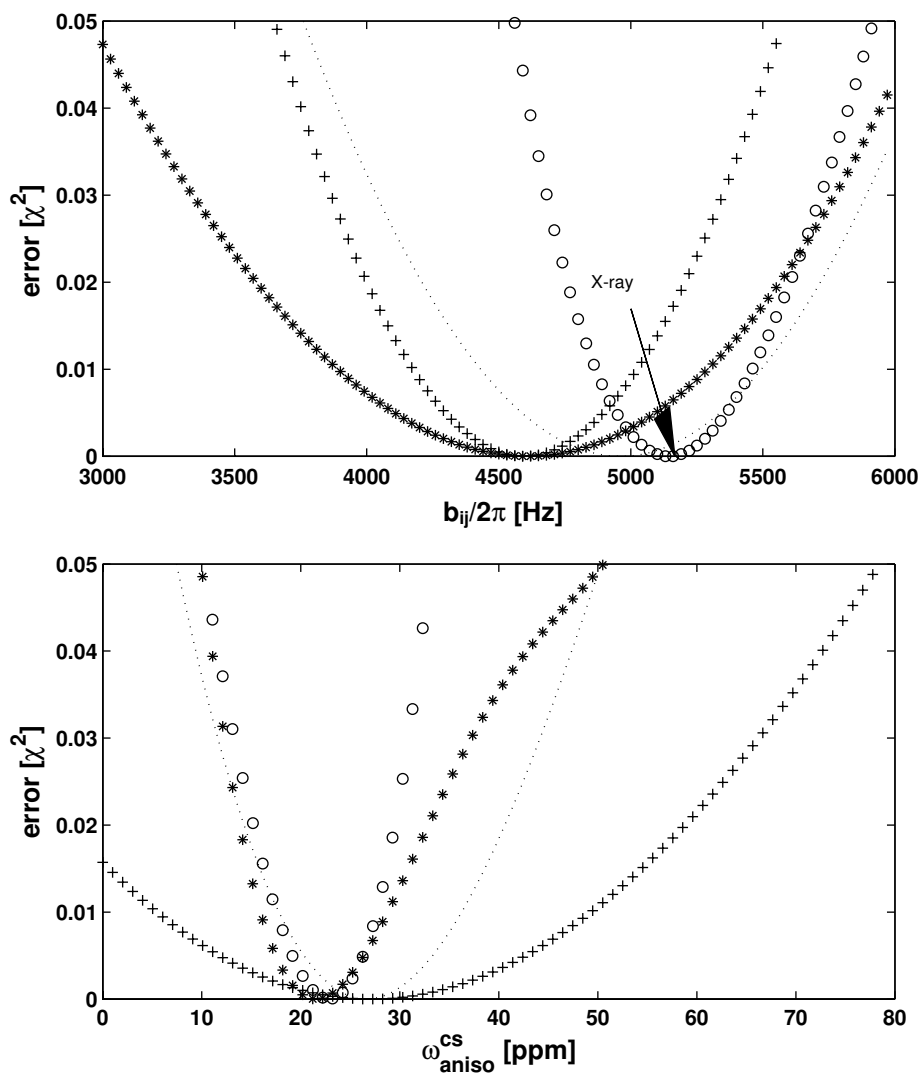


Fig. 4. The impact of the choice of experimental conditions on the sensitivity of fit parameters b_{ij} (top) and ω_{aniso}^{CS} (bottom) in ^{29}Si MAS spectra of the ^{29}Si – ^{19}F spin pair in **1**. The different symbols correspond to the following experimental conditions: + ($\omega_0/2\pi = 19.9$ MHz, $\omega_r/2\pi = 2449$ Hz); o ($\omega_0/2\pi = 59.6$ MHz, $\omega_r/2\pi = 1286$ Hz); * ($\omega_0/2\pi = 119.2$ MHz, $\omega_r/2\pi = 2496$ Hz); ... ($\omega_0/2\pi = 59.6$ MHz, $\omega_r/2\pi = 2640$ Hz). The arrow marks the value of b_{ij} calculated from the internuclear ^{29}Si – ^{19}F distance in **1** determined by single-crystal X-ray diffraction [1].

weighted differently by different MAS and Larmor frequencies. Accordingly, in order to avoid ambiguities in the data-analysis procedure, it is practically important to use a range of experimental spectra, obtained at different MAS and Larmor frequencies, as the basis for numerical analysis. We have employed ^{29}Si Larmor frequencies ranging from 19.9 to 119.2 MHz and MAS frequencies in the range $\omega_r/2\pi = 875\text{--}3700$ Hz. The best-fit simulated spectrum shown in Fig. 3 is based on the analysis of multiple experimental spectra. At all experimental conditions, the Euler angle β_{PC}^{CS} , describing the direction of the most shielded ^{29}Si chemical shielding tensor component relative to the direction of the unique component of the $^{29}\text{Si}\text{--}^{19}\text{F}$ dipolar coupling tensor, is easily identified as indicating collinearity of the two directions. For the remaining two (supposedly) unknown parameters of the $^{29}\text{Si}\text{--}^{19}\text{F}$ spin pair in **1**, ω_{aniso}^{CS} and b_{ij} , complete calculations of the error contours for the dipolar coupling constant b_{ij} and the chemical shielding anisotropy ω_{aniso}^{CS} , based on input from different experimental spectra unambiguously yield the respective minimum regions for the two parameters. The minimum regions of subsequent one-dimensional error scans for these two parameters are depicted in Fig. 4. The plots reveal that, within 95 percent χ^2 -confidence limits, all experimental spectra yield agreement regarding the values of b_{ij} and ω_{aniso}^{CS} . However, the values derived from some experimental spectra are more precisely defined than others. For instance, both b_{ij} and ω_{aniso}^{CS} are derived with the least uncertainty from an experimental ^{29}Si MAS NMR spectrum obtained at $\omega_0/2\pi = 59.6$ MHz and $\omega_r/2\pi = 1286$ Hz (see Fig. 4). Obviously, the choice of the experimental parameters ω_0 and ω_r is an important ingredient in the overall strategy, and it would be highly desirable to be able to predict the most suitable conditions rather than following the trial-and-error approach represented by the data in Fig. 4. Before returning to this point in more detail, we briefly consider the value of the dipolar coupling constant b_{ij} as derived from the various experimental ^{29}Si MAS NMR spectra of **1**. In all cases, within experimental error, the value is in agreement with the value predicted from the internuclear Si–F distance in **1** as determined by single-crystal X-ray diffraction, though with a systematic trend to underestimate b_{ij} or, in other words, to derive from NMR an internuclear Si–F distance which is slightly larger than the one determined by X-ray diffraction techniques. There are two possible explanations for this trend. One possible reason could be molecular vibrations, the stretching mode of the Si–F bond vibrations, similar to the causes of earlier observations of systematic such deviations between diffraction- and NMR-determined internuclear $^{13}\text{C}\text{--}^1\text{H}$ distances [11]. Another possibility would be anisotropy of the heteronuclear J coupling $^1J(^{29}\text{Si}, ^{19}\text{F})$ in **1**. The isotropic J coupling in **1** amounts to $|^1J_{iso}(^{29}\text{Si}, ^{19}\text{F})| = 274$ Hz. One may then expect ω_{aniso}^J to be of a similar order of magnitude of a few hundred Hz, which in effect may lead to an effective dipolar coupling constant b_{eff} that could be either slightly larger or slightly smaller than the ‘true’ dipolar coupling constant b_{ij} , depending on the relative orientation of the dipolar and J -coupling tensors [12]. Regardless of the correct explanation, in a realistic application circumstance we would still have correctly identified the $^{29}\text{Si}\text{--}^{19}\text{F}$ spin pair in **1** as representing a directly bonded Si–F unit.

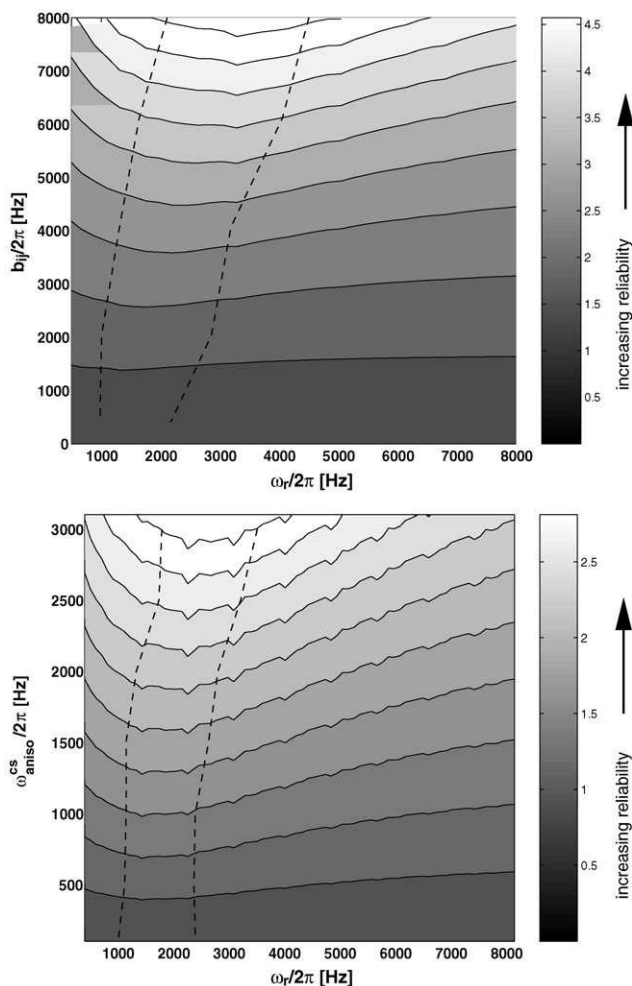


Fig. 5. Contour plots of the expected reliabilities [13] of the parameters b_{ij} (top) and ω_{aniso}^{CS} (bottom) based on the parameters of the ^{29}Si – ^{19}F spin pair in **1**. The areas indicated by the dotted lines denote the region within 5 percent of the optimum experimental conditions.

Fig. 4 clearly demonstrates the impact of the choice of experimental parameters, $\omega_0/2\pi$ and $\omega_r/2\pi$, on the sensitivity of the fit parameters and the accuracy of the final results. Intuitively, one may be tempted to speculate that matters would improve steadily with increasing ω_0 and decreasing ω_r . However, the situation is more complicated. In a careful numerical study by Hodgkinson and Emsley [13] this has been investigated previously for isolated spin-1/2 nuclei with csa. For example, it was found that the determination of ω_{aniso}^{CS} from MAS spectra is always more reliable than from static powder spectra, with optimum conditions realised at a fairly

constant ratio $\omega_r/\omega_{aniso}^{CS}$ such that ca. 6–10 spinning sidebands occur. Applying their reliability-calculation approach [13] to the parameters of the ^{29}Si – ^{19}F spin pair in **1**, we find that again the optimum experimental parameters are in a fairly constant region, but here it is the ratio ω_r/b_{ij} which governs the most suitable experimental conditions: the reliability in characterising the spin pair parameters is best in a MAS regime where ω_r amounts to 15 ± 5 percent of b_{ij} , and where this MAS frequency amounts to ca. 80 percent of ω_{aniso}^{CS} . Note that these optimum conditions will only be valid for dipolar coupled heteronuclear spin pairs with properties similar to the ^{29}Si – ^{19}F spin pair in **1**, that is for an axially symmetric chemical shielding tensor with the direction of its unique component oriented along the direction of the unique component of the dipolar coupling tensor. Different asymmetry parameters and orientations of the chemical shielding tensor will call for different optimum regimes regarding the choice of ω_r . The ^{29}Si MAS spectrum of **1** depicted in Fig. 3 was obtained at $\omega_0/2\pi = 59.6$ MHz and $\omega_r/2\pi = 1286$ Hz. With $\omega_{aniso}^{CS} = 23\pm 2$ ppm of the ^{29}Si chemical shielding tensor, these experimental conditions are in the optimum regime for this particular type of spin pair parameters Fig. 5.

Acknowledgments

Support of this work by the Deutsche Forschungsgemeinschaft is gratefully acknowledged. Some experiments and calculations were carried out at Bayerisches Geoinstitut under the EU “IHP—Access to Research Infrastructures” Programme (Contract No. HPRI-1999-CT-00004 to D. C. Rubie). We thank K. Tamao, Kyoto, for his generous loan of sample **1**, and H. Förster and W. Knöllner, Bruker Analytik GmbH, Rheinstetten, for running ^{29}Si MAS NMR spectra of **1** on the DSX 600 spectrometer and for technical discussions.

References

- [1] S. Yamaguchi, S. Akijama, K. Tamao, Synthesis, Structures, photophysical properties and dynamic stereochemistry of tri-9-anthrylsilane derivatives, *Organometallics* 17 (1998) 4347–4352.
- [2] M.H. Levitt, The signs of frequencies and phases in NMR, *J. Magn. Reson.* 126 (1997) 164–182.
- [3] U. Haerberlen, High resolution NMR in solids. Selective averaging, in: J.S. Waugh (Ed.), *Advances in Magnetic Resonance; Supplement 1*, Academic Press, New York, 1976.
- [4] A.R. Edmonds, *Angular Momentum in Quantum Mechanics*, Princeton University Press, Princeton, 1974.
- [5] M. Hohwy, H. Bildsoe, H.J. Jakobsen, N.C. Nielsen, Efficient spectral simulations in NMR of rotating solids. The γ -COMPUTE algorithm, *J. Magn. Reson.* 136 (1999) 6–14.
- [6] M. Bak, N.C. Nielsen, REPULSION, a novel approach to efficient powder averaging in solid-state NMR, *J. Magn. Reson.* 125 (1997) 132–139.
- [7] MATLAB, Version 6.0; The Mathworks Inc., Natick MA, 2001.
- [8] F. James, M. Roos, MINUIT computer code, Program D-506, CERN, Geneva, 1977.
- [9] The ARRL Radio Amateur Handbook, The American Radio Relay League, Newington CT, 1995.

- [10] F. Bloch, A. Siegert, Magnetic resonance for nonrotating fields, *Phys. Rev.* 57 (1940) 522–527.
- [11] Y. Ishii, T. Terao, S.J. Hayashi, Theory and simulation of vibrational effects on structural measurements by solid-state nuclear magnetic resonance, *J. Chem. Phys.* 107 (1997) 2760–2774.
- [12] S. Dusold, A. Sebald, Magnitudes and orientations of NMR interaction tensors in isolated three-spin systems ABX, *Molec. Phys.* 95 (1998) 1237–1245.
- [13] P. Hodgkinson, L. Emsley, The reliability of the determination of tensor parameters by solid-state nuclear magnetic resonance, *J. Chem. Phys.* 107 (1997) 4808–4816.

B. ^{13}C Chemical Shielding Tensor Orientations in the Phosphoenolpyruvate Moiety from ^{13}C Rotational-Resonance MAS NMR Lineshapes

M. Bechmann, S. Dusold, W.A. Shuttleworth, D.L. Jakeman, D.J. Mitchell, and J.N.S. Evans, *Solid State Sciences*, **6**, 1097–1105 (2004).

doi:10.1016/j.solidstatesciences.2004.04.021

©2004 Elsevier Science SAS.

All rights are reserved by Elsevier Science. The article is reproduced with the rights granted to the author.

^{13}C chemical shielding tensor orientations in a phosphoenolpyruvate moiety from ^{13}C rotational-resonance MAS NMR lineshapes

M. Bechmann^a, S. Dusold^a, A. Sebald^{a,*}, W.A. Shuttleworth^b, D.L. Jakeman^{b,2},
D.J. Mitchell^{b,c}, J.N.S. Evans^{b,c,✱}

^a Bayerisches Geoinstitut, Universität Bayreuth, 95440 Bayreuth, Germany

^b School of Molecular Biosciences, Washington State University, Pullman, WA 99164-4660, USA

^c Center for NMR Spectroscopy, Washington State University, Pullman, WA 99164-4660, USA

Received 30 March 2004; accepted 4 April 2004

Available online 11 September 2004

Abstract

The absolute orientations of the three ^{13}C chemical shielding tensors in the phosphoenolpyruvate (PEP) moiety in a PEP-model compound with known crystal structure are reported. The study uses a fully ^{13}C -enriched polycrystalline sample of triammonium phosphoenolpyruvate monohydrate, $(\text{NH}_4)_3(\text{PEP})\cdot\text{H}_2\text{O}$, and ^{13}C MAS NMR experiments fulfilling various different ^{13}C rotational-resonance conditions. The absolute ^{13}C chemical shielding tensor orientations are derived by iterative fitting, employing numerically exact simulations, of various rotational-resonance ^{13}C MAS NMR lineshapes of the three- ^{13}C -spin system in fully ^{13}C -enriched $(\text{NH}_4)_3(\text{PEP})\cdot\text{H}_2\text{O}$. The implications of the results of this study for future, biochemically oriented solid-state NMR studies on the PEP moiety are outlined.
© 2004 Elsevier SAS. All rights reserved.

Keywords: Phosphoenolpyruvate; ^{13}C solid-state NMR; Rotational resonance; Numerically exact lineshape simulations; Chemical shielding tensor orientations

1. Introduction

Phosphoenolpyruvate (PEP) is a simple three-carbon molecule that occupies a central role in primary metabolism. The transfer of its phosphate group provides free energy for a wide range of metabolic events [1]. It is also important in a class of enzymes called enolpyruvyltransferases, in which PEP participates by providing C3 (see Fig. 1) of its enolpyruvyl moiety rather than its phosphate group. There are at least four known enolpyruvyltransferases: 5-enolpyruvylshikimate-3-phosphate (EPSP) syn-

thase, uridine diphosphate N-acetyl-glucosamine enolpyruvyltransferase (MurA), 3-deoxy-D-manno-2-octulosonate-phosphate (KDO8P) synthase, and 3-deoxy-D-arabinoheptulosonate-7-phosphate (DAHP) synthase. In the reactions catalyzed by these enolpyruvyltransferases, C3 of PEP can react in two significantly different ways: either with a proton (as in EPSP synthase and MurA), or with a carbonyl group (as in KDO8P synthase and DAHP synthase). Ac-

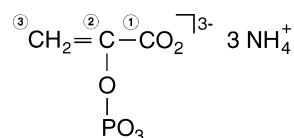


Fig. 1. Schematic representation of the phosphoenolpyruvate moiety in $(\text{NH}_4)_3(\text{PEP})\cdot\text{H}_2\text{O}$, **1**, the numbering of the carbon atoms (and, where applicable, of oxygen atoms) is identical to the numbering scheme used in the description of the X-ray diffraction structure of **1** [30] and will be used throughout.

* Corresponding author.

E-mail address: angelika.sebald@uni-bayreuth.de (A. Sebald).

¹ Current address: Department of Chemistry, University of Exeter, Stocker Road, Exeter EX4 4QD, UK.

² Current address: College of Pharmacy, Dalhousie University, Halifax, Nova Scotia, B3H 3J5, Canada.

✱ Deceased.

According to Pearson's hard–soft acid–base (HSAB) theory [2], these are very different moieties (the proton being a hard acid, and the carbonyl group being a soft acid). We have, therefore, investigated the chemical reactivity of PEP by quantum chemistry methods, through making use of density functional theory in a manner very similar to that of Parr and co-workers [3], but with some modifications [4]. While various versions of this approach have been reported in the literature for small molecules [5], no attempt has been made to use it for predicting reactivity in an enzyme active site. These investigations corroborate the HSAB principle by energy perturbation methods, showing that 'hard likes hard' and 'soft likes soft'. For a 'hard reaction', it is shown, in contrast to the findings predicted by frontier molecular orbital theory, that the site of minimal Fukui function is preferred. The Fukui function is related to the electron density in the frontier molecular orbitals. For a 'soft' reaction, the site of maximal Fukui function is preferred. We have extended [6] this approach to examine three of the enolpyruvyltransferases mentioned above, and it was found that the reactivity of PEP in all these enzymatic reaction mechanisms can be understood in terms of its ionization state and conformation. In particular, varying the torsion angle between the COO plane and the C1–C2–C3 plane would appear to control the reactivity of C3 and C2 towards nucleophiles. Thus the motives by which enzymes control the reactivity of their substrate may be explained in terms of the HSAB principle. This has led to our hypothesis, in which we propose that each enolpyruvyltransferase enzyme controls PEP reactivity through control of the PEP conformation in the enzyme-bound state.

If solid-state NMR techniques are to be used to test this hypothesis, this task cannot be solved by NMR experiments aiming at the determination of, e.g., internuclear ^{13}C – ^{13}C distances. In order to examine the relative orientation of the carboxylate group in the PEP moiety in a variety of biochemically relevant circumstances, instead it is necessary to derive this molecular conformational parameter from consideration of ^{13}C chemical shielding tensor orientations. For instance, it is often assumed that the typical orientation of a carboxylate- ^{13}C chemical shielding tensor is such that the direction of the most shielded tensor component is perpendicular to the molecular carboxylate plane. Several compounds for which the orientations of carboxylate- ^{13}C chemical shielding tensors have been determined experimentally conform to this rule of thumb to within less than 10° deviation from this molecular direction [7–12], but there are also cases where this deviation is considerably larger. This is the case, for instance, in oxalic acid dihydrate [13] and in sodium pyruvate [14]. Accordingly, making assumptions as to the orientation are inadvisable as the starting point for the determination of unknown conformational PEP parameters. To lend validity and reliability to solid-state NMR approaches based on ^{13}C chemical shielding tensor orientations, the ^{13}C chemical shielding tensor orientations in a suitable PEP-model compound with known structure have

to be determined first. We have chosen the triammonium salt monohydrate of PEP, $(\text{NH}_4)_3(\text{PEP})\cdot\text{H}_2\text{O}$, **1** (Fig. 1) for this purpose. ^{13}C NMR experiments on an oriented single crystal of **1** with ^{13}C in natural abundance would seem an obvious choice of solid-state NMR experiment to determine the absolute orientations of the three ^{13}C chemical shielding tensors in **1**. However, the presence of the 100 percent naturally abundant ^{31}P spin-1/2 isotope may necessitate a rather specialized single-crystal probe with the capability to simultaneously decouple ^1H and ^{31}P [15]. We describe a different route to determine the absolute orientations of these three ^{13}C chemical shielding tensors. We use a polycrystalline, fully ^{13}C -enriched sample of $(\text{NH}_4)_3(\text{PEP})\cdot\text{H}_2\text{O}$, **1-U ^{13}C** , and derive the absolute ^{13}C chemical shielding tensor orientations from numerically exact lineshape simulations of various rotational-resonance [16–22] (R^2) ^{13}C MAS NMR experiments on the three- ^{13}C -spin system in **1-U ^{13}C** .

2. Experimental

2.1. Enzymatic synthesis of $(\text{NH}_4)_3(\text{PEP})\cdot\text{H}_2\text{O}$, **1-U ^{13}C**

1-U ^{13}C was synthesized by literature methods [23]. Adenosine triphosphate (ATP, 250 mg), [1,2,3- $^{13}\text{C}_3$] sodium pyruvate (50 mg), and MgCl_2 (0.5 mL of 1 M) were dissolved in TrisHCl (5 mL, 50 mM, pH 8.4). PEP synthetase (1 mL, 18 mg mL $^{-1}$) was added and the pH kept above 8.0 by addition of NaOH (1 M). After 36 h at room temperature, the reaction mixture was passed through a 10 kDa molecular weight cutoff membrane and lyophilized. The sample was taken up in 5 mL ammonium bicarbonate (10 mM, pH 9.0) and loaded onto a FPLC (Pharmacia) MonoQ 16/10 column. Elution with a linear gradient of ammonium bicarbonate (10 mM–1 M, pH 9.0) gave [1,2,3- $^{13}\text{C}_3$]PEP (27 mg, at 0.2 M), which was obtained as the triammonium monohydrate salt, $(\text{NH}_4)_3(\text{PEP})\cdot\text{H}_2\text{O}$, **1-U ^{13}C** , after adjustment to pH 9.0 with ammonium hydroxide and lyophilization. The purity of **1-U ^{13}C** was confirmed by ^1H , ^{13}C , ^{31}P solution-state NMR on a Varian Mercury-300 NMR spectrometer.

2.2. ^{13}C MAS NMR

^{13}C MAS NMR spectra were recorded on Bruker MSL 200, MSL 300, DSX 400 and DSX 500 NMR spectrometers, except where stated otherwise. The corresponding ^{13}C Larmor frequencies $\omega_0/2\pi$ are -50.3 , -75.5 , -100.6 and -125.8 MHz. Standard 4 mm double-bearing probes were used, the sample was contained in a 4 mm o.d. ZrO_2 rotor with a Kel-F insert that restricts the sample to a spherical volume in the center part of the rotor and accommodates approximately 25 mg of sample. MAS frequencies were generally in the range $\omega_r/2\pi = 1$ –14 kHz and were actively controlled to within ± 2 Hz. Lineshapes of experimental ^{13}C MAS NMR spectra were checked to be identical

when using either Hartmann–Hahn cross polarization (CP) or ^{13}C single-pulse excitation. Optimum ^1H decoupling performance is important to obtain reliable ^{13}C R^2 MAS NMR lineshapes [24,25]. Experimental ^{13}C R^2 MAS NMR spectra of $\mathbf{1}\text{-U}^{13}\text{C}$, subsequently used for purposes of iterative lineshape fitting, were recorded on the DSX 400 and DSX 500 NMR spectrometers with TPPM [26] ^1H decoupling (amplitudes of 83–105 kHz) applied during signal acquisition.

2.3. Definitions, notation and numerical methods

Shielding notation [27] is used throughout and ^{13}C chemical shielding is quoted with respect to $\omega_{\text{iso}}^{\text{CS}} = 0$ ppm for the ^{13}C resonance of SiMe_4 . For the interactions $\lambda = \text{CS}$ (chemical shielding), $\lambda = D$ (direct dipolar coupling), and $\lambda = J$ (indirect dipolar (J) coupling) the isotropic part $\omega_{\text{iso}}^\lambda$, the anisotropy δ^λ , and the asymmetry parameter η^λ relate to the principal elements of the interaction tensor ω^λ as follows [28]: $\omega_{\text{iso}}^\lambda = (\omega_{xx} + \omega_{yy} + \omega_{zz})/3$, $\delta^\lambda = \omega_{zz}^\lambda - \omega_{\text{iso}}^\lambda$ and $\eta = (\omega_{yy} - \omega_{xx})/\delta$ with $|\omega_{zz} - \omega_{\text{iso}}| \geq |\omega_{xx} - \omega_{\text{iso}}| \geq |\omega_{yy} - \omega_{\text{iso}}|$. For indirect dipolar coupling $\omega_{\text{iso}}^J = \pi J_{\text{iso}}$, and for direct dipolar coupling $\eta^D = \omega_{\text{iso}}^D = 0$ and $\delta^{Dij} = b_{ij} = -\mu_0 \gamma_i \gamma_j \hbar / (4\pi r_{ij}^3)$, where γ_i , γ_j denote gyromagnetic ratios and r_{ij} is the internuclear distance between spins S_i , S_j . The Euler angles $\Omega_{IJ} = \{\alpha_{IJ}, \beta_{IJ}, \gamma_{IJ}\}$ [29] relate axis system I to axis system J , where I , J denote P (principal axis system, PAS), C (crystal axis system, CAS), R (rotor axis system, RAS), or L (laboratory axis system). For lineshape simulations of R^2 MAS NMR spectra of three-spin systems (S_i , S_j , S_k) fulfilling a $S_i - S_j$ R^2 condition, it is convenient to define the PAS of the corresponding dipolar coupling tensor ω^{Dij} as the CAS C_{ij} , $\Omega_{\text{PC}}^{Dij} = \{0, 0, 0\}$. The known crystal structure of $(\text{NH}_4)_3(\text{PEP})\cdot\text{H}_2\text{O}$, $\mathbf{1}$, [30] provides the recipe for interconversion between the CAS C_{ij} , C_{ik} , C_{jk} of the three- ^{13}C -spin system in the $\mathbf{1}\text{-U}^{13}\text{C}$ PEP moiety.

Our procedures for numerically exact spectral lineshape simulations and iterative fitting are fully described and discussed in detail elsewhere, in particular addressing the $n = 0$ R^2 condition for isolated homonuclear spin pairs [31], various $n = 0, 1, 2$ R^2 conditions in isolated homonuclear ^{13}C two-, three- and four-spin systems [14,24], as well as heteronuclear $^{31}\text{P}\text{-}^{13}\text{C}$ [32] and $^{31}\text{P}\text{-}^{113}\text{Cd}$ [33] spin systems under conditions of rotary resonance recoupling. In general, the numerical simulations employ the REPULSION [34] or Lebedev [35] schemes for the calculation of powder averages, implement some of the routines of the GAMMA package [36] and use, where possible, the γ -COMPUTE or carousel averaging approaches [37–39]. The Migrad method from the MINUIT optimization package [40] is used for error minimization of $e^2 = \sum_{i=1}^N (S_{\text{exp}}(\omega_i) - S_{\text{calc}}(\omega_i))^2$, where $\max(S_{\text{exp}}(\omega_i)) = 1$; the MATLAB program [41] is used for calculating and evaluating error maps and scans.

3. Results and discussion

In order to be able to determine absolute ^{13}C chemical shielding tensor orientations from ^{13}C MAS NMR experiments on polycrystalline powders, ^{13}C isotopic labeling schemes have to be combined with so-called dipolar recoupling MAS NMR [42] experiments. MAS NMR experiments suitable for the determination of chemical shielding tensor orientations must reintroduce all anisotropic interactions and should permit efficient numerical simulations of the spin dynamics to allow for in-depth iterative approaches to extract the unknown parameters. Amongst numerous recoupling schemes applicable for homonuclear spin systems under MAS conditions [42], the rotational-resonance (R^2) [16–22] phenomenon fulfills these criteria particularly well. The R^2 recoupling effect arises at specific MAS frequencies ω_r fulfilling the condition $\omega_{\text{iso}} \approx n\omega_r$ (where ω_{iso} denotes an isotropic chemical shielding difference and n is a small integer). Since the recoupling occurs without application of radio-frequency pulses, R^2 experiments are basically straightforward to carry out and can be simulated efficiently. When applied to an isolated homonuclear two-spin system in a polycrystalline powder sample, the R^2 experiment, like any other dipolar recoupling scheme, can only reveal *relative* chemical shielding tensor orientations. In the general two-spin case rotation around the direction of the unique z -axis of the corresponding dipolar coupling tensor remains undetermined. For homonuclear two-spin systems there is one exception, that is cases where the two chemical shielding tensors are related by a two-fold axis of symmetry which is necessarily perpendicular to the unique z -axis of the corresponding dipolar coupling tensor: here the *absolute* chemical shielding tensor orientations are reflected in $n = 0$ R^2 MAS NMR spectra [31]. Apart from this special two-spin case, it generally takes more than two dipolar coupled spin-1/2 nuclei in order to be able to derive absolute chemical shielding tensor orientations from MAS NMR experiments on powder samples. More specifically, more than one dipolar coupling interaction tensor must be present, and these two (or more) dipolar coupling interaction tensors must not be colinear. Several examples for the complete determination of all interaction tensors form the analysis of MAS NMR experiments on homo- and heteronuclear three- and four-spin-1/2 systems in polycrystalline powders recently have been reported in the literature [24,33,43,44].

Two different ^{13}C R^2 MAS NMR routes exist to determine the absolute ^{13}C chemical shielding tensor orientations in $(\text{NH}_4)_3(\text{PEP})\cdot\text{H}_2\text{O}$, both with distinct advantages and disadvantages. One possibility is to employ selectively pairwise [1,2- $^{13}\text{C}_2$]-, [1,3- $^{13}\text{C}_2$]- and [2,3- $^{13}\text{C}_2$]-labeled samples and to determine the relative ^{13}C chemical shielding tensor orientations for each of these pairs. The resulting relative orientational parameters could then be converted into absolute orientations, by using the known absolute orientations (from the crystal structure) of the dipolar coupling tensors ω^{D12} , ω^{D13} , ω^{D23} .

This approach would solely require two-spin simulations for the complete data analysis. Two-spin simulations are much faster than three-spin simulations, hence this approach would be far preferable from a point of view of efficient numerical analysis. The drawback here is the considerable demand in terms of chemical synthesis. The second route offers convenience in terms of sample preparation, it only requires a fully ^{13}C -enriched sample of $(\text{NH}_4)_3(\text{PEP})\cdot\text{H}_2\text{O}$, $\mathbf{1}\text{-U}^{13}\text{C}$. With the now required three-spin simulations being about an order of magnitude slower than two-spin simulations, the inconvenience of this route rests with the numerical analysis and error minimization procedures, which now become several orders of magnitude more time consuming. It is the $\mathbf{1}\text{-U}^{13}\text{C}$ -based three- ^{13}C -spin-system approach we have chosen for $(\text{NH}_4)_3(\text{PEP})\cdot\text{H}_2\text{O}$.

Neglecting the anisotropy of indirect dipolar coupling $^{13}\text{C}_i\text{-}^{13}\text{C}_j$, it takes thirty parameters for the full description of the ^{13}C three-spin system in $\mathbf{1}\text{-U}^{13}\text{C}$. Several of these parameters are known or can be determined independently. From ^{13}C MAS NMR experiments on $\mathbf{1}$ (with ^{13}C in natural abundance) the magnitudes of the three ^{13}C chemical shielding tensors are obtained, solution-state ^{13}C NMR measurements on $\mathbf{1}\text{-U}^{13}\text{C}$ provide a good estimate of the three values $J_{\text{iso}}(^{13}\text{C}, ^{13}\text{C})$, and the known crystal structure of $(\text{NH}_4)_3(\text{PEP})\cdot\text{H}_2\text{O}$ [30] yields the magnitudes and absolute orientations of the three dipolar coupling tensors in $\mathbf{1}\text{-U}^{13}\text{C}$ (see Tables 1 and 2). Employing all this preliminary information, nine unknown parameters remain to be determined from ^{13}C R^2 MAS NMR experiments on $\mathbf{1}\text{-U}^{13}\text{C}$, that is the Euler angles $\alpha_{\text{PC}}^{\text{CS}_i}$, $\beta_{\text{PC}}^{\text{CS}_i}$, $\gamma_{\text{PC}}^{\text{CS}_i}$ ($i = 1, 2, 3$) representing the orientation of the three ^{13}C chemical shielding tensors. For one of these angles an additional constraint exists from $^{13}\text{C}\text{-}^{31}\text{P}$ rotary-resonance recoupling experiments on $\mathbf{1}$: the angle between the direction of the (least shielded) ω_{zz}^{CS} component of the $^{13}\text{C}2$ chemical shielding tensor and the unique z -axis of the $^{13}\text{C}2\text{-}^{31}\text{P}$ dipolar coupling tensor in $\mathbf{1}$ is known to be $8 \pm 8^\circ$ [32]. The differences in isotropic ^{13}C chemical shieldings for solid $\mathbf{1}\text{-U}^{13}\text{C}$ are $\omega_{\text{iso}}^{12} = 20.3$ ppm, $\omega_{\text{iso}}^{23} = 52.4$ ppm and $\omega_{\text{iso}}^{13} = 72.7$ ppm; the ^{13}C chemical shielding anisotropies $\delta^{\text{CS}_1} = -68$ ppm, $\delta^{\text{CS}_2} = -98$ ppm, $\delta^{\text{CS}_3} = -88$ ppm tend to exceed the values of ω_{iso}^{ij} (see Fig. 2 and Table 1). Accordingly, many different ^{13}C R^2 MAS NMR spectra of $\mathbf{1}\text{-U}^{13}\text{C}$ fulfilling different $\omega_{\text{iso}}^{ij} \approx n\omega_r R^2$ conditions with $n = 1, 2, 3, \dots$, are accessible experimentally over a wide range of ^{13}C Larmor frequencies and should reflect the orientational parameters $\Omega_{\text{PC}}^{\text{CS}_i}$. Further, the differences in ω_{iso}^{ij} in solid $\mathbf{1}\text{-U}^{13}\text{C}$ are such that most of the various $i - j$ R^2 conditions simultaneously represent additional $i - k$, $j - k$ near- R^2 conditions. This broad set of experimental spectra forms the input basis for the numerical lineshape simulations and plays an important role in identifying the correct orientational parameters.

In principle, one could choose one experimental ^{13}C R^2 MAS NMR spectrum of $\mathbf{1}\text{-U}^{13}\text{C}$ and start an iterative line-

Table 1
Magnitudes and orientations of the ^{13}C chemical shielding tensors in $\mathbf{1}\text{-U}^{13}\text{C}$

	$^{13}\text{C}1$	$^{13}\text{C}2$	$^{13}\text{C}3$
$\omega_{\text{iso}}^{\text{CS}}$ (ppm) ^a	-171.5 ± 0.1	-151.2 ± 0.1	-98.8 ± 0.1
δ^{CS} (ppm) ^a	-68 ± 1	-98 ± 1	-88 ± 1
η^{CSa}	0.77 ± 0.05	0.32 ± 0.1	0.77 ± 0.05
$\alpha_{\text{PC}12}^{\text{CS}}$ (deg) ^{b,c}	$334 \pm 33^{\text{d}}$	308	85
$\beta_{\text{PC}12}^{\text{CS}}$ (deg) ^{b,c}	169 ± 13	31	146
$\gamma_{\text{PC}12}^{\text{CS}}$ (deg) ^{b,c}	$249 \pm 33^{\text{d}}$	195	13
$\alpha_{\text{PC}23}^{\text{CS}}$ (deg) ^{b,c}	67	321	$74 \pm 36^{\text{d}}$
$\beta_{\text{PC}23}^{\text{CS}}$ (deg) ^{b,c}	125	88	89 ± 11
$\gamma_{\text{PC}23}^{\text{CS}}$ (deg) ^{b,c}	347	188	7 ± 9
$\alpha_{\text{PC}13}^{\text{CS}}$ (deg) ^{b,c}	51	$316 \pm 29^{\text{d}}$	78
$\beta_{\text{PC}13}^{\text{CS}}$ (deg) ^{b,c}	155	57 ± 2	120
$\gamma_{\text{PC}13}^{\text{CS}}$ (deg) ^{b,c}	334	189 ± 6	8

^a Taken from Ref. [32], determined on $\mathbf{1}$ with ^{13}C in natural abundance.

^b The uncertainties quoted are given in the CAS in which they were calculated, they result from the combined constraints from several experimental spectra, obtained by several one- and/or two-dimensional error calculations at or very near the minimum values of the non-scanned parameters.

^c Although redundant, for the convenience of the reader the Euler angles $\Omega_{\text{PC}}^{\text{CS}_i}$, $i = 1, 2, 3$, are given in the three CAS C_{12} , C_{23} , C_{13} , for which the $C2 \rightarrow C1$, $C3 \rightarrow C2$, $C3 \rightarrow C1$ directions define the $+z$ -directions, respectively. The y -axes of the CAS are taken as perpendicular to the $C1\text{-}C2\text{-}C3$ plane, with the $+y$ -direction (see also Fig. 5(a)) defined such that a right-handed Cartesian coordinate system results.

^d See text for further explanations.

Table 2
Direct and indirect dipolar couplings $^{13}\text{C}_i\text{-}^{13}\text{C}_j$ in $\mathbf{1}\text{-U}^{13}\text{C}$

	$ij = 12$	$ij = 13$	$ij = 23$
$b_{ij}/2\pi$ (Hz) ^a	-2159	-493	-3283
$\omega_{ij}^{J_{\text{iso}}}$ (Hz) ^b	+75.8	± 7.3	+80.7

^a Calculated from the known internuclear distances [30].

^b Determined by solution-state ^{13}C NMR of an aqueous solution of $\mathbf{1}\text{-U}^{13}\text{C}$.

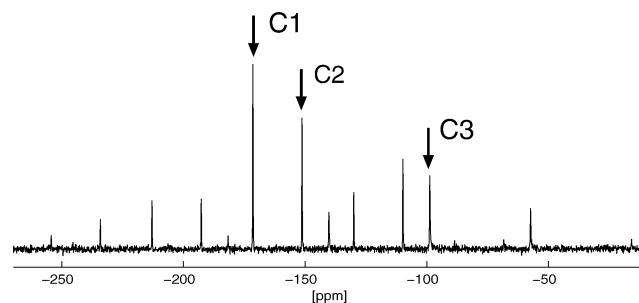


Fig. 2. ^{13}C MAS NMR spectrum of $\mathbf{1}$ ($\omega_0/2\pi = -100.6$ MHz, $\omega_r/2\pi = 4162$ Hz); the assignment of the three ^{13}C resonances is indicated by arrows, all other resonances are spinning sidebands due to anisotropic ^{13}C chemical shielding.

shape fit with all nine Euler angles $\Omega_{PC}^{CS_i}$ as free fit parameters. The fit would converge to some minimum values and would leave us with the task to verify that the minimum found is the correct solution. Clearly, with nine unknown parameters to be determined, precautions have to be taken to ensure that local minima are avoided and that all unknown parameters are indeed sensitively encoded in the particular experimental spectrum chosen.

Our approach to determine the values of the nine Euler angles $\Omega_{PC}^{CS_i}$ exploits a large set of different experimental ^{13}C R^2 MAS NMR spectra of $\mathbf{1-U}^{13}\text{C}$: the sensitivities with which the various Euler angles $\Omega_{PC}^{CS_i}$ are encoded in R^2 spectral lineshapes vary strongly from one R^2 condition and/or Larmor frequency to another. In a first and rather coarse-grid search, we screen the set of different experimental spectra by calculating scans of all orientational parameters for each spectrum to find out which experimental spectra reflect which Euler angles with high or low sensitivities. A suitable subset of experimental spectra is then chosen as the input basis for subsequent stepwise determination and refinement of the unknown parameters. The remaining experimental spectra are saved for later cross checks, but are not actively used for any iterative fitting, error calculations, or parameter-refinement procedures. These initial selection steps are schematically illustrated in Fig. 3, where the relative sensitivities of the fit parameters $\Omega_{PC}^{CS_i}$ for three different experimental ^{13}C R^2 MAS NMR spectra of $\mathbf{1-U}^{13}\text{C}$ are symbolized by the relative heights of bar codes, denoting ratios of maximum to minimum errors over the full range of each fit parameter $\Omega_{PC}^{CS_i}$. Of course, such initial screening calculations neither permit identification of minimum regions, nor do they define how well a particular parameter is characterized. However, in this way we can identify the most promising strategies to make the best (stepwise and complementary) use of the various experimental spectra in the numerical simulations. For instance (see Fig. 3a), the ^{13}C MAS NMR spectrum of $\mathbf{1-U}^{13}\text{C}$ with the $n = 1$ R^2 condition fulfilled for $^{13}\text{C}2-^{13}\text{C}3$ at $\omega_0/2\pi = -100.6$ MHz is strongly dominated by only four orientational parameters, $\beta_{PC}^{CS_2}$, $\beta_{PC}^{CS_3}$, $\gamma_{PC}^{CS_2}$ and $\gamma_{PC}^{CS_3}$ while, in particular, the angles $\Omega_{PC}^{CS_1}$ do not contribute significantly to this R^2 lineshape. This kind of pseudo-spin-pair behavior in a ^{13}C -three-spin system under R^2 conditions also occurs, e.g., for solid sodium pyruvate [14], for $\mathbf{1-U}^{13}\text{C}$ it provides a convenient starting point. The first error-minimization steps based on this experimental spectrum can be focused on only the four parameters $\beta_{PC}^{CS_2}$, $\beta_{PC}^{CS_3}$, $\gamma_{PC}^{CS_2}$, $\gamma_{PC}^{CS_3}$, and the possible minimum regions for those can be considerably narrowed to within ca. $\pm 30^\circ$ by calculations of several complete three-dimensional error maps. The results of these initial calculations regarding $\beta_{PC}^{CS_2}$ turn out immediately compatible with the independent constraint for this parameter from $^{13}\text{C}-^{31}\text{P}$ rotary-resonance recoupling experiments on $\mathbf{1}$ [32]. With possible minimum regions of these four parameters already

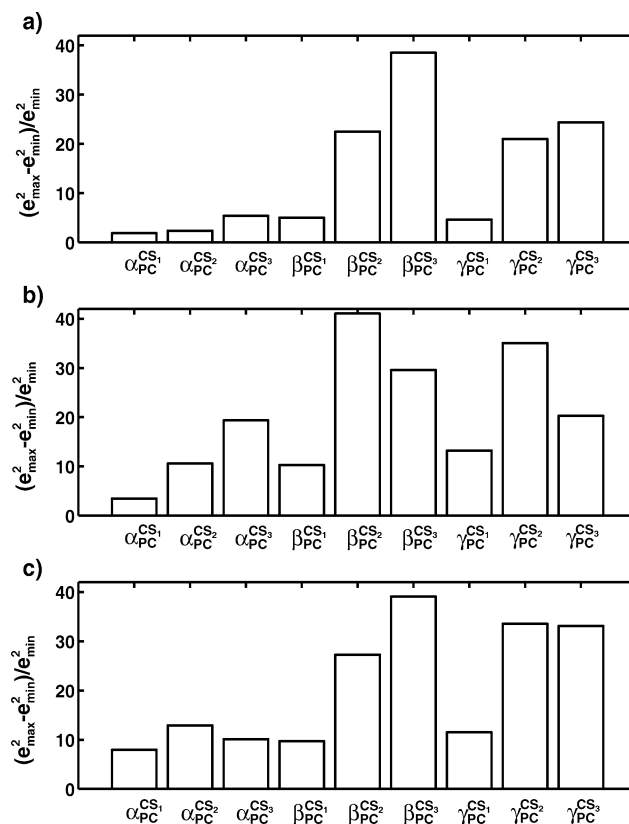


Fig. 3. Graphical representation of the sensitivities of the fit parameters $\Omega_{PC}^{CS_i}$ encoded in different experimental ^{13}C R^2 MAS NMR spectra of $\mathbf{1-U}^{13}\text{C}$; the heights of the bars indicate the values $(e_{\max}^2 - e_{\min}^2)/e_{\min}^2$ (where e^2 is the rms error between experimental and simulated spectra), for each Euler angle from scanning the full range of the respective angle. (a) $n = 1$ R^2 condition fulfilled for $^{13}\text{C}2-^{13}\text{C}3$ at $\omega_0/2\pi = -100.6$ MHz, $\omega_r/2\pi = 5244$ Hz; (b) $n = 2$ R^2 condition fulfilled for $^{13}\text{C}2-^{13}\text{C}3$ at $\omega_0/2\pi = -125.8$ MHz, $\omega_r/2\pi = 3290$ Hz; (c) $n = 1$ R^2 condition fulfilled for $^{13}\text{C}1-^{13}\text{C}2$ at $\omega_0/2\pi = -125.8$ MHz, $\omega_r/2\pi = 2551$ Hz.

fairly well predefined, the numerical calculations are next expanded to include those experimental spectra where more and other Euler angles are sensitively encoded in the R^2 lineshapes (see, for instance, Fig. 3(b) and 3(c)). Not unexpectedly, the ^{13}C MAS NMR spectrum of $\mathbf{1-U}^{13}\text{C}$ with the $n = 2$ R^2 condition fulfilled for $^{13}\text{C}2-^{13}\text{C}3$ at $\omega_0/2\pi = -125.8$ MHz (Fig. 3(b)) reflects all orientational parameters, including those of $^{13}\text{C}1$, with higher sensitivities than at the $n = 1$ R^2 condition. The ^{13}C MAS NMR spectrum of $\mathbf{1-U}^{13}\text{C}$ with the $n = 1$ R^2 condition fulfilled for $^{13}\text{C}1-^{13}\text{C}2$ at $\omega_0/2\pi = -125.8$ MHz (Fig. 3(c)) serves as an illustrative example that in a three-spin system it is not necessarily the set of Euler angles of the ‘actively’ recoupled pair of spins which is most sensitively reflected in the corresponding R^2 lineshapes. The numerical refinement procedures continue to switch between different experimental spectra, include numerous versions of iterative fits, calculations of error maps, single-parameter scans, as well as occasional cross-check calculations of spectra not actively used in the refinement, until no further improvement in agreement be-

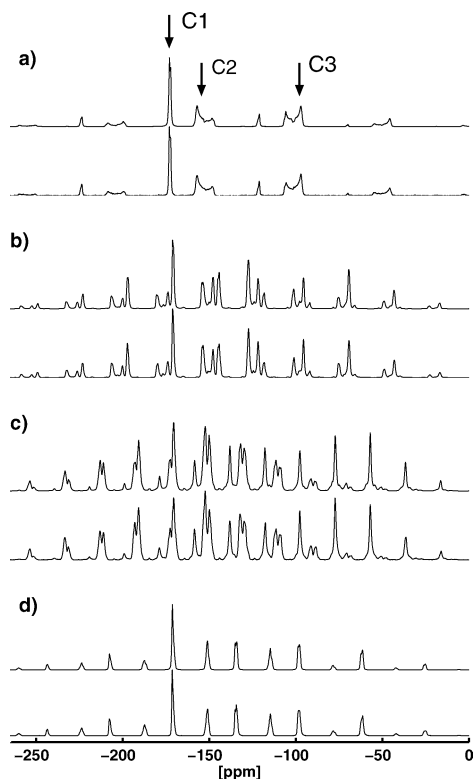


Fig. 4. Comparison of experimental (lower traces) and best-fit calculated (upper traces) ^{13}C R^2 MAS NMR spectra of $1\text{-U}^{13}\text{C}$. (a) $n = 1$ R^2 condition fulfilled for $^{13}\text{C}2\text{-}^{13}\text{C}3$ at $\omega_0/2\pi = -100.6$ MHz, $\omega_r/2\pi = 5244$ Hz; (b) $n = 2$ R^2 condition fulfilled for $^{13}\text{C}2\text{-}^{13}\text{C}3$ at $\omega_0/2\pi = -125.8$ MHz, $\omega_r/2\pi = 3290$ Hz; (c) $n = 1$ R^2 condition fulfilled for $^{13}\text{C}1\text{-}^{13}\text{C}2$ at $\omega_0/2\pi = -125.8$ MHz, $\omega_r/2\pi = 2551$ Hz; (d) $n = 2$ R^2 condition fulfilled for $^{13}\text{C}1\text{-}^{13}\text{C}3$ at $\omega_0/2\pi = -125.8$ MHz, $\omega_r/2\pi = 4565$ Hz. The spectra shown in (a)–(c) were actively used for the refinement of the fit parameters. The experimental spectrum shown in the lower trace in (d) was not used for any parameter determination. The calculated spectra in (a)–(d) are based on the (minimum) parameters given in Tables 1 and 2.

tween *all* experimental R^2 spectra and the corresponding calculated spectra from a single set of ‘best-fit’ parameters can be achieved. The ‘best-fit’ set of Euler angles $\Omega_{\text{PC}}^{\text{CS}_i}$, resulting from this ‘interactive’ numerical procedure is given in Table 1. A comparison of various experimental to ‘best-fit’ calculated R^2 spectra of $1\text{-U}^{13}\text{C}$ is shown in Fig. 4. Note the strong variations in the R^2 lineshapes with differing R^2 conditions and Larmor frequencies. Fig. 4(a)–4(c) display spectra which were actively used in the parameter refinement. Fig. 4(d) shows ^{13}C MAS NMR spectra of $1\text{-U}^{13}\text{C}$ with the $n = 2$ R^2 condition fulfilled for $^{13}\text{C}1\text{-}^{13}\text{C}3$ at $\omega_0/2\pi = -125.8$ MHz; at no point this experimental spectrum was used for error minimization calculations, the corresponding calculated spectrum results from the ‘best-fit’ parameters derived from the spectra shown in Fig. 4(a)–4(c).

The orientational parameters of the three ^{13}C chemical shielding tensors in relation to the molecular geometry of the PEP moiety in **1** are illustrated in Fig. 5. The O5–C1–O6 and the C1–C2–C3 planes in **1** are close to, but not exactly, coplanar. The torsion angle of 5.6° [30] between these two

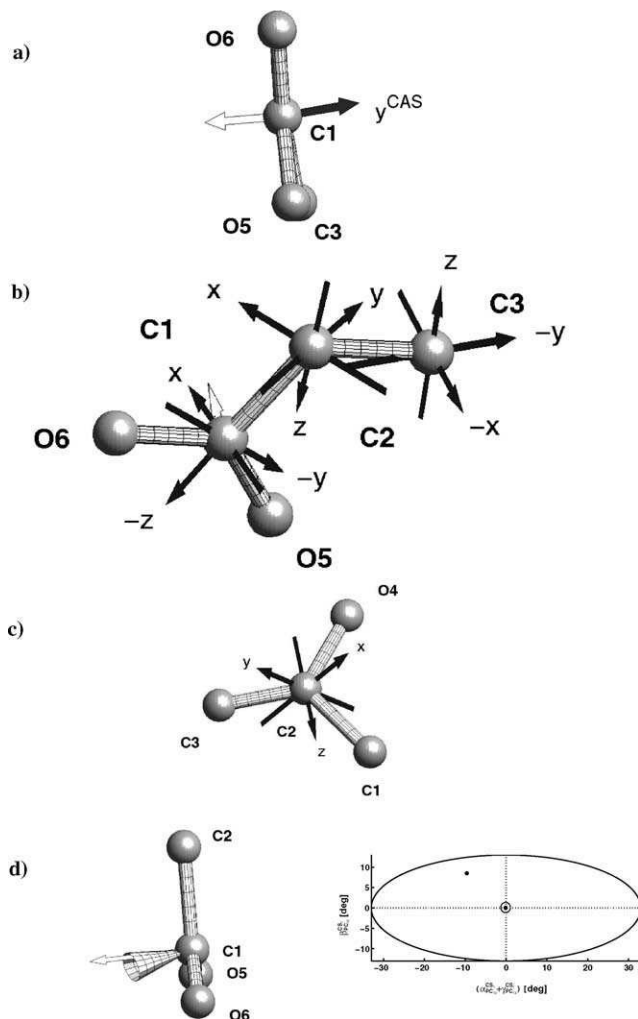


Fig. 5. The structure of the PEP moiety in **1** and the orientations of the three ^{13}C chemical shielding tensors. (a) The PEP moiety viewed along the C1–C2 bond direction, highlighting the torsion angle between the molecular C1–O5–O6 and C1–C2–C3 planes; also shown are the normal to the C1–O5–O6 plane (transparent arrow) and the direction of the $+y$ -axis of the CAS (shaded arrow, denoted y^{CAS}), taken as perpendicular to the C1–C2–C3 plane. (b) The ‘best fit’ orientations of the $^{13}\text{C}1$, $^{13}\text{C}2$ and $^{13}\text{C}3$ chemical shielding tensors in **1**; the orientation of the principal directions (denoted x , y , z) associated with the ^{13}C chemical shielding tensors is indicated by arrows, for all three tensors the z -direction corresponds to the least shielded direction, also shown is the normal to the C1–O5–O6 plane (transparent arrow). (c) The orientation of the $^{13}\text{C}2$ chemical shielding tensor in relation to the C3–C2–O4 plane in **1**. (d) Left: the possible directions of the (most shielded) $\omega_{xx}^{\text{CS}1}$ component of the $^{13}\text{C}1$ chemical shielding tensor in relation to the C1–O5–O6 plane in **1**, the arrow indicates the normal to the C1–O5–O6 plane, the cone describes the set of possible directions of the $\omega_{xx}^{\text{CS}1}$ component, for the sake of clarity the corresponding ‘error cone’ for the possible directions of the $\omega_{yy}^{\text{CS}1}$ component is omitted. Right: view onto the base plane of the $\omega_{xx}^{\text{CS}1}$ ‘error cone’, defined by the error limits of $\beta_{\text{PC}}^{\text{CS}1}$ vs. $(\alpha_{\text{PC}}^{\text{CS}1} + \gamma_{\text{PC}}^{\text{CS}1})$ (deg), the main cone axis is indicated by \odot , the location of the normal to the C1–O5–O6 plane is given by \bullet .

molecular planes is best seen in a view along the C1–C2 bond direction (Fig. 5(a)). The directions of the ω_{xx}^{CS} , ω_{yy}^{CS} , ω_{zz}^{CS} components of the three $^{13}\text{C}1$, $^{13}\text{C}2$ and $^{13}\text{C}3$ chemical

shielding tensors in the three-dimensional structure of the PEP moiety in **1** according to the ‘best-fit’ values (Table 1) are shown in Fig. 5(b), while Fig. 5(c) and 5(d) display zoom versions of the $^{13}\text{C}2$ and $^{13}\text{C}1$ chemical shielding tensor orientations when viewing selected parts of the PEP fragment from different directions.

Two independent sets of constraints exist for the orientation of the $^{13}\text{C}2$ chemical shielding tensor, there are ‘best-fit’ values from the various ^{13}C R^2 MAS NMR experiments on **1- U^{13}C** and from ^{13}C – ^{31}P rotary-resonance-recoupling (R^3) experiments on **1** [32]. Each of the two approaches separately yields $\beta_{\text{PC}}^{\text{CS}_2}$ with an accuracy of $\pm 8^\circ$ in the two different CAS, while consideration of the combined R^2 and R^3 constraints defines this angle as $\beta_{\text{PC}}^{\text{CS}_2} = 57 \pm 2^\circ$ (in CAS C_{13} , see Table 1). Accordingly, the direction of the $\omega_{zz}^{\text{CS}_2}$ component is known with very good precision. Neither the R^2 nor the R^3 experiments alone yield high precision for the angle $\gamma_{\text{PC}}^{\text{CS}_2}$. Again, the constraints from both independent experiments together define $\gamma_{\text{PC}}^{\text{CS}_2} = 189 \pm 6^\circ$ (in CAS C_{13} , see Table 1). Owing to the small asymmetry parameter of the $^{13}\text{C}2$ chemical shielding tensor ($\eta^{\text{CS}_2} = 0.32 \pm 0.1$) not even the combined consideration of the R^2 and R^3 constraints defines $\alpha_{\text{PC}}^{\text{CS}_2}$ any better than within $\pm 29^\circ$. The Euler angles $\Omega_{\text{PC}}^{\text{CS}_2}$ describe the following orientation of the $^{13}\text{C}2$ chemical shielding tensor in the PEP moiety of **1**. The direction of the (least shielded) $\omega_{zz}^{\text{CS}_2}$ component lies nearly in the C1–C2–C3 plane (within $8^\circ \pm 5^\circ$) and is perpendicular to the C2=C3 bond direction (within $2^\circ \pm 2^\circ$), it subtends an angle of $30^\circ \pm 1^\circ$ with the C1–C2 bond direction. The direction of the (most shielded) $\omega_{xx}^{\text{CS}_2}$ component subtends an angle of $39^\circ \pm 27^\circ$ with the C1–C2–C3 plane, the angle between the C1–C2–C3 plane and the $\omega_{yy}^{\text{CS}_2}$ component amounts to $50^\circ \pm 29^\circ$. The directions of the $\omega_{xx}^{\text{CS}_2}$ and $\omega_{yy}^{\text{CS}_2}$ components of the $^{13}\text{C}2$ chemical shielding tensor flank the C2=C3 bond direction at angles of $39^\circ \pm 25^\circ$ ($\omega_{xx}^{\text{CS}_2}$) and $51^\circ \pm 30^\circ$ ($\omega_{yy}^{\text{CS}_2}$), respectively. The relatively large uncertainties in the directions of the $\omega_{xx}^{\text{CS}_2}$ and $\omega_{yy}^{\text{CS}_2}$ components arise as a consequence of the imprecision of the value for $\alpha_{\text{PC}}^{\text{CS}_2}$. Since the $^{13}\text{C}2$ chemical shielding tensor does not deviate much from being axially symmetric, in practical terms it is more important that the direction of the $\omega_{zz}^{\text{CS}_2}$ component is known with good precision. Recasting these $^{13}\text{C}2$ data for the C3=C2–O4 molecular plane in **1**, which characterizes the typical bonding environment of the enolic C2 site, yields the following picture for the orientation of the $^{13}\text{C}2$ chemical shielding tensor (see Fig. 5(c)). The direction of the (most shielded) $\omega_{xx}^{\text{CS}_2}$ tensor component is oriented at an angle of $39^\circ \pm 27^\circ$ to the C3=C2–O4 molecular plane, while the (least shielded) $\omega_{zz}^{\text{CS}_2}$ tensor component is tilted away from the C2–O4 bond direction by $39^\circ \pm 2^\circ$. Our findings for the orientation of the $^{13}\text{C}2$ chemical shielding tensor in **1** favorably agree with the results of ^{13}C single-crystal NMR studies of other enolic ^{13}C sites [45,46].

For the $^{13}\text{C}1$ chemical shielding tensor the direction of the (least shielded) $\omega_{zz}^{\text{CS}_1}$ component subtends an angle of $11^\circ \pm 13^\circ$ with the direction of the C1–C2 bond direction. Thus, within the error limits for $\beta_{\text{PC}}^{\text{CS}_1}$, the directions of the principal z -axes of the $^{13}\text{C}1$ chemical shielding tensor and the $^{13}\text{C}1$ – $^{13}\text{C}2$ dipolar coupling tensor coincide. This coincidence (or nearly so) of two principal z -axis directions is of consequence for the determination of $\alpha_{\text{PC}}^{\text{CS}_1}$ and $\gamma_{\text{PC}}^{\text{CS}_1}$. With $\alpha_{\text{PC}}^{\text{CS}_1}$ describing a rotation around the z -axis of the $^{13}\text{C}1$ chemical shielding tensor and $\gamma_{\text{PC}}^{\text{CS}_1}$ corresponding to a rotation around the z -axis of the $^{13}\text{C}1$ – $^{13}\text{C}2$ dipolar coupling tensor, $\alpha_{\text{PC}}^{\text{CS}_1}$ and $\gamma_{\text{PC}}^{\text{CS}_1}$ become highly correlated parameters and cannot be considered separately. The presence of a third interacting spin, $^{13}\text{C}3$, in **1- U^{13}C** helps to restrict the possible minimum range for $(\alpha_{\text{PC}}^{\text{CS}_1} + \gamma_{\text{PC}}^{\text{CS}_1})$, but cannot resolve it completely: within the minimum region the two parameters remain highly correlated. The consequences regarding the possible directions of the (most shielded) $\omega_{xx}^{\text{CS}_1}$ component relative to the O5–C1–O6 plane are illustrated in Fig. 5(d). The possible directions of the $\omega_{xx}^{\text{CS}_1}$ component are described by a cone at a certain angle to the O5–C1–O6 plane, also drawn is the normal to this plane. Note that the main axis of the cone is tilted away (by 13°) from the normal to the carboxylate plane, towards the O5, O6 oxygen atoms of the carboxylate group. One of the limits of the $\omega_{xx}^{\text{CS}_1}$ ‘error cone’ just includes the orientation of the (most shielded) $\omega_{xx}^{\text{CS}_1}$ component perpendicular to the O5–C1–O6 plane, the other limit of the ‘error cone’ corresponds to a direction of the $\omega_{xx}^{\text{CS}_1}$ component 26° away from the normal to the O5–C1–O6 plane. The combined effects of the uncertainties in $\beta_{\text{PC}}^{\text{CS}_1}$ and $(\alpha_{\text{PC}}^{\text{CS}_1} + \gamma_{\text{PC}}^{\text{CS}_1})$ on the possible directions of the $\omega_{xx}^{\text{CS}_1}$ component are further illustrated in Fig. 5(d), where in addition a view onto the base plane of the ‘error cone’ for $\omega_{xx}^{\text{CS}_1}$ is depicted. Similarly, of course, also a cone of possible corresponding directions of the intermediate $\omega_{yy}^{\text{CS}_1}$ component of the $^{13}\text{C}1$ chemical shielding tensor results; for the sake of clarity this $\omega_{yy}^{\text{CS}_1}$ ‘error cone’ has been omitted from Fig. 5(d). Tilting of the most shielded ^{13}COO tensor component towards the two oxygen atoms in the COO plane has been reported for the ^{13}COO chemical shielding tensors in, e.g., solid oxalic acid dihydrate [13] and sodium pyruvate [14]. These two compounds and the PEP moiety have in common that in all three cases a carbon atom engaged in a C–O bond of some sort is directly attached to the COO group. This structural motive is absent in most of those cases where the direction of the most shielded ^{13}COO tensor component is found to be very nearly perpendicular to the COO plane [7–12,24]. The ^{13}C spin systems in **1** and in sodium pyruvate have something else in common. For the ^{13}COO shielding tensor in sodium pyruvate, it is also the $\omega_{zz}^{\text{CS}_1}$ component which corresponds to the least shielded direction, and it is again this direction which coincides with the unique z -axis of the $^{13}\text{C}1$ – $^{13}\text{C}2$ dipolar coupling tensor,

creating a similar condition of highly correlated orientational parameters [14].

The most prominent features of the orientation of the ^{13}C chemical shielding tensor are the following. The direction of the (least shielded) $\omega_{zz}^{\text{CS}_3}$ tensor component is well defined and is, within experimental error, parallel to that of the $\omega_{zz}^{\text{CS}_2}$ tensor component (see Fig. 5(b)) and thus nearly perpendicular to the C2=C3 bond direction and nearly in the C1–C2–C3 plane. The direction of the (most shielded) $\omega_{xx}^{\text{CS}_3}$ tensor component subtends an angle of $74^\circ \pm 36^\circ$ with the C1–C2–C3 plane. This reflects the large uncertainty we ascribe to the minimum value for the angle $\alpha_{\text{PC}}^{\text{CS}_3} = 74^\circ \pm 36^\circ$ (in CAS C₂₃, see Table 1). These large error margins occur because the minimum region for $\alpha_{\text{PC}}^{\text{CS}_3}$, in fact, consists of two, poorly resolved and indistinguishable minima, at $\alpha_{\text{PC}}^{\text{CS}_3} = 65^\circ$ and $\alpha_{\text{PC}}^{\text{CS}_3} = 89^\circ$ with individually much smaller error margins. These two minima would correspond to a deviation of the direction of the (intermediate) $\omega_{yy}^{\text{CS}_3}$ tensor component from the C2=C3 bond direction by 25° ($\alpha_{\text{PC}}^{\text{CS}_3} = 65^\circ$) and by 1° ($\alpha_{\text{PC}}^{\text{CS}_3} = 89^\circ$), respectively. ^{13}C R^2 MAS NMR experiments on a selectively [1,3- $^{13}\text{C}_2$]-labeled sample of $(\text{NH}_4)_3(\text{PEP})\cdot\text{H}_2\text{O}$ should be able to resolve this remaining ambiguity.

4. Summary and conclusions

A certain unavoidable degree of uncertainty is inherent to all solid-state NMR experiments designed to derive molecular torsion angles from chemical shielding tensor orientations, simply because small differences in bonding and geometry between the model case and an application–target compound will be accompanied by small changes in magnitudes and orientations of the chemical shielding tensors. The more important it appears that applications of chemical shielding tensor correlation experiments are backed up by precise characterization of closely related model-spin systems. The accuracy with which the ^{13}C chemical shielding tensor orientations in **1-U ^{13}C** have now been characterized, will be adequate to test the conformational modulation hypothesis, where specific predictions for the PEP dihedral angles have been made for several enzymes (EPSP synthase and MurA: $30^\circ \pm 10^\circ$, KDO8P synthase and DAHP synthase: $80^\circ \pm 10^\circ$) [6]. At the same time, the results of our ^{13}C MAS NMR study of **1-U ^{13}C** outline the most promising ^{13}C -labeling strategies for such experiments. With the $^{13}\text{C}_2$ chemical shielding tensor not deviating much from axial symmetry and with the direction of the (least shielded) ω_{zz}^{CS} component of the $^{13}\text{C}_1$ chemical shielding tensor nearly coinciding with the direction of the z -axis of the $^{13}\text{C}_1$ – $^{13}\text{C}_2$ dipolar coupling tensor, it is likely that ^{13}C NMR experiments on selectively [1,2- $^{13}\text{C}_2$]-enriched PEP samples may meet serious difficulties in providing unambiguous information about the torsion angle between the O5–C1–O6 and the C1–C2–C3 plane. Despite the smaller dipolar coupling con-

stant involved, selectively [1,3- $^{13}\text{C}_2$]-enriched PEP samples should be more suitable: the $^{13}\text{C}_1$ – $^{13}\text{C}_3$ spin pair avoids potential problems arising from nearly axially symmetric chemical shielding tensors and nearly coinciding directions of principal z -directions of chemical shielding and dipolar coupling tensors. Alternatively, one could use fully [1,2,3- $^{13}\text{C}_3$]-enriched PEP samples. However, iterative fitting with numerically exact simulation approaches for a three-spin system under conditions of MAS NMR pulse sequences more sophisticated than the R^2 phenomenon, will only come at a dear price in terms of computation times.

The protocol we describe to derive quasi single-crystal-NMR-like information from the lineshapes of R^2 MAS NMR spectra of dipolar (re)coupled spin-1/2 systems in powder samples is quite generally applicable. Invariably, for all dipolar coupled, larger-than-two-spin-1/2 systems, for which information about absolute interaction tensor orientations is encoded in R^2 MAS NMR spectra of powder samples, this will involve the simultaneous determination of multiple unknown parameters. The most suitable and economic strategies to keep multiple unknown parameters under control will vary slightly from case to case. The properties of the ^{13}C -three-spin system in **1-U ^{13}C** make numerous *different* experimental R^2 MAS NMR spectra accessible, which greatly helps to disentangle the multiple-parameter space in the numerical minimization procedures. For cases with a slimmer input basis of experimental data, suitable numerical procedures have to rely more heavily on iterative fitting strategies, followed by sometimes brute-force and often time consuming numerical verification of the best-fit parameters. Regardless of the relative weight of experimental and numerical data in such R^2 MAS NMR lineshape-based approaches, the feasibility and accuracy limits are more tightly defined by the number and the nature of the unknown parameters than by the size of the spin system.

Acknowledgements

This research was supported by the Deutsche Forschungsgemeinschaft, the Fonds der Chemischen Industrie, and NIH Grant R01 GM43215. The WSU NMR Center equipment was supported by NIH Grants RR0631401 and RR12948, NSF Grants CHE-9115282 and DBI-9604689, and a grant from the Murdock Charitable Trust. We thank H. Förster and S. Steuernagel, Bruker Analytik GmbH, Rheinstetten, for generous access to the DSX 400 and DSX 500 NMR spectrometers and for experimental support. B. Wrackmeyer, Bayreuth, is thanked for recording solution-state ^{13}C NMR spectra of **1-U ^{13}C** , and T. Lis, Wrocław, for providing a sample of **1**.

References

- [1] C.T. Walsh, T.E. Benson, D.H. Kim, W. Lees, J. Chem. Biol. 3 (1996) 83.

- [2] R.G. Pearson, *J. Amer. Chem. Soc.* 85 (1963) 3533.
- [3] R.G. Parr, W. Yang, *Density Functional Theory of Atoms and Molecules*, Oxford Univ. Press, New York, 1989.
- [4] Y. Li, J.N.S. Evans, *J. Amer. Chem. Soc.* 117 (1995) 7756.
- [5] M. Galván, A. Dal Pino Jr., J.D. Joannopoulos, *Phys. Rev. Lett.* 70 (1993) 21.
- [6] Y. Li, J.N.S. Evans, *Proc. Natl. Acad. Sci. USA* 93 (1996) 4612.
- [7] A. Pines, J.J. Chang, R.G. Griffin, *J. Chem. Phys.* 61 (1974) 1021.
- [8] J.L. Ackermann, J. Tegenfeldt, J.S. Waugh, *J. Amer. Chem. Soc.* 96 (1974) 6843.
- [9] J.J. Chang, R.G. Griffin, A. Pines, *J. Chem. Phys.* 62 (1975) 4923.
- [10] J. Tegenfeldt, H. Feucht, G. Ruschitzka, U. Haeberlen, *J. Magn. Reson.* 39 (1980) 509.
- [11] K. Takegoshi, C.A. McDowell, *J. Amer. Chem. Soc.* 108 (1986) 6852.
- [12] W. Scheubel, H. Zimmermann, U. Haeberlen, *J. Magn. Reson.* 80 (1988) 401.
- [13] R.G. Griffin, A. Pines, S. Pausak, J.S. Waugh, *J. Chem. Phys.* 63 (1975) 1267.
- [14] S. Dusold, A. Sebald, *J. Magn. Reson.* 145 (2000) 340.
- [15] C.A. McDowell, A. Naito, D.L. Sastry, K. Takegoshi, *J. Magn. Reson.* 78 (1988) 498.
- [16] E.R. Andrew, A. Bradbury, R.G. Eades, V.T. Wynn, *Phys. Lett.* 4 (1963) 99.
- [17] D.P. Raleigh, M.H. Levitt, R.G. Griffin, *Chem. Phys. Lett.* 146 (1988) 71.
- [18] M.H. Levitt, D.P. Raleigh, F. Creuzet, R.G. Griffin, *J. Chem. Phys.* 92 (1990) 6347.
- [19] A. Kubo, C.A. McDowell, *J. Chem. Phys.* 92 (1990) 7156.
- [20] A. Schmidt, S. Vega, *J. Chem. Phys.* 96 (1992) 2655.
- [21] T. Nakai, C.A. McDowell, *Mol. Phys.* 77 (1992) 569.
- [22] T. Nakai, C.A. McDowell, *J. Chem. Phys.* 96 (1992) 3452.
- [23] D.L. Jakeman, J.N.S. Evans, *Bioorg. Chem.* 26 (1998) 245.
- [24] S. Dusold, H. Maisel, A. Sebald, *J. Magn. Reson.* 141 (1999) 78.
- [25] M. Helmle, Y.K. Lee, P.J.E. Verdegem, X. Feng, T. Karlsson, J. Lugtenburg, H.J.M. de Groot, M.H. Levitt, *J. Magn. Reson.* 140 (1999) 379.
- [26] A.E. Bennett, C.M. Rienstra, M. Auger, K.V. Lakshmi, R.G. Griffin, *J. Chem. Phys.* 103 (1995) 6951.
- [27] M.H. Levitt, *J. Magn. Reson.* 126 (1997) 164.
- [28] U. Haeberlen, High resolution NMR in solids. Selective averaging, in: J.S. Waugh (Ed.), *Advances in Magnetic Resonance*, Supplement 1, Academic Press, New York, 1976.
- [29] A.R. Edmonds, *Angular Momentum in Quantum Mechanics*, Princeton Univ. Press, Princeton, NJ, 1974.
- [30] A. Weichsel, T. Lis, *Polish J. Chem.* 68 (1994) 2079.
- [31] S. Dusold, W. Milius, A. Sebald, *J. Magn. Reson.* 135 (1998) 500.
- [32] M. Bechmann, S. Dusold, H. Förster, U. Haeberlen, T. Lis, A. Sebald, M. Stumber, *Mol. Phys.* 98 (2000) 605.
- [33] S. Dusold, A. Sebald, *Mol. Phys.* 95 (1998) 1237.
- [34] M. Bak, N.C. Nielsen, *J. Magn. Reson.* 125 (1997) 132.
- [35] M. Edén, M.H. Levitt, *J. Magn. Reson.* 132 (1998) 220.
- [36] S.A. Smith, T.O. Levante, B.H. Meier, R.R. Ernst, *J. Magn. Reson.* A 106 (1994) 75.
- [37] T. Charpentier, C. Fermon, J. Virlet, *J. Magn. Reson.* 132 (1998) 181.
- [38] M. Hohwy, H. Bildsoe, H.J. Jakobsen, N.C. Nielsen, *J. Magn. Reson.* 136 (1999) 6.
- [39] M.H. Levitt, M. Edén, *Mol. Phys.* 95 (1998) 879.
- [40] F. James, M. Roos, MINUIT computer code, Program D-506, CERN, Geneva, 1977.
- [41] MATLAB, Version 5.3, The Mathworks Inc., Natick MA, 1999.
- [42] For general review articles on dipolar recoupling under MAS NMR conditions see:
(a) A.E. Bennett, R.G. Griffin, S. Vega, Recoupling of homo- and heteronuclear dipolar interactions in rotating solids, in: B. Blümich (Ed.), *Solid-State NMR IV: Methods and Applications of Solid-State NMR*, in: *NMR Basic Principles and Progress*, vol. 33, Springer-Verlag, Berlin, 1994, pp. 1–78;
(b) S. Dusold, A. Sebald, Dipolar recoupling under magic-angle-spinning conditions, in: G. Webb (Ed.), *Annual Reports on NMR Spectroscopy*, vol. 41, Academic Press, London, 2000, pp. 185–264, and references given in (a) and (b) on methodology and applications of rotational-resonance NMR.
- [43] M. Bak, N.C. Nielsen, *J. Chem. Phys.* 106 (1997) 7587.
- [44] J.T. Rasmussen, M. Hohwy, H.J. Jakobsen, N.C. Nielsen, *Chem. Phys. Lett.* 314 (1999) 239.
- [45] K. Takegoshi, C.A. McDowell, *Chem. Phys. Lett.* 123 (1986) 159.
- [46] K. Takegoshi, A. Naito, C.A. McDowell, *J. Magn. Reson.* 65 (1985) 34.

C. Double-Quantum Filtered Rotational-Resonance MAS NMR in the Presence of Large Chemical Shielding Anisotropies

M. Bechmann, X. Helluy, and A. Sebald, *Journal of Magnetic Resonance*, **152**, 14–25 (2001).

doi:10.1006/jmre.2001.2393

©2001 Academic Press.

All rights are reserved by Academic Press. The article is reproduced with the rights granted to the author.

Double-Quantum-Filtered Rotational-Resonance MAS NMR in the Presence of Large Chemical Shielding Anisotropies

Matthias Bechmann, Xavier Helluy, and Angelika Sebald¹

Bayerisches Geoinstitut, Universität Bayreuth, D-95440 Bayreuth, Germany

Received October 30, 2000; revised May 24, 2001

Double-quantum filtration under rotational resonance MAS NMR conditions where the chemical shielding anisotropies involved exceed the differences in isotropic chemical shielding is considered by means of numerical simulations and ¹³C MAS NMR experiments. The responses of two different pulse sequences, suitable for double-quantum filtration specifically under rotational resonance conditions, to large chemical shielding anisotropies are compared. In the presence of large chemical shielding anisotropies a very recently introduced pulse sequence (T. Karlsson, M. Edén, H. Luthman, and M. H. Levitt, *J. Magn. Reson.* 145, 95–107, 2000) suffers losses in double-quantum-filtration efficiencies. The double-quantum-filtration efficiency of another pulse sequence (N. C. Nielsen, F. Creuzet, R. G. Griffin, and M. H. Levitt, *J. Chem. Phys.* 96, 5668–5677, 1992) is less afflicted by the presence of large chemical shielding anisotropies. Both sequences deliver double-quantum-filtered lineshapes that sensitively reflect chemical shielding tensor orientations. It is further shown that double-quantum-filtered rotational-resonance lineshapes of spin systems composed of more than two spins offer a suitable experimental approach for determining chemical shielding tensor orientations for cases where conventional rotational-resonance experiments are not applicable due to the presence of additional background resonances. © 2001 Academic Press

Key Words: MAS NMR; rotational resonance; double-quantum filtration; numerical simulations; ¹³C spin systems; chemical shielding tensors.

INTRODUCTION

Consider a scenario where magic-angle spinning (MAS) NMR techniques are faced with the task of determining a molecular conformational parameter. Further suppose that neither MAS NMR experiments designed for the determination of internuclear distances nor so-called double-quantum (DQ) heteronuclear local field (HLF) experiments (*I*) can solve the problem posed. As an example, consider a carboxylate group and its orientation in an organic molecule, in the absence of structural motifs that would enable DQ-HLF experiments. Obviously, measurements of internuclear ¹³C–¹³C distances are also unable

to reveal the orientation of this COO group in the molecule. To solve a task of this kind, MAS NMR must rely on ¹³C chemical shielding tensor orientations. Whenever reasonably accurate assumptions about the relationships between ¹³C chemical shielding tensor orientations and molecular geometries for a given class of compounds or molecular fragments can be made, knowledge of the mutual orientations of ¹³C chemical shielding tensors can be translated to the desired information about molecular conformations, for instance, about the orientation of a COO group in an organic molecule.

The rotational-resonance (*R*²) condition (2–8) makes information about chemical shielding tensor orientations in small, isolated homonuclear spin systems accessible in an experimentally straightforward manner. With a *R*² condition fulfilled (i.e., when the MAS frequency matches an integer multiple of the isotropic chemical shielding difference between two spins, $\omega_{iso}^{\Delta} \approx n\omega_r$, where *n* is a small integer), all anisotropic interactions are reintroduced into the *R*² MAS NMR spectra. It has been demonstrated that chemical shielding tensor orientations can be reliably extracted from *R*² lineshapes by iterative fitting approaches, based on numerically exact lineshape simulations (9–13). This conventional *R*² MAS NMR approach, however, is limited to cases where the (re)coupled spin system is spatially isolated in the crystal lattice and where no additional resonances interfere with the lineshape-analysis procedures. Combining the *R*² MAS NMR approach with double-quantum filtration (DQF) circumvents these severe restrictions on sample properties and considerably broadens the application range of lineshape-based one-dimensional MAS NMR experiments. Most of the currently known, quite numerous MAS NMR recoupling schemes (*I*) that may be employed for *R*²-DQF purposes suffer reductions in DQF efficiency as soon as nonnegligible chemical shielding anisotropies (*csa*) are involved. The presence of considerable *csa*, preferably under conditions of relatively slow MAS, however, forms the basis of a problem-solving strategy for the scenario mentioned above.

The purpose of this study is to investigate how well *csa* orientational parameters may be derived from experimental *R*²-DQF lineshapes. We will do so by means of numerical simulations and ¹³C MAS NMR experiments. Different ¹³C isotopomers of three different compounds will be used (see Fig. 1). The crystal

¹ To whom correspondence should be addressed. E-mail: angelika.sebald@uni-bayreuth.de.

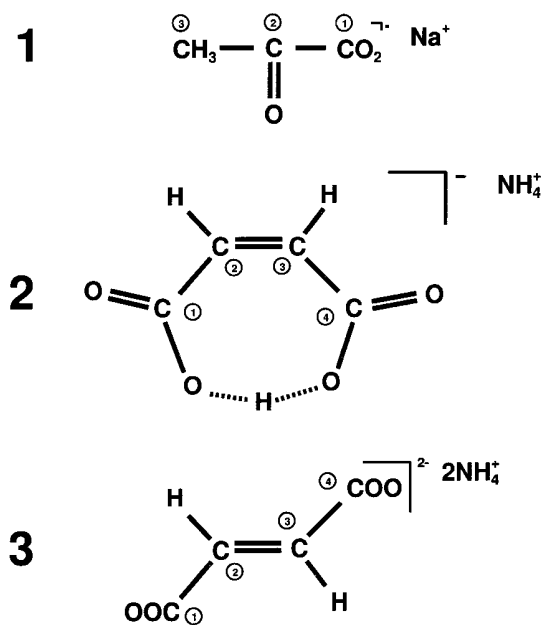


FIG. 1. Schematic representation of the molecular structures of **1**, **2**, and **3**; the numbering scheme of the carbon atoms is used throughout. It is identical to the numbering schemes in the description of the crystal structures of **1** (14) and **2** (15), but differs from that used in the description of the crystal structure of **3** (16).

structures of **1** (14), **2** (15), and **3** (16), as well as all parameters of the ^{13}C spin systems of **1** (12) and **2** (11) are known. The known parameters of the ^{13}C spin systems of **1** and **2** will serve to study the properties of two different R^2 -DQF pulse experiments (17, 18) in the presence of considerable csa. Criteria for the selection of these two pulse sequences were the ease and robustness of their experimental implementation, the absence of potentially limiting ^1H -decoupling requirements, and the narrowbandedness of the R^2 condition, which holds promise for some naturally occurring degrees of selectivity in multiple spin systems. Finally, we will determine the so far unknown ^{13}C chemical shielding tensor orientations of **3** from ^{13}C R^2 -DQF lineshapes of a fully ^{13}C -enriched sample of diammonium fumarate.

EXPERIMENTAL

Samples

The sodium pyruvate samples used in this study are commercially available (**1**, with ^{13}C in natural abundance (Aldrich Chemicals); **1-C1/C2**, selectively $^{13}\text{C}1$, $^{13}\text{C}2$ -enriched sodium pyruvate (Isotec Inc.)). The educts (maleic anhydride and fumaric acid: natural ^{13}C abundance (Aldrich Chemicals); $^{13}\text{C}2$, $^{13}\text{C}3$ -enriched, and fully ^{13}C -enriched (Isotec Inc. and CIL)) for the synthesis of various ^{13}C isotopomers of monoammonium maleate (**2**, with ^{13}C in natural abundance) and diammonium fumarate (**3**, with ^{13}C in natural abundance) are also commercially

available. **2-C2/C3** (selectively $^{13}\text{C}2$, $^{13}\text{C}3$ -enriched monoammonium maleate), **2-U ^{13}C** (fully ^{13}C -enriched monoammonium maleate), and **3-U ^{13}C** (fully ^{13}C -enriched diammonium fumarate) were synthesized by reacting the respective educts with the appropriate amounts of $(\text{NH}_4)(\text{HCO}_3)$ in aqueous solution under ambient conditions in the dark. In addition, isotopically diluted samples of almost all ^{13}C -enriched compounds were made by cocrystallization of the ^{13}C -enriched compounds with their counterparts with ^{13}C in natural abundance. The ratios of enriched to unenriched materials (by weight) are the following: **1-C1/C2_{dil}** 1 : 5, **2-U ^{13}C _{dil}** 1 : 9, **3-U ^{13}C _{dil}** 1 : 10. R^2 -DQF MAS NMR experiments were run on the diluted and undiluted ^{13}C -enriched samples. In all cases identical R^2 -DQF lineshapes for the diluted and undiluted ^{13}C -enriched samples were found. Consequently, the experimental lineshapes obtained from the undiluted ^{13}C -enriched samples were used as experimental data input in lineshape simulations.

^{13}C MAS NMR

^{13}C MAS NMR spectra were recorded on Bruker MSL 100, MSL 200, MSL 300, and DSX 500 NMR spectrometers. The corresponding ^{13}C Larmor frequencies $\omega_0/2\pi$ are -25.2 , -50.3 , -75.5 , and -125.8 MHz. The ^{13}C resonance of SiMe_4 serves as the 0 ppm reference of ^{13}C chemical shielding. MAS frequencies were generally in the range $\omega_r/2\pi = 0.8$ – 10.0 kHz and were actively controlled to within ± 2 Hz. Lineshapes of experimental ^{13}C MAS NMR spectra were checked to be identical when using either Hartmann-Hahn cross-polarization (CP) or ^{13}C single-pulse excitation. ^{13}C R^2 -DQF MAS NMR spectra of **3-U ^{13}C** for purposes of iterative lineshape fitting were recorded on the DSX 500 NMR spectrometer with ^{13}C $\pi/2$ pulse durations of $4.0 \mu\text{s}$ and TPPM (19) ^1H decoupling (amplitude of 83 kHz) applied throughout. ^{13}C MAS NMR experiments on the MSL 100 spectrometer employed 7 mm o.d. ZrO_2 rotors, $^{13}\text{C}\pi/2$ pulse durations of $4.0 \mu\text{s}$, and c.w. ^1H decoupling amplitudes of 62.5 kHz; on the MSL 200 and MSL 300 spectrometers, 4 mm o.d. ZrO_2 rotors, ^{13}C $\pi/2$ pulse durations of $3.5 \mu\text{s}$, and c.w. ^1H decoupling amplitudes of 71.4 kHz were used.

Two different pulse sequences for purposes of DQ filtration under R^2 conditions in the presence of considerable chemical shielding anisotropies will be considered. The two pulse sequences chosen are depicted in Fig. 2. Both sequences are experimentally straightforward and robust. The two sequences differ with respect to their highest possible DQF efficiencies in powder samples under ideal conditions, that is, in the presence of dipolar coupling and the absence of csa and isotropic J coupling. The sequence depicted in Fig. 2a (17) only depends on the powder angle β_{PR}^D and thus its highest theoretically possible DQF efficiency amounts to 73%. The sequence depicted in Fig. 2b (18) has an upper theoretical limit of its DQF efficiency of 50% due its orientation dependence on two angles, β_{PR}^D and γ_{PR}^D . For the sake of brevity, we will refer to the two pulse sequences as

TABLE 1
Typical Times [s] Required to Calculate R^2 -DQF Spectra
(See Text for Details) of 2-, 3-, and 4-Spin Systems^a

	2-spin system	3-spin system	4-spin system
Direct method, single processor	8016	<i>b</i>	<i>b</i>
Mixed method, single processor	291	1454	9395
Mixed method, parallel mode	23	100	654

^a See text for a description of the Linux cluster used. The savings in parallel mode are only slightly less than the values expected when dividing the single-processor-based durations by the number (16 in our case) of CPUs used.

^b Not determined.

(23) powder angles, a duration of $\tau = 1$ ms, and a FID lasting for 17 ms have been assumed. Some simulations reported in this study were carried out in single-processor mode, while calculations of error scans and planes, R^2 -DQF efficiency curves, and iterative lineshape fits employed parallel computing. For iterative minimizations, our simulation programs are combined with the optimization routines of the MINUIT package (34).

RESULTS AND DISCUSSION

The following is organized in three sections. The first section examines the performance of the R^2 -DQF $_{\beta}$ experiment ((17), Fig. 2a) in the presence of large chemical shielding anisotropies; this part takes advantage of the known parameters of the ^{13}C spin system in sodium pyruvate, **1** (12). The second section deals in a similar manner with the properties of the R^2 -DQF $_{\beta,\gamma}$ experiment ((18), Fig. 2b), including the $n = 0$ R^2 condition encountered in various, fully characterized, ^{13}C isotopomers of monoammonium maleate, **2** (11). The third section is devoted to the determination of the ^{13}C chemical shielding tensor orientations in the fumarate anion in diammonium fumarate, **3**, from ^{13}C R^2 -DQF $_{\beta,\gamma}$ lineshapes of **3**-U ^{13}C .

The R^2 -DQF $_{\beta}$ MAS NMR Experiment in the Presence of *c**s**a*

For the R^2 -DQF $_{\beta}$ MAS NMR experiment (17) it has been demonstrated that experimental lineshapes can be reproduced well numerically and reflect the anisotropic interaction parameters of a given spin system with similar sensitivities as the corresponding conventional R^2 lineshapes (12). This demonstration employed the $^{13}\text{C}2$ - $^{13}\text{C}3$ spin pair in selectively ^{13}C -labeled sodium pyruvate, **1-C2/C3**, under the $n = 1$ R^2 condition. This spin pair is characterized by a large difference in isotropic chemical shielding values ($\omega_{iso}^{\Delta_{23}} = 176.8$ ppm), and a small chemical shielding anisotropy of $^{13}\text{C}3$ ($\delta^{CS_3} = 0.14 \omega_{iso}^{\Delta_{23}}$). Under these conditions b_{23} is by far the most sensitively encoded parameter in the $n = 1$ R^2 as well as in the R^2 -DQF $_{\beta}$ lineshapes. In addition, for the parameters describing the spin pair in **1-C2/C3** a maximum $n = 1$ R^2 -DQF $_{\beta}$ efficiency of 47% was predicted numerically, while 35% were found experimentally (both at a Larmor frequency $\omega_0/2\pi = -50.3$ MHz).

We continue to use the ^{13}C spin system in solid sodium pyruvate, but now switch to **1-C1/C2**. The most prominent features of this spin pair are a large dipolar coupling constant b_{12} ($b_{12}/2\pi = -2004$ Hz), a small difference in isotropic chemical shielding ($\omega_{iso}^{\Delta_{12}} = 37.3$ ppm), and large *c**s**a* at both ^{13}C sites ($\delta^{CS_1} = 2.20\omega_{iso}^{\Delta_{12}}$, $\delta^{CS_2} = 2.95\omega_{iso}^{\Delta_{12}}$). Figure 3 displays a selection of different experimental R^2 -DQF $_{\beta}$ spectra of **1-C1/C2** in comparison with the corresponding simulated spectra, employing the known spin-pair parameters of **1-C1/C2** (12). The spectra shown in Fig. 3 emphasize two points: (i) The R^2 -DQF $_{\beta}$ lineshapes are very sensitive to the choice of the experimental parameter τ (while slight misjudgments of the pulse durations by up to ca. 0.3 μs are found to have no significant impact on the resulting lineshapes). (ii) The simulated spectra, based on the known parameters of the spin pair in **1-C1/C2**, reproduce well the experimentally observed R^2 -DQF $_{\beta}$ lineshapes. With our original goal in mind, that is, the determination of molecular conformations based on *c**s**a* tensor orientations, we need to examine in more detail how sensitively the Euler angles $\Omega_{PC}^{CS_i,j}$, $i, j = 1, 2$ are encoded in these lineshapes.

This examination follows a purely numerical approach and is illustrated in Fig. 4. First, a R^2 spectrum based on the experimentally determined best-fit parameters of the spin pair in **1-C1/C2** (12) is calculated, followed by one-dimensional error scans for each of the Euler angles $\Omega_{PC}^{CS_i,j}$. The resulting error curves for this

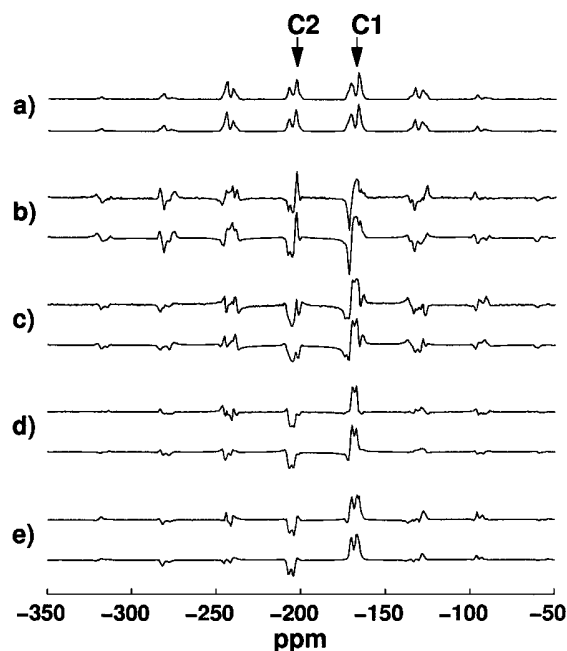


FIG. 3. Comparison of experimental (top traces) and simulated (bottom traces) ^{13}C $n=1$ R^2 and R^2 -DQF $_{\beta}$ lineshapes of the spin pair in **1-C1/C2** at $\omega_0/2\pi = -75.5$ MHz and $\omega_r/2\pi = 2793$ Hz; the simulations employ the known parameters of this spin pair (12). (a) Conventional R^2 spectra of **1-C1/C2**; arrows indicate the isotropic chemical shielding of $^{13}\text{C}1$, $^{13}\text{C}2$. (b-e) R^2 -DQF $_{\beta}$ spectra of **1-C1/C2**, where $\tau = 0.1$ ms (b), $\tau = 0.3$ ms (c), $\tau = 0.5$ ms (d), and $\tau = 0.7$ ms (e).

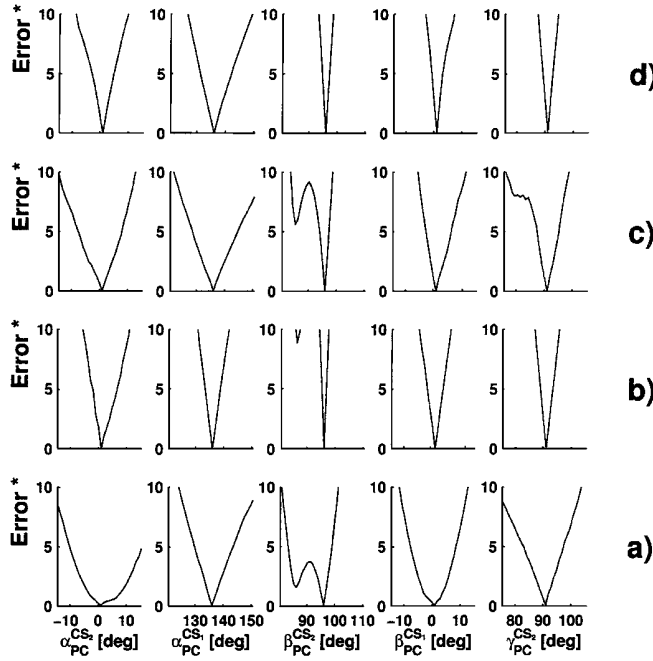


FIG. 4. One-dimensional error scans, illustrating the sensitivity of conventional $n = 1$ R^2 and R^2 -DQF $_{\beta}$ lineshapes to the Euler angles $\Omega_{PC}^{CS_{1,2}}$ in **1-C1/C2** at $\omega_0/2\pi = -75.5$ MHz and $\omega_r/2\pi = 2793$ Hz. The error scans are based on simulated spectra according to the parameters of the spin pair in **1-C1/C2**, so that each individual error scan addresses the situation where all other parameters are at precisely their optimum values. (a) Error scans for the conventional R^2 lineshape. (b–d) Error scans for the R^2 -DQF $_{\beta}$ lineshapes with $\tau = 0.1$ ms (b), $\tau = 0.7$ ms (c), and $\tau = 2.0$ ms (d). The vertical axes in the plots are defined as

$$\text{Error}^* = \sqrt{\frac{\sum_i [(s(i) - \text{ref}(i))]^2}{\sum_i [\text{ref}(i)]^2}} \cdot 100.$$

This purely numerical comparison can give only an impression of ideal circumstances, in the absence of any (unavoidable) experimental imperfections.

purely numerical conventional R^2 spectrum are shown in Fig. 4a as a reference. The same procedure is then carried out with several numerically simulated R^2 -DQF $_{\beta}$ spectra for a range of different values of τ . The one-dimensional error curves for the five Euler angles $\Omega_{PC}^{CS_{i,j}}$ resulting from these numerically generated R^2 -DQF $_{\beta}$ spectra are depicted in Figs. 4b–d. Obviously, these virtual experiments indicate that for a whole range of values τ the Euler angles $\Omega_{PC}^{CS_{i,j}}$ might be slightly more sensitively encoded in the R^2 -DQF $_{\beta}$ lineshapes than in the conventional R^2 lineshapes. In practice, based on lineshape fitting of real experimental R^2 -DQF $_{\beta}$ spectra, we have been unable to refine the csa orientational parameters of the spin pair in **1-C1/C2** beyond the precision previously obtained from conventional R^2 lineshapes (12).

As far as the sensitivities of the lineshape-fit parameters $\Omega_{PC}^{CS_{i,j}}$ are concerned, the R^2 -DQF $_{\beta}$ experiment in the presence of considerable csa's is promising, but less so when considering the achievable R^2 -DQF $_{\beta}$ efficiencies under these conditions. In Fig. 5a the R^2 -DQF $_{\beta}$ efficiencies for **1-C1/C2** are plotted as a function of τ , the expected simulated efficiency curve (—) is compared to the experimentally measured curve (○). The theo-

retically highest possible efficiency of 9% for this spin pair is predicted to occur at $\tau = 0.7$ ms, while 6% are reached experimentally. The strong fluctuations in R^2 -DQF $_{\beta}$ efficiency as a function of τ lead to relative maxima not only at or near values of τ that are multiples of the rotation period. This feature makes it rather difficult to select optimum experimental parameters in a realistic application situation, unless all parameters of the spin system are known in advance and the best choice of τ can thus be predicted from numerical simulations. A sharp drop in DQF efficiency accompanying the presence of nonnegligible csa from the theoretically highest possible efficiencies under “ideal circumstances” is nothing unique to the R^2 -DQF $_{\beta}$ experiment. This problem afflicts, more or less, many pulse sequences suitable for DQF experiments on polycrystalline powders under MAS conditions. When the R^2 -DQF $_{\beta}$ experiment was originally introduced (17), it was pointed out that the presence of csa will generally degrade the DQF efficiency of the experiment. It was further noted that replacing the first three-pulse subsequence (the inversion subsequence, see Fig. 2a) by more sophisticated inversion sequences might improve efficiency matters in the presence of csa. This idea can be tested by numerical simulations. Numerically it is easy to produce not just an improved, but a perfect, inversion condition at the beginning of the pulse sequence. As can be seen in Fig. 5b, again for the parameters of the **1-C1/C2** spin pair, an assumed perfect inversion situation smoothes the oscillations in the R^2 -DQF $_{\beta}$ efficiency as a function of τ , but only slightly boosts the overall R^2 -DQF $_{\beta}$ efficiency in the presence of large csa's.

For very trivial but important reasons of experimentally achievable signal-to-noise ratio, it is desirable to have additional experimental options where informative R^2 -DQF lineshapes are obtained with higher efficiencies in the presence of large csa's (i.e., when $\delta^{CS_{i,j}} \geq 2\omega_{iso}^{\Delta ij}$), and where it is easier to predict suitable experimental conditions without extensive advance knowledge of all spin-system parameters.

The R^2 -DQF $_{\beta,\gamma}$ MAS NMR Experiment in the Presence of csa

At a first glance, it may seem surprising that we explore the practical performance of the R^2 -DQF $_{\beta,\gamma}$ MAS NMR experiment (Fig. 2b), a pulse sequence that is characterized by a considerably lower limit (50%) of its highest theoretical R^2 -DQF efficiency under ideal circumstances (18). However, the presence of large chemical shielding anisotropies presents rather “nonideal circumstances,” leading to less obvious choices of the most suitable experimental approach.

Again, we take the ^{13}C spin pair in **1-C1/C2** as the model case. Figure 5c compares the numerically expected to the experimentally observed R^2 -DQF $_{\beta,\gamma}$ efficiencies for this spin pair, plotted as a function of τ . This comparison yields two arguments for the R^2 -DQF $_{\beta,\gamma}$ experiment for spin systems with large csa's. First, the optimum choice of experimental values τ is easily predictable, as maxima of the DQF efficiency occur only for values of τ very close to integer multiples of the rotation

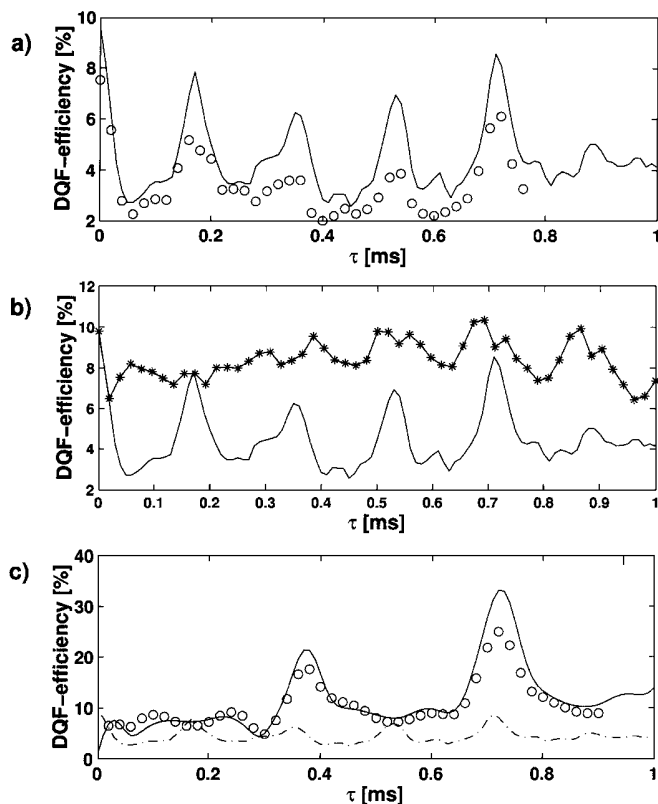


FIG. 5. Numerically predicted and experimentally observed ^{13}C R^2 -DQF efficiencies for the ^{13}C spin pair in **1-C1/C2** at $\omega_0/2\pi = -75.5$ MHz and $\omega_r/2\pi = 2793$ Hz. (a) Plot of numerically predicted (—) and experimentally observed (○) $n = 1$ R^2 -DQF $_{\beta}$ efficiencies as a function of τ . (b) Plot of numerically predicted R^2 -DQF $_{\beta}$ efficiencies as a function of τ , where (—) refers to assuming the three-pulse inversion subsequence (see Fig. 2a) inverting the less shielded $^{13}\text{C}2$ resonance, and (*) refers to assuming perfect inversion at the beginning of the pulse sequence. (c) Plot of numerically predicted (—) and experimentally observed (○) $n = 1$ R^2 -DQF $_{\beta,\gamma}$ efficiencies as a function of τ . Also shown are the corresponding numerically predicted (---) $n = 1$ R^2 -DQF $_{\beta}$ efficiencies.

period. Second, the efficiency maxima are considerably higher than for the R^2 -DQF $_{\beta}$ MAS NMR experiment under otherwise identical conditions. The highest R^2 -DQF $_{\beta,\gamma}$ efficiencies for the ^{13}C spin pair in **1-C1/C2** (33% theoretical, 26% experimental at $\tau = 0.72$ ms and $\omega_0/2\pi = -75.5$ MHz; see Fig. 5c) are quite reasonable. Experimental ^{13}C R^2 -DQF $_{\beta,\gamma}$ lineshapes of

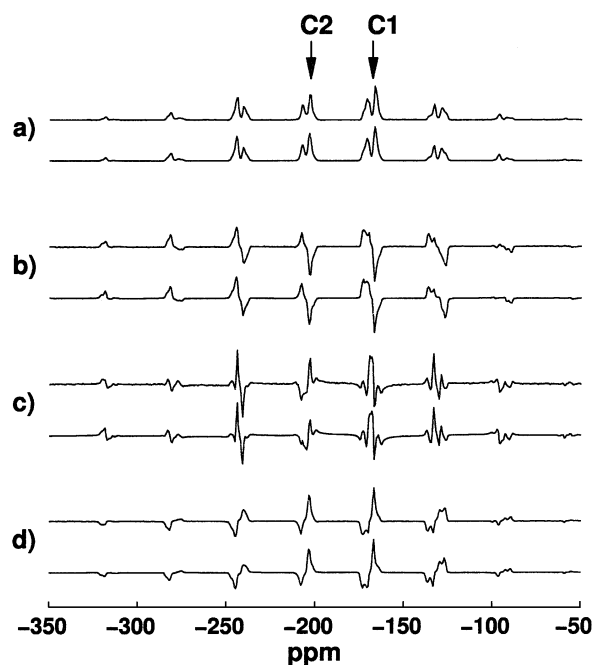


FIG. 6. Comparison of experimental (top traces) and simulated (bottom traces) ^{13}C $n = 1$ R^2 and R^2 -DQF $_{\beta,\gamma}$ lineshapes of the spin pair in **1-C1/C2** at $\omega_0/2\pi = -75.5$ MHz and $\omega_r/2\pi = 2793$ Hz; the simulations employ the known parameters of this spin pair (12). (a) Conventional R^2 spectra of **1-C1/C2**; arrows indicate the isotropic chemical shielding of $^{13}\text{C}1$, $^{13}\text{C}2$. (b–d) R^2 -DQF $_{\beta,\gamma}$ spectra of **1-C1/C2**, where $\tau = 0.36$ ms (b), $\tau = 0.54$ ms (c), and $\tau = 0.72$ ms (d).

1-C1/C2 are well reproduced numerically by the known parameters of this spin pair, as can be seen in Fig. 6. Closer inspection of the sensitivity of the R^2 -DQF $_{\beta,\gamma}$ lineshapes to the $^{13}\text{C}1$, $^{13}\text{C}2$ chemical shielding tensor orientations in **1-C1/C2** reveals that the Euler angles $\Omega_{PC}^{CS_{1,2}}$ are about equally sensitively encoded as in the corresponding conventional R^2 lineshapes. This comparison is depicted in Fig. 7, where the purely numerical exploration from Fig. 4, employing the parameters of the ^{13}C spin pair in **1-C1/C2** for the calculation of one-dimensional error scans is now extended to include the R^2 -DQF $_{\beta,\gamma}$ lineshapes and their sensitivities to chemical shielding tensor orientations.

Another useful feature of the R^2 -DQF $_{\beta,\gamma}$ experiment is that it also works under the $n = 0$ R^2 condition, as was already

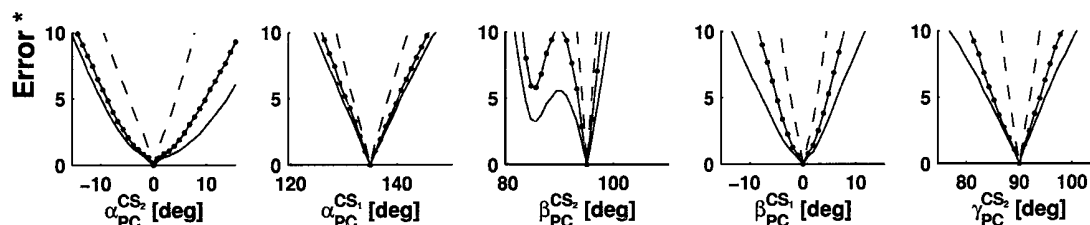


FIG. 7. One-dimensional error scans, illustrating the sensitivity of conventional $n = 1$ R^2 (—), R^2 -DQF $_{\beta,\gamma}$ (---), and R^2 -DQF $_{\beta}$ (· · ·) lineshapes to the Euler angles $\Omega_{PC}^{CS_{1,2}}$ in **1-C1/C2** at $\omega_0/2\pi = -75.5$ MHz and $\omega_r/2\pi = 2793$ Hz. The procedure is the same as described in the legend of Fig. 4. The error curves are calculated for values of $\tau = 0.30$ ms for the R^2 -DQF $_{\beta}$ sequence and $\tau = 0.72$ ms for the R^2 -DQF $_{\beta,\gamma}$ sequence.

demonstrated for the ^{13}C spin pair in diammonium oxalate monohydrate in the original paper describing the experiment (18), with roughly 15% R^2 -DQF $_{\beta,\gamma}$ efficiency reported for this spin pair at a relatively low MAS frequency ($\omega_0/2\pi = -79.9$ MHz, $\omega_r/2\pi = 1560$ Hz, $\tau = 2\tau_r = 1.28$ ms). Another $n = 0$ R^2 case is encountered in the ^{13}C spin pair in the maleate

anion in **2-C2/C3**: here the two ^{13}C chemical shielding tensors are related by mirror-plane symmetry, in the former spin pair a twofold symmetry axis relates the two sites. The known parameters of the spin pair in **2-C2/C3** (11) yield simulations of R^2 -DQF $_{\beta,\gamma}$ spectra that match the experimentally observed line-shapes very well (see Fig. 8a). Also under the $n = 0$ R^2 condition

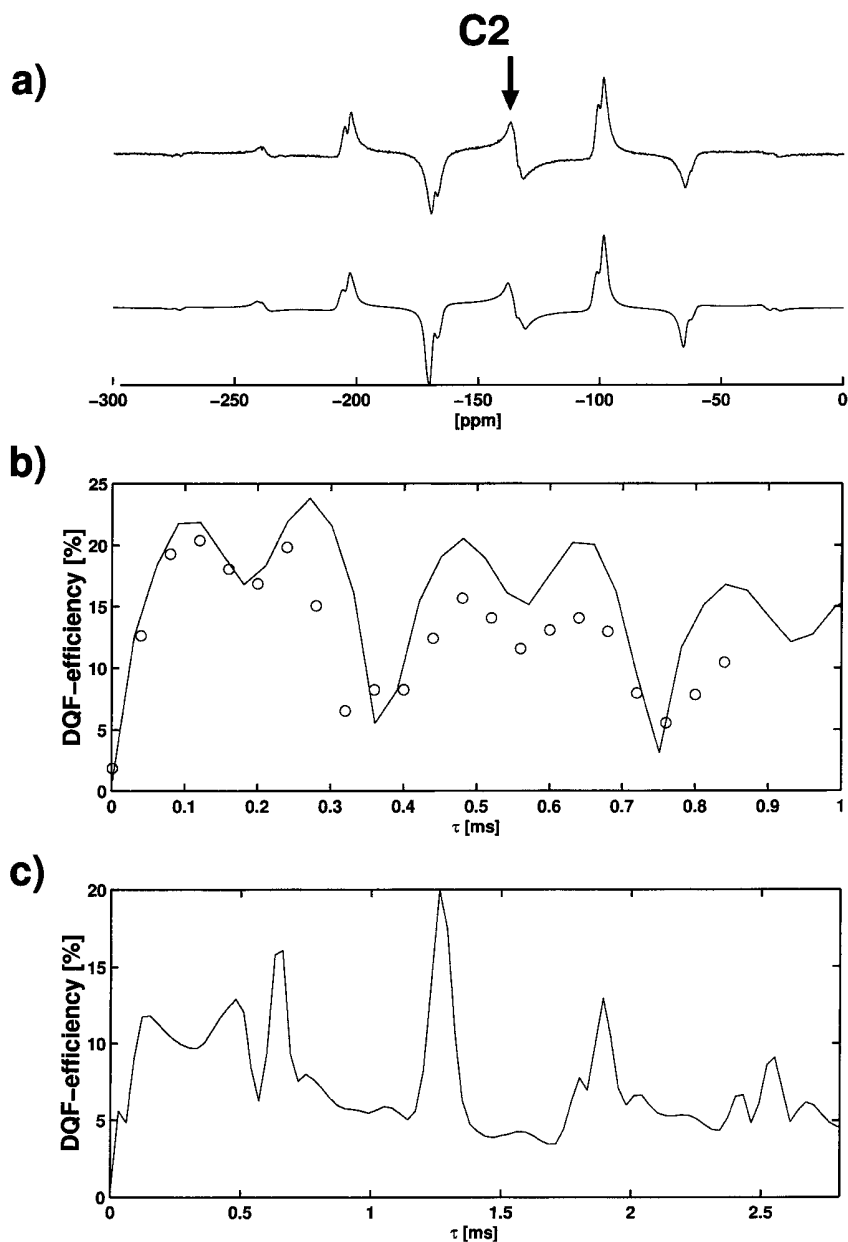


FIG. 8. ^{13}C R^2 -DQF $_{\beta,\gamma}$ experiments at the $n = 0$ R^2 condition. (a) Experimental (top) and simulated (bottom) $n = 0$ R^2 -DQF $_{\beta,\gamma}$ spectra of **2-C2/C3** at $\omega_0/2\pi = -75.5$ MHz, $\omega_r/2\pi = 2626$ Hz, and $\tau = 0.12$ ms; the simulation employs the known parameters of this spin pair (11), the arrow indicates the isotropic $^{13}\text{C}_2$, $^{13}\text{C}_3$ chemical shielding. (b) Numerically predicted (\rightarrow) and experimentally observed (\circ) $n = 0$ R^2 -DQF $_{\beta,\gamma}$ efficiencies as a function of τ , for **2-C2/C3** at $\omega_0/2\pi = -75.5$ MHz and $\omega_r/2\pi = 2626$ Hz; note the mirror-plane symmetry of **2-C2/C3** and the minima in the R^2 -DQF efficiency at $\tau = N\tau_r$. (c) Numerically predicted R^2 -DQF $_{\beta,\gamma}$ efficiencies as a function of τ , for the ^{13}C spin pair in diammonium oxalate monohydrate (18); note the C_2 symmetry of this spin system and the occurrence of maxima in the R^2 -DQF efficiency at $\tau = N\tau_r$.

in the presence of large c_{sa} 's, fairly high R^2 -DQF $_{\beta,\gamma}$ efficiencies can be achieved, but under the $n=0$ R^2 condition the maxima in the efficiency as a function of τ are less obviously related to the rotation period than under the $n=1$ R^2 condition (35). This is illustrated in Figs. 8b and c. In Fig. 8b the theoretically expected (\rightarrow) and the experimentally observed (\circ) R^2 -DQF $_{\beta,\gamma}$ efficiencies for the **2-C2/C3** spin pair are plotted as a function of τ . Under the $n=0$ R^2 condition involving mirror-plane symmetry, the efficiency is minimal at τ values that are integer multiples, N of the rotation period τ_r . In contrast, the $n=0$ R^2 condition involving C_2 symmetry yields maxima of the efficiency when $\tau = N\tau_r$. This is shown in Fig. 8c, where the theoretically expected R^2 -DQF $_{\beta,\gamma}$ efficiency as a function of τ is plotted for the ^{13}C spin pair in diammonium oxalate monohydrate (18).

In **2-U ^{13}C** , the $^{13}\text{C}1$ - $^{13}\text{C}4$ and the $^{13}\text{C}2$ - $^{13}\text{C}3$ pairs always fulfill the $n=0$ R^2 condition due to the molecular mirror-plane symmetry. If the MAS frequency is chosen such that $\omega_r/2\pi$ fulfills in addition the $n=1$ or $n=2$ R^2 condition between $^{13}\text{C}1$ - $^{13}\text{C}2$ and $^{13}\text{C}3$ - $^{13}\text{C}4$, the resulting conventional ^{13}C R^2 lineshapes sensitively reflect all Euler angles $\Omega_{PC}^{CS_{1,2}}$ in this ^{13}C 4-spin system. The ^{13}C chemical shielding tensor orientations in **2-U ^{13}C** deviate slightly, but significantly from the typically assumed orientations. For instance, the directions of the most shielded $^{13}\text{C}1$, $^{13}\text{C}2$ tensor components are not exactly perpendicular to the molecular plane, and the directions of the intermediate shielded $^{13}\text{C}1$, $^{13}\text{C}2$ tensor components deviate slightly from the $^{13}\text{C}1=\text{O}$ and $^{13}\text{C}2=\text{C}3$ bond directions, respectively (11). These minor deviations from the "typical ^{13}C shielding tensor orientation" are sensitively reflected in the conventional $n=2$ R^2 spectral lineshapes of **2-U ^{13}C** . This is also true for the corresponding R^2 -DQF $_{\beta,\gamma}$ lineshapes. Figure 9a depicts an experimental R^2 -DQF $_{\beta,\gamma}$ spectrum of **2-U ^{13}C** , obtained at $\omega_0/2\pi = -125.8$ MHz under the $n=2$ R^2 condition with $\tau = 0.453$ ms. The corresponding simulated spectrum in Fig. 9b is based on the best-fit values of the Euler angles $\Omega_{PC}^{CS_{1,2}}$ previously obtained from conventional $n=2$ R^2 spectral lineshapes of **2-U ^{13}C** (11), the simulated spectrum in Fig. 9c assumes Euler angles $\Omega_{PC}^{CS_{1,2}}$ such that the "typical orientation scenario" would be precisely realized (i.e., the directions of the most shielded tensor components are taken as exactly perpendicular to the molecular plane, and the directions of the intermediate tensor components are assumed to be precisely collinear with the C=C and C=O bond directions, respectively). Clearly, the two simulated R^2 -DQF $_{\beta,\gamma}$ spectra are significantly different, despite the relative small differences in Euler angles $\Omega_{PC}^{CS_{1,2}}$ between them. The simulated spectrum in Fig. 9b agrees much better with the experimental R^2 -DQF $_{\beta,\gamma}$ spectrum than the typical orientation scenario simulation in Fig. 9c. Obviously, experimental R^2 -DQF $_{\beta,\gamma}$ spectra not only of spin pairs but also of spin systems composed of more than two spins may well serve as the starting point for the determination of chemical shielding tensor orientations.

The ^{13}C Chemical Shielding Tensors in Diammonium Fumarate, **3**

The ^{13}C chemical shielding tensor orientations in diammonium fumarate, **3**, are not known, but various ^{13}C isotopomers of diammonium fumarate have been adopted as model compounds to illustrate the performance of novel MAS NMR pulse sequences and recoupling schemes (36–39). The crystal structure of **3** (16) explains the difficulties in determining the chemical shielding tensor orientations for **3** by means of conventional ^{13}C R^2 MAS NMR experiments. The fumarate anion in solid **3** possesses a center of inversion symmetry, which renders ^{13}C MAS NMR spectra of the pairwise labeled $^{13}\text{C}1$, $^{13}\text{C}4$ and $^{13}\text{C}2$, $^{13}\text{C}3$ isotopomers uninformative regarding the ^{13}C chemical shielding tensor orientations. Further, the limited mutual spatial isolation of the fumarate anions in the crystal lattice of **3** *a priori* discourages the use of undiluted ^{13}C -labeled isotopomers of **3**. The fully ^{13}C enriched fumarate moiety in **3-U ^{13}C** (and/or **3-U $^{13}\text{C}_{\text{dil}}$**) lifts the symmetry-related problems with the pairwise ^{13}C -labeled isotopomers of **3**. A modest difference in isotropic ^{13}C chemical shielding $\omega_{iso}^{\Delta_{12}} = \omega_{iso}^{\Delta_{34}} = 35.6$ ppm in **3** makes $n=1, 2$ R^2 conditions experimentally accessible, where the lineshapes sensitively reflect the ^{13}C chemical shielding tensor orientations. While conventional ^{13}C R^2 lineshapes of **3-U $^{13}\text{C}_{\text{dil}}$** are not suitable for purposes of iterative lineshape fitting, the corresponding R^2 -DQF lineshapes eliminate the problem of natural-abundance ^{13}C background resonances. Above we have demonstrated that indeed the (known) ^{13}C chemical shielding tensor orientations of the closely related ^{13}C 4-spin system in **2-U ^{13}C** are sensitively encoded in the R^2 -DQF lineshapes. We are now ready to determine the ^{13}C chemical shielding tensor orientations in the fumarate moiety of diammonium fumarate.

Of the numerous parameters characterizing the ^{13}C 4-spin system in **3-U ^{13}C** , many can be determined independently. The known crystal structure of **3** (16) yields magnitudes and orientations of the dipolar coupling interaction tensors $\omega^{D_{ij}}$, while solution-state ^{13}C NMR spectra of **3-U ^{13}C** provide the values of the isotropic J -coupling constants (see Table 2). Isotropic ^{13}C chemical shielding values and the magnitudes of the ^{13}C chemical shielding tensors are obtained from ^{13}C MAS NMR experiments on **3** (see Table 3). The inversion symmetry of the fumarate anion in **3** reduces the number of Euler angles, needed to describe the orientation of the four ^{13}C chemical shielding tensors, to six ($\alpha_{PC}^{CS_i}, \beta_{PC}^{CS_i}, \gamma_{PC}^{CS_i}; i = 1, 2$). These are the remaining six unknown parameters which must be determined by iterative fitting of ^{13}C R^2 -DQF lineshapes. The very first practical step is devoted to the decision whether or not ^{13}C R^2 -DQF spectra of the undiluted sample **3-U ^{13}C** can serve as experimental input data for the numerical minimization. Experimentally we find identical R^2 -DQF lineshapes for **3-U ^{13}C** and **3-U $^{13}\text{C}_{\text{dil}}$** under a variety of experimental conditions. Accordingly, experimental ^{13}C R^2 -DQF spectra of **3-U ^{13}C** may serve as experimental input

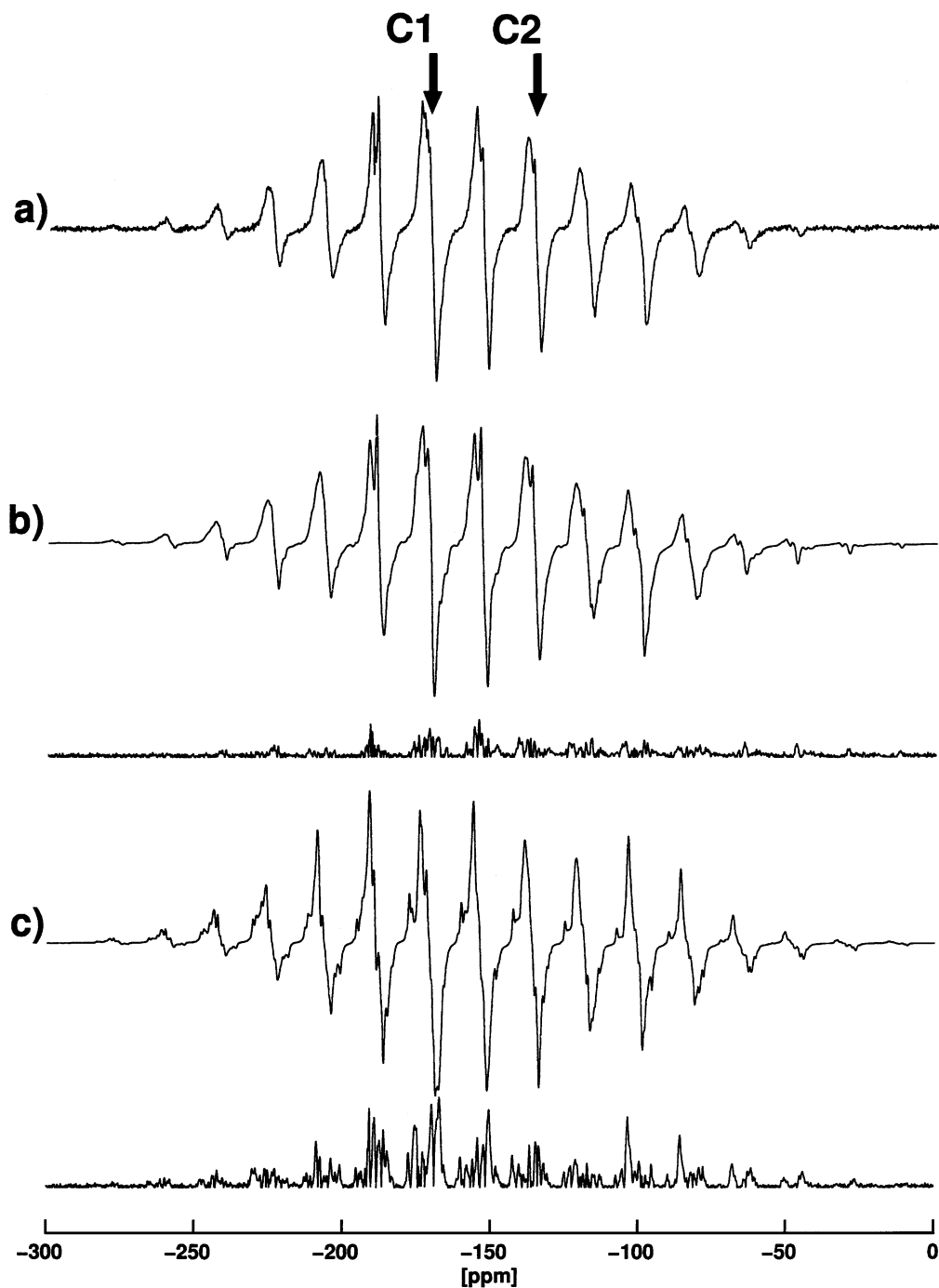


FIG. 9. Comparison of experimental (a) and simulated (b, c) ^{13}C $n = 2$ R^2 -DQF $_{\beta,\gamma}$ spectra of $2\text{-U}^{13}\text{C}$ at $\omega_0/2\pi = -125.8$ MHz, $\omega_r/2\pi = 2207$ Hz, and $\tau = 0.453$ ms; the arrows indicate the $^{13}\text{C}2$, $^{13}\text{C}3$ and $^{13}\text{C}1$, $^{13}\text{C}4$ isotropic chemical shielding regions. The simulated spectrum b is based on the best-fit ^{13}C chemical shielding tensor orientations derived from conventional $n = 2$ R^2 spectra of $2\text{-U}^{13}\text{C}$ (11). The simulated spectrum c assumes Euler angles $\Omega_{PC}^{CSi,j}$ corresponding to the “typical csa orientation” scenario (see text). Also shown are the difference curves between experimental and calculated spectra a, b, and a, c, respectively.

data. The results of subsequent iterative lineshape fits are summarized in Table 3 and Fig. 10. The experimental R^2 -DQF $_{\beta,\gamma}$ spectrum of $3\text{-U}^{13}\text{C}$, obtained at $\omega_0/2\pi = -125.8$ MHz under the $n = 2$ R^2 condition with $\tau = 0.446$ ms (Fig. 10a) agrees very

well with the simulated spectrum, based on the best-fit values of $\Omega_{PC}^{CS1,2}$ (Fig. 10b). The simulated spectrum, based on a typical csa orientation assumption (Fig. 10c) disagrees significantly with the spectra shown in Figs. 10a and b, even though the best-fit

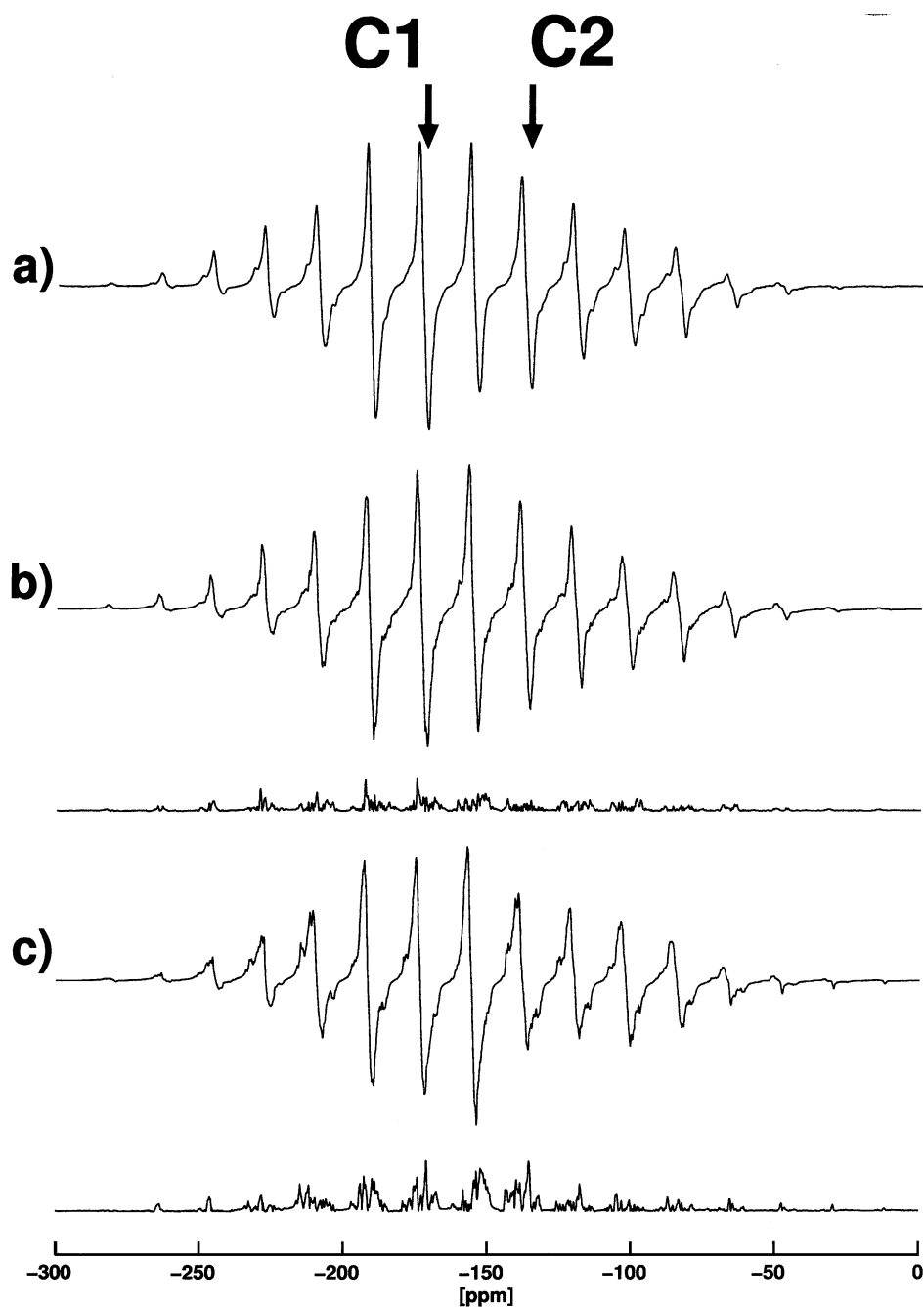


FIG. 10. Comparison of experimental (a) and simulated (b, c) ^{13}C $n = 2$ R^2 -DQF $_{\beta,\gamma}$ spectra of $3\text{-U}^{13}\text{C}$ at $\omega_0/2\pi = -125.8$ MHz, $\omega_r/2\pi = 2240$ Hz, and $\tau = 0.446$ ms; the arrows indicate the $^{13}\text{C}1$, $^{13}\text{C}4$ and $^{13}\text{C}2$, $^{13}\text{C}3$ isotropic chemical shielding regions. The simulated spectrum b is based on the best-fit ^{13}C chemical shielding tensor orientations derived from the experimental spectrum a. The simulated spectrum c assumes Euler angles $\Omega_{PC}^{CS_{i,j}}$ corresponding precisely to a “typical csa orientation” scenario. Also shown are the difference curves between experimental and calculated spectra a, b, and a, c, respectively.

values of $\Omega_{PC}^{CS_{1,2}}$ do not deviate much from the Euler angles corresponding to the typical csa orientations (see Table 3). In addition, the best-fit values of $\Omega_{PC}^{CS_{1,2}}$ equally well reproduce experimental R^2 -DQF spectra of $3\text{-U}^{13}\text{C}$ obtained under other experimental conditions. Figures 9 and 10 underscore the importance of a very

good signal-to-noise ratio in experimental spectra that serve for purposes of iterative lineshape fitting. Figures 9 and 10 further illustrate the similarities of the four- ^{13}C spin systems in $2\text{-U}^{13}\text{C}$ and $3\text{-U}^{13}\text{C}$: in both cases the R^2 -DQF lineshapes reveal small, but significant, deviations of the ^{13}C chemical shielding tensor

TABLE 2
Direct and Indirect Dipolar $^{13}\text{C}_i\text{--}^{13}\text{C}_j$ Couplings
in Diammonium Fumarate, **3**

	$ij = 12$ or 34	$ij = 13$ or 24	$ij = 23$	$i, j = 14$
$b_{ij}/2\pi$ [Hz] ^a	−2274	−500	−3355	−130
β_{PC}^D [°] ^{a,b}	+56.3	+30.1	0	+39.9
ω_{ij}^{iso} [Hz] ^c	+64.5	+1.5	+68.0	(±)7.0

^a Calculated from the known crystal structure of **3** (16).

^b Taking $\Omega_{PC}^{D_{23}} = (0, 0, 0)$.

^c Determined by solution-state ^{13}C NMR of an aqueous solution of **3- U^{13}C** (Larmor frequency $\omega_0/2\pi = -125.8$ MHz, Bruker DRX 500 NMR spectrometer).

orientations from the typical csa orientations scenario. In relation to the geometry of the fumarate anion in **3**, the best-fit values of the Euler angles $\Omega_{PC}^{\text{CS}_{1,2}}$ describe the following ^{13}C chemical shielding tensor orientations. The directions of the most shielded components of the $^{13}\text{C}_1/^{13}\text{C}_4$ and $^{13}\text{C}_2/^{13}\text{C}_3$ shielding tensors both deviate from being perpendicular to the molecular C1–C2–C3–C4 plane by 15 and 25°, respectively. The direction of the least shielded component of the $^{13}\text{C}_1/^{13}\text{C}_4$ shielding tensors subtends an angle of 11° with the C1–C2 and C3–C4 bond directions, respectively. The direction of the least shielded component of the $^{13}\text{C}_2/^{13}\text{C}_3$ shielding tensors is nearly perpendicular to the C2=C3 bond direction (102°) and nearly lies in the molecular plane (within 8°). The direction of the intermediate shielded component of the $^{13}\text{C}_2/^{13}\text{C}_3$ shielding tensors deviates by 28° from being collinear with the C2=C3 bond direction.

TABLE 3
 ^{13}C Chemical Shielding in Diammonium Fumarate, **3**

	$^{13}\text{C}_1, ^{13}\text{C}_4$	$^{13}\text{C}_2, ^{13}\text{C}_3$
$\omega_{\text{iso}}^{\text{CS}}$ [ppm]	−173.6	−138.0
δ^{CS} [ppm]	64.8	−94.2
η^{CS}	0.82	0.59
$\alpha_{PC_{23}}^{\text{CS}}$ [°] ^a	−126 ± 28 ^b	−65 ± 30 ^b
$\beta_{PC_{23}}^{\text{CS}}$ [°] ^a	−75 ± 28 ^c	−102 ± 13
$\gamma_{PC_{23}}^{\text{CS}}$ [°] ^a	−93 ± 12	+9 ± 12

^a Euler angles $\Omega_{PC_{23}}^{\text{CS}}$ relate to the principal axis system of the $^{13}\text{C}_2\text{--}^{13}\text{C}_3$ dipolar coupling tensor as the CAS, with its y axis defined as perpendicular to the molecular C1–C2–C3–C4 plane. $^{13}\text{C}_1/^{13}\text{C}_4$ (and $^{13}\text{C}_2/^{13}\text{C}_3$) in the fumarate anion of **3** are related by inversion symmetry (16), implying identical orientations of the $^{13}\text{C}_1/^{13}\text{C}_4$ (and $^{13}\text{C}_2/^{13}\text{C}_3$) chemical shielding tensor directions. The “typical csa orientations” in the fumarate anion of **3** would correspond to Euler angles $\Omega_{PC_{23}}^{\text{CS}_1} = (-124, -90, -90)$ and $\Omega_{PC_{23}}^{\text{CS}_2} = (-90, -90, 0)$. Uncertainties of the best-fit values $\Omega_{PC_{23}}^{\text{CS}}$ are quoted for the range spanning $2e_{\text{min}}^2$ in one-dimensional error scans of each of the individual best-fit parameters.

^b The error curve in the $2e_{\text{min}}^2$ minimum region in one-dimensional error scans of this parameter is broad and featureless.

^c The error curve in the $2e_{\text{min}}^2$ minimum region in one-dimensional error scans of this parameter displays a sharp (−75 ± 8°) minimum within a broader curve.

SUMMARY

In concluding, we briefly summarize, in our view, the most important findings of our combined numerical and experimental study.

1. The $R^2\text{-DQF}_\beta$ and $R^2\text{-DQF}_{\beta,\gamma}$ pulse sequences (17, 18) have experimental and numerical robustness and ease in common.

2. Both pulse sequences considerably expand the practical range of spin systems on which R^2 experiments may be successfully carried out in terms of lineshape simulations but where conventional R^2 lineshapes cannot be used. A general area of application where this is important is, for instance, MAS NMR applications on inorganic solids with spin-1/2 isotopes in low natural abundance (40).

3. The $R^2\text{-DQF}_\beta$ and $R^2\text{-DQF}_{\beta,\gamma}$ pulse sequences complement each other. In the presence of large chemical shielding anisotropies and modest differences in isotropic chemical shielding, the $R^2\text{-DQF}_{\beta,\gamma}$ sequence (18) is the preferable experimental choice for the determination of chemical shielding tensor orientations from $R^2\text{-DQF}$ lineshapes. The $R^2\text{-DQF}_\beta$ sequence (17) works best where large isotropic chemical shielding differences and small chemical shielding anisotropies are involved, especially including cases with relative small dipolar coupling constants (12, 17), and thus is the preferable experimental tool when aiming at the determination of internuclear distances in such spin systems.

4. Provided sufficiently fast and exact numerical methods are available, $R^2\text{-DQF}$ experiments can be expanded, in a quantitative and reliable manner, to spin systems composed of more than two spins.

5. Finally, it should be noted that both pulse sequences preserve the narrowbandedness and, hence, selectivity, of the correspondin conventional R^2 condition in multiple-spin systems (41).

ACKNOWLEDGMENTS

Financial support of our work by the Deutsche Forschungsgemeinschaft and Aventis Pharma, Paris, France, is gratefully acknowledged. We thank Bruker Analytik GmbH, Rheinstetten, for generous access to the DSX 500 NMR spectrometer, and in particular S. Steuernagel for experimental support. We thank H. Maisel, Bayreuth, for the synthesis of all fumaric and maleic acid salts used in this study, and B. Wrackmeyer, Bayreuth, for recording solution-state ^{13}C NMR spectra of **3- U^{13}C** . Last but not least we thank S. Dusold, Bayreuth, for scientific discussions, for his support in the early stages and his continued interest in the later stages of this project.

REFERENCES

- For general review articles on recoupling methods under MAS NMR conditions see: (i) A. E. Bennett, R. G. Griffin, and S. Vega, Recoupling of homo- and heteronuclear dipolar interactions in rotating solids, in “Solid-State NMR IV: Methods and Applications of Solid-State NMR,” Vol. 33, “NMR Basic Principles and Progress” (B. Blülich, Ed.), pp. 1–78, Springer

- Verlag, Berlin (1994); (ii) S. Dusold and A. Sebald, Dipolar recoupling under magic-angle-spinning conditions, in "Annual Reports on NMR Spectroscopy" (G. Webb, Ed.), Vol. 41, pp. 185–264, Academic Press, London (2000), and references given therein.
2. E. R. Andrew, A. Bradbury, R. G. Eades, and V. T. Wynn, Nuclear cross relaxation induced by specimen rotation, *Phys. Lett.* **4**, 99–100 (1963).
 3. D. P. Raleigh, M. H. Levitt, and R. G. Griffin, Rotational resonance in solid state NMR, *Chem. Phys. Lett.* **146**, 71–76 (1988).
 4. M. H. Levitt, D. P. Raleigh, F. Creuzet, and R. G. Griffin, Theory and simulations of homonuclear spin pairs in rotating solids, *J. Chem. Phys.* **92**, 6347–6364 (1990).
 5. A. Kubo and C. A. McDowell, One- and two-dimensional ^{31}P cross-polarization magic-angle-spinning nuclear magnetic resonance studies on two-spin systems with homonuclear dipolar and J coupling, *J. Chem. Phys.* **92**, 7156–7170 (1990).
 6. A. Schmidt and S. Vega, The Floquet theory of nuclear magnetic resonance spectroscopy of single spins and dipolar coupled spin pairs in rotating solids, *J. Chem. Phys.* **96**, 2655–2680 (1992).
 7. T. Nakai and C. A. McDowell, An analysis of NMR spinning sidebands of homonuclear two-spin systems using Floquet theory, *Mol. Phys.* **77**, 569–584 (1992).
 8. T. Nakai and C. A. McDowell, Application of Floquet theory to the nuclear magnetic resonance spectra of homonuclear two-spin systems in rotating solids, *J. Chem. Phys.* **96**, 3452–3466 (1992).
 9. S. Dusold, E. Klaus, A. Sebald, M. Bak, and N. C. Nielsen, Magnitudes and relative orientations of chemical shielding, dipolar, and J coupling tensors for isolated ^{31}P - ^{31}P spin pairs determined by iterative fitting of ^{31}P MAS NMR spectra, *J. Am. Chem. Soc.* **119**, 7121–7129 (1997).
 10. S. Dusold, W. Milius, and A. Sebald, Iterative lineshape fitting of MAS NMR spectra: A tool to investigate homonuclear J couplings in isolated spin pairs, *J. Magn. Reson.* **135**, 500–513 (1998).
 11. S. Dusold, H. Maisel, and A. Sebald, Magnitudes and orientations of interaction tensors determined from rotational resonance MAS NMR lineshapes of a four- ^{13}C spin system, *J. Magn. Reson.* **141**, 78–90 (1999).
 12. S. Dusold and A. Sebald, Double-quantum filtration under rotational-resonance conditions: Numerical simulations and experimental results, *J. Magn. Reson.* **145**, 340–356 (2000).
 13. D. L. Bryce and R. E. Wasylshen, *J. Phys. Chem. A* **104**, 7700–7710 (2000).
 14. W. Rach, G. Kiel, and G. Gattow, Untersuchungen über Salze der Pyruvinsäure. 2. Kristallstruktur von Kaliumpyruvat, Neubestimmung der Struktur von Natriumpyruvat, *Z. Anorg. Allg. Chem.* **563**, 87–95 (1988).
 15. L. Golic and I. Leban, The crystal structure of ammonium hydrogen maleate, *Croat. Chim. Acta* **55**, 41–45 (1982).
 16. H. Hosomi, Y. Ito, and S. Ohba, Ammonium and isopropylammonium salts of the fumaric acid dianion, *Acta Cryst. C* **54**, 142–145 (1998).
 17. T. Karlsson, M. Edén, H. Luthman, and M. H. Levitt, Efficient double-quantum excitation in rotational resonance NMR, *J. Magn. Reson.* **145**, 95–107 (2000).
 18. N. C. Nielsen, F. Creuzet, R. G. Griffin, and M. H. Levitt, Enhanced double-quantum nuclear magnetic resonance in spinning solids at rotational resonance, *J. Chem. Phys.* **96**, 5668–5677 (1992).
 19. A. E. Bennett, C. M. Rienstra, M. Auger, K. V. Lakshmi, and R. G. Griffin, Heteronuclear decoupling in rotating solids, *J. Chem. Phys.* **103**, 6951–6958 (1995).
 20. M. H. Levitt, The signs of frequencies and phases in NMR, *J. Magn. Reson.* **126**, 164–182 (1997).
 21. U. Haeberlen, High resolution NMR in solids. Selective averaging, in "Advances in Magnetic Resonance" (J. S. Waugh, Ed.), Suppl. 1, Academic Press, New York (1976).
 22. A. R. Edmonds, "Angular Momentum in Quantum Mechanics," Princeton Univ. Press, Princeton, NJ (1974).
 23. M. Bak and N. C. Nielsen, REPULSION, a novel approach to efficient powder averaging in solid-state NMR, *J. Magn. Reson.* **125**, 132–139 (1997).
 24. M. Edén and M. H. Levitt, Computation of orientational averages in solid state NMR by Gaussian spherical quadrature, *J. Magn. Reson.* **132**, 220–239 (1998).
 25. S. A. Smith, T. O. Levante, B. H. Meier, and R. R. Ernst, Computer simulations in magnetic resonance. An object oriented programming approach, *J. Magn. Reson. A* **106**, 75–105 (1994).
 26. M. Edén, Y. K. Lee, and M. H. Levitt, Efficient simulation of periodic problems in NMR: Application to decoupling and rotational resonance, *J. Magn. Reson. A* **120**, 56–71 (1996).
 27. T. Charpentier, C. Fermon, and J. Virlet, Efficient time propagation technique for MAS NMR simulation: Application to quadrupolar nuclei, *J. Magn. Reson.* **132**, 181–190 (1998).
 28. M. Hohwy, H. Bildsoe, H. J. Jakobsen, and N. C. Nielsen, Efficient spectral simulations in NMR of rotating solids. The γ -COMPUTE algorithm, *J. Magn. Reson.* **136**, 6–14 (1999).
 29. M. H. Levitt and M. Edén, Numerical simulation of periodic NMR problems: Fast calculation of carousel averages, *Molec. Phys.* **95**, 879–890 (1998).
 30. S. Dusold, Ph.D. thesis, University of Bayreuth (2000).
 31. P. Hodgkinson and L. Emsley, Numerical simulations of solid-state NMR experiments, *Progr. Nucl. Magn. Reson. Spectrosc.* **36**, 201–239 (2000).
 32. R. R. Ernst, G. Bodenhausen, and A. Wokaun, "Principles of Nuclear Magnetic Resonance in One and Two Dimensions," Clarendon, Oxford (1987).
 33. <http://www.epm.ornl.gov/pvml/>.
 34. F. James and M. Roos, MINUIT computer code, Program D-506, CERN, Geneva (1977).
 35. M. Bechmann and A. Sebald, to be published.
 36. X. Feng, Y. K. Lee, D. Sandström, M. Edén, H. Maisel, A. Sebald, and M. H. Levitt, Direct determination of a molecular torsional angle by solid-state NMR, *Chem. Phys. Lett.* **257**, 314–320 (1996).
 37. M. Hohwy, H. J. Jakobsen, M. Edén, M. H. Levitt, and N. C. Nielsen, Broadband dipolar recoupling in the nuclear magnetic resonance of rotating solids: A compensated $C7$ pulse sequence, *J. Chem. Phys.* **108**, 2686–2694 (1998).
 38. M. Carravetta, M. Edén, X. Zhao, A. Brinkmann, and M. H. Levitt, Symmetry principles for the design of radiofrequency pulse sequences in the nuclear magnetic resonance of rotating solids, *Chem. Phys. Lett.* **321**, 205–215 (2000).
 39. M. Carravetta, M. Edén, O. G. Johannessen, H. Luthman, P. E. Verdegem, J. Lugtenburg, A. Sebald, and M. H. Levitt, submitted for publication.
 40. M. Bechmann, X. Helluy, C. Marichal, and A. Sebald, submitted for publication.
 41. M. Bechmann, X. Helluy, and A. Sebald, Selectivity of double-quantum-filtered rotational-resonance experiments on larger-than-two-spin systems, in "Perspectives on Solid-State NMR in Biology" (S. Kiihne and H. J. M. de Groot, Eds.), Kluwer, Dordrecht, The Netherlands (2001), in press.

D. Double-Quantum Filtered MAS NMR in the Presence of Chemical Shielding Anisotropies and Direct Dipolar and J Coupling

M. Bechmann, X. Helluy, C. Marichal, and A. Sebald, *Solid State Nuclear Magnetic Resonance*, **21**, 71–85 (2002).

doi:10.1006/snmr.2001.0042

©2002 Elsevier Science (USA).

All rights are reserved by Elsevier Science. The article is reproduced with the rights granted to the author.

Double-Quantum Filtered MAS NMR in the Presence of Chemical Shielding Anisotropies and Direct Dipolar and *J* Couplings

Matthias Bechmann,* Xavier Helluy,*
Claire Marichal,[†] and Angelika Sebald*,¹

**Bayerisches Geoinstitut, Universität Bayreuth, D-95440 Bayreuth, Germany, and*

[†]*Laboratoire de Matériaux Minéraux, 3 rue Alfred Werner, F-68093 Mulhouse Cedex, France*

E-mail: angelika.sebald@uni-bayreuth.de

Received July 6, 2001; published online February 19, 2002

Double-quantum filtered MAS NMR spectra of an isolated homonuclear spin-1/2 pair are considered, at and away from rotational resonance conditions. The pulse sequence used is the solid-state NMR equivalent of double-quantum filtered COSY, known from solution-state NMR. The ¹¹⁹Sn spin pair in [(chex₃Sn)₂S] is characterized by a difference in isotropic chemical shielding smaller than the two chemical shielding anisotropies and by direct dipolar and isotropic *J*-coupling constants of similar magnitudes. At rotational resonance, one-dimensional double-quantum filtered ¹¹⁹Sn lineshapes yield the relative orientation of the two ¹¹⁹Sn chemical shielding tensors. Good double-quantum filtration efficiencies are found at and away from rotational resonance conditions, despite the presence of large chemical shielding anisotropies. Numerical simulations illustrate the interplay of the direct dipolar and *J*-coupling pathways and identify the latter as the main pathway even at rotational resonance conditions. © 2002 Elsevier Science (USA)

Key Words: rotational resonance; double-quantum filtration; numerical simulations; direct dipolar and *J* coupling; chemical shielding tensors.

INTRODUCTION

Small isolated dipolar (re)coupled spin-1/2 systems play an important role in many contemporary solid-state magic-angle spinning (MAS) NMR approaches as applied to homonuclear or heteronuclear spin systems. Full or selective isotopic enrichment schemes are often feasible for spin-1/2 isotopes such as ¹³C or ¹⁵N in (bio)organic compounds and make accessible a plethora of recoupling MAS NMR experiments for structural studies on this class of compounds (1). Isotopic enrichment, however, is usually impractical for other rare spin-1/2 isotopes such as ²⁹Si or ¹¹⁹Sn in many non-(bio)organic compounds. Under these conditions, only those naturally occurring rare isotopomers that contain two or more of these spin-1/2 nuclei may give rise to structurally informative spectral features originating from recoupling effects under MAS. A practical way to reveal this information by suppressing the otherwise

¹To whom correspondence should be addressed.



dominant spectral contributions from the single-spin-1/2 isotopomers is to combine recoupling MAS NMR sequences with double-quantum filtration (DQF).

In nonorganic compounds the missing option of being able to manipulate the spin-system size and abundance by synthetic isotopic labeling is not the only difference from the ^{13}C , ^{15}N (bio)organic scenario. Direct chemical bonding between carbon atoms is the most common motif in organic compounds, in contrast to heteroatom chemistry where direct chemical bonding between like elements is the exception rather than the rule. Except for rather special cases, such as superstructures or incommensurably modulated structures, the number of inequivalent heteroatom sites in the asymmetric unit will usually be less than the number of inequivalent carbon sites in the asymmetric unit of a typical organic crystalline solid. These differences in bonding and structure account for spin-system properties that differ from the ^{13}C case in organic solids, with concomittant implications for the choice of the most suitable MAS NMR experiments for solving a given problem. For example, one-dimensional experiments and chemical shielding anisotropies as well as J couplings will play a more prominent role than is commonly the case with ^{13}C spin systems in organic solids.

Here we apply ^{119}Sn rotational-resonance R^2 (2–5) recoupling with DQF to a sample with ^{119}Sn in natural abundance, [(chex₃Sn)₂S] (chex = cyclohexyl, C₆H₁₁), **1**. The natural abundance of the ^{119}Sn isotope is 8.58%, the crystal structure of **1** is known (6). Specific to this compound, the relative orientations of the two ^{119}Sn chemical shielding tensors will be obtained from one-dimensional R^2 -DQF spectral lineshapes. The performance of the pulse sequence used (7), known in solution-state NMR as DQF-COSY at and away from the $n = 1$ R^2 condition will be examined by numerical simulations. In particular we will consider the roles of the direct dipolar and the J -coupling pathways.

EXPERIMENTAL

Sample

[(chex₃Sn)₂S], **1**, is commercially available (Aldrich Chemicals). Single crystals of **1**, suitable for structure determination by X-ray diffraction were obtained by crystallization from a chloroform solution at ambient conditions. The recrystallized material also served for ^{119}Sn MAS NMR experiments. Solid **1** is stable in air.

^{119}Sn MAS NMR

^{119}Sn MAS NMR spectra were recorded on Bruker MSL 200, MSL 300, and DSX 400 NMR spectrometers. The corresponding ^{119}Sn Larmor frequencies $\omega_0/2\pi$ are 74.6, 111.9, and 149.2 MHz. ^{119}Sn chemical shielding is referenced to the ^{119}Sn resonance of SnMe₄ at 0 ppm. MAS frequencies $\omega_r/2\pi$ were generally in the range 1.2–3.4 kHz and were actively controlled to within ± 2 Hz. The sample was contained in a 4-mm o.d. ZrO₂ rotor. All ^{119}Sn MAS NMR experiments were obtained with Hartmann–Hahn cross polarization (CP) with a contact time of 1 ms and a recycle delay of 5 s. ^{119}Sn $\pi/2$ pulse durations were in the range 3.0–4.6 μs ; c.w.

^1H decoupling with amplitudes of 45–83 kHz was used. The pulse sequence chosen to record ^{119}Sn DQF MAS NMR spectra of **1**, $\text{CP}_{(x)}-\tau-\pi/2_{(y)}-\Delta-\pi/2_{(z)}$ acquisition (7), employed 64-step phase cycling according to standard procedures (8). The duration of τ was adjusted to last for integer multiples N of the rotation period, τ_r , with N chosen for optimum DQF efficiency (see further below); the duration of Δ was a fixed short delay of 3 μs .

Definitions, Notation, and Numerical Methods

Shielding notation (9) is used throughout. For the interactions $\lambda = \text{CS}$ (chemical shielding), $\lambda = D$ (direct dipolar coupling), and $\lambda = J$ (indirect dipolar (J) coupling) the isotropic part $\omega_{\text{iso}}^\lambda$, the anisotropy $\omega_{\text{aniso}}^\lambda$, and the asymmetry parameter η^λ relate to the principal elements of the interaction tensor ω^λ as follows (10): $\omega_{\text{iso}}^\lambda = (\omega_{xx}^\lambda + \omega_{yy}^\lambda + \omega_{zz}^\lambda)/3$, $\omega_{\text{aniso}}^\lambda = \omega_{zz}^\lambda - \omega_{\text{iso}}^\lambda$, and $\eta^\lambda = (\omega_{yy}^\lambda - \omega_{xx}^\lambda)/\omega_{\text{aniso}}^\lambda$ with $|\omega_{zz}^\lambda - \omega_{\text{iso}}^\lambda| \geq |\omega_{xx}^\lambda - \omega_{\text{iso}}^\lambda| \geq |\omega_{yy}^\lambda - \omega_{\text{iso}}^\lambda|$. For indirect dipolar coupling $\omega_{\text{iso}}^J = \pi J_{\text{iso}}$, and for direct dipolar coupling $\eta^D = \omega_{\text{iso}}^D = 0$ and $\omega_{\text{aniso}}^{Dij} = b_{ij} = -\mu_0 \gamma_i \gamma_j \hbar / (4\pi r_{ij}^3)$, where γ_i, γ_j denote gyromagnetic ratios and r_{ij} is the internuclear distance between spins S_i, S_j . The Euler angles $\Omega_{IJ} = \{\alpha_{IJ}, \beta_{IJ}, \gamma_{IJ}\}$ (11) relate axis system I to axis system J , where I, J denote P (principal axis system, PAS) and C (crystal axis system, CAS). For simulations of MAS NMR spectra of isolated two-spin systems (S_i, S_j) it is

TABLE 1
Parameters of the ^{119}Sn Spin Pair in $[(\text{chex}_3\text{Sn})_2\text{S}]$, **1**

	$^{119}\text{Sn}_{(1)}$	$^{119}\text{Sn}_{(2)}$
$\omega_{\text{iso}}^{\text{CS}}$ [ppm]	−26.6	−4.4
$\omega_{\text{aniso}}^{\text{CS}}$ [ppm]	+39.0	−48.8
η^{CS}	0.5 ± 0.1	0.0 ± 0.1
$\alpha_{PC}^{\text{CS}} [^\circ] (^2J_{\text{iso}} > 0)$	27 ± 20^a	—
$\beta_{PC}^{\text{CS}} [^\circ] (^2J_{\text{iso}} > 0)$	74 ± 13	37 ± 7
$\gamma_{PC}^{\text{CS}} [^\circ] (^2J_{\text{iso}} > 0)$	0^b	34 ± 20
$\alpha_{PC}^{\text{CS}} [^\circ] (^2J_{\text{iso}} < 0)$	60 ± 27^a	—
$\beta_{PC}^{\text{CS}} [^\circ] (^2J_{\text{iso}} < 0)$	30 ± 16	114 ± 13
$\gamma_{PC}^{\text{CS}} [^\circ] (^2J_{\text{iso}} < 0)$	0^b	128 ± 22
$b_{12}/2\pi$ [Hz] ^c		−254
$ ^2J_{\text{iso}} $ [Hz] ^d		230 ± 3

^aA second solution exists with $\alpha_{PC}^{\text{CS}} + 90^\circ$; this solution, however, does not correspond to a ^{119}Sn chemical shielding tensor orientation relating to the molecular Sn(A)–S–Sn(B) geometry in any obvious way.

^bArbitrarily defined.

^cCalculated from the internuclear distance Sn(A)–Sn(B) as determined by single-crystal X-ray diffraction (6).

^dTaken from Ref. (15), confirmed in this work (see Fig. 5).

convenient to take the PAS of the corresponding dipolar coupling tensor $\omega^{D_{ij}}$ as the CAS, $\Omega_{PC}^{D_{ij}} = \{0, 0, 0\}$.

With one of the two ^{119}Sn chemical shielding tensors in **1** being axially symmetric, $\eta^{CS_2} = 0$ (see Table 1), only four Euler angles, $\alpha_{PC}^{CS_1}$, $\beta_{PC}^{CS_1}$, $\beta_{PC}^{CS_2}$, and $\gamma_{PC}^{CS_2}$, are needed to describe the relative orientation of the two ^{119}Sn chemical shielding tensors in **1**. In order to determine these parameters, complete calculations of the corresponding four-dimensional error maps, assuming either ${}^2J_{\text{iso}}(^{119}\text{Sn}_{(1)}, ^{119}\text{Sn}_{(2)}) = +230$ Hz or ${}^2J_{\text{iso}}(^{119}\text{Sn}_{(1)}, ^{119}\text{Sn}_{(2)}) = -230$ Hz, were carried out based on experimental ^{119}Sn $n = 1$ R^2 -DQF data obtained at $\omega_0/2\pi = 74.6$ MHz and at $\omega_0/2\pi = 149.2$ MHz. The resulting two different sets of Euler angles $\Omega_{PC}^{CS_{1,2}}$ for ${}^2J_{\text{iso}} > 0$ and ${}^2J_{\text{iso}} < 0$ as the ‘best-fit’ solutions are listed in Table 1. Our numerical simulation procedures have been outlined elsewhere (12, 13). Some additional numerical investigations employed iterative lineshape fitting methods. For iterative minimizations, our simulation programs are combined with the optimization routines of the MINUIT package (14).

RESULTS AND DISCUSSION

Characterization of the $^{119}\text{Sn}_{(1)}\text{-S-}^{119}\text{Sn}_{(2)}$ Spin Pair in **1**

Single-crystal X-ray diffraction (6) shows the two tin sites per molecule in **1** to be crystallographically independent and provides the Sn–S bond lengths and angle of the Sn(A)–S–Sn(B) moiety (distance Sn(A)–S: 241.1 pm, distance Sn(B)–S:

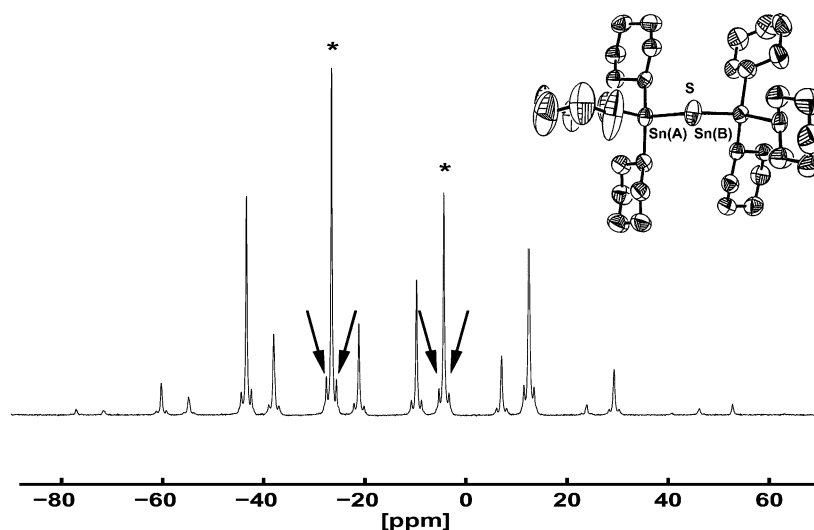


FIG. 1. ^{119}Sn MAS NMR spectrum of **1** ($\omega_0/2\pi = 111.9$ MHz, $\omega_r/2\pi = 1884$ Hz); also shown is an ORTEP plot of the molecular structure of solid **1**. Asterisks mark the centre-band regions of the two ^{119}Sn resonances, arrows highlight the (unresolved) spectral contributions originating from the ^{119}Sn – ^{119}Sn and the ^{119}Sn – ^{117}Sn isotopomers in the isotropic ^{119}Sn chemical shielding region.

242.2 pm, angle Sn(A)–S–Sn(B) 113.4°; see Fig. 1). Thus the Sn(A)–Sn(B) distance in **1** amounts to 404.0 pm, corresponding to a $^{119}\text{Sn}_{(1)}\text{--}^{119}\text{Sn}_{(2)}$ dipolar coupling constant $b_{12}/2\pi = -254$ Hz. ^{119}Sn MAS NMR spectra of **1** (Fig. 1) are dominated by the spectral contributions from the single- ^{119}Sn isotopomers of **1**, yielding $\omega_{\text{iso}}^{CS_{1,2}}$ and $\omega_{\text{aniso}}^{CS_{1,2}}$, but no assignment of the two ^{119}Sn resonances to the two crystallographic tin sites Sn(A), Sn(B). ^{119}Sn is not the only spin-1/2 isotope of the element tin. ^{117}Sn is another spin-1/2 isotope of tin, with a natural abundance and a gyromagnetic ratio similar to ^{119}Sn . The splittings due to $^2J_{\text{iso}}(^{119}\text{Sn}, ^{117/119}\text{Sn})$ are not resolved in the ^{119}Sn MAS NMR spectrum of **1** (see arrows in Fig. 1), but the value of $|^2J_{\text{iso}}(^{119}\text{Sn}_{(1)}, ^{119}\text{Sn}_{(2)})| = 230 \pm 3$ Hz is known from an earlier ^{119}Sn MAS INADEQUATE experiment on **1** (15).

Determination of the remaining unknowns, that is, the relative orientation of the two ^{119}Sn chemical shielding tensors, assignment of the two ^{119}Sn resonances to the two tin sites, and the sign of $^2J_{\text{iso}}(^{119}\text{Sn}_{(1)}, ^{119}\text{Sn}_{(2)})$, relies on the $^{119}\text{Sn}_{(1)}\text{--}^{119}\text{Sn}_{(2)}$ isotopomer of **1**. When a so-called rotational-resonance (R^2) condition (2–5) is fulfilled, all anisotropic spin-pair interactions are reflected in the lineshape of the MAS NMR spectrum of a homonuclear spin pair. Without DQF this informative ^{119}Sn R^2 lineshape of the rare $^{119}\text{Sn}_{(1)}\text{--}^{119}\text{Sn}_{(2)}$ spin-pair isotopomer would be buried by the spectral contributions from the other isotopomers of **1**. A relatively small difference in isotropic ^{119}Sn chemical shielding, $\omega_{\text{iso}}^{\Delta_{12}} = 22.2$ ppm, compared with the corresponding chemical shielding anisotropies (here: $\omega_{\text{aniso}}^{CS_1} = 1.76 \omega_{\text{iso}}^{\Delta_{12}}$, $\omega_{\text{aniso}}^{CS_2} = -2.20 \omega_{\text{iso}}^{\Delta_{12}}$) is a useful condition for the determination of chemical shielding tensor orientations from R^2 lineshapes, but is also a regime where the efficiencies of many DQF MAS recoupling sequences are severely degraded. The pulse sequence

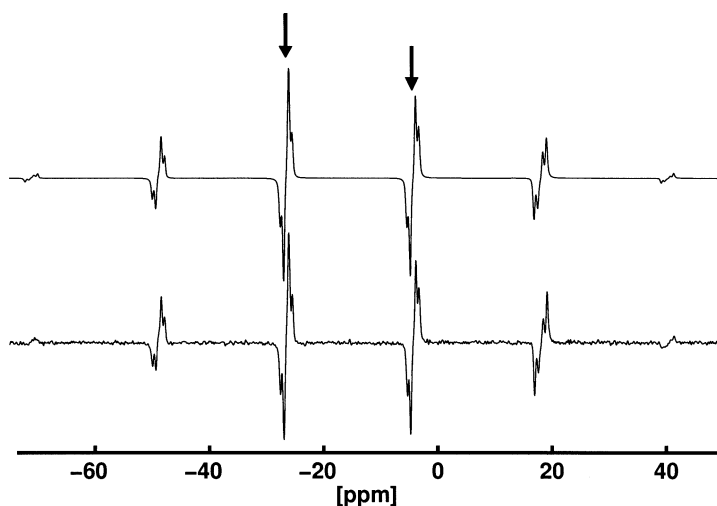


FIG. 2. Double-quantum filtered ^{119}Sn MAS NMR spectra of **1**, at the $n = 1$ R^2 condition ($\omega_0/2\pi = 149.2$ MHz, $\omega_r/2\pi = 3326$ Hz, $\tau = 1.80$ ms ($\tau = 6\tau_r$)); bottom trace: experimental spectrum, top trace: “best-fit” simulated spectrum (with $^2J_{\text{iso}}(^{119}\text{Sn}_{(1)}, ^{119}\text{Sn}_{(2)}) = +230$ Hz), the arrows mark the two center band regions.

$CP_{(x)} - \tau - \pi/2_{(y)} - \Delta - \pi/2_{(\phi)}$ - acquisition (7), with the period τ being a suitably chosen integer multiple N of the rotation period τ_r , has been shown to deliver satisfactory R^2 -DQF efficiency and informative R^2 -DQF lineshapes in the presence of large chemical shielding anisotropies (13). Here we apply this pulse sequence in the characterization of the $^{119}\text{Sn}_{(1)}\text{-}^{119}\text{Sn}_{(2)}$ spin pair in **1**.

Figure 2 displays an experimental ^{119}Sn $n = 1$ R^2 -DQF MAS NMR spectrum of **1**, together with the corresponding “best-fit” simulated spectrum taking ${}^2J_{\text{iso}}(^{119}\text{Sn}_{(1)}, ^{119}\text{Sn}_{(2)}) = +230$ Hz. With $\eta^{\text{CS}_2} = 0$ only four Euler angles are needed to describe the relative orientation of the two ^{119}Sn chemical shieldings tensors in **1**. Instead of using iterative lineshape fitting as the route to determining the best fit set of these Euler angles, the complete four-dimensional error maps of the four unknown angles was calculated, once assuming a positive sign of ${}^2J_{\text{iso}}$, once assuming a negative sign. When affordable in terms of computational times, this brute-force numerical approach offers an advantage over iterative fitting in that it avoids possible pitfalls of local minima in multiple parameter fits. The resulting sets of Euler angles, describing the relative orientations of the two ^{119}Sn chemical shielding tensors with ${}^2J_{\text{iso}} > 0$ and with ${}^2J_{\text{iso}} < 0$ are given in Table 1. In principle it should be possible to unambiguously identify the correct sign of ${}^2J_{\text{iso}}$ by selecting the solution with the better agreement between experimental and simulated “best fit” spectrum. For the ^{119}Sn spin pair in **1**, this distinction turns out impossible on purely numerical grounds—the two sets of “best-fit” parameters agree equally well with the experimental data, but correspond to different chemical shielding tensor orientations. Empirical trends from solution-state NMR data $|{}^2J_{\text{iso}}(^{119}\text{Sn}, ^{119}\text{Sn})|$ for Sn–E–Sn moieties in organotin compounds (16) strongly suggest a positive sign of ${}^2J_{\text{iso}}(^{119}\text{Sn}_{(1)}, ^{119}\text{Sn}_{(2)})$ in **1**. An illustration of the ^{119}Sn chemical shielding tensor orientations in the molecular Sn(A)–S–Sn(B) plane is shown in Fig. 3. It depicts the assignment permutation with Sn(A) = $^{119}\text{Sn}_{(1)}$, Sn(B) = $^{119}\text{Sn}_{(2)}$. There is little difference in the local $\text{C}_3\text{Sn(A)S}$ and $\text{C}_3\text{Sn(B)S}$ geometries in **1**; only the three bond

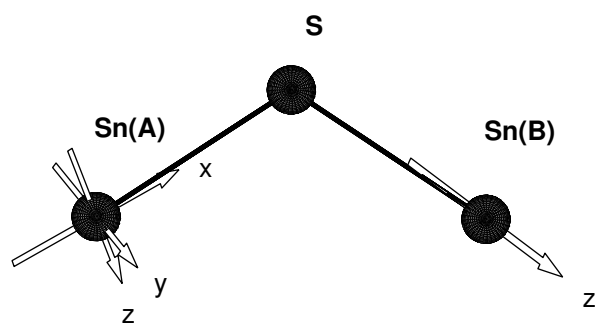


FIG. 3. View perpendicular onto the molecular Sn(A)–S–Sn(B) plane of **1**, illustrating the ^{119}Sn chemical shielding tensor orientations with $^{119}\text{Sn}_{(1)} = \text{Sn(A)}$, $^{119}\text{Sn}_{(2)} = \text{Sn(B)}$ and adjusting $\gamma_{PC}^{\text{CS}_{1,2}}$ such that for both ^{119}Sn chemical shielding tensors the directions of the least shielded component (ω_{xx} for $^{119}\text{Sn}_{(1)}$ and ω_{zz} for $^{119}\text{Sn}_{(2)}$) are very nearly in the molecular Sn(A)–S–Sn(B) plane and nearly coincide with the Sn(A)–S, Sn(B)–S bond directions.

angles C–Sn(B)–C (110.3°, 112.1°, 113.6°) are slightly more uniform than the corresponding set of bond angles C–Sn(A)–C (108.6°, 112.8°, 114.3°). We may take this as a qualitative argument in support of assigning the axially symmetric $^{119}\text{Sn}_{(2)}$ chemical shielding tensor to tin site Sn(B). Further taking $\gamma_{PC}^{CS_1} = -45^\circ$ (and accordingly $\gamma_{PC}^{CS_2} = -11^\circ$) we arrive at the orientation of the ^{119}Sn chemical shielding tensors in the molecular Sn(A)–S–Sn(B) plane shown in Fig. 3. The directions of the least shielded components of the two ^{119}Sn chemical shielding tensors are nearly in the Sn(A)–S–Sn(B) plane and nearly coincide with the respective Sn–S bond directions (within 12° for $\text{Sn}_{(2)}$ –S, within 9° for $\text{Sn}_{(1)}$ –S). Note, however, that the alternative assignment permutation (Sn(A) = $^{119}\text{Sn}_{(2)}$, Sn(B) = $^{119}\text{Sn}_{(1)}$) after appropriate adjustment of the Euler angles $\gamma_{PC}^{CS_{1,2}}$ would correspond to a similar orientation of the directions of the two least shielded components in the molecular frame. Finally, the disregarded “best-fit” set of Euler angles $\Omega_{PC}^{CS_{1,2}}$ for ${}^2J_{\text{iso}}(^{119}\text{Sn}_{(1)}, ^{119}\text{Sn}_{(2)}) = -230$ Hz describes an orientation of the two ^{119}Sn chemical shielding tensors with larger deviations of the least-shielded tensor components from the local Sn–S bond directions (34° away from the $\text{Sn}_{(2)}$ –S and 35° away from the $\text{Sn}_{(1)}$ –S bond directions). We are not aware of further studies on ^{119}Sn chemical shielding tensor orientations in related organotin compounds, so that it would seem premature to consider the orientational parameters found for **1** as typical of a C_3SnS moiety in organotin compounds.

Having described our experimental findings, we need to consider next if it is justified to ignore the anisotropy of the J coupling in **1**. This question is best answered by numerical simulations. For many ^{13}C spin systems it is a reasonable assumption to ignore the anisotropy of the homonuclear J couplings, given that usually the magnitudes of the direct dipolar coupling constants exceed the magnitudes of the corresponding J -coupling constants by two orders of magnitude. The situation is different with the ^{119}Sn spin pair in **1**, where the values of b_{12} and $|{}^2J_{\text{iso}}|$ are very similar to each other. In addition, it was demonstrated that J coupling via two intervening bonds, ${}^2J(^{119}\text{Sn}, ^{117}\text{Sn})$, displays J anisotropy $\omega_{\text{aniso}}^{2J}$ of comparable magnitude to the value $|{}^2J_{\text{iso}}|$ in a linear Sn–O–Sn molecular fragment (17). If $\omega_{\text{aniso}}^{2J}$ would play a significant role for the ^{119}Sn spin pair in **1**, it would reveal itself in iterative lineshape fits with the four angles $\Omega_{PC}^{CS_{1,2}}$ and the magnitude of b_{12} as free fit parameters as a best-fit value b_{eff} , significantly different from b_{12} (18). We find that lineshape fits with b_{12} as an additional free fit parameter converge to the same orientational parameters as determined previously from calculations of the four-dimensional error maps, where $b_{12}/2\pi = -254$ Hz was fixed to the value calculated from the Sn(A)–Sn(B) distance determined by X-ray diffraction. The best-fit value $b_{\text{eff}} = -302 \pm 88$ Hz would correspond to a Sn(A)–Sn(B) distance of 381 ± 35 pm, not significantly different from the distance determined by single-crystal X-ray diffraction (404 pm). This leaves two possible interpretations. (i) $\omega_{\text{aniso}}^{2J}$ in **1** is indeed insignificantly small and hence does not contribute to a value b_{eff} from the combined effects of direct dipolar coupling and $\omega_{\text{aniso}}^{2J}$; or (ii) $\omega_{\text{aniso}}^{2J}$ is not insignificantly small, but $\omega_{\text{aniso}}^{2J}$ and the orientation of the J -coupling tensor in **1** are such that again an insignificant contribution to b_{eff} results. Regardless of the true explanation, not explicitly taking $\omega_{\text{aniso}}^{2J}$ into account obviously does not distort the results in terms of

^{119}Sn chemical shielding tensor orientations for **1**. While this can be verified for the specific case at hand, it would be unwise to generalise this finding to all 2J -coupling tensors of non- ^{13}C spins.

Up to this point we have used the R^2 -DQF pulse sequence $\text{CP}_{(x)}-\tau-\pi/2_{(y)}-\Delta-\pi/2_{(\phi)}$ -acquisition (7) as a tool to characterize the $^{119}\text{Sn}_{(1)}-^{119}\text{Sn}_{(2)}$ spin pair in **1**. In the following we turn our attention to the working of the pulse sequence itself when applied to spin systems with properties similar to those of the ^{119}Sn spin pair in **1**.

DQF MAS NMR—The Role of Direct Dipolar and J Coupling

We continue using the set of parameters describing the ^{119}Sn spin pair **1** in order to explore the working of the $\text{CP}_{(x)}-\tau-\pi/2_{(y)}-\Delta-\pi/2_{(\phi)}$ -acquisition (7) pulse sequence under MAS conditions. Now these ^{119}Sn spin-pair parameters merely serve as a model case. They can be seen as a general type of homonuclear spin-1/2 pair, characterized by chemical shielding anisotropies much larger than the difference in isotropic chemical shielding, by a fairly small direct dipolar coupling constant and a sizeable J -coupling constant of similar magnitude, leading to resolved J -coupling in a MAS NMR spectrum.

Figure 4 demonstrates how this kind of spin-pair properties is reflected in the R^2 -DQF efficiencies as a function of the duration of τ . The numerical simulations

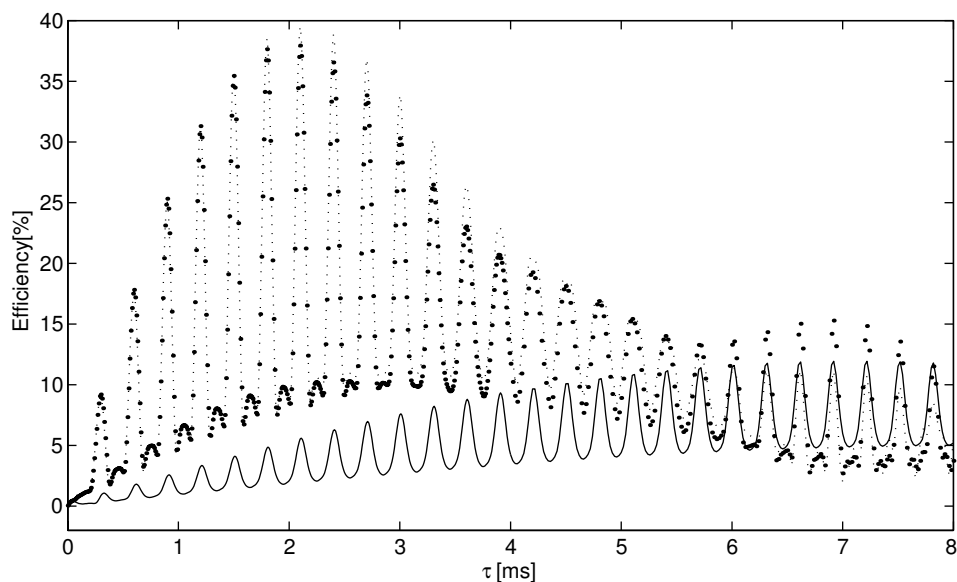


FIG. 4. Numerically predicted ^{119}Sn R^2 -DQF efficiencies for the ^{119}Sn spin pair in **1** at the $n = 1$ R^2 condition ($\omega_0/2\pi = 149.2$ MHz, $\omega_r/2\pi = 3326$ Hz), plotted as a function of τ [ms]. The trace (\cdots) refers to the combined effects of b_{12} and $^2J_{iso}$; the drawn line (—) depicts the contribution of the direct dipolar coupling pathway, the thin dotted line (\cdots) refers to the contribution from the J -coupling pathway. Note that J coupling is the far more efficient pathway and that at some durations of τ a slight negative interference of the two transfer mechanisms occurs.

employ the set of parameters describing the ^{119}Sn spin pair in **1** at the $n = 1$ R^2 condition with $\omega_0/2\pi = 149.2$ MHz. The highest DQF efficiency from the combined effects of direct dipolar and J coupling (\cdots) is predicted to occur at a fairly short duration of $\tau = 2.1$ ms (equivalent to $\tau = 7\tau_r$ and similar to $(2J)^{-1} = 2.2$ ms) and amounts to ca. 38 percent. These numerical predictions are well reproduced in ^{119}Sn $n = 1$ R^2 -DQF experiments on **1**. Numerically one can easily break down this overall R^2 -DQF efficiency curve into the individual contributions from the direct dipolar and the J -coupling pathways. Not surprisingly, the major efficiency contribution originates from the (isotropic) J coupling (\cdots), while the direct dipolar coupling (—) contributes much less to the overall R^2 -DQF efficiency. The J -coupling pathway is further responsible for the maximum R^2 -DQF efficiency occurring at fairly short durations of τ , while direct dipolar coupling alone would lead to a lesser maximum R^2 -DQF efficiency (ca. 12%) at much longer durations of τ .

The dominating influence of the J -coupling pathway even at the $n = 1$ R^2 -DQF condition implies that efficient DQF may also be expected away from any R^2 condition. Experimental and simulated ^{119}Sn DQF spectra of **1**, recorded at $\omega_0/2\pi = 74.6$ MHz and at a MAS frequency $\omega_r/2\pi = 1223$ Hz (inbetween the $n = 1$ and the $n = 2$ R^2 conditions) are shown in Fig. 5. A closer examination and comparison of the DQF efficiencies at and away from R^2 is shown in Fig. 6. At the $n = 1$ R^2 conditions at $\omega_0/2\pi = 149.2$ MHz (—) and at $\omega_0/2\pi = 74.6$ MHz (\cdots), the overall R^2 -DQF efficiencies are nearly identical, both with a maximum of ca. 38%. However, a higher optimum DQF efficiency of nearly 60% is realised away from R^2 (\cdots), corresponding to the experimental parameters chosen when recording the spectrum depicted in Fig. 5. Breaking down the away-from- R^2 efficiency curve into the contributions from direct dipolar and J coupling reveals that away from

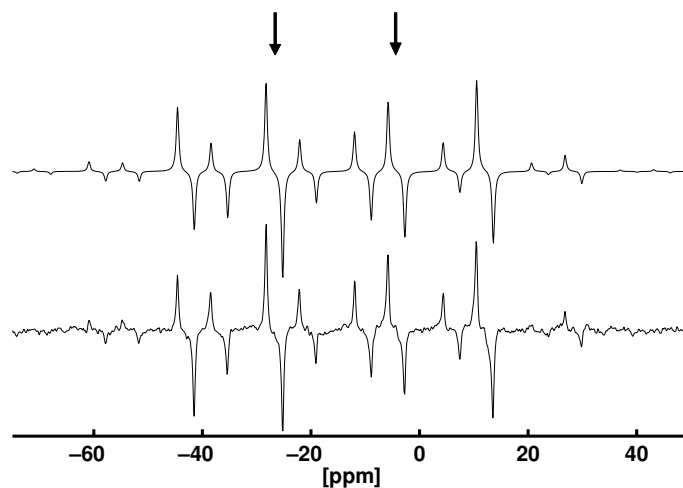


FIG. 5. Double-quantum filtered ^{119}Sn MAS NMR spectra of **1**, away from a R^2 condition ($\omega_0/2\pi = 74.6$ MHz, $\omega_r/2\pi = 1223$ Hz, $\tau = 2.49$ ms ($\tau = 3\tau_r$)); bottom trace: experimental spectrum, top trace: “best-fit” simulated spectrum (with ${}^2J_{\text{iso}}(^{119}\text{Sn}_{(1)}, ^{119}\text{Sn}_{(2)}) = +230$ Hz), the arrows mark the two centre band regions.

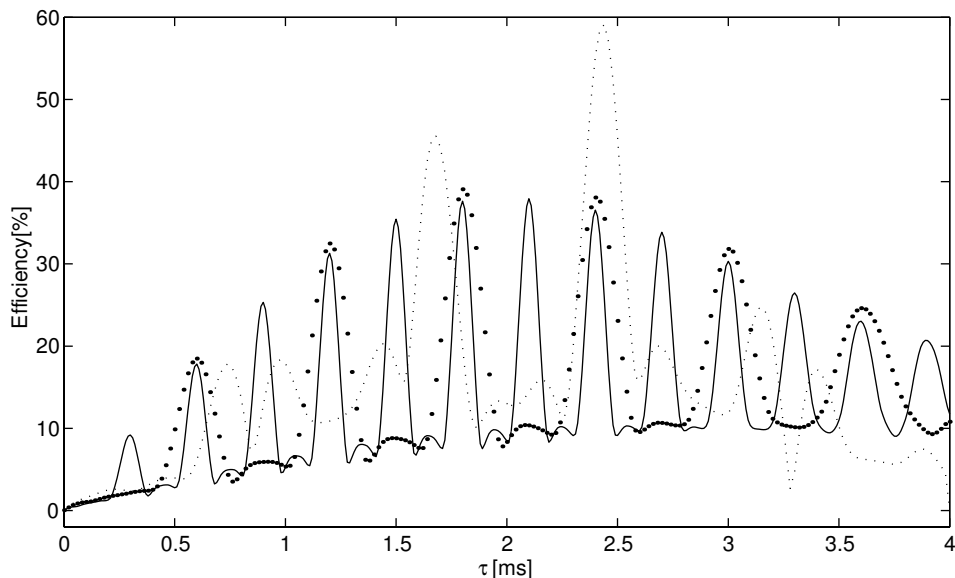


FIG. 6. Comparison of the ^{119}Sn DQF efficiencies for the ^{119}Sn pair in **1**, on and away from the $n = 1$ R^2 condition, plotted as a function of τ [ms]. (\cdots) traces the DQF efficiency away from R^2 , at $\omega_0/2\pi = 74.6$ MHz and $\omega_r/2\pi = 1223$ Hz; the other two curves refer to the $n = 1$ R^2 -DQF efficiencies at $\omega_0/2\pi = 149.2$ MHz and $\omega_r/2\pi = 3326$ Hz (—), and at $\omega_0/2\pi = 74.6$ MHz and $\omega_r/2\pi = 1663$ Hz (\cdots).

R^2 , not surprisingly, the contribution from the direct dipolar coupling pathway is effectively zero throughout the entire range of τ values, even if the MAS frequency chosen deviates by only ca. 400 Hz from the $n = 1$ R^2 condition. Very recently, it has been pointed out that under fast-spinning conditions in a closely related two-dimensional R^2 -DQ experiment the direct dipolar and J -coupling contributions may be separated from each other in the double-quantum dimension, enabling the estimation of internuclear distances provided the magnitude of the isotropic J -coupling constant is known (19). Under slow-spinning conditions and/or in one-dimensional DQF experiments, this separation is preferably obtained by recording experimental spectra at and away from a R^2 condition.

Even if at the $n = 1$ R^2 condition, the direct dipolar coupling pathway is less efficient than the (isotropic) J -coupling pathway (see Fig. 4), the participation of the direct dipolar coupling pathway at R^2 is essential in encoding the orientational parameters $\Omega_{PC}^{CS_{1,2}}$ in the resulting spectral lineshapes. This is illustrated in Fig. 7. Being able to numerically reproduce well the experimental ^{119}Sn R^2 -DQF lineshapes (see Fig. 2) is clearly not a sufficient criterion to postulate that all the Euler angles $\Omega_{PC}^{CS_{1,2}}$ are sensitively encoded in the experimental lineshapes. How well these angles are defined by the experimental lineshapes, we can investigate by a purely numerical approach. First, we calculate the lineshape corresponding precisely to the “best-fit” values of all parameters. Next, this numerically generated “ideal” spectrum forms the basis of one-dimensional

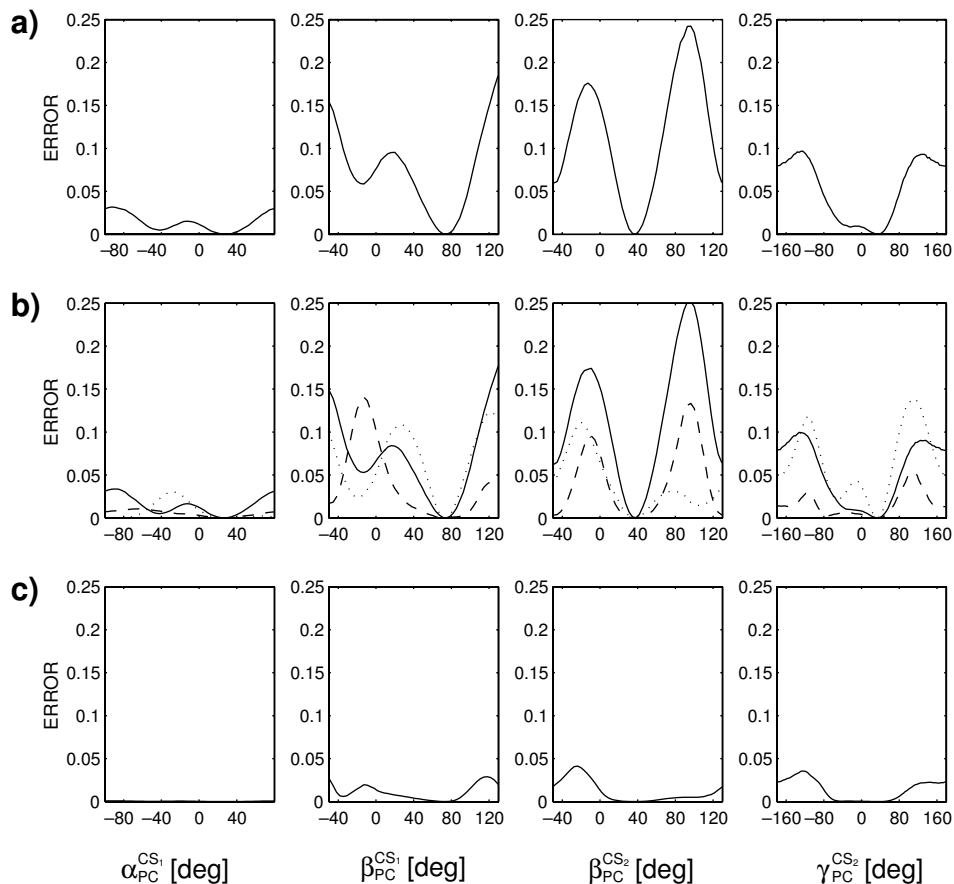


FIG. 7. One-dimensional error scans, illustrating the sensitivity of the DQF ^{119}Sn MAS NMR line-shapes to the Euler angles $\Omega_{PC}^{\text{CS}_{1,2}}$ in **1**; the error scans are based on simulated spectra employing the “best-fit” values for all parameters. The vertical axes in the plots are defined as $\text{ERROR} = \sum_i [(\text{sim}(i) - \exp(i))^2 / \sum_i [\exp(i)]^2]$. (a) At the $n = 1 R^2$ condition, with $\omega_0/2\pi = 74.6$ MHz and $\omega_r/2\pi = 1663$ Hz. (b) At the $n = 1 R^2$ condition, with $\omega_0/2\pi = 149.2$ MHz and $\omega_r/2\pi = 3326$ Hz; the traces refer to the combined $b_{12} + 2J_{\text{iso}}$ effects (—), and to the expected sensitivities if there were only b_{12} (- -) or only $2J_{\text{iso}}$ (⋯) involved. (c) Away from the $n = 1 R^2$ condition, with $\omega_0/2\pi = 149.2$ MHz and $\omega_r/2\pi = 2228$ Hz.

error scans for each individual parameter, while keeping the other parameters fixed. This approach may have its dangers when applied directly to an experimental spectrum, as there all best-fit parameters are only known within certain error margins and there will be unavoidable experimental imperfections, including the noise in the experimental spectrum. These problems are avoided by the indirect way of characterising the basic sensitivity of fit parameters from a numerically generated “ideal” spectrum representing the spin-system properties. Of course, this

indirect method can only give a measure for the best possible sensitivities. The results of this purely numerical characterisation of the sensitivities of the ^{119}Sn $n = 1$ R^2 -DQF lineshapes of **1** to the Euler angles $\Omega_{PC}^{CS_{1,2}}$ are shown in Fig. 7a, 7b. Despite the relative small value of the dipolar coupling constant $b_{12}/2\pi = -254$ Hz, at the $n = 1$ R^2 condition the angles are sensitively encoded in the spectral lineshapes, with essentially equal sensitivities at $\omega_0/2\pi = 74.6$ MHz (Fig. 7a) and at $\omega_0/2\pi = 149.2$ MHz (— in Fig. 7b). As usual, $\beta_{PC}^{CS_2}$ and $\beta_{PC}^{CS_1}$, defining the angles subtended between the direction of the unique component of the dipolar coupling tensor and the directions of the (largest) zz -components of the two chemical shielding tensors, are most sensitively encoded. In between the $n = 1$ and $n = 2$ R^2 conditions (at $\omega_0/2\pi = 149.2$ MHz, with $\omega_r/2\pi = 2228$ Hz) the sensitivity of the DQF lineshapes to the angles $\Omega_{PC}^{CS_{1,2}}$ is much reduced, as can be seen in Fig. 7c. Finally, Fig. 7b in addition shows that at the $n = 1$ R^2 condition the direct dipolar (- - -) and the J -coupling (\cdots) contributions constructively interfere with each other in providing a higher overall (—) lineshape sensitivity to the angles $\Omega_{PC}^{CS_{1,2}}$ than would be obtained from direct dipolar coupling alone.

Adapting solution-state NMR experiments to usage in MAS NMR is certainly not a new concept. About a decade ago COSY and INADEQUATE MAS NMR experiments have already been applied successfully for purposes of spectral assignments based on J -coupling connectivities (20–22), or to measure homonuclear J -coupling constants in crystalline solids (15, 23, 24). Most of these earlier experiments (and some more recent applications (25–27)) were dealing with spin systems in low isotopic abundance in crystalline solids. For example ^{29}Si INADEQUATE experiments on inorganic solids such as zeolites very closely mimic typical “solution-state” spin system properties, where under MAS conditions essentially the only relevant spectral parameters are the isotropic chemical shieldings and (small) J -coupling constants. Nowadays, with more efficient numerical simulation methods available, it becomes more attractive to apply these and similar “solution-state”-like NMR experiments under MAS conditions to dilute spin systems with more expressed “solid-state”-like properties, such as, for instance, the ^{119}Sn spin pair in **1** under R^2 conditions. The selective through-bond character of the J -coupling interaction is an attractive feature for purposes of spectral assignments not only in dilute spin systems. Recent progress in the symmetry-based design of pulse sequences has resulted in the development of MAS recoupling experiments permitting the selective exploitation of the J -coupling interactions also in extended spin systems in the presence of multiple direct dipolar couplings of substantial magnitudes (28, 29). Sophisticated J -selective pulse sequences are crucial for the successful exploitation of J -coupling information for spectral assignment in tightly dipolar coupled multi-spin systems, such as in fully ^{13}C enriched organic solids (30) or ^{31}P in inorganic condensed phosphate phases (31, 32). Where it comes to spin-1/2 systems in low natural abundance, it is often neither necessary nor desirable to use J -selective recoupling experiments: at low natural abundance DQF essentially reduces the individual subsets of spin systems present in the sample to an ensemble of isolated spin-1/2 pairs. Recording of the signatures of these rare spin-1/2 pairs usually requires large amounts of spectrometer time. Under these conditions it is both affordable in terms of numerical efforts and desirable in terms of maximum information per time

unit spent on the spectrometer, to characterize as many parameters of these rare spin pairs in one experiment as is possible, for example including chemical shielding tensor orientations. With this scenario in mind and mainly as a matter of completeness, we briefly consider for comparison another pulse sequence, INADEQUATE (33) when applied to a spin system with properties similar to those of the ^{119}Sn pair in solid **1**. The INADEQUATE sequence is derived from the $\text{CP}_{(x)}-\tau-\pi/2_{(y)}-\Delta-\pi/2_{(\phi)}$ -acquisition sequence by inserting a nonselective $\pi_{(\pm x)}$ pulse in the middle of

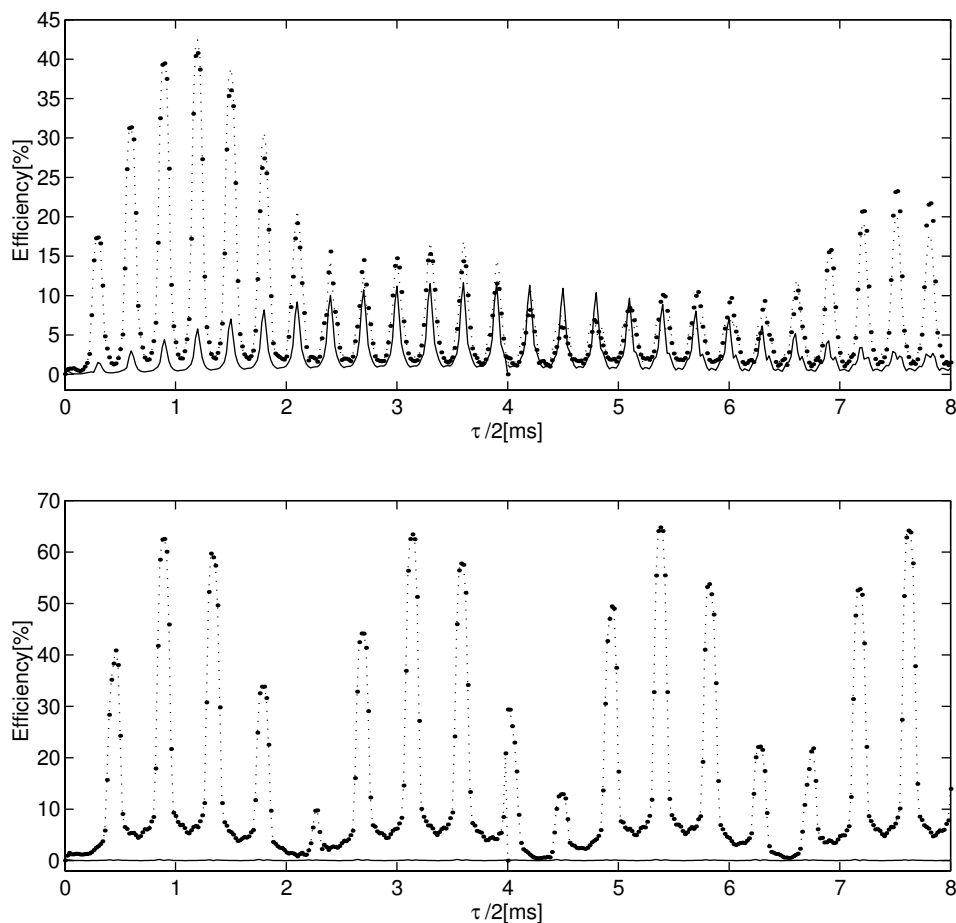


FIG. 8. Numerical simulations of the INADEQUATE DQF efficiencies for the ^{119}Sn pair in **1**, plotted as a function of $\tau/2$ [ms]; top: at the $n = 1 R^2$ condition with $\omega_0/2\pi = 149.2$ MHz and $\omega_r/2\pi = 3326$ Hz, bottom: away from the $n = 1 R^2$ condition, with $\omega_0/2\pi = 149.2$ MHz and $\omega_r/2\pi = 2228$ Hz. In both parts the trace (\cdots) indicates the overall DQF efficiency from $b_{12} + {}^2J_{iso}$, the expected DQF efficiencies in the presence of only b_{12} (---) or only ${}^2J_{iso}$ (\cdots) are also shown. Note that away from the $n = 1 R^2$ condition the b_{12} contribution is effectively zero and that the overall efficiencies as a function of $2 \cdot \tau/2$ are very similar to the efficiencies of the $\text{CP}_{(x)}-\tau-\pi/2_{(y)}-\Delta-\pi/2_{(\phi)}$ -acquisition sequence (compare Figs. 4 and 6).

the period τ , with an optimum duration of $\tau/2 = (4J)^{-1}$. Figure 8 shows the numerically expected INADEQUATE DQF efficiencies at (top) and away from (bottom) R^2 , plotted as a function of $\tau/2$. The INADEQUATE behavior is extremely similar to that of the $CP_{(x)}-\tau-\pi/2_{(y)}-\Delta-\pi/2_{(\phi)}$ -acquisition sequence. Accordingly, when investigating spin systems with properties similar to those of the ^{119}Sn pair in **1**, one may omit, without losses, the $\pi_{(\pm x)}$ pulse in the middle of the period τ .

ACKNOWLEDGMENTS

Financial support of our work by the Deutsche Forschungsgemeinschaft and by Aventis Pharma, Paris, France, is gratefully acknowledged. Some experiments and calculations were carried out at the Bayerisches Geoinstitut under the EU Programme "IHP—Access to Research Infrastructures" Programme (Contract HPRI-1999-CT-00004 to D. C. Rubie). We thank W. Milius, Bayreuth, for providing the molecular structure of **1** from single-crystal X-ray diffraction measurements.

REFERENCES

1. For general review articles on recoupling methods under MAS NMR conditions see (i) A. E. Bennett, R. G. Griffin, and S. Vega, Recoupling of homo- and heteronuclear dipolar interactions in rotating solids, in: "Solid-State NMR. IV. Methods and Applications of Solid-State NMR" (B. Blümich, Ed.), NMR Basic Principles and Progress, Vol. 33, pp. 1–78, Springer-Verlag, Berlin (1994); (ii) S. Dusold and A. Sebald, Dipolar recoupling under magic-angle-spinning conditions, in: "Annual Reports on NMR Spectroscopy" (G. Webb, Ed.), Vol. 41, pp. 185–264, Academic Press, London (2000); and references given there.
2. E. R. Andrew, A. Bradbury, R. G. Eades, and V. T. Wynn, Nuclear cross relaxation induced by specimen rotation, *Phys. Lett.* **4**, 99–100 (1963).
3. D. P. Raleigh, M. H. Levitt, and R. G. Griffin, Rotational resonance in solid state NMR, *Chem. Phys. Lett.* **146**, 71–76 (1988).
4. M. H. Levitt, D. P. Raleigh, F. Creuzet, and R. G. Griffin, Theory and simulations of homonuclear spin pairs in rotating solids, *J. Chem. Phys.* **92**, 6347–6364 (1990).
5. A. Schmidt and S. Vega, The Floquet theory of nuclear magnetic resonance spectroscopy of single spins and dipolar coupled spin pairs in rotating solids, *J. Chem. Phys.* **96**, 2655–2680 (1992).
6. W. Milius, unpublished results.
7. N. C. Nielsen, F. Creuzet, R. G. Griffin, and M. H. Levitt, Enhanced double-quantum nuclear magnetic resonance in spinning solids at rotational resonance, *J. Chem. Phys.* **96**, 5668–5677 (1992).
8. R. R. Ernst, G. Bodenhausen, and A. Wokaun, "Principles of Nuclear Magnetic Resonance in One and Two Dimensions," Clarendon Press, Oxford (1987).
9. M. H. Levitt, The signs of frequencies and phases in NMR, *J. Magn. Reson.* **126**, 164–182 (1997).
10. U. Haeberlen, High resolution NMR in solids. Selective averaging, in: "Advances in Magnetic Resonance" (J. S. Waugh, Ed.), Supplement 1, Academic Press, New York (1976).
11. A. R. Edmonds, "Angular Momentum in Quantum Mechanics," Princeton Univ. Press, Princeton, NJ (1974).
12. S. Dusold and A. Sebald, Double-quantum filtration under rotational-resonance conditions: Numerical simulations and experimental results, *J. Magn. Reson.* **145**, 340–356 (2000).
13. M. Bechmann, X. Helluy, and A. Sebald, Double-quantum Filtered rotational-resonance MAS NMR in the Presence of large chemical shielding anisotropies, *J. Magn. Reson.* **152**, 14–25 (2001).
14. F. James and M. Roos, MINUIT computer code, Program D-506, CERN, Geneva (1977).
15. R. Challoner and A. Sebald, A double-quantum ^{119}Sn rotational-resonance study, *J. Magn. Reson. A* **122**, 85–89 (1996).

16. T. P. Lockhart, H. Puff, W. Schuh, H. Reuter, and T. N. Mitchell, *J. Organomet. Chem.* **366**, 61–72 (1989).
17. C. Marichal and A. Sebald, Anisotropy of $^2J(^{119}\text{Sn}, ^{117}\text{Sn})$ determined by off-magic-angle spinning ^{119}Sn NMR, *Chem. Phys. Lett.* **286**, 298–304 (1998).
18. S. Dusold and A. Sebald, Magnitudes and orientations of NMR interaction tensors in isolated three-spin systems ABX, *Mol. Phys.* **95**, 1237–1245 (1998).
19. C. Filip, X. Filip, M. Bertmer, D. E. Demco, and B. Blümich, Dipolar and J encoded DQ MAS spectra under rotational resonance, *J. Magn. Reson.* **150**, 184–193 (2001).
20. R. Benn, H. Grondey, C. Brevard, and A. Pagelot, The detection of connectivities of rare spin-1/2 nuclei in the solid state using natural abundance samples: ^{13}C and ^{29}Si INADEQUATE and COSY type experiments, *J. Chem. Soc. Chem. Commun.*, 102–103 (1988).
21. C. A. Fyfe, H. Gies, and Y. Feng, Demonstration of three-dimensional lattice connectivities in zeolites by two-dimensional high resolution solid state N.M.R. spectroscopy, *J. Chem. Soc. Chem. Commun.*, 1240 (1989).
22. C. A. Fyfe, Y. Feng, H. Gies, H. Grondey, and G. T. Kokotailo, Natural-abundance two-dimensional solid-state ^{29}Si NMR investigations of three-dimensional lattice connectivities in zeolite structures, *J. Am. Chem. Soc.* **112**, 3264–3270 (1990).
23. T. A. Early, B. K. John, and L. F. Johnson, Observation of homonuclear double-quantum correlations in plastic crystals using cross polarization and magic-angle spinning, *J. Magn. Reson.* **75**, 134–138 (1987).
24. I. D. Gay, C. H. W. Jones, and R. D. Sharma, INADEQUATE in the solid state. Homonuclear couplings in $[(\text{CH}_3)_2\text{SnE}]_3$, *J. Magn. Reson.* **91**, 186–189 (1991).
25. S. C. Christiansen, D. Zhao, M. T. Janicke, C. C. Landry, G. D. Stucky, and B. F. Chmelka, *J. Am. Chem. Soc.* **123**, 4519–4529 (2001).
26. A. Lesage, C. Auger, S. Caldarelli, and L. Emsley, Determination of through-bond carbon–carbon connectivities in solid-state NMR using the INADEQUATE experiment, *J. Am. Chem. Soc.* **119**, 7867–7868 (1997).
27. A. Lesage, M. Bardet, and L. Emsley, Through-bond carbon–carbon connectivities in disordered solids by NMR, *J. Am. Chem. Soc.* **121**, 10,987–10,993 (1999).
28. M. Baldus and B. H. Meier, Total correlation spectroscopy in the solid state. The use of scalar couplings to determine the through-bond connectivity, *J. Magn. Reson. A* **121**, 65–69 (1996).
29. M. Carravetta, M. Edén, X. Zhao, A. Brinkmann, and M. H. Levitt, Symmetry principles for the design of radiofrequency pulse sequences in the nuclear magnetic resonance of rotating solids, *Chem. Phys. Lett.* **321**, 205–215 (2000).
30. M. Baldus, R. J. Iulucci, and B. H. Meier, Probing through-bond connectivities and through-space distances in solids by magic-angle-spinning nuclear magnetic resonance, *J. Am. Chem. Soc.* **119**, 1121–1124 (1997).
31. R. J. Iulucci and B. H. Meier, A characterization of the linear P–O–P Bonds in $\text{M}^{4+}(\text{P}_2\text{O}_7)$ Compounds: Bond-angle determination by solid-state NMR, *J. Am. Chem. Soc.* **120**, 9059–9062 (1998).
32. X. Helluy, C. Marichal, and A. Sebald, Through-bond indirect and through-space direct dipolar coupling ^{31}P MAS NMR constraints for spectral assignment in the cubic $3 \times 3 \times 3$ superstructure of TiP_2O_7 , *J. Phys. Chem. B* **104**, 2836–2845 (2000).
33. (i) A. Bax, R. Freeman, and S. P. Kempell, Natural abundance ^{13}C – ^{13}C coupling observed via double-quantum coherence, *J. Am. Chem. Soc.* **102**, 4849–4951 (1980); (ii) A. Bax, R. Freeman, and S. P. Kempell, Investigation of ^{13}C – ^{13}C long-range couplings in natural-abundance samples, *J. Magn. Reson.* **41**, 349–353 (1980).

E. Selectivity of Double-Quantum Filtered Rotational-Resonance Recoupling Experiments on Larger-than-Two-Spin Systems

M. Bechmann, X. Helluy, and A. Sebald, *Perspectives on Solid State NMR in Biology*, series: *Focus on Structural Biology*, volume 1, Kihne, S.R.; de Groot, H.J.M. (eds.), 2001, 248 pages, Hardcover, Dordrecht/Netherlands, ISBN: 0-7923-7102-X.

<http://www.wkap.nl>

©2001 Kluwer Academic Publishers.

All rights are reserved by Kluwer Academic Publishers. The article is reproduced with the rights granted to the author.

Selectivity of Double-Quantum Filtered Rotational-Resonance Experiments on Larger-than-Two-Spin Systems

Matthias Bechmann, Xavier Helluy, and Angelika Sebald

Bayerisches Geoinstitut, Universität Bayreuth, 95440 Bayreuth, Germany

Introduction

Characterizing the orientation and molecular conformation of small organic molecules bound to the inner or outer surfaces of proteins represents an important step in drug design and in understanding the mechanisms of biochemical reactions, and similarly, of non-biological catalytic reactions. In a biochemical context, such molecular units or subunits may often contain only three or four carbon atoms, examples being the pyruvate anion, fumaric and maleic acid derivatives, or the phosphoenolpyruvate moiety in differing degrees of ionization. Magic-angle spinning (MAS) NMR experiments, capable of delivering reliable information about the conformational properties of these molecular units, have to combine several properties in order to be able to fulfill these tasks in realistic application situations. First, the ^{13}C resonances originating from the (fully or partially) ^{13}C enriched substrate molecules of interest have to be separable from additional natural-abundance ^{13}C resonances; this calls for the application of double-quantum filtration (DQF) techniques. Second, many of these small substrate molecules feature structural subunits that require using the orientation dependence of ^{13}C chemical shielding as the source of information about molecular conformation; this calls for MAS NMR experiments where magnitudes and orientations of chemical shielding tensors are sensitively reflected. Third, for reasons of synthetic feasibility, the chosen MAS NMR techniques must be applicable in a quantifiable manner to larger-than-two-spin systems. The ease and robustness of the experimental and numerical implementations are an additional consideration.

With these selection criteria in mind, we turn to the so-called rotational-resonance (R^2) condition [1-5] in conjunction with double-quantum filtration (DQF). In the context of larger-than-two-spin systems, a certain preserved narrowbandedness of (some of) the R^2 condition(s) can be at an advantage over more broadbanded alternatives, such as the DQ-DRAWS experiment [6] or the C7 sequence [7] and its

derivatives [8]. We will employ a recently introduced R^2 -DQF pulse sequence [9] to investigate aspects of selectivity when applying R^2 -DQF experiments to spin systems composed of more than two ^{13}C spins. We use the ^{13}C -three spin system in fully ^{13}C enriched sodium pyruvate, 1- U^{13}C , as our model case. 1- U^{13}C was chosen because i) the

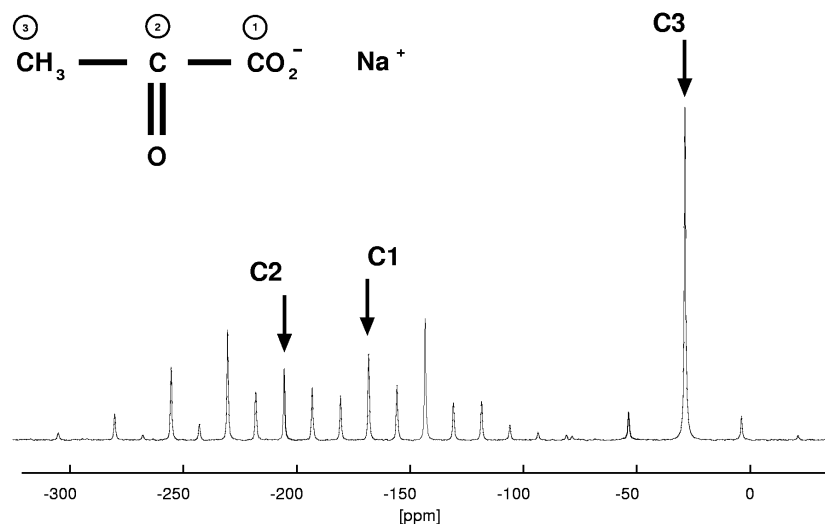


Fig. 1: ^{13}C MAS NMR spectrum of sodium pyruvate ($\omega_0/2\pi = -75.5$ MHz; $\omega_r/2\pi = 1888$ Hz) with ^{13}C in natural abundance; the assignment of the three ^{13}C isotropic chemical shielding values is indicated.

crystal structure of sodium pyruvate is known [10], ii) the parameters of its ^{13}C three-spin system have been determined [11], and iii) this spin system makes a range of rather different R^2 conditions accessible, as can be seen in Fig. 1, where a ^{13}C MAS NMR spectrum of sodium pyruvate with ^{13}C in natural abundance is depicted.

Methods

Fully ^{13}C -enriched sodium pyruvate, 1- U^{13}C , is commercially available (ISOTECH Inc., USA) and was used as received. ^{13}C R^2 -DQF experiments at ^{13}C Larmor frequency $\omega_0/2\pi = -50.3$ MHz were run on a Bruker MSL 200 NMR spectrometer using a 4 mm double-bearing CP MAS probe. A range of ^{13}C R^2 -DQF experiments on 1- U^{13}C and 1- $\text{U}^{13}\text{C}_{\text{dil}}$ (sample diluted by co-crystallization with ^{13}C natural abundance material in a 1:5 enriched:unenriched ratio) yielded identical spectral lineshapes.

The pulse sequence used for DQF at the $n = 1$ R^2 condition [9] is depicted in Fig. 2. Experimentally ^{13}C $\pi/2$ pulse durations of 3.5 μs and a c.w. ^1H decoupling amplitude of 83 kHz were employed.

The parameters of the ^{13}C spin system in solid sodium pyruvate [11] and a full description of the notation, definitions, and numerical simulation methods used are given elsewhere. [12]

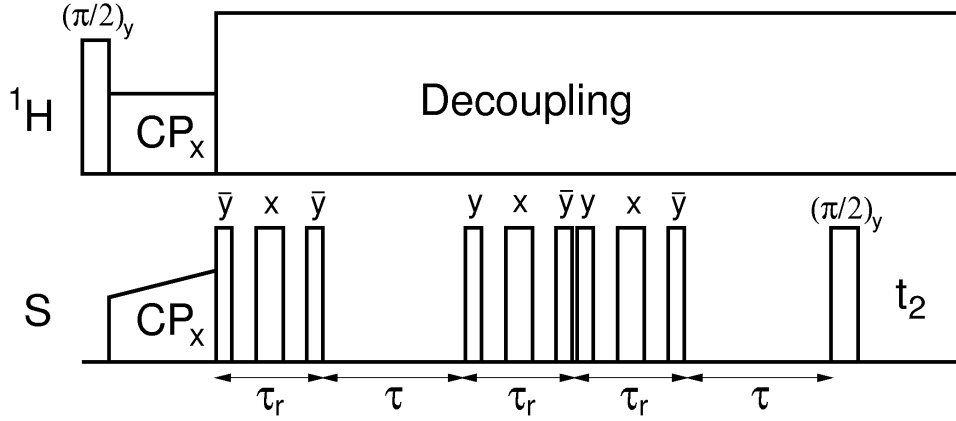


Fig. 2: Pulse sequence to achieve DQF at the $n = 1$ R^2 condition, where τ_r denotes rotation period, and the three-pulse subsequences consist of $\pi/4$ - $\pi/2$ - $\pi/4$ pulses [9].

Results and Discussion

For the R^2 -DQF pulse sequence ([9], see Fig. 2) it has been demonstrated that high R^2 -DQF efficiencies are achieved for large and small dipolar coupling interactions, provided that the chemical shielding anisotropies (csa; δ^{CS}) are substantially less than the difference in the isotropic chemical shielding, $n\omega_r = \omega_{iso}^\Delta \times \delta^{CS_{i,j}}$, with n being a small integer [11]. In the presence of large CSA's, another R^2 -DQF pulse sequence [13] maintains higher R^2 -DQF efficiencies.

The ^{13}C three-spin system in $\mathbf{1-U}^{13}\text{C}$ presents a set of three, rather different $n = 1$ R^2 conditions. When choosing the $^{13}\text{C}2$ - $^{13}\text{C}3$ pair, $\omega_{iso}^{\Delta_{23}} = \omega_r$ substantially exceeds the magnitude of all spin interactions in $\mathbf{1-U}^{13}\text{C}$. The $^{13}\text{C}1$ - $^{13}\text{C}3$ pair is similarly characterized by a fairly large value $\omega_{iso}^{\Delta_{13}}$, but features a much smaller dipolar coupling constant b_{13} than the $^{13}\text{C}2$ - $^{13}\text{C}3$ pair. The $n = 1$ R^2 condition for the $^{13}\text{C}1$ - $^{13}\text{C}2$ pair in $\mathbf{1-U}^{13}\text{C}$ differs strongly: these two ^{13}C spins are characterized by a small value of $\omega_{iso}^{\Delta_{12}}$, by substantial chemical shielding anisotropies, $\delta^{CS_{1,2}}$, and by a large value of b_{12} . At a ^{13}C Larmor frequency of $\omega_0/2\pi = -50.3$ MHz, $\delta^{CS_{1,2}}$ (considerably) and b_{12} (slightly) exceed ω_r . A comparison of theoretically expected (—) and experimentally observed (o) R^2 -DQF efficiencies, plotted as a function of τ , for these three $n = 1$ R^2 conditions in $\mathbf{1-U}^{13}\text{C}$ is shown in Fig. 3.

The trends in R^2 -DQF efficiencies for $\mathbf{1-U}^{13}\text{C}$ follow the expectations based on previous investigations of pairwise selectively $^{13}\text{C}2, ^{13}\text{C}3$ [11] and $^{13}\text{C}1, ^{13}\text{C}2$ [12] isotopomers of sodium pyruvate. The pulse sequence depicted in Fig. 2 yields fairly

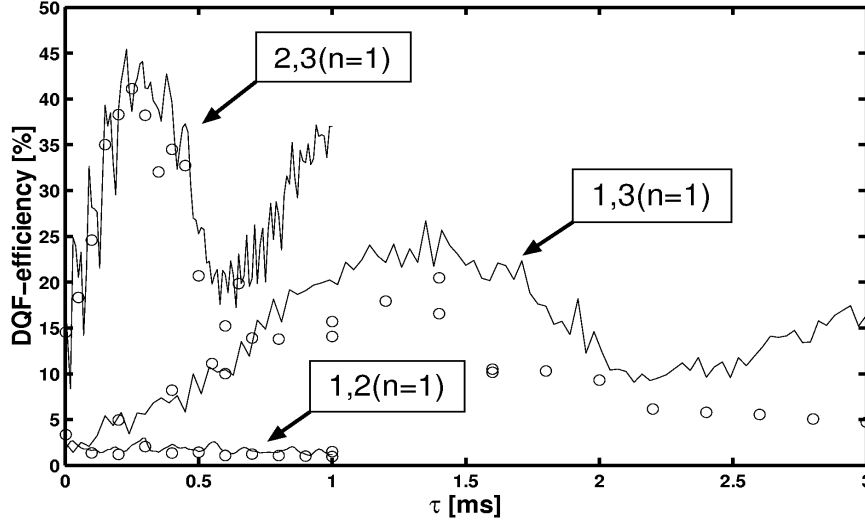


Fig. 3: Theoretically expected (—) and experimentally observed (o) $n = 1$ R^2 -DQF efficiencies in $\mathbf{1-U}^{13}\text{C}$, plotted as a function of τ . The simulations employ the known parameters of this ^{13}C three-spin system [11]; the individually chosen i,j R^2 conditions are indicated. The experimental data were obtained at $\omega_0 / 2\pi = -50.3$ MHz, with $\omega_r / 2\pi = 1832$ Hz ($^{13}\text{C1}, ^{13}\text{C2}$ pair), $\omega_r / 2\pi = 7020$ Hz ($^{13}\text{C1}, ^{13}\text{C3}$ pair), and $\omega_r / 2\pi = 8882$ Hz ($^{13}\text{C2}, ^{13}\text{C3}$ pair). The efficiency is given in percent with the integrated spectral intensity of the chosen i,j pair in the corresponding conventional R^2 spectrum taken as 100 percent.

high to high efficiencies for small and large dipolar coupling constants at R^2 conditions where ω_r considerably exceeds the chemical shielding anisotropies present. In the presence of substantial chemical shielding anisotropies, other sequences [13] yield higher efficiencies and offer a more suitable experimental route to the determination of chemical shielding tensor orientations from R^2 -DQF lineshapes [12].

The R^2 -DQF efficiency curves for the $^{13}\text{C2}, ^{13}\text{C3}$ pair in $\mathbf{1-U}^{13}\text{C}$ follow very closely the corresponding curves for the pairwise selectively $^{13}\text{C2}, ^{13}\text{C3}$ enriched isotopomer; in addition, the experimentally observed R^2 -DQF lineshapes for this spin pair in the two isotopomers were found to be indistinguishable [11]. This is further corroborated by numerical simulations employing three-spin calculations (see Fig. 4 a) or two-spin simulations (see Figure 4 b). The large difference in isotropic chemical shielding $\omega_{iso}^{\Delta_{23}}$ in conjunction with the $^{13}\text{C2}, ^{13}\text{C3}$ $n = 1$ R^2 (-DQF) condition reduces the three-spin system in $\mathbf{1-U}^{13}\text{C}$ to an effective $^{13}\text{C2}, ^{13}\text{C3}$ two-spin system. This simplification is accompanied by a reduced information content: under these specific $n = 1$ R^2 and R^2 -DQF conditions, only the magnitude of the dipolar coupling constant b_{23} is sensitively reflected in the resulting lineshapes.

Analogously, the situation for the $^{13}\text{C1}, ^{13}\text{C3}$ $n = 1$ R^2 -DQF lineshapes of $\mathbf{1-U}^{13}\text{C}$ is now examined more closely, addressing the situation where $\omega_{iso}^{\Delta_{13}} < \omega_{iso}^{\Delta_{23}}$, and $b_{13} \times$

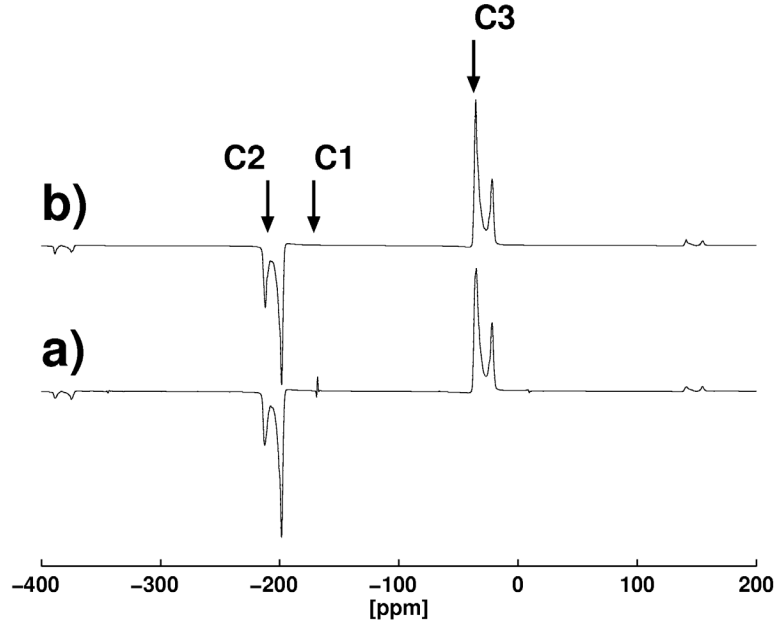


Fig. 4: Simulated $n = 1$ R^2 -DQF spectra for the $^{13}\text{C}2, ^{13}\text{C}3$ pair in $\mathbf{1-U}^{13}\text{C}$, with $\omega_0 / 2\pi = -50.3$ MHz, $\omega_r / 2\pi = 8882$ Hz, $\tau = 250$ μs , employing the known parameters of the pyruvate ^{13}C spin system. a): full three-spin simulation; b): two-spin simulation ignoring $^{13}\text{C}1$.

b_{23} . The smaller value $b_{13} / 2\pi = -430$ Hz does not dramatically reduce the R^2 -DQF efficiency since $\omega_{iso}^{\Delta_{13}} > \delta^{CS_1}$; but the slightly reduced overall efficiency as compared to the previous $^{13}\text{C}2, ^{13}\text{C}3$ case does arise as a function of the now slightly increased 'relative weight' of δ^{CS_1} in relation to $\omega_{iso}^{\Delta_{13}}$ as compared to the δ^{CS_2} to $\omega_{iso}^{\Delta_{23}}$ ratio. Of course, the smaller value $b_{13} / 2\pi = -430$ Hz is reflected in less pronounced splittings of the $^{13}\text{C}1, ^{13}\text{C}3$ selected $n = 1$ R^2 -DQF lineshapes of $\mathbf{1-U}^{13}\text{C}$. An experimental $^{13}\text{C}1, ^{13}\text{C}3$ selected $n = 1$ R^2 -DQF spectrum is shown in Fig. 5 a, in comparison with the corresponding simulated spectrum employing a three-spin simulation in Fig. 5 b. The two lineshapes agree quite well. Describing the spectrum by a $^{13}\text{C}1, ^{13}\text{C}3$ two-spin simulation with the known parameters of the two spins does not give acceptable agreement between experimentally measured and simulated lineshapes. Extending the $^{13}\text{C}1, ^{13}\text{C}3$ two-spin simulation to iterative fitting with b_{13} as a free fit parameter eventually leads to good agreement between experimental and best-fit simulated lineshapes (see Fig. 5 c). However, then the two-spin best-fit value found for b_{13} is -510 Hz. In other words: treating the $^{13}\text{C}1, ^{13}\text{C}3$ $n = 1$ R^2 -DQF lineshapes of $\mathbf{1-U}^{13}\text{C}$ as originating from a $^{13}\text{C}1, ^{13}\text{C}3$ two-spin system, underestimates the $^{13}\text{C}1$ - $^{13}\text{C}3$ internuclear distance as being 246 pm, compared to the known value of 260.5 pm. Similar deviations are found when using other experimental $^{13}\text{C}1, ^{13}\text{C}3$ selected $n = 1$ R^2 -DQF lineshapes of $\mathbf{1-U}^{13}\text{C}$ as input for simulations and iterative lineshape fits. There

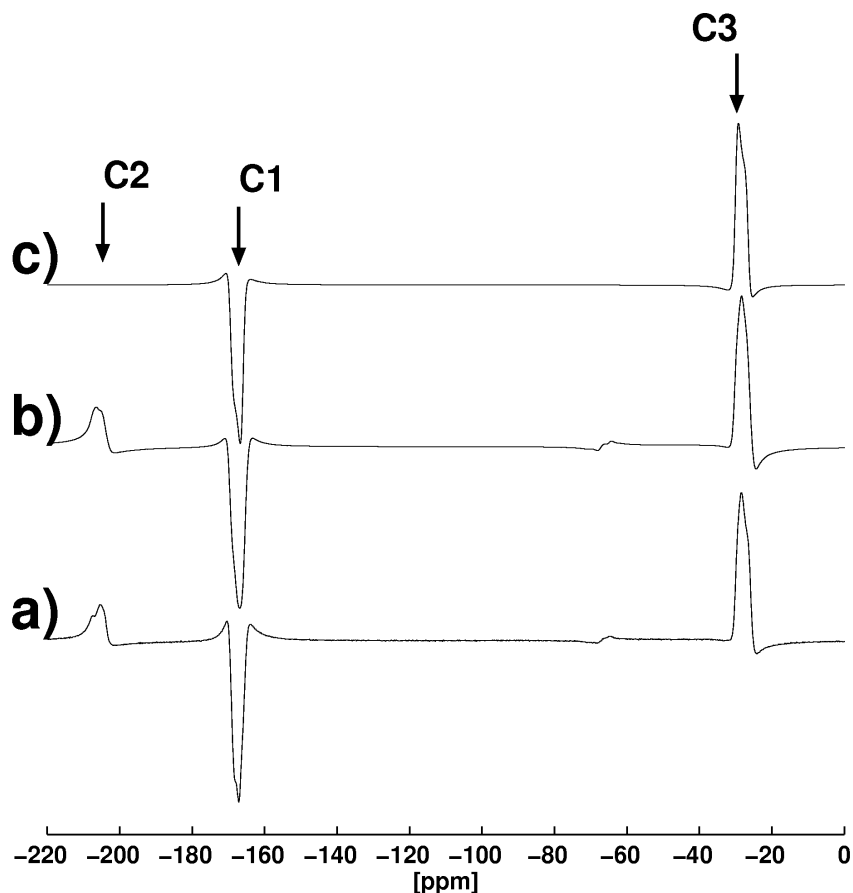


Fig. 5: $n = 1$ R^2 -DQF spectra for the $^{13}\text{C}1, ^{13}\text{C}3$ pair in $\mathbf{1-U}^{13}\text{C}$, with $\omega_0 / 2\pi = -50.3$ MHz, $\omega_r / 2\pi = 7020$ Hz, $\tau = 400$ μs , and employing the known parameters of the pyruvate ^{13}C spin system in the simulations. a): experimental spectrum; b): three-spin simulation; c): best-fit simulation with a $^{13}\text{C}1, ^{13}\text{C}3$ two-spin approximation, corresponding to $b_{13} / 2\pi = -510$ Hz. The simulations shown in b) and c) employ the known Euler angles $\Omega_{PC}^{CS_{1,3}}$.

may well be applications where this approximation would appear as sufficiently accurate.

A completely different situation is encountered with the R^2 -DQF spectra of $\mathbf{1-U}^{13}\text{C}$ adjusted for the $^{13}\text{C}1, ^{13}\text{C}2$ $n = 1$ R^2 condition, with $\delta^{CS_1} = 2.20 \omega_{iso}^{\Delta_{12}}$ and $\delta^{CS_2} = 2.95 \omega_{iso}^{\Delta_{12}}$. At $\omega_0 / 2\pi = -50.3$ MHz, the appropriate MAS frequency $\omega_r / 2\pi = 1832$ Hz is slightly less than the dipolar coupling constants b_{12} and b_{23} , and is fairly close to the $n = 4$ $^{13}\text{C}1, ^{13}\text{C}2$ and $n = 5$ $^{13}\text{C}2, ^{13}\text{C}3$ R^2 conditions, respectively. Figure 6 illustrates the properties of the $^{13}\text{C}1, ^{13}\text{C}2$ $n = 1$ selected R^2 -DQF spectra of $\mathbf{1-U}^{13}\text{C}$.

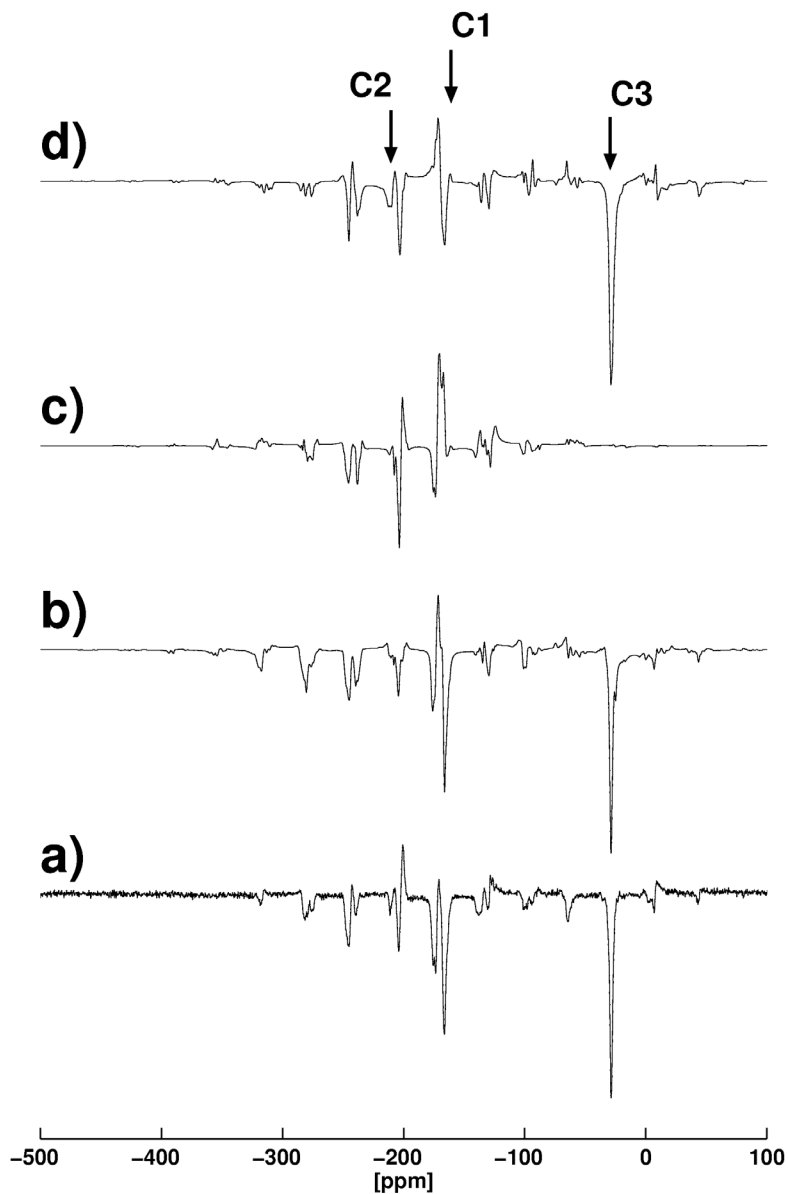


Fig. 6: $n = 1$ R^2 -DQF spectra for the $^{13}\text{C}1, ^{13}\text{C}2$ pair in $1\text{-U}^{13}\text{C}$, with $\omega_0 / 2\pi = -50.3$ MHz, $\omega_r / 2\pi = 1832$ Hz, $\tau = 700$ μs . a): experimental spectrum; b): three-spin simulation based on the known parameters from R^2 spectra [11]; c): same, but $^{13}\text{C}1, ^{13}\text{C}2$ two-spin simulation; d): three-spin simulation based on the known parameters of the spin system, but orientation of the ^{13}C chemical shielding tensors changed from the correct values $\Omega_{PC}^{\text{CS}_1} = \{135, 0, 0\}$, $\Omega_{PC}^{\text{CS}_2} = \{0, 95, 90\}$ to $\Omega_{PC}^{\text{CS}_1}_{\text{assumed}} = \{180, 90, 0\}$, $\Omega_{PC}^{\text{CS}_2}_{\text{assumed}} = \{0, 45, 0\}$.

An experimental spectrum, obtained with $\tau = 0.7$ ms is shown in Fig. 6 a, the corresponding simulated spectrum is displayed in Fig. 6 b. Agreement of the two

lineshapes is fairly good, though with some room for improvement: the spin system parameters of $\mathbf{1-U}^{13}\text{C}$ had previously been determined by iterative lineshape fitting of conventional R^2 spectra; it has been shown that csa orientational parameters are more sensitively reflected in R^2 -DQF lineshapes than in the corresponding R^2 spectra [12]. Clearly, describing this R^2 -DQF spectrum of $\mathbf{1-U}^{13}\text{C}$ by a $^{13}\text{C1}, ^{13}\text{C2}$ two-spin approximation is an invalid approximation (see Fig. 6 c). The simulated R^2 -DQF spectrum in Fig. 6 d illustrates that changes in the Euler angles $\Omega_{PC}^{CS_{1,2}}$, describing the orientations of the chemical shielding tensor orientations, are sensitively reflected in the R^2 -DQF lineshapes. Depending on the kind of information one is aiming to extract, one may consider the 'all included' character of these $^{13}\text{C1}, ^{13}\text{C2}$ $n = 1$ selected R^2 -DQF spectra of $\mathbf{1-U}^{13}\text{C}$ as a blessing or a curse. It is a blessing if, for instance, one wants to determine the absolute orientations of the chemical shielding tensors in a three-spin system from as few experimental spectra as possible. It is a curse if the main interest is focussed on the $^{13}\text{C1}, ^{13}\text{C2}$ pair itself. Then, however, it would be straightforward to emphasize the $^{13}\text{C1}, ^{13}\text{C2}$ two-spin character of these spectra, simply by running similar experiments at a (much) higher Larmor frequency.

Conclusions

A protocol that combines R^2 -DQF experiments [9,13] with iterative lineshape fitting approaches, based on numerically exact simulations should be capable of delivering complete information on the geometry of small, isolated molecules or molecular fragments in nearly unrestricted circumstances. With only minimal advance knowledge of the spin-system properties, it is possible to predefine a suitable set of three to four different R^2 -DQF experiments (pulse sequence, R^2 order, and/or Larmor frequency). Since the degree of selectivity of the various R^2 -DQF experiments can be tailored to some extent by the choice of the experimental R^2 conditions, a small set of one-dimensional R^2 -DQF spectra with complementary properties will be sufficient for the determination of the complete geometry of small molecular (sub)units. The R^2 -DQF sequence depicted in Fig. 2 [9] is particularly useful at R^2 conditions corresponding to high MAS frequencies and in the absence of chemical shieldings anisotropies. Other R^2 -DQF schemes [13] are more suitable for spin systems characterized by large chemical shielding anisotropies [12]. By focussing on short-range order questions, this combined experimental / numerical R^2 -DQF MAS NMR approach should be particularly useful in complementing diffraction experiments. Furthermore, it offers an experimental alternative for the indirect determination of molecular torsion angles from csa orientations for cases where a direct determination of these molecular geometries from so-called double-quantum heteronuclear local field experiments [14] is not possible, either due to the lack of a suitable $^1\text{H}, ^{13}\text{C}$ spin-(sub)system or due to a lack of spatial isolation of the ^1H part of an otherwise suitable $^1\text{H}, ^{13}\text{C}$ spin-(sub)system.

Acknowledgement

Support of our work by the Deutsche Forschungsgemeinschaft and the Fonds der Chemischen Industrie is gratefully acknowledged. X.H. acknowledges financial support by Aventis Pharma, Paris.

References

- [1] Andrew, E.R., Bradbury, A., Eades, R.G. and Wynn, V.T., *Phys. Lett.* 4 (1963) 99.
- [2] Raleigh, D. P., Levitt, M. H. and Griffin, R. G., *Chem. Phys. Lett.* 146 (1988) 71.
- [3] Levitt, M. H., Raleigh, D. P., Cruzet, F., and Griffin, R. G., *J. Chem. Phys.* 92 (1990) 6347.
- [4] Schmidt, A. and Vega, S., *J. Chem. Phys.* 96 (1992) 2655.
- [5] Nakai, T. and McDowell, C. A., *J. Chem. Phys.* 96 (1992) 3452.
- [6] Gregory, D. M., Wolfe, G. M., Jarvie, T. P., Sheils, J. C. and Drobny, G. P., *Molec. Phys.* 89 (1996) 1835.
- [7] Lee, Y. K., Kurur, N. D., Helmle, M., Johannessen, O. G., Nielsen, N. C. and Levitt, M. H., *Chem. Phys. Lett.* 242 (1995) 304.
- [8] For general review articles on recoupling methods under MAS NMR conditions see: i) Bennett, A. E., Griffin, R. G. and Vega, S., Recoupling of homo- and heteronuclear dipolar interactions in rotating solids, in: *Solid-State NMR IV: Methods and Applications of Solid-State NMR*, Vol. 33 NMR Basic principles and Progress (B. Blümich, Ed.), pp. 1-78, Springer Verlag, Berlin (1994); ii) Dusold, S. and Sebald A., Dipolar recoupling under magic-angle-spinning conditions, in: *Annual Reports on NMR Spectroscopy*, Vol. 41 (G. Webb, Ed.), pp. 185-264, Academic Press, London (2000); and references given therein.
- [9] Karlsson, T., Edén, M., Luthman, H. and Levitt, M. H., *J. Magn. Reson.* 145 (2000) 95.
- [10] Rach, W., Kiel, G. and Gattow, G., *Z. Anorg. Allg. Chem.* 563 (1988) 87.
- [11] Dusold, S. and Sebald, A., *J. Magn. Reson.* 145 (2000) 340.
- [12] Bechmann, M., Helluy, X. and Sebald, A., *J. Magn. Reson.* (2000), submitted.
- [13] Nielsen, N. C., Cruzet, F., Griffin, R. G. and Levitt, M. H., *J. Chem. Phys.* 96 (1992) 5668.
- [14] Feng, X., Lee, Y. K., Sandström, D., Edén, M., Maisel, H., Sebald, A. and Levitt, M. H., *Chem. Phys. Lett.* 257 (1996) 314.

F. MAS NMR with and without Double-Quantum Filtration at and near the $n = 0$ Rotational-Resonance Condition

M. Bechmann and A. Sebald, *Journal of Magnetic Resonance*, **173**, 296–304 (2005).

doi:10.1016/j.jmr.2004.12.012

©2005 Elsevier Inc.

All rights are reserved by Elsevier Science. The article is reproduced with the rights granted to the author.



MAS NMR with and without double-quantum filtration at and near the $n = 0$ rotational resonance condition

Matthias Bechmann¹, Angelika Sebald^{*1}

Bayrisches Geoinstitut, Universität Bayreuth, D-95440 Bayreuth, Germany

Received 26 September 2004; revised 20 December 2004

Available online 1 February 2005

Abstract

Spectral lineshapes of MAS NMR spectra of dipolar (re)coupled spin pairs exhibiting considerable chemical shielding anisotropies at and near the so-called $n = 0$ rotational resonance (R^2) condition are considered. The $n = 0$ R^2 condition is found to be not extremely sharp. Anisotropic interaction parameters such as chemical shielding tensor orientations and the magnitude of the dipolar coupling constant remain sensitively encoded in such lineshapes even when differences in isotropic chemical shielding values of up to 400 Hz (corresponding to ca. half the size of the dipolar coupling constant) are present. Additional double-quantum filtration (DQF) may enhance the sensitivity of spectral lineshapes to anisotropic interaction parameters for even larger differences in isotropic chemical shielding values. The dependence of the DQF efficiency on spin-system parameters as well as on external parameters (Larmor and MAS frequencies) is investigated. Away from R^2 conditions a trend to lower DQF efficiencies is found whereas some spin-system parameters are more sensitively encoded in the corresponding spectral lineshapes. Our study is based on numerical simulations, with the known parameters of the ^{31}P spin pair in $\text{Na}_4\text{P}_2\text{O}_7 \cdot 10\text{H}_2\text{O}$ representing our model case.

© 2005 Elsevier Inc. All rights reserved.

Keywords: MAS NMR; Rotational resonance; Double-quantum filtration; Numerical simulations

1. Introduction

Amongst the numerous solid-state NMR techniques designed to recouple anisotropic interactions in homo- and heteronuclear spin systems under magic angle spinning (MAS) conditions [1,2], the rotational resonance (R^2) phenomenon is quite unique [3–5]. R^2 recoupling is not achieved by the application of r.f. pulses but is triggered by the mechanical spinning of the rotor at specific MAS frequencies, matching small integer multiples of the isotropic chemical shielding difference ω_{iso}^A in homonuclear pairs of spins $S = 1/2$ such that $\omega_{\text{iso}}^A \approx n\omega_r$, where n is a small integer. Numerous stud-

ies in the literature have been concerned with the theoretical description of the R^2 phenomenon [6–10], with the exploitation of straightforward R^2 MAS NMR spectra for purposes of complete characterisation of small isolated clusters of spins [11–14] as well as of extended spin systems [15,16], with combining R^2 and double-quantum filtration (DQF) [17–21], and with expanding the applicability of the R^2 phenomenon to spin systems featuring small homonuclear dipolar coupling constants [22,23].

Here we focus on a specific R^2 condition, the so-called $n = 0$ R^2 condition [24]. This condition arises for homonuclear spin pairs with vanishing difference in isotropic chemical shielding, $\omega_{\text{iso}}^A = 0$, but with differing orientations of the two chemical shielding tensors. As there is no difference in isotropic shielding, the $n = 0$ R^2 condition persists at arbitrary spinning frequencies, including spinning frequencies greatly exceeding the

* Corresponding author. Fax: +49 921 55 3769.

E-mail address: angelika.sebald@uni-bayreuth.de (A. Sebald).

¹ Present address: Universität Dortmund, Fachbereich Physik, D-44221 Dortmund, Germany.

value of the dipolar coupling constant within the spin pair. The effect is the consequence of an intrinsic property of a given spin pair and obviously, if present but unwanted, a $n=0$ R^2 condition cannot be avoided or circumvented by choice of external experimental parameters such as MAS frequency or magnetic field strength. For instance, spins belonging to molecular sites related to each other by mirror symmetry or by a C_2 symmetry axis fulfill the requirements for the occurrence of the $n=0$ R^2 condition [11,24,25]. In fact, the presence of such symmetry-related (molecular) sites is fairly common in small molecules as well as in extended three-dimensional network structures. Even more common as a structural motif are pairs of sites representing a situation close to the $n=0$ R^2 condition, that is the two sites are not strictly related by a proper symmetry operation but are not deviating much from this situation. In terms of MAS NMR, this $n \approx 0$ R^2 scenario will often lead to spin pairs characterised by a small difference in isotropic chemical shielding ω_{iso}^A , with ω_{iso}^A often being smaller than any of the remaining interaction parameters. Distinguishing MAS NMR spectra of spin pairs at or near the $n=0$ R^2 condition from each other is not possible simply by inspection, the distinction requires careful analysis by means of numerically exact simulations [26].

Because of the common occurrence of structural features leading to MAS NMR conditions at or near the $n=0$ R^2 condition, in the following we will investigate in some detail the dependence of $n=0$ and $n \approx 0$ R^2 conditions on spin-system properties and on external experimental parameters. We will consider straightforward MAS NMR spectra as well as spectra obtained under DQF conditions. Our starting point is represented by the known properties of the ^{31}P spin pair in $\text{Na}_4\text{P}_2\text{O}_7 \cdot 10\text{H}_2\text{O}$ [11]: since the two phosphorus sites in the P_2O_7 unit are related by a C_2 axis bisecting the P–O–P bond angle, the two ^{31}P spins constitute a $n=0$ R^2 case. Our investigation will mainly rest on numerically exact simulations.

2. Experimental

2.1. ^{31}P MAS NMR

Some experimental ^{31}P MAS NMR spectra of $\text{Na}_4\text{P}_2\text{O}_7 \cdot 10\text{H}_2\text{O}$ (commercially available (Aldrich Chemicals)) were recorded on Bruker MSL 200 and MSL 300 NMR spectrometers. The corresponding ^{31}P Larmor frequencies $\omega_0/2\pi$ are -81.0 and -121.5 MHz, respectively. ^{31}P chemical shielding is quoted with respect to $\omega_{\text{iso}}^{\text{CS}} = 0$ ppm for the ^{31}P resonance of 85% H_3PO_4 . MAS frequencies were generally in the range $\omega_r/2\pi = 2400$ – 8000 Hz and were actively controlled to within ± 2 Hz. The sample was contained in a standard 4 mm o.d. ZrO_2 rotor. Cross polarisation with a contact

time of 1 ms was employed, ^{31}P $\pi/2$ pulse durations were 3.0 μs , c.w. ^1H decoupling with amplitudes of 83.3 kHz was applied during signal acquisition.

The R^2 -DQF MAS NMR experiment chosen for recording some experimental spectra as well as for all simulations, is the simple COSY-like sequence $\text{CP}_{(x)} - \tau - (\pi/2)_{(y)} - \Delta - (\pi/2)_{(x)}$ -acquisition [17] where ϕ indicates phase cycling suitable for DQF [27]. The duration of Δ was fixed as $\Delta = 3 \mu\text{s}$, the duration of τ was varied.

2.2. Definitions, notation, and numerical simulations

Shielding notation [28] is used throughout. For the interactions $\lambda = \text{CS}$ (chemical shielding), $\lambda = \text{D}$ (direct dipolar coupling), and $\lambda = \text{J}$ (indirect dipolar (J) coupling) the isotropic part $\omega_{\text{iso}}^\lambda$, the anisotropy $\omega_{\text{aniso}}^\lambda$, and the asymmetry parameter η^λ relate to the principal elements of the interaction tensor ω^λ as follows [29]: $\omega_{\text{iso}}^\lambda = (\omega_{xx}^\lambda + \omega_{yy}^\lambda + \omega_{zz}^\lambda)/3$, $\omega_{\text{aniso}}^\lambda = \omega_{zz}^\lambda - \omega_{\text{iso}}^\lambda$, and $\eta^\lambda = (\omega_{yy}^\lambda - \omega_{xx}^\lambda)/\omega_{\text{aniso}}^\lambda$ with $|\omega_{zz}^\lambda - \omega_{\text{iso}}^\lambda| \geq |\omega_{xx}^\lambda - \omega_{\text{iso}}^\lambda| \geq |\omega_{yy}^\lambda - \omega_{\text{iso}}^\lambda|$. For indirect dipolar coupling $\omega_{\text{iso}}^J = \pi J_{\text{iso}}$, and for direct dipolar coupling $\eta^D = \omega_{\text{iso}}^D = 0$ and $\omega_{\text{aniso}}^{Dij} = b_{ij} = -\mu_0 \gamma_i \gamma_j \hbar / (4\pi r_{ij}^3)$, where γ_i , γ_j denote gyromagnetic ratios and r_{ij} is the internuclear distance between spins S_i , S_j . The Euler angles $\Omega_{IJ} = \{\alpha_{IJ}, \beta_{IJ}, \gamma_{IJ}\}$ [30] relate axis system I to axis system J , where I , J denote P (principal axis system, PAS) and C (crystal axis system, CAS), respectively. Here it is convenient to define the PAS of the dipolar coupling tensor ω_{ij}^D as the CAS, $\Omega_{PC}^{Dij} = \{0, 0, 0\}$.

Our procedures for numerically exact spectral line-shape simulations and iterative fitting are fully described and discussed in detail elsewhere, in particular addressing the $n=0$ R^2 condition for isolated homonuclear spin pairs [11] and various $n=0, 1, 2$ R^2 conditions in an isolated homonuclear ^{13}C four-spin system [13]. In general, these numerical procedures employ the REPULSION [31] scheme for the calculation of powder averages, implement some of the routines of the GAMMA package [32] and use, where possible, the γ -COMPUTE approach [33–36]. The pulse sequence of the R^2 -DQF experiment [17] is not synchronous with the MAS rotation period and simulation of the underlying spin dynamics hence requires application of the so-called direct method for the calculation of the time evolution. Calculations may be considerably accelerated by using a cluster of processors and splitting up, for instance, the calculation of powder averages into several parallel calculations. The Linux PC cluster used here consists of 16 processors (450 MHz). This combination of hard- and software leads to typical computation times of 23 s for the calculation of a R^2 -DQF MAS NMR spectrum. Calculations of error scans and other error minimisation tasks employ the MINUIT [37] and MATLAB packages [38].

Table 1 lists the parameters of the ^{31}P spin pair in $\text{Na}_4\text{P}_2\text{O}_7 \cdot 10\text{H}_2\text{O}$ [11].

Table 1
NMR parameters of the ^{31}P spin pair in $\text{Na}_4\text{P}_2\text{O}_7 \cdot 10\text{H}_2\text{O}$ [11]

	$^{31}\text{P}_1$	$^{31}\text{P}_2$
$\omega_{\text{iso}}^{\text{CS}}$ (ppm) ^a	+2.3	+2.3
$\omega_{\text{aniso}}^{\text{CS}}$ (ppm)	-79 ± 1	-79 ± 1
η^{CS}	0.35 ± 0.1	0.35 ± 0.1
$\alpha_{\text{PC}}^{\text{CS}}$ (°) ^a	-117 ± 4	-117 ± 4
$\beta_{\text{PC}}^{\text{CS}}$ (°) ^a	-23 ± 2	157 ± 2
$\gamma_{\text{PC}}^{\text{CS}}$ (°) ^a	0 ± 6	180 ± 6
$b_{12}/2\pi$ (Hz)	-791	-791
$^2J_{\text{iso}}$ (Hz)	-19.5 ± 2.5	-19.5 ± 2.5

^a The two ^{31}P chemical shielding tensors are related by C_2 symmetry; the Euler angles are given relative to the principal axis system of the $^{31}\text{P}_1$ - $^{31}\text{P}_2$ dipolar coupling tensor.

3. Results and discussion

Some experimental and best-fit simulated (see Table 1) $n = 0$ R^2 ^{31}P MAS NMR spectra of $\text{Na}_4\text{P}_2\text{O}_7 \cdot 10\text{H}_2\text{O}$, with and without DQF, are shown in Fig. 1, illustrating the typical lineshape effects, broadenings and splittings, encountered at the $n = 0$ R^2 condition as well as the commonly observed dispersion lineshapes under these DQF conditions. The ^{31}P spin pair in $\text{Na}_4\text{P}_2\text{O}_7 \cdot 10\text{H}_2\text{O}$ may be considered as a prototype of an isolated spin pair where chemical shielding is the largest anisotropic interaction tensor but not overwhelmingly so: with the ^{31}P chemical shielding anisotropy amounting to $\omega_{\text{aniso}}^{\text{CS}} = -79 \pm 1$ ppm, at $\omega_0/2\pi = -81.0$ MHz and at $\omega_0/2\pi = -121.5$ MHz, $\omega_{\text{aniso}}^{\text{CS}}$ is about 8–10 times larger

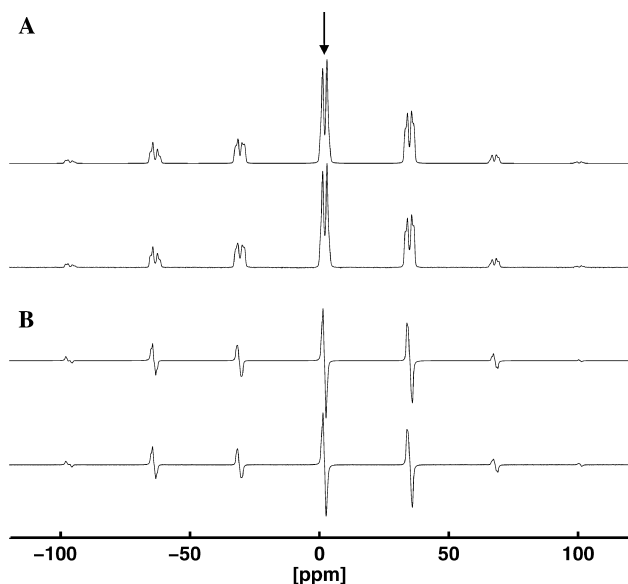


Fig. 1. ^{31}P MAS NMR spectra of $\text{Na}_4\text{P}_2\text{O}_7 \cdot 10\text{H}_2\text{O}$ ($\omega_0/2\pi = -121.5$ MHz, $\omega_r/2\pi = 4000$ Hz). (A) Conventional $n = 0$ R^2 MAS NMR spectrum, experimental spectrum (bottom trace) and best-fit simulation (top trace). (B) $n = 0$ R^2 -DQF MAS NMR spectrum, experimental spectrum (bottom trace) and best-fit simulation (top trace). The arrow indicates isotropic chemical shielding, parameters see Table 1.

than the dipolar coupling constant ($b_{ij}/2\pi = -791$ Hz), whereas the indirect coupling constant, $^2J_{\text{iso}}(^{31}\text{P}, ^{31}\text{P}) = -19.5 \pm 2.5$ Hz is comparatively small [11]. This constellation is not only typical for ^{31}P spin systems in many inorganic condensed phosphates but may also be encountered, at various magnetic field strengths, in spin systems composed of other isotopes in a wide range of chemical compounds, including ^{13}C in isotopically labelled organic molecules. Accordingly, our results do not only reflect the NMR properties of a particular spin system in a particular compound but should be seen as representative for spin systems with properties similar to those of the ^{31}P spin pair chosen as our example.

In the following we will first consider lineshapes of a range of MAS NMR spectra at and near the $n = 0$ R^2 condition, focussing on the sensitivity with which various anisotropic interaction tensors are reflected by these spectral lineshapes, both with and without the application of DQF. Section 2 will deal with aspects of DQF efficiencies, again for a range of differences in isotropic chemical shielding, covering the whole range from $\omega_{\text{iso}}^A = 0$ up to values of ω_{iso}^A being equivalent to $n = 1$ R^2 conditions, assuming different Larmor and MAS frequencies.

3.1. Sensitivities of lineshapes to spin-pair parameters

All anisotropic interaction parameters present are usually sensitively encoded in the spectral lineshapes at the $n = 0$ R^2 condition (see Fig. 1, Table 1) at modest MAS frequencies. In practical terms this means that such experimental lineshapes may be used to extract these parameters by lineshape simulations in conjunction with iterative fitting approaches, and thus to characterise the parameters of a spin pair in a comprehensive way from few, experimentally straightforward spectra. Here we take essentially the opposite approach. We take the known set of parameters describing the ^{31}P spin pair in $\text{Na}_4\text{P}_2\text{O}_7 \cdot 10\text{H}_2\text{O}$ and use these parameters to calculate hypothetical spectra for a range of values ω_{iso}^A , ranging from $\omega_{\text{iso}}^A = 0$ to ω_{iso}^A being equivalent to the $n = 1$ R^2 condition. These calculations are carried out for several different Larmor frequencies $\omega_0/2\pi$ and for several different MAS frequencies $\omega_r/2\pi$. Each of these calculated spectra in a next step is subjected to computing error scans for each of the anisotropic interaction parameters of the spin pair. In this way a map is created that permits us to predict which parameters are likely to be sensitively encoded in MAS NMR spectra, depending on the value of the difference in isotropic chemical shielding, ω_{iso}^A , of the two spins in a spin pair.

The results of these calculations for the Euler angle $\beta_{\text{PC}}^{\text{CS}}$ and for the dipolar coupling constant $b_{ij}/2\pi$ are summarised in Fig. 2, assuming straightforward MAS NMR spectra being recorded. The rows (A), (B), and (C) in Fig. 2 assume different MAS frequencies $\omega_r/2\pi =$

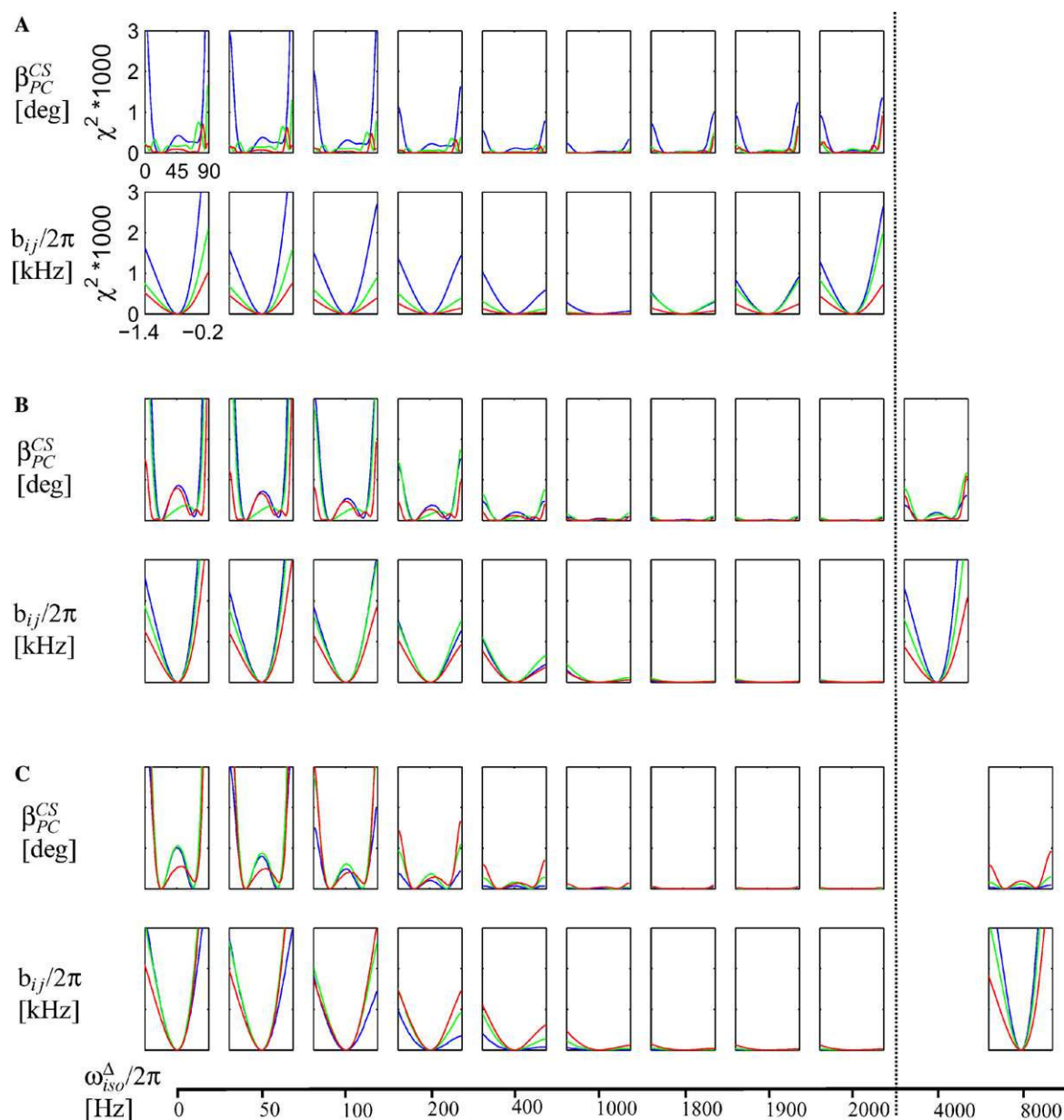


Fig. 2. Selection of error scans for β_{PC}^{CS} (0° – 90°) and $b_{ij}/2\pi$ (-1400 to -200 Hz) each, based on simulated MAS NMR spectra (parameters see Table 1). In the columns from left to right ω_{iso}^A is incremented as indicated by the scale at the bottom. Colours indicate different Larmor frequencies where red corresponds to $\omega_0/2\pi = -202.5$ MHz, green to $\omega_0/2\pi = -121.5$ MHz, and blue to $\omega_0/2\pi = -81.0$ MHz, respectively. Scans are shown for $\omega_r/2\pi = 2000$ Hz (A), $\omega_r/2\pi = 4000$ Hz (B), and $\omega_r/2\pi = 8000$ Hz (C).

2 kHz, $\omega_r/2\pi = 4$ kHz, and $\omega_r/2\pi = 8$ kHz, respectively. The columns in Fig. 2 increment the value of ω_{iso}^A from $\omega_{iso}^A = 0$ to ω_{iso}^A being equivalent to the three $n = 1$ R^2 conditions, as indicated by the scale at the bottom. The colours in each segment indicate three different Larmor frequencies, blue traces assume $\omega_0/2\pi = -81.0$ MHz, green traces $\omega_0/2\pi = -121.5$ MHz, and red traces $\omega_0/2\pi = -202.5$ MHz. Only the minimum regions of each error scan are plotted. The main findings are as follows. Clearly, the $n = 0$ R^2 condition is not extremely sharp. Independent of the Larmor frequency, always up to $\omega_{iso}^A \approx 400$ Hz, that is up to $\omega_{iso}^A \approx 0.5 b_{ij}/2\pi$,

both β_{PC}^{CS} and b_{ij} remain encoded in the spectral lineshapes. Increasing ω_{iso}^A further, covering the region in-between the $n = 0$ R^2 condition and the $n = 1$ R^2 conditions, not surprisingly leaves a region in which none of these parameters are encoded in the lineshapes. In this intermediate region, spectra are strongly dominated by the magnitude of the chemical shielding tensors. Sensitivity of the spectral lineshapes to further anisotropic interaction parameters is recovered upon increasing ω_{iso}^A further, approaching the $n = 1$ R^2 regime. Again, also the $n = 1$ R^2 condition is not extremely sharp, displaying a similar $n \approx 1$ R^2 region as does the

$n = 0$ R^2 condition, spanning approximately ± 400 Hz, equivalent to approximately $0.5 b_{ij}/2\pi$.

Fig. 2 further indicates that, at and near the $n = 0$ R^2 condition, both the dipolar coupling constant b_{ij} and the Euler angle β_{PC}^{CS} are best defined from the lineshapes of ^{31}P MAS NMR spectra obtained at $\omega_0/2\pi = -81.0$ MHz. As far as b_{ij} is concerned one may be intuitively inclined to predict that this parameter might be best obtained from experimental spectra run at a moderate Larmor frequency. Regarding the orientation of the ^{31}P chemical shielding tensor, this finding may seem more surprising as one may tend to predict that chemical shielding tensor parameters may become more sensitively encoded as one operates at higher Larmor frequencies. An optimum Larmor frequency where simultaneously chemical shielding and dipolar coupling parameters are encoded with the highest sensitivities in spectral lineshapes of homonuclear spin pairs at or near the $n = 0$ R^2 condition depends on the ratio of the chemical shielding anisotropy $\omega_{\text{aniso}}^{CS}$ to the dipolar coupling constant b_{ij} , as well as on the spinning frequency ω_r . The optimum choice of experimental conditions is then in a regime where $\omega_{\text{aniso}}^{CS} \leq 8b_{ij}$ and $\omega_r \leq \omega_{\text{aniso}}^{CS} \leq 2\omega_r$. The same choice of the experimental parameters ω_r and ω_0 remains the optimum regime with the highest sensitivities of spectral lineshapes to all interaction parameters for a wide range of chemical shielding tensor orientations (simulations not shown). Fig. 2 illustrates another general trend. One can generally expect to be able to extract magnitudes of interaction tensors with the highest accuracy from those experimental spectra in which these parameters are encoded with the highest sensitivity. The situation regarding expected accuracies is slightly more complicated regarding the orientational parameters where highest sensitivities do not necessarily correlate with highest accuracies. For example (see Fig. 2A), β_{PC}^{CS} is most sensitively encoded at a Larmor frequency $\omega_0/2\pi = -81.0$ MHz, though with a fairly broad minimum-error region, whereas a slightly lower sensitivity combined with a more sharply defined minimum region is found at $\omega_0/2\pi = -121.5$ MHz.

Similar to the $n \approx 0$ R^2 scenario considered here, optimum experimental conditions exist for isolated spin-1/2 cases when aiming at the determination of the eigenvalues of the chemical shielding tensor from MAS NMR spectra, where an optimum choice of Larmor and MAS frequency would generate about 6–10 spinning sidebands [39]. Also for the full characterisation of some heteronuclear spin pairs from MAS NMR spectra an optimum choice of the experimental parameters can be predicted, where a ratio of $\omega_r:b_{ij} \approx 1:6$ turns out the most suitable condition for full spectral analysis [40].

Next, we consider the spectral lineshapes resulting from additional application of DQF. This is summarised in Fig. 3. The set of error scans is identical to the set dis-

played in Fig. 2, except that now all error scans refer to spectral lineshapes obtained after application of a COSY-like DQF pulse sequence. Whereas under conventional MAS NMR conditions an intermediate regime of ω_{iso}^A exists where spectral lineshapes are insensitive to chemical shielding tensor orientations and dipolar coupling, no such regime exists anymore after DQF. Essentially for the entire range of values ω_{iso}^A , from the $n = 0$ R^2 condition all the way to the $n = 1$ R^2 condition, spectral lineshapes now reflect all anisotropic parameters of the spin pair. Note that in some regions orientational and dipolar coupling parameters are more sensitively encoded away from the $n = 0$ R^2 condition than at or very near the $n = 0$ R^2 condition. All other trends remain the same as under conventional MAS NMR conditions. This increased sensitivity of the lineshapes to all spin-system parameters could be seen as good news if one is aiming at the full characterisation of these parameters from spectral lineshapes. In fact, applying DQF even if not necessary for reasons of background suppression of unwanted signals, can be beneficial for the characterisation of homonuclear spin pairs at or near the $n = 0$ R^2 condition [26]. The vanishing of an intermediate regime inbetween R^2 conditions which is insensitive to orientational parameters, however, may also be an unwanted feature. For instance, when aiming to determine internuclear distances without having to pay attention to magnitudes and orientations of the chemical shielding tensors involved, sensitivity of experimental spectra to these parameters is certainly not a helpful feature. The extent and precise location of regions where spectra are highly sensitive to all spin-system parameters will vary slightly, depending on the pulse sequence used (including so-called γ -encoded pulse sequences [41]). Nevertheless, it is to be expected that almost always for certain regions over the range of ω_{iso}^A all spin-system parameters need to be taken into account to obtain precise information, for instance, about internuclear distances based on the evaluation of dipolar coupling interactions [42].

3.2. DQF efficiencies at and near the $n = 0$ R^2 condition

Excellent signal-to noise ratio in experimental spectra is an important prerequisite for the meaningful analysis of spectral lineshapes. Accordingly, consideration of DQF efficiencies plays an important part in the experimental work. Fig. 4 gives an overview of trends for the COSY-like DQF approach. Fig. 4A depicts DQF efficiencies at the $n = 0$ R^2 condition, plotted as a function of the duration of the excitation period τ , and considers the effect of different MAS frequencies ω_r . As one can see (from left to right), increasing ω_r leads to a decrease in overall DQF efficiency, and the overall maximum shifts to longer durations of τ . As usual, maxima of DQF efficiency occur when τ equals an integer

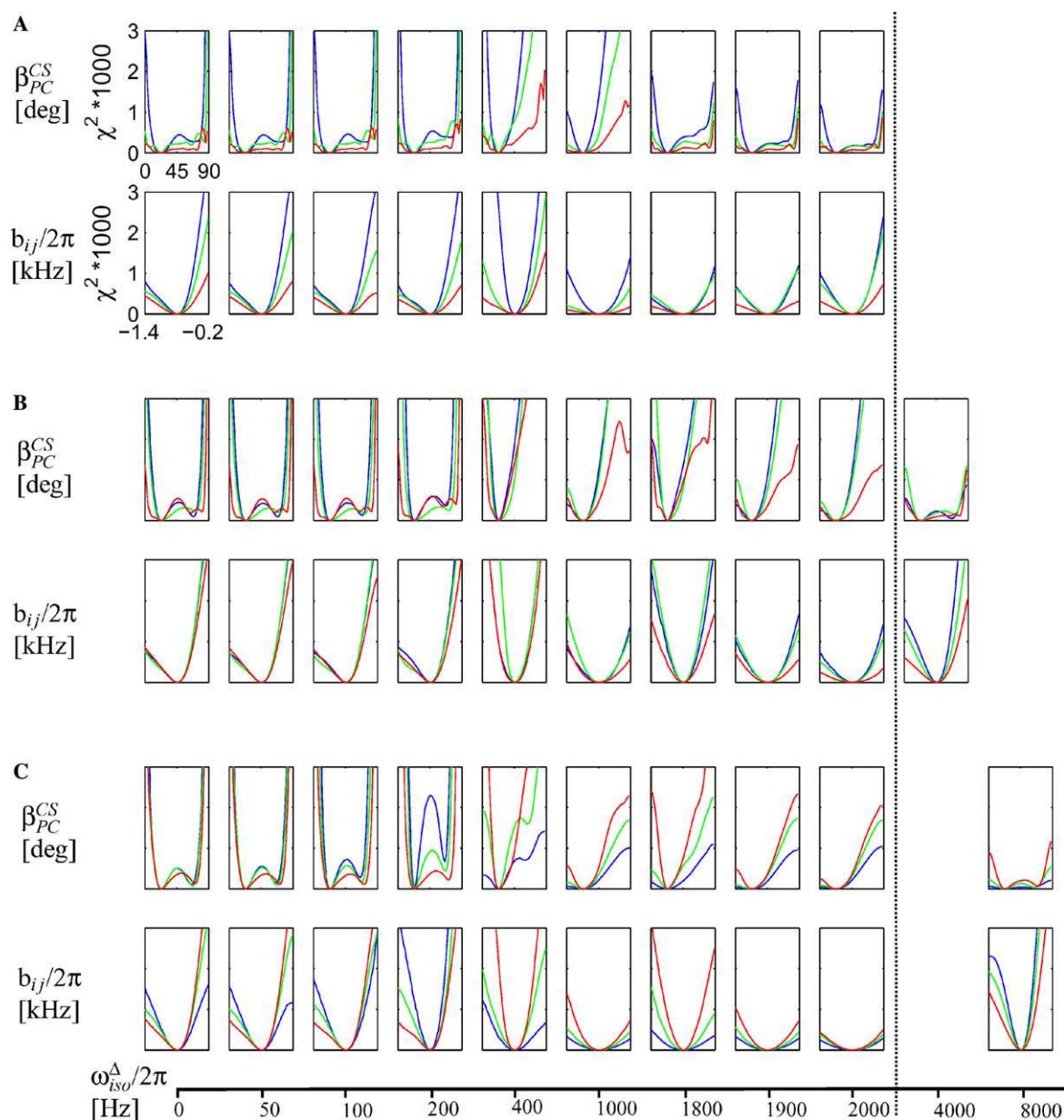


Fig. 3. Same as Fig. 2, except that now error scans are shown for R^2 -DQF MAS NMR spectra with $\tau = 2$ ms.

multiple of a rotation period. Fig. 4B illustrates another practically important point. The only difference between this graph and Fig. 4A is that now ω_{iso}^A is taken as $\omega_{\text{iso}}^A = 400$ Hz, whereas before $\omega_{\text{iso}}^A = 0$. Obviously, away from the $n = 0$ R^2 condition, there is a general decrease in DQF efficiency with maxima in DQF efficiency now appearing at durations of τ that are quite different from those where maximum DQF efficiency occurs when the $n = 0$ R^2 condition is fulfilled. Fig. 4C expands on this aspect by depicting DQF efficiencies for several different durations of τ plotted as a function of ω_{iso}^A . The ‘broadness’ of the regions around the R^2 conditions with reasonable DQF efficiencies varies as a function of τ , as does the maximum DQF efficiency. DQF efficiencies of

approximately 25% at the $n = 0$ R^2 condition and approximately 10% when $\omega_{\text{iso}}^A = 400$ Hz may seem rather low and will only be sufficient for some practical applications where signal-to-noise is not a limiting factor. In the presence of fairly large chemical shielding anisotropies, however, DQF efficiencies are generally low [41]. Amongst the many pulse sequences suitable for DQF under MAS conditions, the simple COSY-like sequence performs relatively well in the presence of large chemical shielding anisotropies [20].

Here we have not varied any of the spin-system parameters except ω_{iso}^A . Of course, also the relative magnitudes and orientations of $\omega_{\text{aniso}}^{\text{CS}}$ and b_{ij} generally play an important role in defining the maximum DQF effi-

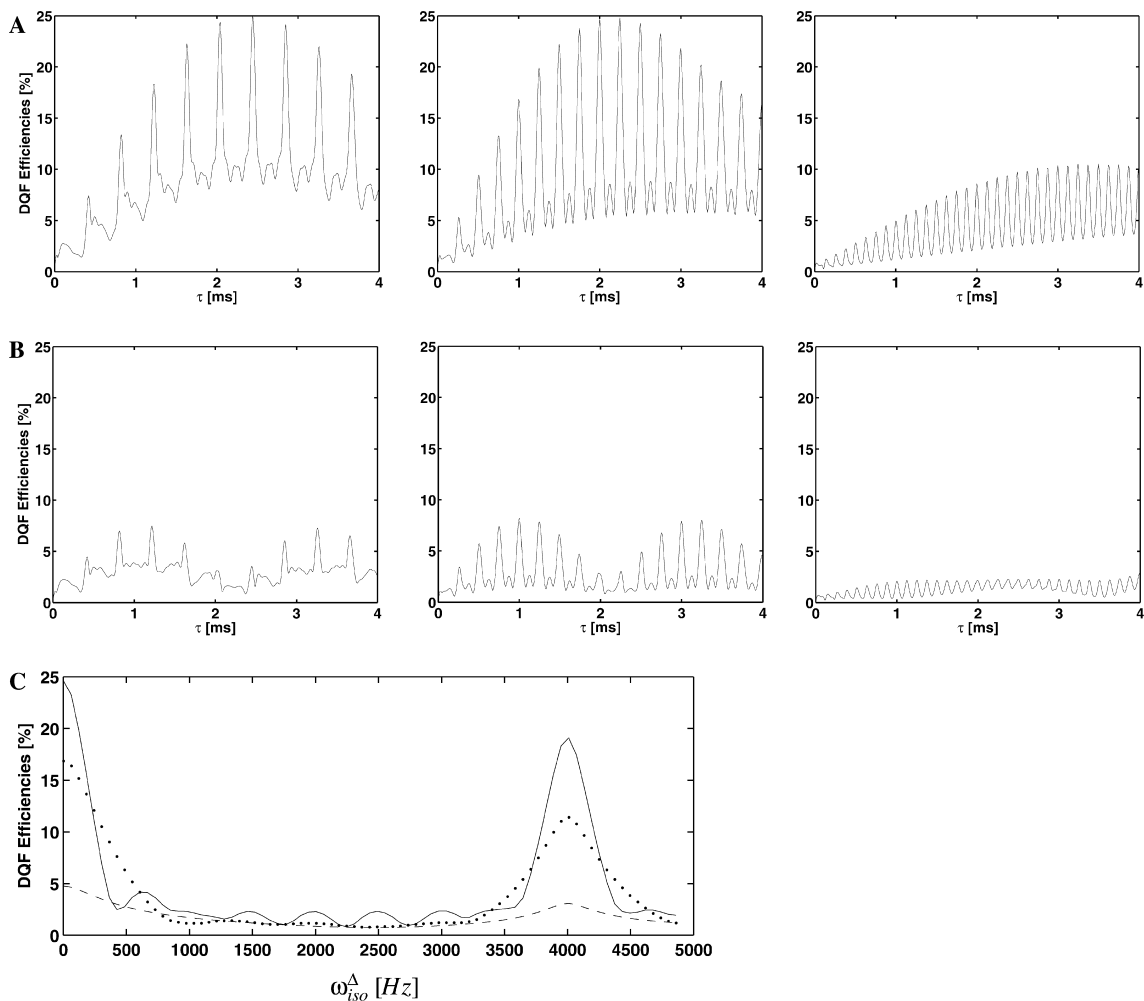


Fig. 4. DQF efficiencies plotted as a function of τ (A and B) and ω_{iso}^A (C); simulations based on spin-pair parameters given in Table 1 and assuming $\omega_0/2\pi = -121.5$ MHz. (A) $\omega_{iso}^A = 0$; from left to right $\omega_r/2\pi = 2454$ Hz, $\omega_r/2\pi = 4000$ Hz, and $\omega_r/2\pi = 8000$ Hz. (B) $\omega_{iso}^A = 400$ Hz; from left to right $\omega_r/2\pi = 2454$ Hz, $\omega_r/2\pi = 4000$ Hz, and $\omega_r/2\pi = 8000$ Hz. (C) $\omega_r/2\pi = 4000$ Hz, $\tau = 8\tau_r = 2$ ms (—), $\tau = 4\tau_r = 1$ ms (●●●), $\tau = \tau_r = 0.5$ ms (- - -).

ciencies. For instance, we find that increasing ω_{aniso}^{CS} at the $n = 0$ R^2 condition tends to shift the DQF maximum to occur at longer durations of τ , whereas no such clear-cut trends can be seen away from the $n = 0$ R^2 condition.

4. Summary and conclusions

The so-called $n = 0$ R^2 condition covers a considerable range of values ω_{iso}^A , from $\omega_{iso}^A = 0$ up to $\omega_{iso}^A \approx 0.5b_{ij}$ (here ca. 400 Hz). This perseverance of linebroadening and -splitting effects may add complexity to the interpretation of simple MAS NMR spectra of dipolar coupled spin systems, for instance ^{31}P MAS NMR spectra of condensed phosphates or ^{13}C MAS NMR spectra of ^{13}C enriched compounds. On the other hand, this property lends a higher information content to simple MAS NMR spectra as these then sensitively reflect anisotropic spin-system parameters such as the orientation of chemical shielding tensors as well as dipolar cou-

pling constant. Additional r.f. irradiation at and near the $n = 0$ R^2 condition by applying pulse sequences, for instance for purposes of DQF, may extend the occurrence of R^2 effects to even larger values ω_{iso}^A . This may sometimes be a welcome feature. In many application circumstances aiming at the determination of internuclear distances, dependence of experimental data on magnitudes and orientations of chemical shielding tensors adds further complications. These effects are not easy to predict when dealing with spin systems characterised by largely unknown parameters but will mainly affect pairs of spins with similar isotropic chemical shielding values, displaying considerable chemical shielding anisotropies and relatively large dipolar coupling constants. Such R^2 effects may contribute systematically to e.g., the intensity of off-diagonal peaks in two-dimensional dipolar recoupling experiments. Since the evaluation of short-range dipolar coupling constants from such experiments usually is the starting point in series of experiments aiming to construct three-dimen-

sional structural constraints for multi-spin systems, we feel that it is important not to neglect these effects in the data analysis [42].

Acknowledgments

Financial support of our work by the Deutsche Forschungsgemeinschaft and by Aventis Pharma, Paris, is gratefully acknowledged. We thank X. Helluy, Würzburg, for his cooperation in the early stages of the project, and an unknown reviewer for constructive comments.

References

- [1] A.E. Bennett, R.G. Griffin, S. Vega, Recoupling of homo- and heteronuclear dipolar interactions in rotating solids, in: B. Blümich (Ed.), *Solid-State NMR IV: Methods and Applications of Solid-State NMR, NMR Basic Principles and Progress*, vol. 33, Springer, Berlin, 1994, pp. 1–78.
- [2] S. Dusold, A. Sebald, Dipolar recoupling under magic-angle-spinning conditions, in: G. Webb (Ed.), *Annual Reports on NMR Spectroscopy*, vol. 41, Academic Press, London, 2000, pp. 185–264.
- [3] E.R. Andrew, A. Bradbury, R.G. Eades, V.T. Wynn, Nuclear cross relaxation induced by specimen rotation, *Phys. Lett.* 4 (1963) 99–100.
- [4] D.P. Raleigh, M.H. Levitt, R.G. Griffin, Rotational resonance in solid state NMR, *Chem. Phys. Lett.* 146 (1988) 71–76.
- [5] D.P. Raleigh, F. Creuzet, S.K. Gupta, M.H. Levitt, R.G. Griffin, Measurement of internuclear distances in polycrystalline solids: rotationally enhanced transfer of nuclear spin magnetization, *J. Am. Chem. Soc.* 111 (1989) 4502–4503.
- [6] M.H. Levitt, D.P. Raleigh, F. Creuzet, R.G. Griffin, Theory and simulations of homonuclear spin pairs in rotating solids, *J. Chem. Phys.* 92 (1990) 6347–6364.
- [7] A. Kubo, C.A. McDowell, One- and two-dimensional ^{31}P cross-polarization magic-angle-spinning nuclear magnetic resonance studies on two-spin systems with homonuclear dipolar and J coupling, *J. Chem. Phys.* 92 (1990) 7156–7170.
- [8] A. Schmidt, S. Vega, The Floquet theory of nuclear magnetic resonance spectroscopy of single spins and dipolar coupled spin pairs in rotating solids, *J. Chem. Phys.* 96 (1992) 2655–2680.
- [9] T. Nakai, C.A. McDowell, An analysis of NMR spinning sidebands of homonuclear two-spin systems using Floquet theory, *Mol. Phys.* 77 (1992) 569–584.
- [10] T. Nakai, C.A. McDowell, Application of Floquet theory to the nuclear magnetic resonance spectra of homonuclear two-spin systems in rotating solids, *J. Chem. Phys.* 96 (1992) 3452–3466.
- [11] S. Dusold, W. Milius, A. Sebald, Iterative lineshape fitting of MAS NMR spectra: a tool to investigate homonuclear J couplings in isolated spin pairs, *J. Magn. Reson.* 135 (1998) 500–513.
- [12] S. Dusold, E. Klaus, A. Sebald, M. Bak, N.C. Nielsen, Magnitudes and relative orientations of chemical shielding, dipolar, and J coupling tensors for isolated ^{31}P - ^{31}P spin pairs determined by iterative fitting of ^{31}P MAS NMR spectra, *J. Am. Chem. Soc.* 119 (1997) 7121–7129.
- [13] S. Dusold, H. Maisel, A. Sebald, Magnitudes and orientations of interaction tensors determined from rotational resonance MAS NMR lineshapes of a four- ^{13}C spin system, *J. Magn. Reson.* 141 (1999) 78–90.
- [14] M. Bechmann, S. Dusold, A. Sebald, W.A. Shuttleworth, D.L. Jakeman, D.J. Mitchell, J.N.S. Evans, ^{13}C chemical shielding tensor orientations in a phosphoenolpyruvate moiety from ^{13}C rotational-resonance MAS NMR lineshapes, *Solid State Sci.* 6 (2004) 1097–1105.
- [15] M. Bechmann, X. Helluy, A. Sebald, Selectivity of double-quantum filtered rotational-resonance experiments on larger-than-two-spin systems, in: S. Kiihne, H.J.M. de Groot (Eds.), *Perspectives on Solid-State NMR in Biology*, Kluwer, Dordrecht, The Netherlands, 2001, pp. 23–32.
- [16] P.T.F. Williamson, A. Verhoeven, M. Ernst, B.H. Meier, Determination of internuclear distances in uniformly labeled molecules by rotational-resonance in solid-state NMR, *J. Am. Chem. Soc.* 124 (2003) 2718–2722.
- [17] N.C.N. Nielsen, F. Creuzet, R.G. Griffin, M.H. Levitt, Enhanced double-quantum nuclear magnetic resonance in spinning solids at rotational resonance, *J. Chem. Phys.* 96 (1992) 5668–5677.
- [18] T. Karlsson, M. Edén, H. Luthman, M.H. Levitt, Efficient double-quantum excitation in rotational resonance NMR, *J. Magn. Reson.* 145 (2000) 95–107.
- [19] S. Dusold, A. Sebald, Double-quantum filtration under rotational-resonance conditions: numerical simulations and experimental results, *J. Magn. Reson.* 145 (2000) 340–356.
- [20] M. Bechmann, X. Helluy, A. Sebald, Double-quantum filtered rotational-resonance MAS NMR in the presence of large chemical shielding anisotropies, *J. Magn. Reson.* 152 (2001) 14–25.
- [21] M. Bechmann, X. Helluy, C. Marichal, A. Sebald, Double-quantum filtered MAS NMR in the presence of chemical shielding anisotropies and direct dipolar and J couplings, *Solid State Nucl. Magn. Reson.* 21 (2002) 71–85.
- [22] P.R. Costa, B. Sun, R.G. Griffin, Rotational resonance tickling: accurate internuclear distance measurements in solids, *J. Am. Chem. Soc.* 119 (1997) 10821–10830.
- [23] K. Takegoshi, S. Nakamura, T. Terao, ^{13}C - ^1H dipolar-assisted rotational-resonance in magic-angle spinning NMR, *Chem. Phys. Lett.* 344 (2001) 631–637.
- [24] M.M. Maricq, J.S. Waugh, NMR in rotating solids, *J. Chem. Phys.* 70 (1979) 3300–3316.
- [25] P. Tekely, C. Gardiennet, M.J. Potrzebowski, D. Reichert, Z. Luz, A. Sebald, Probing molecular geometry of solids by NMR spin exchange at the $n=0$ rotational-resonance condition, *J. Chem. Phys.* 116 (2002) 7607–7616.
- [26] M. Bechmann, S. Dusold, F. Geipel, A. Sebald, D. Sellmann, Magnitudes and orientations of ^{31}P chemical shielding tensors in Pt(II)-phosphine complexes and other four-fold coordinated phosphorus sites, 2004 (submitted).
- [27] R.R. Ernst, G. Bodenhausen, A. Wokaun, *Principles of Nuclear Magnetic Resonance in One and Two Dimensions*, Clarendon Press, Oxford, 1987.
- [28] M.H. Levitt, The signs of frequencies and phases in NMR, *J. Magn. Reson.* 126 (1997) 164–182.
- [29] U. Haeberlen, High resolution NMR in solids. Selective averaging, in: J.S. Waugh (Ed.), *Advances in Magnetic Resonance*, Academic Press, New York, (Suppl. 1), 1976.
- [30] A.R. Edmonds, *Angular Momentum in Quantum Mechanics*, Princeton University Press, Princeton, 1974.
- [31] M. Bak, N.C. Nielsen, REPULSION, a novel approach to efficient powder averaging in solid-state NMR, *J. Magn. Reson.* 125 (1997) 132–139.
- [32] S.A. Smith, T.O. Levante, B.H. Meier, R.R. Ernst, Computer simulations in magnetic resonance. An object oriented programming approach, *J. Magn. Reson. A* 106 (1994) 75–105.
- [33] M. Edén, Y.K. Lee, M.H. Levitt, Efficient simulation of periodic problems in NMR: application to decoupling and rotational resonance, *J. Magn. Reson. A* 120 (1996) 56–71.
- [34] T. Charpentier, C. Fermon, J. Virlet, Efficient time propagation technique for MAS NMR simulation: application to quadrupolar nuclei, *J. Magn. Reson.* 132 (1998) 181–190.

- [35] M.H. Levitt, M. Edén, Numerical simulation of periodic NMR problems: fast calculation of carousel averages, *Mol. Phys.* 95 (1998) 879–890.
- [36] M. Hohwy, H. Bildsoe, H.J. Jakobsen, N.C. Nielsen, Efficient spectral simulations in NMR of rotating solids. The γ -COMPUTE algorithm, *J. Magn. Reson.* 136 (1999) 6–14.
- [37] F. James, M. Roos, MINUIT computer code, Program D-506, CERN, Geneva, 1977.
- [38] MATLAB, Version 6.0; The Mathworks Inc., Natick, MA, 2001.
- [39] P. Hodgkinson, L. Emsley, The reliability of the determination of tensor parameters by solid-state nuclear magnetic resonance, *J. Chem. Phys.* 107 (1997) 4808–4816.
- [40] M. Bechmann, K. Hain, C. Marichal, A. Sebald, X- $\{^1\text{H}, ^{19}\text{F}\}$ triple resonance with a X- $\{^1\text{H}\}$ CP MAS probe and characterisation of a ^{29}Si - ^{19}F spin pair, *Solid State Nucl. Magn. Reson.* 23 (2003) 50–61.
- [41] T. Karlsson, J.M. Popham, J.R. Long, N. Oyler, G.P. Drobny, A study of homonuclear dipolar recoupling sequences in solid-state nuclear magnetic resonance, *J. Am. Chem. Soc.* 125 (2003) 7394–7407.
- [42] M. Carravetta, M. Edén, O.G. Johannessen, H. Luthman, P.E. Verdegem, J. Lugtenburg, A. Sebald, M.H. Levitt, Estimation of carbon-carbon bond lengths and medium-range internuclear distances by solid-state nuclear magnetic resonance, *J. Am. Chem. Soc.* 123 (2001) 10628–10638.

G. Magnitudes and Orientations of ^{31}P Chemical-Shielding Tensors in Pt(II)–Phosphine Complexes and Other Four-Fold Coordinated Phosphorus Sites

M. Bechmann, S. Dusold, F. Geibel, S. Sellmann, and A. Sebald, *Journal of Physical Chemistry A*, **109**, 5275–5280 (2005).

doi:10.1021/jp045353p

©2005 American Chemical Society.

Reproduced with permission from Journal of Physical Chemistry. Copyright 2005 American Chemical Society.

Magnitudes and Orientations of ^{31}P Chemical Shielding Tensors in Pt(II)–Phosphine Complexes and Other Four-Fold Coordinated Phosphorus Sites

Matthias Bechmann,^{†,‡} Stephan Dusold,[†] Franz Geipel,[§] Angelika Sebald,^{*,†,‡} and Dieter Sellmann^{§,||}

Bayerisches Geoinstitut, Universität Bayreuth, D-95440 Bayreuth, Germany, and Institut für Anorganische Chemie II, Universität Erlangen, Egerlandstr. 1, D-91058 Erlangen, Germany

Received: October 11, 2004; In Final Form: March 26, 2005

^{31}P MAS and double-quantum filtered ^{31}P MAS NMR experiments at and near the $n = 0$ rotational resonance condition, as well as off-magic angle spinning ^{31}P NMR experiments on two polycrystalline samples of Pt(II)–phosphine thiolate complexes are reported. Numerical simulations yield complete descriptions of the two ^{31}P spin pairs. ^{195}Pt MAS NMR spectra are straightforward to obtain but sensitively reflect only some parameters of the $^{195}\text{Pt}(^{31}\text{P})_2$ three-spin system. Based on the ^{31}P NMR results obtained and in conjunction with a large body of literature data and irrespective of the chemical nature of the specimen, a unified picture of the dominating motif of ^{31}P chemical shielding tensor orientations of phosphorus sites with 4-fold coordination is identified as a local (pseudo)plane rather than the directions of P element bond directions.

Introduction

Small isolated spin systems play an important role in the context of many contemporary solid-state NMR approaches, ranging from applications aiming at structure elucidation to the evaluation of the performance of newly developed pulse sequences. Isolated homonuclear ^{31}P spin pairs occur, for instance, in molecular fragments P–M–P in transition-metal–phosphine complexes. If M happens to be a magnetically active isotope, then the P–M–P fragment represents an isolated three-spin system. It is usually straightforward to obtain high-quality experimental ^{31}P solid-state NMR spectra of these (and similar) spin systems in polycrystalline samples. The more challenging aspects are concerned with the extraction of the full set of unknown parameters describing these spin systems. Analysis of such experimental ^{31}P NMR spectra requires numerically exact spectral line shape simulations in conjunction with iterative fitting procedures. The challenge for ^{31}P spin systems mainly arises as a consequence of the 100 percent natural abundance of the isotope ^{31}P , causing the need to determine simultaneously relatively large numbers of unknown parameters even for small spin systems.

Here we take the *cis*-PtP₂ fragment in two square-planar Pt(II)–phosphine complexes as representative examples. The spin $1/2$ isotope ^{195}Pt has a natural abundance of 33.8%. Accordingly, the PtP₂ fragment consists of 33.8% isotopomers containing a $(^{31}\text{P})_2(^{195}\text{Pt})$ three-spin system and 66.2% $(^{31}\text{P})_2$ spin-pair isotopomers. Typical orders of magnitude of the NMR interactions in the *cis*-PtP₂ fragment are as follows. Chemical shielding anisotropies are of the order 10^3 – 10^4 Hz (^{31}P) or 10^5 Hz (^{195}Pt) for common external magnetic field strengths, homonuclear ^{31}P – ^{31}P and heteronuclear ^{195}Pt – ^{31}P direct dipolar coupling constants both are of the order 10^2 Hz, magnitudes of

indirect heteronuclear dipolar coupling constants $^1J_{\text{iso}}(^{195}\text{Pt}, ^{31}\text{P})$ are of the order 10^3 Hz, whereas indirect homonuclear dipolar coupling constants $^2J_{\text{iso}}(^{31}\text{P}, ^{31}\text{P})$ are of the order 10^0 – 10^1 Hz and may have either positive or negative sign.^{1,2} The anisotropy of indirect dipolar coupling ^{31}P – ^{31}P may be neglected, but the anisotropy of indirect dipolar coupling ^{195}Pt – ^{31}P may amount to the order of 10^3 Hz and thus may exceed the magnitude of the corresponding direct dipolar coupling constants.

The two compounds containing *cis*-PtP₂ fragments chosen for this study represent one case for which the crystal structure is not known (compound **1**) whereas the crystal structure of compound **2** is known (Figure 1). ^{31}P MAS NMR spectra with and without double-quantum filtration (DQF), as well as ^{31}P NMR spectra obtained under off-magic-angle spinning (OMAS) conditions serve as the basis for the determination of all ^{31}P NMR parameters in **1** and **2**. In addition, we consider briefly ^{195}Pt MAS NMR spectra of **1** and **2** and will discuss in more general terms the orientation of ^{31}P chemical shielding tensors in molecular moieties with phosphorus in 4-fold coordination.

Experimental Section

Samples. *Compound 1.* Following a published synthesis procedure,³ pure **1** was obtained in 92% yield after recrystallization from CH₂Cl₂/Et₂O. Solution-state ^{31}P NMR (CD₂Cl₂) of **1**: $\omega_{\text{iso}}^{\text{CS}} = -52.2$ ppm, $^1J_{\text{iso}}(^{195}\text{Pt}, ^{31}\text{P}) = 2702$ Hz; ^{13}C CP/MAS NMR of **1** (aromatic region): $\omega_{\text{iso}}^{\text{CS}} = -150.5$ ppm; -130.9 ppm ($^2J_{\text{iso}}(^{195}\text{Pt}, ^{13}\text{C}) = 63$ Hz); -121.3 ppm.

Compound 2. Reaction of *cis*-(ⁿBu₃P)₂PtCl₂ with an equimolar amount of 1,2-dimercapato-benzene in CH₂Cl₂ in the presence of a small amount of NEt₃ at ambient conditions for 12 h yielded crude **2** after evaporation of the solvent. Pure **2** was obtained in 63% yield after recrystallization from MeOH at $T = 243$ K. Solution-state ^{31}P NMR (CD₂Cl₂) of **2**: $\omega_{\text{iso}}^{\text{CS}} = 5.0$ ppm, $^1J_{\text{iso}}(^{195}\text{Pt}, ^{31}\text{P}) = 2745$ Hz; ^{13}C CP/MAS NMR of **2** (aromatic region): $\omega_{\text{iso}}^{\text{CS}} = -149.8$ ppm and -146.8 ppm; -129.4 ppm ($^2J_{\text{iso}}(^{195}\text{Pt}, ^{13}\text{C}) = 63$ Hz) and -128.5 ppm ($^2J_{\text{iso}}(^{195}\text{Pt}, ^{13}\text{C}) = 68$ Hz); -121.5 ppm and -120.8 ppm. Crystals of **2** suitable

* Corresponding author. E-mail: sebald@e3.physik.uni-dortmund.de.

[†] Universität Bayreuth.

[‡] Current address: Universität Dortmund, Fachbereich Physik, D-44221 Dortmund, Germany.

[§] Universität Erlangen.

^{||} Deceased.

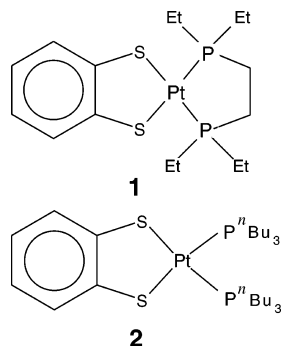


Figure 1. Schematic representation of molecules **1** and **2**.

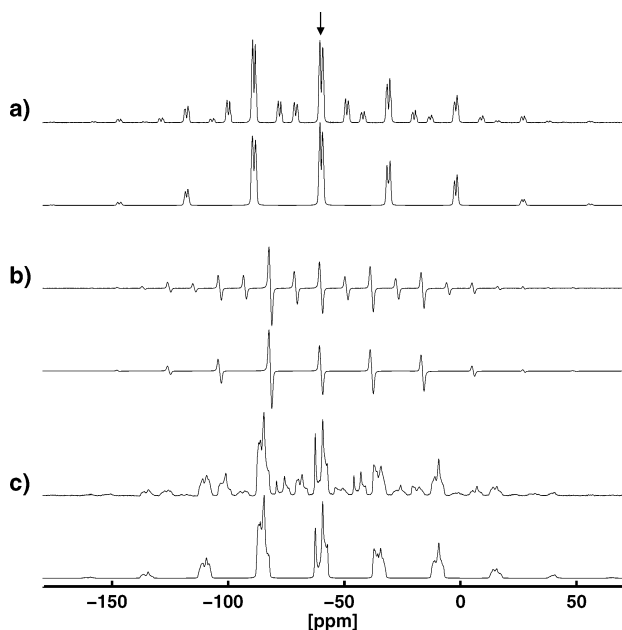


Figure 2. Experimental (upper traces) and best-fit simulated (lower traces) ^{31}P NMR spectra of **1**. The arrow indicates the isotropic region of the $(^{31}\text{P})_2$ -isotopomer spectrum, simulated spectra only take the $(^{31}\text{P})_2$ isotopomer into account. (a) ^{31}P $n = 0$ R^2 MAS NMR, $\omega_0/2\pi = -121.5$ MHz, $\omega_r/2\pi = 3521$ Hz; (b) R^2 -DQF ^{31}P MAS NMR, $\omega_0/2\pi = -121.5$ MHz, $\omega_r/2\pi = 2650$ Hz, $\tau = 3.0$ ms, $\Delta = 3.5$ μs ; (c) ^{31}P OMAS NMR, $\omega_0/2\pi = -81.0$ MHz, $\omega_r/2\pi = 2028$ Hz, $\beta_{\text{RL}} = 56.023^\circ$.

for structure determination by single-crystal X-ray diffraction were obtained by slow crystallization from a MeOH solution at room temperature. **2** crystallizes in space group $Pbca$,⁴ the relevant internuclear distances are Pt–P1, 229.4 pm, and Pt–P2, 229.3 pm, and the P1–Pt–P2 bond angle is 98.0° . The molecular structure of **2** is depicted in Figure 4.

^{31}P and ^{195}Pt MAS NMR. ^{31}P MAS NMR spectra were recorded on Bruker MSL 100, MSL 200, MSL 300, and DSX 500 NMR spectrometers, equipped with standard 4 or 7 mm double-resonance double-bearing CP MAS probes. The corresponding ^{31}P Larmor frequencies $\omega_0/2\pi$ are -40.5 , -81.0 , -121.5 , and -202.5 MHz. Hartmann–Hahn cross polarization (CP) was used (^1H $\pi/2$ -pulse durations 2.5–3.5 μs , recycle delays 3–5 s, and CP contact times 0.5–2.0 ms). Line shapes of experimental ^{31}P MAS NMR spectra were checked to be identical when using either cross polarization or ^{31}P single-pulse excitation. ^{31}P chemical shielding is quoted with respect to $\omega_{\text{iso}}^{\text{CS}} = 0$ ppm for the ^{31}P resonance of 85% H_3PO_4 . ^{195}Pt CP MAS NMR spectra were recorded on the MSL 100 (7 mm rotor, $\omega_0/2\pi = -21.4$ MHz) and MSL 200 (4 mm rotor, $\omega_0/2\pi = -42.8$ MHz) spectrometers, employing ^1H $\pi/2$ -pulse durations

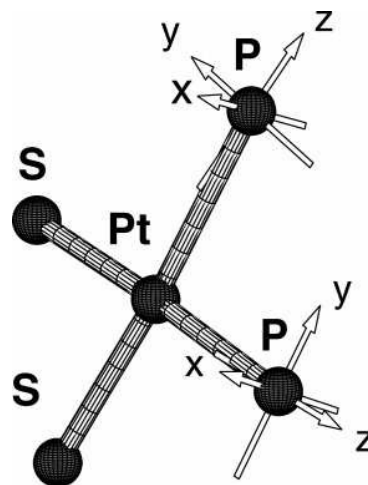


Figure 3. Illustration of the orientation of the ^{31}P chemical shielding tensors in the S_2PtP_2 fragment of molecule **1**.

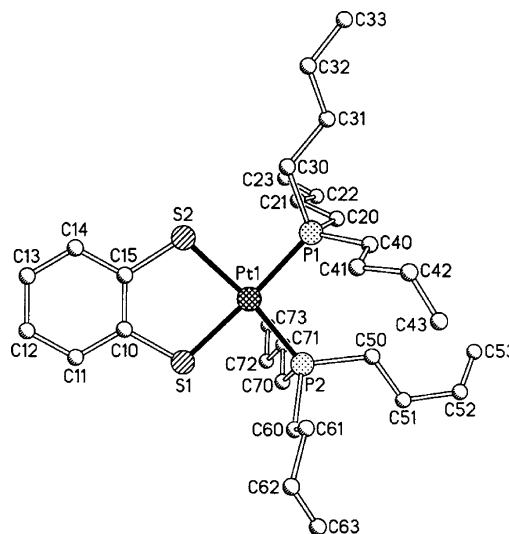


Figure 4. Molecular structure of solid **2** according to single-crystal X-ray diffraction.⁴

of 3.5–4.5 μs and CP contact times of 5 ms. ^{195}Pt chemical shielding is given relative to $\Xi(^{195}\text{Pt}) = 21.4$ MHz.⁵

MAS frequencies were generally in the range $\omega_r/2\pi = 1$ –10 kHz and were actively controlled to within ± 2 Hz. ^1H c.w. decoupling with amplitudes in the range 55 kHz to 85 kHz was employed during signal acquisition. Special care was taken to adjust the magic angle $\beta_{\text{RL}} = \tan^{-1}\sqrt{2}$ for all MAS NMR experiments as accurately as possible by optimizing the line shape of the ^{31}P resonance of $(\text{Et}_2\text{P}=\text{S})_2$ under MAS conditions.⁶ The shape of the ^{31}P resonance of $\text{P}(\text{C}_6\text{H}_{11})_3$ served for calibration of the spinning angle in OMAS NMR experiments. For double-quantum filtration experiments the COSY-like sequence $\text{CP}_{(x)} - \tau - (\pi/2)_{(y)} - \Delta - (\pi/2)_{(\phi)}$ - acquisition was used⁷ where ϕ indicates phase cycling suitable for DQF.⁸ The duration of Δ was fixed as $\Delta = 3.5$ μs , the duration of τ was varied.

Definitions, Notation, and Numerical Methods. Shielding notation⁹ is used throughout. For the interactions $\lambda = \text{CS}$ (chemical shielding), $\lambda = \text{D}$ (direct dipolar coupling), and $\lambda = \text{J}$ (indirect dipolar (J) coupling) the isotropic part $\omega_{\text{iso}}^\lambda$, the anisotropy $\omega_{\text{aniso}}^\lambda$, and the asymmetry parameter η^λ relate to the principal elements of the interaction tensor ω^λ as follows:¹⁰ $\omega_{\text{iso}}^\lambda = (\omega_{xx}^\lambda + \omega_{yy}^\lambda + \omega_{zz}^\lambda)/3$, $\omega_{\text{aniso}}^\lambda = \omega_{zz}^\lambda - \omega_{\text{iso}}^\lambda$, and $\eta^\lambda = (\omega_{yy}^\lambda - \omega_{xx}^\lambda)/\omega_{\text{aniso}}^\lambda$.

– $\omega_{xx}^\lambda/\omega_{\text{aniso}}^\lambda$ with $|\omega_{zz}^\lambda - \omega_{\text{iso}}^\lambda| \geq |\omega_{xx}^\lambda - \omega_{\text{iso}}^\lambda| \geq |\omega_{yy}^\lambda - \omega_{\text{iso}}^\lambda|$. For indirect dipolar coupling $\omega_{\text{iso}}^J = \pi J_{\text{iso}}$, and for direct dipolar coupling $\eta^D = \omega_{\text{iso}}^D = 0$ and $\omega_{\text{aniso}}^D = b_{ij} = -\mu_0 \gamma_i \gamma_j \hbar / (4\pi r_{ij}^3)$, where γ_i and γ_j denote gyromagnetic ratios and r_{ij} is the internuclear distance between spins S_i and S_j , $i, j = 1, 2$ refers to the homonuclear (³¹P)₂ part of the (³¹P)₂(¹⁹⁵Pt) three-spin system. The Euler angles $\Omega_{IJ} = \{\alpha_{IJ}, \beta_{IJ}, \gamma_{IJ}\}$ relate axis system I to axis system J ; I, J denote P (principal axis system, PAS), C (crystal axis system, CAS), R (rotor axis system, RAS), or L (laboratory axis system).¹¹ In the context of MAS NMR experiments on the (³¹P)₂(¹⁹⁵Pt) spin system, it is convenient to define the PAS of $\omega^{\text{D}12}$ as the CAS, $\Omega_{\text{PC}}^{\text{D}12} = \{0, 0, 0\}$. Our procedures for numerically exact spectral line shape simulations and iterative fitting are fully described and discussed in detail elsewhere, in particular addressing the $n = 0$ rotational resonance (R^2) condition for isolated homonuclear spin pairs,^{12,13} various $n = 0, 1, 2$ R^2 conditions in an isolated homonuclear four-spin system,¹³ and different heteronuclear dipolar de- and recoupling MAS conditions for isolated heteronuclear two-¹⁴ and three-spin systems.^{15,16} For meaningful simulations of OMAS NMR spectra, larger sets of powder angles are needed (e.g., 700 sets of angles selected by REPULSION¹⁷) than in simulations of MAS NMR spectra (e.g., 232 sets).

Results and Discussion

The following section is organized into three parts. First, we will discuss the experimental determination of the parameters of the ³¹P spin pairs in **1** and **2**. The second part will briefly describe ¹⁹⁵Pt MAS NMR spectra of **1** and **2**. In the third part we will discuss general trends in the orientations of ³¹P chemical shielding tensors for phosphorus atoms in 4-fold coordination.

³¹P NMR of Solid **1 and **2**.** Experimental options to generate ³¹P NMR spectra of polycrystalline powder samples containing the PtP₂ fragment include experiments on nonspinning samples, on samples spinning under off-magic-angle (OMAS) conditions, and on samples under MAS conditions with or without so-called dipolar recoupling¹⁶ and/or double-quantum filtration techniques applied. With the exception of ³¹P NMR spectra of nonspinning samples of **1** and **2** here all these experimental techniques are used. Static powder patterns of samples such as **1** or **2**, containing not only isolated ³¹P spin pairs but also isotopomers ¹⁹⁵Pt(³¹P)₂, are not a suitable starting point for the full characterization of the ³¹P spin pair as ³¹P spectral contributions from both isotopomers overlap heavily. This is not a problem for the simulation of spectra, but it would be a major problem for the extraction of multiple parameters from experimental spectra. Therefore, our data analysis is based on experimental data for which sample spinning provides a separation of the ³¹P spectral contributions from the two isotopomers.

(i) ³¹P NMR of **1.** Inspection of a ¹³C MAS NMR spectrum of **1** is a good starting point for the analysis of ³¹P MAS NMR spectra of **1**. Only three sharp ¹³C resonances are observed for the aromatic thiolate ligand, indicating molecular symmetry (see the Experimental Section). Either a C₂ axis or a mirror plane bisecting the P–Pt–P angle are possible, both rendering the two phosphorus sites in a molecule of **1** crystallographically equivalent. The corresponding two ³¹P chemical shielding tensors thus represent a so-called $n = 0$ rotational resonance (R^2) condition^{12,18} with identical isotropic chemical shielding values but nonidentical chemical shielding tensor orientations. The $n = 0$ rotational resonance R^2 condition gives rise to complicated spectral line shapes in which the magnitudes and orientations of all interaction tensors of the spin pair are usually sensitively encoded^{12–14} at arbitrary spinning frequencies. A

TABLE 1

	1 (C ₂) ^a	1 (σ) ^a	2
$\omega_{\text{iso}}^{\text{CS}_1}$ [ppm]	–60.0	–60.0	+2.1
$\omega_{\text{iso}}^{\text{CS}_2}$ [ppm]	–60.0	–60.0	+2.5
$\omega_{\text{aniso}}^{\text{CS}_1}$ [ppm]	78.0 ± 1	77.8 ± 1	–57 ± 3
$\omega_{\text{aniso}}^{\text{CS}_2}$ [ppm]	78.0 ± 1	77.8 ± 1	–68 ± 3
η^{CS_1}	0.52 ± 0.02	0.50 ± 0.02	0.35 ± 0.1
η^{CS_2}	0.52 ± 0.02	0.50 ± 0.02	0.35 ± 0.1
$\alpha_{\text{PC}}^{\text{CS}_1}$ [°] ^b	90 ± 9	92 ± 9	95 ± 21
$\beta_{\text{PC}}^{\text{CS}_1}$ [°] ^b	51 ± 3	45 ± 3	40 ± 11
$\gamma_{\text{PC}}^{\text{CS}_1}$ [°] ^b	0 ± 3	0	43 ± 30
$\alpha_{\text{PC}}^{\text{CS}_2}$ [°] ^b	90 ± 9	–92 ± 9	49 ± 21
$\beta_{\text{PC}}^{\text{CS}_2}$ [°] ^b	231 ± 3	88 ± 9	130 ± 10
$\gamma_{\text{PC}}^{\text{CS}_2}$ [°] ^b	180 ± 3	0	0
${}^2J_{\text{iso}}(^{31}\text{P}, ^{31}\text{P})$ [Hz]	–9.3 ± 5	–13.0 ± 5	–23.0 ± 6
$b_{12}/2\pi$ [Hz]	–708 ± 31	–683 ± 31	–475 ^c

^a The Euler angles $\Omega_{\text{PC}}^{\text{CS}_{1,2}}$ are related by symmetry. If related by C₂ symmetry: $\alpha_{\text{PC}}^{\text{CS}_2} = \alpha_{\text{PC}}^{\text{CS}_1}$; $\beta_{\text{PC}}^{\text{CS}_2} = \beta_{\text{PC}}^{\text{CS}_1} + \pi$; $\gamma_{\text{PC}}^{\text{CS}_2} = -\gamma_{\text{PC}}^{\text{CS}_1} + \pi$. If related by a mirror plane σ : $\alpha_{\text{PC}}^{\text{CS}_2} = -\alpha_{\text{PC}}^{\text{CS}_1}$; $\beta_{\text{PC}}^{\text{CS}_2} = \pi - \beta_{\text{PC}}^{\text{CS}_1}$; $\gamma_{\text{PC}}^{\text{CS}_2} = \gamma_{\text{PC}}^{\text{CS}_1}$. ^b The Euler angles $\Omega_{\text{PC}}^{\text{CS}}$ are given relative to $\Omega_{\text{PC}}^{\text{D}12} = \{0, 0, 0\}$ with the x axis of the dipolar coupling tensor taken as parallel to the C₂ symmetry axis. ^c Calculated from the crystal structure.⁴

priori, in the absence of knowledge of the crystal structure of **1**, we do not know which of the two symmetry operations is present, and experimental ³¹P MAS NMR spectra of **1**, obtained at different MAS and Larmor frequencies, have to be fitted for either of the two possibilities. Note that the presence of a C₂ symmetry element is a special case for a spin pair as it defines the absolute orientation of the two ³¹P chemical shielding tensors¹³ whereas a symmetry plane only defines their relative orientations, leaving free rotation of the tensors around the unique axis of the ³¹P–³¹P dipolar coupling tensor possible.

Figure 2a depicts a ³¹P MAS NMR spectrum of **1**, together with the corresponding final best-fit simulated spectrum. Iterative fitting of various different straightforward ³¹P MAS NMR spectra of **1** converges to identical solutions when assuming either of the two symmetry elements to be present. In principle the two different symmetries are distinguishable but they turn out indistinguishable for the ³¹P spin pair in **1** because of the values of the Euler angles being $\alpha_{\text{PC}}^{\text{CS}_1} = 90^\circ \pm 9^\circ$ and $\gamma_{\text{PC}}^{\text{CS}_1} = 0^\circ \pm 3^\circ$ (see Table 1). Iterative fitting of several ³¹P MAS NMR spectra of **1** defines, for instance, the set of angles $\Omega_{\text{PC}}^{\text{CS}_1} = \{87 \pm 11, 51 \pm 6, 0 \pm 6\}$. This result can be further improved by applying a COSY-like pulse sequence with double-quantum filtration (DQF) under MAS conditions and by analyzing experimental spectra obtained under OMAS conditions. Experimental ³¹P R^2 -DQF and OMAS NMR spectra of **1** are depicted in Figure 2, panels b and c, together with the corresponding best-fit simulations. R^2 -DQF MAS NMR line shapes at and near the $n = 0$ R^2 condition are known to exhibit higher sensitivities toward anisotropic interaction parameters than conventional R^2 line shapes.¹² Spinning the sample at an angle $\beta_{\text{RL}} \neq \tan^{-1}\sqrt{2}$ (OMAS) leads to spinning sideband patterns where each sideband represents a scaled powder pattern, slightly different from the spinning sideband pattern obtained when spinning exactly at the magic angle.^{19–23} With OMAS conditions only slightly deviating from the magic angle we find that often minima regions in error maps are more sharply defined than based on R^2 or R^2 -DQF MAS NMR line shapes. The uncertainties of the data given in Table 1 are the combined constraints from fitting experimental ³¹P R^2 and R^2 -DQF MAS as well OMAS spectra of **1**. Our ³¹P NMR data yield a P–P distance in **1** of 305 ± 2 pm, in excellent agreement with the

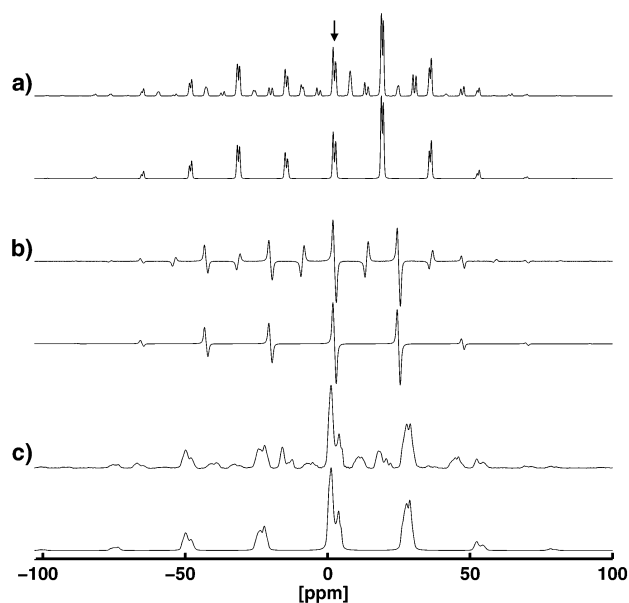


Figure 5. Experimental (upper traces) and best-fit simulated (lower traces) ^{31}P NMR spectra of **2**. The arrow indicates the isotropic region of the $(^{31}\text{P})_2$ -isotopomer spectrum, simulated spectra only take the $(^{31}\text{P})_2$ isotopomer into account. (a) ^{31}P $n = 0$ R^2 MAS NMR, $\omega_0/2\pi = -121.5$ MHz, $\omega_r/2\pi = 2046$ Hz; (b) R^2 -DQF ^{31}P MAS NMR, $\omega_0/2\pi = -121.5$ MHz, $\omega_r/2\pi = 2740$ Hz, $\tau = 3.3$ ms, $\Delta = 3.5$ μs ; (c) ^{31}P OMAS NMR, $\omega_0/2\pi = -81.0$ MHz, $\omega_r/2\pi = 2075$ Hz, $\beta_{\text{RL}} = 56.196^\circ$.

results of X-ray diffraction studies of numerous closely related compounds containing a *cis*- S_2PtP_2 moiety.²⁴

Figure 3 illustrates the orientation of the two ^{31}P chemical shielding tensors in the molecule **1**. For the ^{31}P chemical shielding tensors in **1**, the zz component represents the *most* shielded direction and is oriented along the direction of the respective Pt–P bonds. For the moment, we leave the issue of the ^{31}P chemical shielding tensor orientation at this stage but will return to this topic later (see below).

(ii) ^{31}P NMR of **2**. The starting point for the analysis of ^{31}P MAS NMR spectra of **2** is the crystal structure. The molecular structure of solid **2** is shown in Figure 4. The two phosphorus sites in the molecule are not crystallographically equivalent and will thus give rise to two slightly different ^{31}P resonances. In accordance with the crystal structure data, ^{13}C MAS NMR spectra of **2** display six ^{13}C resonances for the aromatic ring of the thiolate ligand (see the Experimental Section). From the known internuclear ^{31}P – ^{31}P distance in **2**, the corresponding dipolar coupling constant is calculated and does not have to be determined from iterative fitting of ^{31}P MAS NMR spectra of **2**. Other than for **1**, however, in **2** there is no symmetry relationship between the two ^{31}P chemical shielding tensors, and accordingly, simulations have to allow for a (small) difference in isotropic chemical shielding of the two resonances as well as for unrelated Euler angles describing the orientations of the two ^{31}P chemical shielding tensors. Despite the known crystal structure, simulations of the ^{31}P MAS NMR spectra of **2** involve more unknown parameters than was the case for **1**.

We follow the same procedure as before. After recording several different ^{31}P R^2 and R^2 -DQF MAS as well OMAS NMR spectra of **2** and combining all results, we obtain the data given in Table 1. These best-fit parameters yield the simulated spectra shown in Figure 5, together with the corresponding experimental ^{31}P NMR spectra of **2**. Determination of the ^{31}P chemical shielding values of **2**, representing a near $n = 0$ ^{31}P R^2 spin system, particularly gains from R^2 -DQF MAS NMR experiments

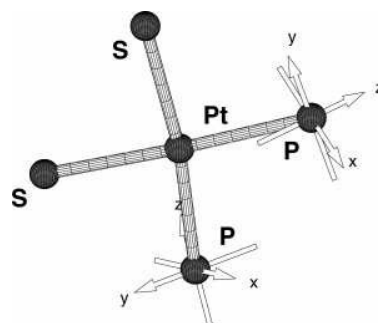


Figure 6. Illustration of the orientation of the ^{31}P chemical shielding tensors in the S_2PtP_2 fragment of molecule **2**.

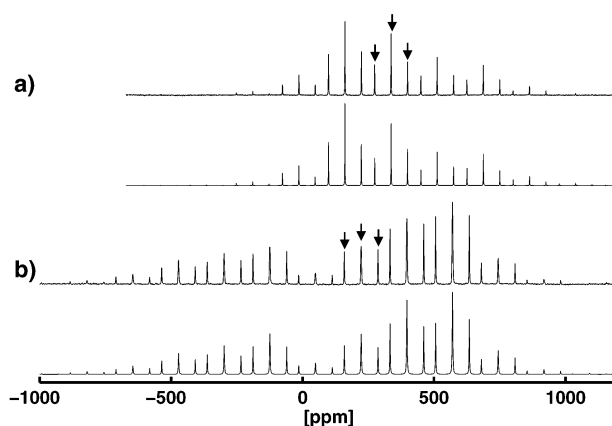


Figure 7. Experimental (upper traces) and simulated (lower traces) ^{195}Pt MAS NMR spectra of **1** (a) and **2** (b); arrows indicate center band resonances, $\omega_0/2\pi = -42.8$ MHz. (a) $\omega_r/2\pi = 7449$ Hz; (b) $\omega_r/2\pi = 7439$ Hz.

where all orientational parameters are more sensitively encoded than in the conventional R^2 MAS or OMAS NMR spectra.¹² Note that for **1** and **2** the values as well as the signs of the isotropic J -coupling constants $^2J_{\text{iso}}(^{31}\text{P}, ^{31}\text{P})$ are well defined from the line shape analyses even if these J couplings are not resolved in the spectra and none of the splittings visible in some of the spectra directly depict these J couplings.

Again, just as before for **1** (see Figure 3), we illustrate the orientations of the two ^{31}P chemical shielding tensors in **2** in Figure 6. Also for **2** the direction of the zz components of the two chemical shielding tensors nearly coincide with the directions of the corresponding Pt–P bond directions. However, in contrast to **1**, for **2** the zz components of the two chemical shielding tensors represent the *least* shielded components. We will return to this seeming puzzle below.

^{195}Pt MAS NMR of **1** and **2**. ^{195}Pt MAS NMR spectra of **1** and **2** are depicted in Figure 7. Given that we observe the X-part spectrum of the $^{195}\text{Pt}(^{31}\text{P})_2$ three-spin systems in **1** and **2** and that we know all parameters of the ^{31}P parts of these spin systems, one might expect to be able to fully characterize also the ^{195}Pt part of the spin systems, provided some heteronuclear dipolar recoupling pulse sequence¹⁶ is applied, or a sufficiently slow MAS rate is used so that the heteronuclear ^{195}Pt – ^{31}P direct dipolar coupling interactions are not completely averaged out.

Obviously (Figure 7), experimental ^{195}Pt MAS NMR spectra of **1** and **2** are well reproduced by numerical simulations. Closer inspection of various experimental data, however, reveals that even at a low Larmor frequency $\omega_0/2\pi = -21.4$ MHz and at very slow spinning rates $\omega_r/2\pi \leq 800$ Hz, the only sensitively encoded fit parameters are the anisotropy of the ^{195}Pt chemical shielding and the isotropic J -coupling constants $^1J_{\text{iso}}(^{195}\text{Pt}, ^{31}\text{P})$.

In addition, it turns out that the spinning angle is a highly sensitive fit parameter: deviations from the magic angle as small as $\pm 0.05^\circ$ lead to significant changes in the spinning sideband patterns of these ^{195}Pt MAS NMR spectra. This finding for MAS NMR spectra of spin-1/2 isotopes with very large chemical shielding anisotropies is familiar from MAS NMR experiments on quadrupolar nuclei where large quadrupolar interactions also lead to spectra being highly sensitive to the accurate setting of the magic angle.²⁵ Even if the large ^{195}Pt chemical shielding anisotropy would not be the overwhelmingly large interaction parameter in the $^{195}\text{Pt}(^{31}\text{P})_2$ three-spin systems in **1** and **2**, we may be faced with another difficulty in determining the geometry of the PtP_2 moiety from ^{31}P and ^{195}Pt MAS NMR experiments. The values of the J -coupling constants $^1J_{\text{iso}}(^{195}\text{Pt}, ^{31}\text{P})$ in **1** and **2** are ca. 2700 Hz. Therefore, an anisotropy of this J -coupling interaction of a similar magnitude is likely to be present. ω_{aniso}^J may add to, or subtract from, the respective dipolar coupling constants, with the J -coupling tensor having an unknown orientation. This may then lead to an apparent dipolar coupling constant b_{eff} which would not directly reflect the internuclear $^{195}\text{Pt}-^{31}\text{P}$ distances, making it impossible to deduce these internuclear distances. In fact, it has been found earlier for the CdP_2 fragment in a Cd(II) -phosphine complex that the heteronuclear $^{113}\text{Cd}-^{31}\text{P}$ dipolar coupling and the anisotropy of the J coupling $^1J(^{113}\text{Cd}, ^{31}\text{P})$ essentially cancel each other.¹⁵

^{31}P Chemical Shielding Tensor Orientations. There is a fair number of ^{31}P solid-state NMR studies in the literature in which ^{31}P chemical shielding tensor orientations have been determined experimentally. ^{31}P NMR experiments on oriented single crystals^{14,26-43} as well as ^{31}P NMR studies on polycrystalline powders^{1,13-15,44-47} have been reported. Most often, the ^{31}P chemical shielding tensor orientations are being discussed by describing the orientation of certain bond directions relative to the directions of the xx , yy , and zz components of the ^{31}P chemical shielding tensors. Implicitly, we have so far followed this common practice (see Figures 3 and 6) by mentioning that in both **1** and **2** the ^{31}P chemical shielding tensors are oriented such that the directions of their zz components nearly coincide with the respective $\text{Pt}-\text{P}$ bond directions. This line of argument, however, leads to some confusion. Why should in one of these two very closely related compounds the *most* shielded direction coincide with $\text{Pt}-\text{P}$ bond direction, and why should this be the *least* shielded direction in the second compound? Obviously, it is not the $\text{Pt}-\text{P}$ bond direction that reveals the common pattern of these ^{31}P chemical shielding tensor orientations.

Here it helps to consult results in the literature which cover a wide range in terms of chemistry, ranging from phosphorus in organophosphates and in inorganic phosphates all the way to phosphorus in transition-metal phosphine complexes. All these diverse compounds have in common that the phosphorus atom is 4-fold coordinated in a more or less distorted tetrahedral PE_4 environment ($\text{E} = \text{C}, \text{O}, \text{S}, \text{Pt}, \text{Hg}, \text{Cd}, \dots$). The corresponding ^{31}P chemical shielding tensors also have something in common, irrespective of the chemical nature of the compounds. One can always find a local (pseudo)plane of symmetry, defined by the P atom and two of its neighbored atoms, and always the direction of one of the ^{31}P chemical shielding tensor components is perpendicular to this plane. Sometimes the final result is such that one of the remaining two components of the ^{31}P chemical shielding tensor will actually coincide with a molecular $\text{P}-\text{E}$ bond direction (for example, in **1** and **2**), but the local plane is the dominating element in defining the ^{31}P chemical shielding tensor orientation. Recasting our results on

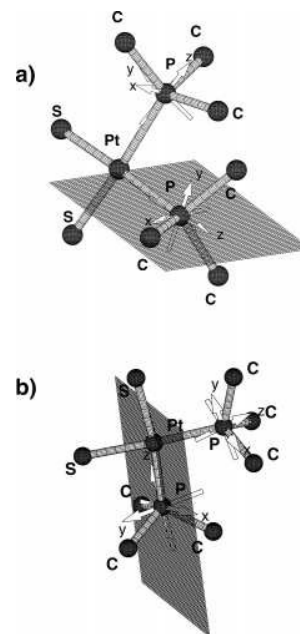


Figure 8. Orientations of the ^{31}P chemical shielding tensors in **1** (a) and **2** (b) with the local planes defined by $\text{C}-\text{P}-\text{Pt}$ shown; the directions of the intermediate yy components of the shielding tensors are perpendicular to these planes.

1 and **2** in the light of a local plane as the determining element, immediately reveals the common property of the ^{31}P chemical shielding tensors in these two compounds. Drawing a plane defined by the local coordination PtPC_3 , containing the central P atom in its distorted tetrahedron environment, the platinum atom and the directly bonded carbon atom of one of the three organic substituents of the phosphine ligand, identifies that in both cases the direction of the intermediate yy -component of the ^{31}P chemical shielding tensor is oriented perpendicular to this idealized local plane. This is illustrated in Figure 8.

The determining role of a local plane in defining ^{31}P chemical shielding tensor orientations becomes particularly clear from the example of an organic phosphate salt. The ^{31}P chemical shielding tensor in tris-ammonium phosphoenolpyruvate¹⁴ has a very small asymmetry parameter η^{CS} and the P atom is in a nearly tetrahedral local $\text{O}_3\text{PO}-\text{C}$ coordination. Chemical intuition might thus suggest that the direction of the nearly unique zz -component of this ^{31}P chemical shielding tensor should approximately coincide with the chemically distinct $\text{P}-\text{C}$ bond direction in this $\text{O}_3\text{PO}-\text{C}$ moiety. This is not the case as is revealed by ^{31}P single-crystal NMR, again it is a local plane spanned by two of the oxygen atoms and the phosphorus atom that marks the orientation of the ^{31}P chemical shielding tensor, the directions of neither of the shielding tensor components coincide with a bond direction in this molecule.

Summary and Conclusions

Combining ^{31}P R^2 and R^2 -DQF MAS NMR and OMAS NMR experiments provides a good database for the full characterization of ^{31}P spin pairs in polycrystalline powder samples by line shape analysis. Even if not necessary for reasons of background-signal suppression, R^2 -DQF MAS experiments and in particular OMAS NMR spectra are a useful complement to conventional R^2 MAS NMR experiments in that these additional experiments display different, and often higher, sensitivities to the various anisotropic interaction parameters of the spin pair. Owing to the very large ^{195}Pt chemical shielding anisotropies and the

TABLE 2: ^{195}Pt NMR Data of **1** and **2**

	1	2
$\omega_{\text{iso}}^{\text{CS}}$ [ppm]	338	225
$\omega_{\text{iso}}^{\text{CS}}$ [ppm]	550	-907
η^{CS}	0.4	0.1
$^1J_{\text{iso}}(^{195}\text{Pt}, ^{31}\text{P})$ [Hz]	2666	2708; 2772

unknown anisotropies of the J couplings $^1J(^{195}\text{Pt}, ^{31}\text{P})$ it turns out impossible to derive the orientation of the ^{195}Pt chemical shielding tensor in molecular fragments P_2Pt from ^{195}Pt MAS NMR experiments, although good quality ^{195}Pt MAS NMR spectra are easily obtained. From the ^{31}P NMR results on **1** and **2** and from numerous literature data a unified picture concerning the dominating motif of the orientation of ^{31}P chemical shielding tensors of phosphorus sites in 4-fold coordination emerges as a local (pseudo)plane rather than the directions of the P-element bond directions, irrespective of the chemical nature of the specimen.

Acknowledgment. Financial support of our work by the Deutsche Forschungsgemeinschaft is gratefully acknowledged. We thank Bruker Biospin GmbH, Rheinstetten, for providing generous access to the DSX 500 NMR spectrometer, F. W. Heinemann, Erlangen, for making the single-crystal X-ray diffraction data of **2** available to us, and O. J. Price, Exeter, for helping with some simulations.

References and Notes

- Dusold, S.; Klaus, E.; Sebald, A.; Bak, M.; Nielsen, N. C. *J. Am. Chem. Soc.* **1997**, *119*, 7121.
- Davies, J. A.; Dutremez, S. *Coord. Chem. Rev.* **1992**, *114*, 61.
- Fazlur-Rahman, A. K.; Verkade, J. G. *Inorg. Chem.* **1992**, *31*, 5331.
- Geipel, F.; Heinemann, F. W.; Sellmann, D. Unpublished work.
- Sebald, A. MAS and CP/MAS NMR of Less Common Spin-1/2 Nuclei. In *NMR Basic Principles and Progress*; Springer-Verlag: Berlin, 1994; Vol. 31, pp 91–131.
- Challoner, R.; Sebald, A. *Solid State Nucl. Magn. Reson.* **1995**, *4*, 39.
- Nielsen, N. C. N.; Cruzet, F.; Griffin, R. G.; Levitt, M. H. *J. Chem. Phys.* **1992**, *96*, 5668.
- Ernst, R. R.; Bodenhausen, G.; Wokaun, A. *Principles of Nuclear Magnetic Resonance in One and Two Dimensions*; Clarendon Press: Oxford, U.K., 1987.
- Levitt, M. H. *J. Magn. Reson.* **1997**, *126*, 164.
- Haerberlen, U. *Advances in Magnetic Resonance*, Supplement 1; Academic Press: New York, 1976.
- Edmonds, A. R. *Angular momentum in quantum mechanics*; Princeton University Press: Princeton, NJ, 1974.
- Bechmann, M.; Sebald, A. *J. Magn. Reson.* **2005**, *173*, 296.
- Dusold, S.; Milius, W.; Sebald, A. *J. Magn. Reson.* **1998**, *135*, 500.
- Dusold, S.; Maisel, H.; Sebald, A. *J. Magn. Reson.* **1999**, *141*, 78.
- Bechmann, M.; Dusold, S.; Förster, H.; Haerberlen, U.; Lis, T.; Sebald, A.; Stumber, M. *Mol. Phys.* **2000**, *98*, 605.
- Dusold, S.; Sebald, A. *Mol. Phys.* **1998**, *95*, 1237.
- Dusold, S.; Sebald, A. Dipolar Recoupling under Magic-Angle Spinning Conditions. In *Annual Reports on NMR Spectroscopy*; Academic Press: London, 2000; Vol. 41, pp 185–264.
- Bak, M.; Nielsen, N. C. *J. Magn. Reson.* **1997**, *125*, 132.
- Maricq, M. M.; Waugh, J. S. *J. Chem. Phys.* **1979**, *70*, 3300.
- Nakai, T.; McDowell, C. A. *Mol. Phys.* **1992**, *77*, 569.
- Nakai, T.; McDowell, C. A. *J. Chem. Phys.* **1992**, *96*, 3452.
- Miura, H.; Terao, T.; Saika, A. *J. Chem. Phys.* **1986**, *85*, 2458.
- Marichal, C.; Sebald, A. *Chem. Phys. Lett.* **1998**, *286*, 298.
- Hoffmann, A.; Schnell, I. *ChemPhysChem.* **2004**, *5*, 966.
- Crystal-structure determinations of several closely related Pt(II) complexes with a *cis*- S_2PtP_2 core have been reported in the literature: Fenn, R. H.; Segrott, G. R. *J. Chem. Soc. A* **1970**, 2781. Lin, I. J. B.; Chen, H. W.; Fackler, J. P. *Inorg. Chem.* **1978**, *17*, 394. Dudis, D.; Fackler, J. P. *Inorg. Chem.* **1982**, *21*, 3577. Bryan, S. A.; Roundhill, D. M. *Acta Crystallogr. C* **1983**, *39*, 184. Briant, C. E.; Calhorda, M. J.; Hor, T. S. A.; Howells, N. D.; Mingos, D. M. P. *J. Chem. Soc., Dalton Trans.* **1983**, 1325. Shaver, A.; Lai, R. D.; Bird, P. H.; Wickramasinghe, W. *Can. J. Chem.* **1985**, *63*, 2555. Vicente, R.; Ribas, J.; Solans, X.; Font-Altaba, M.; Mari, A.; de Loth, P.; Cassoux, P. *Inorg. Chim. Acta* **1987**, *132*, 229. Weigand, W.; Bosl, G.; Polborn, K. *Chem. Ber.* **1990**, *123*, 1339. Dudis, D. S.; King, C.; Fackler, J. P. *Inorg. Chim. Acta* **1991**, *181*, 99. Bevilacqua, J. M.; Zuleta, J. A.; Eisenberg, R. *Inorg. Chem.* **1994**, *33*, 258. Belluco, U.; Bertani, R.; Michelin, R. A.; Mozzon, M.; Bombieri, G.; Benetollo, F. *Gazz. Chim. Ital.* **1994**, *124*, 487. Chen, Q.; Boehm, F.; Dabrowiak, J.; Zubietta, J. *Inorg. Chim. Acta* **1994**, *216*, 83.
- Ashbrook, S. E.; Wimperis, S. *High-resolution NMR of quadrupolar nuclei in solids: The satellite-transition magic angle spinning (STMAS) experiment*. *Prog. Nucl. Magn. Reson. Spectrosc.* **2004**, *45*, 53–108.
- Kohler, S. J.; Ellett, D. J., jr.; Klein, M. P. *J. Chem. Phys.* **1976**, *64*, 4451.
- Kohler, S. J.; Klein, M. P. *Biochem.* **1976**, *15*, 967.
- Kohler, S. J.; Klein, M. P. *J. Am. Chem. Soc.* **1977**, *99*, 8290.
- Herzfeld, G.; Griffin, R. G.; Haberkorn, R. A. *Biochem.* **1978**, *17*, 2711.
- Tutunjian, P. N.; Waugh, J. S. *J. Chem. Phys.* **1982**, *76*, 1223.
- Tutunjian, P. N.; Tropp, J.; Waugh, J. S. *J. Am. Chem. Soc.* **1983**, *105*, 4848.
- Naito, A.; Sastry, D. L.; McDowell, C. A. *Chem. Phys. Lett.* **1985**, *115*, 19.
- Hauser, H.; Radloff, C.; Ernst, R. R.; Sundell, S.; Pascher, I. *J. Am. Chem. Soc.* **1988**, *110*, 1054.
- McDowell, C. A.; Naito, A.; Sastry, D. L.; Takegoshi, K. *J. Magn. Reson.* **1988**, *78*, 498.
- Ermak, F.; Topic, B.; Haerberlen, U.; Blinc, R. *J. Phys.: Condens. Matter* **1989**, *1*, 5489.
- Eichele, K.; Wasylishen, R. E. *J. Phys. Chem.* **1994**, *98*, 3108.
- Eichele, K.; Wu, G.; Wasylishen, R. E.; Britten, J. F. *J. Phys. Chem.* **1995**, *99*, 1030.
- Lumsden, M. D.; Wasylishen, R. E.; Britten, J. F. *J. Phys. Chem.* **1995**, *99*, 16602.
- Eichele, K.; Wasylishen, R. E.; Maitra, K.; Nelson, J. H.; Britten, J. F. *Inorg. Chem.* **1997**, *36*, 3539.
- Jensen, T. R.; Hazell, R. G.; Vosegaard, T.; Jakobsen, H. *J. Inorg. Chem.* **2000**, *39*, 2026.
- Gee, M.; Wasylishen, R. E.; Eichele, K.; *J. Phys. Chem. A* **2000**, *104*, 4598.
- Grossmann, G.; Scheller, D.; Malkina, O. L.; Malkin, V. G.; Zahn, G.; Schmidt, H.; Haerberlen, U. *Solid State Nucl. Magn. Reson.* **2000**, *17*, 22.
- Eichele, K.; Wasylishen, R. E.; Corrigan, J. F.; Taylor, N. J.; Carty, A. J.; Feindel, K. W.; Benard, G. M. *J. Am. Chem. Soc.* **2002**, *124*, 1541.
- Power, W. P.; Wasylishen, R. E. *Inorg. Chem.* **1992**, *31*, 2176.
- Eichele, K.; Ossenkamp, G. C.; Wasylishen, R. E.; Cameron, T. S. *Inorg. Chem.* **1999**, *38*, 639.
- Bernard, G. M.; Wu, G.; Lumsden, M. D.; Wasylishen, R. E.; Maigrot, N.; Charrier, C.; Mathey, F. *J. Phys. Chem. A* **1999**, *103*, 1029.
- Potrzebowski, M. J.; Assfeld, X.; Ganicz, K.; Olejniczak, S.; Cartier, A.; Garsiennet, C.; Tekely, P. *J. Am. Chem. Soc.* **2003**, *125*, 4223.

H. Double-Quantum Filtered ^1H MAS NMR Spectra

M. Bechmann, H. Förster, H. Maisel, and A. Sebald, *Journal Solid State Nuclear Magnetic Resonance*, **27**, 174–179 (2005).

doi:10.1016/j.ssnmr.2004.11.001

©2004 Elsevier Science.

All rights are reserved by Elsevier Science. The article is reproduced with the rights granted to the author.



Double-quantum filtered ^1H MAS NMR spectra

Matthias Bechmann^a, Hans Foerster^b, Heidi Maisel^c, Angelika Sebald^{a,*}

^a*Bayerisches Geoinstitut, Universität Bayreuth, D-95440 Bayreuth, Germany*

^b*Bruker Biospin GmbH, D-76287 Rheinstetten, Germany*

^c*Laboratorium für Anorganische Chemie, Universität Bayreuth, D-95440 Bayreuth, Germany*

Received 7 October 2004

Available online 7 January 2005

Abstract

It is shown that straightforward double-quantum filtered ^1H MAS NMR experiments yield spectral lineshapes that permit to estimate the minimum number of ^1H spins in a cluster. The approach may offer an alternative to multiple-quantum experiments for the characterisation of ^1H spin clusters of moderate size. The duration of the double-quantum excitation period has to be chosen suitably, it is necessary to find a practical compromise between optimum double-quantum filtration efficiency and optimum information content of the spectral lineshapes. Some ^1H MAS NMR experiments on partially deuterated maleic acid are reported as well as numerical simulations.

© 2004 Elsevier Inc. All rights reserved.

Keywords: MAS NMR; Rotational resonance; Double-quantum filtration; Numerical simulations; ^1H spin systems

1. Introduction

Of all NMR active spin- $\frac{1}{2}$ isotopes commonly used ^1H has the largest gyromagnetic ratio and is nearly 100 percent naturally abundant. In principle, these properties lead to high sensitivity and render spin systems involving ^1H spins suitable for probing relatively large internuclear distances by measurements based on the exploitation of direct dipolar coupling. In solid-state NMR, however, these promising properties are usually counterbalanced by less desirable side effects such as lack of spectral resolution and and/or complications caused by very large spin systems unless one is confronted with samples in which dilute ^1H spin systems occur naturally, as is sometimes found in inorganic solid materials. Generally speaking, however, conventional ^1H MAS NMR spectra are not sufficiently informative

and many efforts have been devoted to improve spectral resolution by the application of multiple pulse sequence under MAS conditions [1–8]. Another area of activity in ^1H solid-state NMR has been the characterisation of the cluster size of networks of coupled spins [9,10]. Such spin-counting experiments usually involve the excitation of multiple coherences and provide an estimate of the minimum number of coupled spins in a cluster. A difficulty with this approach is a rapidly decaying signal amplitude when recording the signatures of high(er) order coherences. More recently, patterns of spinning sidebands in ^1H MAS NMR spectra have been exploited to determine internuclear ^1H – ^1H distances and thus to characterise the topologies in supramolecular solid materials [11,12].

Here we will investigate how spectral ^1H MAS NMR lineshapes under conditions of double-quantum filtration (DQF) reflect the size of ^1H spin clusters. We use a straightforward COSY-like pulse sequence [13]. Our model compound is maleic acid in which all acid protons have been replaced by deuterium (Fig. 1), **1**, and will consider the ^1H spin system of the olefinic protons in **1**. The single-crystal structure of maleic acid is known

*Corresponding author. Current address: Department of Chemistry, Physical Chemistry Section, University of Exeter, Stocker Road, Exeter EX4 4QD, England, UK. Fax: +44 1392 263434.

E-mail addresses: a.sebald@exeter.ac.uk, angelika.sebald@uni-bayreuth.de (A. Sebald).

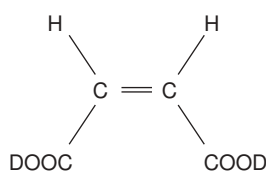


Fig. 1. Schematic representation of the molecular structure of partially deuterated maleic acid, **1**.

[14,15] and also the ^1H spin system in solid maleic acid has been fully characterised [16,17].

2. Experimental

2.1. Preparation of samples

The starting materials, D_2O , maleic acid anhydride (Aldrich Chemicals) and fully deuterated maleic acid anhydride (Isotec Inc.), are commercially available. Fully deuterated maleic acid and maleic acid with only the acid protons replaced by deuterium, **1**, are obtained by dissolving deuterated maleic acid anhydride or maleic acid anhydride, respectively, in D_2O at ambient conditions. Deuterium-diluted versions of **1** were obtained by co-crystallization of **1** and fully deuterated maleic acid in a 1:3 ($\mathbf{1}_{1:3}$) molar ratio. After isolation of the crude material from D_2O by evaporation, the sample was recrystallised from acetone as described in the literature [14,15].

2.2. ^1H MAS NMR

^1H MAS NMR spectra were recorded on Bruker MSL 300 and Avance 600 NMR spectrometers using standard 4 mm MAS probes. The corresponding ^1H Larmor frequencies, $\omega_0/2\pi$ are -300.1 and -600.1 MHz. ^1H shielding is quoted with respect to $\omega_{iso}^{CS} = 0$ ppm for the ^1H resonance of SiMe_4 . MAS frequencies were $\omega_r/2\pi = 10$ kHz and were actively controlled to within ± 2 Hz. ^1H $\pi/2$ pulse durations were $2.7 \mu\text{s}$, recycle delays were 600 s. The straightforward COSY-like pulse sequence $\pi/2_{(x)}-\tau-\pi/2_{(y)}-\Delta-\pi/2_{(\phi)}-\tau$ -acquisition [13] with 16-step phase cycling according to standard procedures [18] was used to record ^1H DQF MAS NMR spectra of **1** and $\mathbf{1}_{1:3}$. The duration of Δ was set to $3 \mu\text{s}$.

2.3. Definitions, notation, and numerical methods

Shielding notation [19] is used throughout. Homonuclear J coupling $^3J(^1\text{H}, ^1\text{H})$ is negligible for the spin system in **1**, for the interactions $\lambda = CS$ (chemical shielding) and $\lambda = D$ (direct dipolar coupling), the isotropic part ω_{iso}^λ , the anisotropy ω_{aniso}^λ , and the

asymmetry parameter η^λ relate to the principal elements of the interaction tensor ω^λ as follows [20]: $\omega_{iso}^\lambda = (\omega_{xx}^\lambda + \omega_{yy}^\lambda + \omega_{zz}^\lambda)/3$, $\omega_{aniso}^\lambda = \omega_{zz}^\lambda - \omega_{iso}^\lambda$, and $\eta^\lambda = (\omega_{yy}^\lambda - \omega_{xx}^\lambda)/\omega_{aniso}^\lambda$ with $|\omega_{zz}^\lambda - \omega_{iso}^\lambda| \geq |\omega_{xx}^\lambda - \omega_{iso}^\lambda| \geq |\omega_{yy}^\lambda - \omega_{iso}^\lambda|$. For direct dipolar coupling $\eta^D = \omega_{iso}^D = 0$ and $\omega_{aniso}^D = b_{ij} = -\mu_0\gamma_i\gamma_j\hbar/(4\pi r_{ij}^3)$, where γ_i , γ_j denote gyromagnetic ratios and r_{ij} is the internuclear distance between spins S_i , S_j . The Euler angles $\Omega_{IJ} = \{\alpha_{IJ}, \beta_{IJ}, \gamma_{IJ}\}$ [21] relate axis system I to axis system J , where I, J denote P (principal axis system, PAS), C (crystal axis system, CAS), R (rotor axis system, RAS), or L (laboratory axis system). For simulations of ^1H DQF MAS NMR spectra of **1** and $\mathbf{1}_{1:3}$ it is convenient to define the PAS of the intramolecular $^1\text{H}_i-^1\text{H}_j$ dipolar coupling tensor as the CAS, $\Omega_{PC}^{Dij} = \{0, 0, 0\}$. Our procedures for numerically exact spectral lineshape simulations and iterative fitting are fully described and discussed in detail elsewhere [22–24]. In general, these numerical procedures employ the REPULSION [25] schemes for the calculation of powder averages, implement some of the routines of the GAMMA package [26], use, where possible, the γ -COMPUTE approach [27–30], and take advantage of accelerated multi-processor computations in calculating powder averages [24]. Error minimisations employ routines from the MINUIT package [31].

3. Results and discussion

The solid-state structure of maleic acid is illustrated in Fig. 2. The acid hydrogen atoms form strong intra- and intermolecular hydrogen bonds, leading to a layered structure of ribbons of linked maleic acid molecules. The distance between the two olefinic protons in a molecule is 224 pm, corresponding to a dipolar coupling constant $b_{ij}/2\pi = -10,686$ Hz between these two protons. There are several further olefinic protons in neighbouring molecules in spatial proximity to each of these two olefinic protons, for instance within 322, 337, 410, and 583 pm. Accordingly, even in our sample **1** with all acidic protons replaced by deuterium atoms, the question arises whether the two olefinic protons per maleic acid molecule represent isolated ^1H spin pairs in solid **1**. Not only the crystal structure of maleic acid is known, also the ^1H spin system in solid maleic acid has been characterised by means of ^1H single-crystal NMR [16,17] and by ^1H multiple pulse experiments [1]. The ^1H chemical shielding parameters of the two olefinic protons are given in Table 1. With a difference in isotropic ^1H chemical shielding $\omega_{iso}^A = 0.2$ ppm and ^1H chemical shielding anisotropies $\omega_{aniso}^{CS1} = \omega_{aniso}^{CS2} = -3.0$ ppm, these two ^1H spins thus constitute a (more or less isolated) spin pair near the $n = 0$ rotational resonance (R^2) condition [32,33], with direct dipolar coupling being the largest anisotropic interaction

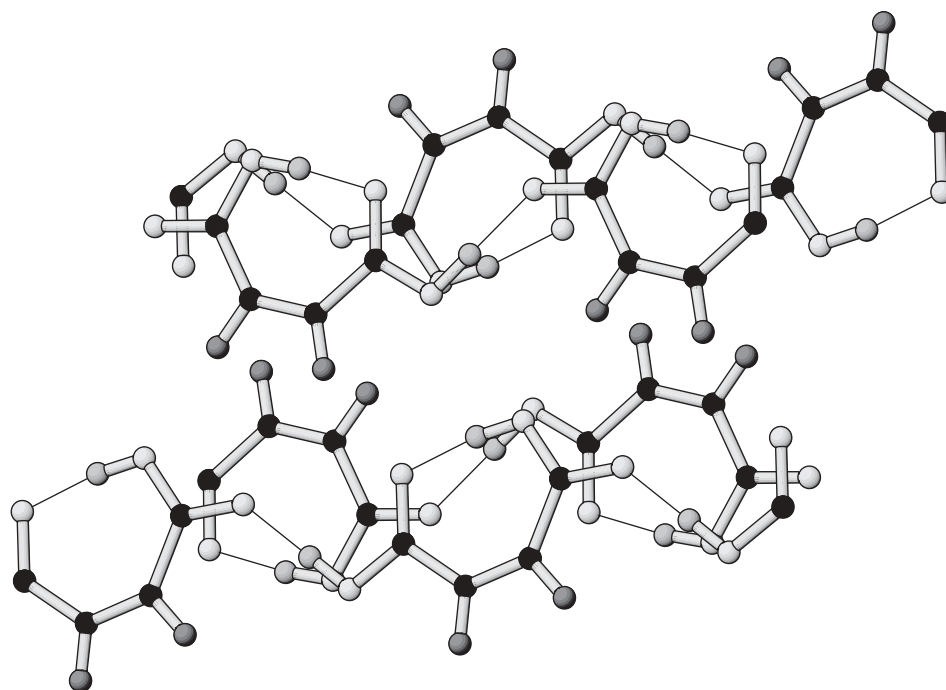


Fig. 2. The solid-state structure of maleic acid according to single-crystal X-ray diffraction [14,15], hydrogen bonds are indicated. Carboxylic acid hydrogen positions are labelled light grey, olefinic hydrogen atoms dark grey, carbon atoms black, and oxygen atoms white.

Table 1
 ^1H chemical shielding tensors of the olefinic proton sites in maleic acid [17]

	$^1\text{H}_2^a$	$^1\text{H}_3^a$
ω_{iso}^{CS} (ppm)	-5.9 ± 0.2	-5.9 ± 0.2
ω_{aniso}^{CS} (ppm)	-3.0	-3.0
η^{CS}	0.96	0.96
$\alpha_{PC_{12}}^{CS}$ (deg) ^b	0	0
$\beta_{PC_{12}}^{CS}$ (deg) ^b	0	0
$\gamma_{PC_{12}}^{CS}$ (deg) ^b	0	0

^aNumbering of hydrogen atoms according to numbering scheme of the crystal structure [14,15].

^bEuler angles given relative to the principal axes system of the $^1\text{H}_2$ – $^1\text{H}_3$ dipolar coupling tensor with its x -axis defined as perpendicular to the molecular plane.

present. ^1H MAS NMR spectra of **1** (not shown) do not give any convincing evidence about the degree of isolation of this spin pair from nearby further ^1H spins. It has been shown recently [33] that spectral lineshapes of isolated spin pairs at and near the $n = 0$ R^2 condition, in particular with double-quantum filtration (DQF) applied, very sensitively reflect all anisotropic interaction parameters of isolated homonuclear spin pairs. Here we apply this DQF-based approach, combined with numerical simulations, as a tool to estimate the lower limit of the number of spins coupled in the ^1H cluster. An experimental ^1H DQF MAS NMR spectrum of **1** is shown in Fig. 3 (top trace), together with

simulated spectra assuming an isolated ^1H spin pair (second trace), coupling of the spin pair with two nearest olefinic ^1H spins (third trace), and with four nearest olefinic ^1H spins (bottom trace). Clearly, the experimental spectral lineshape cannot be reproduced by simulations assuming an isolated ^1H spin pair, whereas simulations including six ^1H spins agree very well with the experimental data.

The experimental spectrum (Fig. 3) was obtained with a duration of $\tau = \tau_r = 0.1$ ms. From the point of view of DQF efficiency for a spin pair such as the ^1H spin pair in **1**, choosing $\tau = \tau_r/2 = 0.05$ ms would be far preferable as maxima in DQF efficiency are achieved for durations of τ matching integer multiples of a half rotation period $\tau_r/2$, here the maximum possible DQF efficiency would be achieved for $\tau = \tau_r/2 = 0.05$ ms. However, with regard to informative spectral lineshapes, reflecting the number of ^1H spins coupled to each other, it is much better to choose τ to match an integer multiple of a rotation period. This is illustrated in Fig. 4. A significant reduction in DQF efficiency (3 percent for $\tau = \tau_r = 0.1$ ms vs. 49 percent for $\tau = \tau_r/2 = 0.05$ ms) is easily affordable when dealing with ^1H spin systems when it comes with the added benefit of spectral lineshapes reflecting the size of the ^1H spin cluster.

Fig. 5 depicts experimental ^1H DQF MAS NMR spectra of **1** and **1**_{1:3} in comparison with a simulated spectrum assuming an isolated ^1H spin pair of the two olefinic protons. In order for these two ^1H spins to represent an isolated spin pair, it is obviously necessary

to dilute **1** in fully deuterated maleic acid. The experimental spectrum of **1**_{1,3} resembles the simulated spectrum for an isolated spin pair but some differences in amplitudes and phases remain. Further dilution of **1** in fully deuterated maleic acid, approximately in a molar ratio 1:10 would be needed to render the olefinic ¹H spin pair truly isolated.

Finally, we will briefly consider a scenario as it may arise when employing such ¹H DQF MAS NMR experiments for purposes of structure elucidation. We

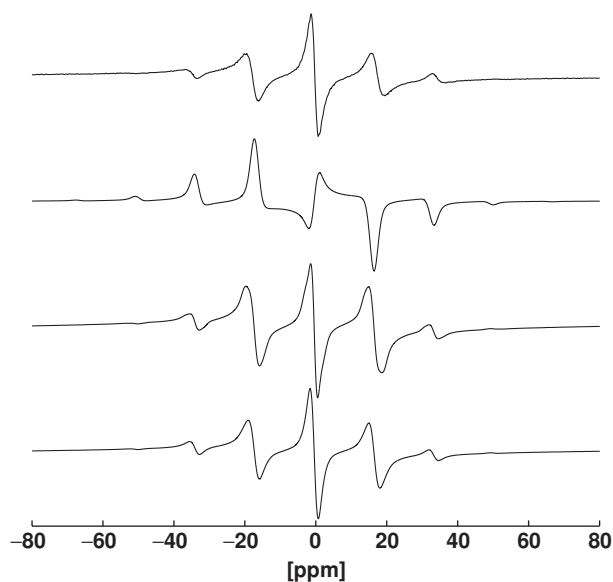


Fig. 3. Top row: ¹H DQF MAS NMR spectrum of **1** ($\omega_0/2\pi = -600.1$ MHz, $\omega_r/2\pi = 10$ kHz, $\tau = \tau_r = 0.1$ ms). Second row: Simulated spectrum, assuming an isolated olefinic ¹H spin pair in **1**. Third row: Simulated spectrum, taking the two nearest additional olefinic ¹H spins into account. Fourth row: Simulated spectrum, including the olefinic ¹H spin pair plus the four nearest additional ¹H spins.

start with the experimental ¹H DQF MAS NMR spectrum of **1** (top row, Fig. 3) and use four-spin simulations taking two nearest pairs of olefinic ¹H spins into account. In these simulations we take the location of three hydrogen atoms as known and search for the location of the fourth hydrogen atom by means of iterative fitting of the experimental spectrum. The result of this search is shown in Fig. 6. Iterative fitting locates the fourth hydrogen atom in a well-defined area around the position predicted by X-ray diffraction, yielding internuclear distances $r_{H3'H2'} = 223 \pm 45$ pm and $r_{H3H2'} = 326 \pm 93$ pm in very good agreement with the values determined by single-crystal X-ray diffraction. The shape of the volume element defining the position of H2' reflects the magnitudes of the dipolar coupling constants involved, the uncertainty in the direction of the unique axis of the intramolecular ¹H–¹H dipolar coupling tensor is considerable smaller than the uncertainty in the direction connecting H3 with H2'.

4. Summary and conclusions

We have shown that straightforward ¹H DQF MAS NMR experiments yield spectral lineshapes that permit an estimate of the minimum number of ¹H spins in a cluster. Provided that suitable durations of the double-quantum excitation period are used, this DQF approach may thus offer an alternative to multiple-quantum experiments for the characterisation of ¹H spin clusters of moderate size. In particular when combined with experimental MAS NMR strategies that provide an estimate of the maximum number of spins in cluster [34], a very good estimate of the size of a spin cluster should be possible.

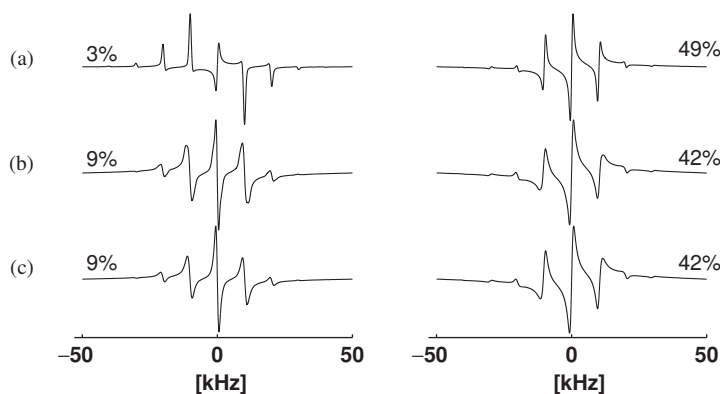


Fig. 4. Simulated ¹H DQF MAS NMR spectra ($\omega_0/2\pi = -600.1$ MHz, $\omega_r/2\pi = 10$ kHz); left column corresponds to $\tau = \tau_r = 0.1$ ms, right column corresponds to $\tau = \tau_r/2 = 0.05$ ms. (a) Assuming an isolated ¹H spin pair in **1**. (b) Taking the olefinic ¹H spin pair plus the two nearest additional ¹H spins into account. (c) Taking the olefinic ¹H spin pair plus the four nearest additional ¹H spins into account. Note the large difference in DQF efficiency (indicated in the figure) for the two different durations of τ ; for $\tau = \tau_r$ the DQF efficiencies are lower but the spectral lineshapes are more informative.

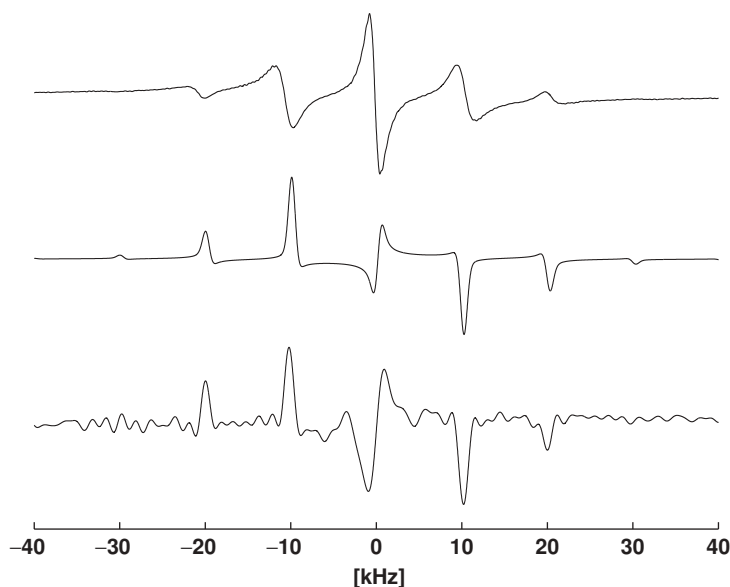


Fig. 5. Experimental ^1H DQF MAS NMR spectra ($\omega_0/2\pi = -300.1$ MHz, $\omega_r/2\pi = 10$ kHz, $\tau = \tau_r = 0.1$ ms) of **1** (top row) and **1**_{1.3} (bottom row). Also shown is a simulated spectrum assuming an isolated olefinic ^1H spin pair (second row).

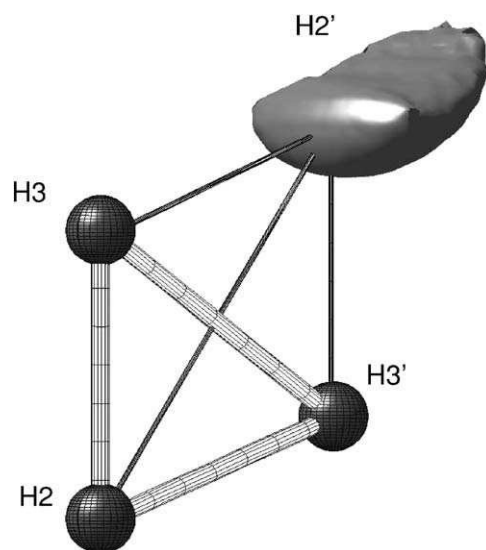


Fig. 6. Illustration of the localisation of the fourth proton from iterative fitting of the experimental ^1H MAS DQF NMR spectrum depicted in Fig. 3, top row. The positions of three of the four olefinic hydrogen atoms (H2, H3, H3') as well as the numbering are taken from the single-crystal X-ray diffraction structure (distances: $r_{\text{H2H3}} = 224$ pm, $r_{\text{H3H3'}} = 337$ pm, angle: $\text{H3H2H3}' = 73.6^\circ$ [14,15]). The shaded volume area for the position of hydrogen atom H2' is derived from $2\chi^2$ error values from iterative fitting.

Acknowledgments

Financial support of our work by the Deutsche Forschungsgemeinschaft is gratefully acknowledged. We thank Bruker Biospin GmbH, Rheinstetten, for providing generous access to the Avance 600 NMR spectrometer.

References

- [1] G. Scheler, U. Haubenreisser, H. Rosenberger, *J. Magn. Reson.* 44 (1981) 134–144.
- [2] J. Gottwald, D.E. Demco, R. Graf, H.W. Spiess, High-resolution double-quantum NMR spectroscopy of homonuclear spin pairs and proton connectivities in solids, *Chem. Phys. Lett.* 243 (1995) 314–323.
- [3] I. Schnell, H.W. Spiess, High-resolution ^1H NMR spectroscopy in the solid state: very fast sample rotation and multiple-quantum coherences, *J. Magn. Reson.* 151 (2001) 153–227.
- [4] P.K. Madhu, X. Zhao, M.H. Levitt, High-resolution ^1H NMR in the solid state using symmetry-based pulse sequences, *Chem. Phys. Lett.* 346 (2001) 142–148.
- [5] B. Reif, C.P. Jaroniec, C.M. Rienstra, M. Hohwy, R.G. Griffin, ^1H – ^1H correlation spectroscopy and distance measurements in a deuterated peptide, *J. Magn. Reson.* 151 (2001) 320–327.
- [6] A. Lesage, L. Duma, D. Sakellariou, L. Emsley, Improved resolution in proton NMR spectroscopy of powdered solids, *J. Am. Chem. Soc.* 123 (2001) 5747–5752.
- [7] E. Vinogradov, P.K. Madhu, S. Vega, Proton spectroscopy in solid state nuclear magnetic resonance with windowed phase modulated Lee–Goldburg decoupling sequences, *Chem. Phys. Lett.* 354 (2002) 193–202.
- [8] A.J. Vega, Controlling the effects of pulse transients and RF inhomogeneity in phase-modulated multiple-pulse sequences for homonuclear decoupling in solid-state proton NMR, *J. Magn. Reson.* 170 (2004) 22–41.
- [9] J. Baum, M. Munowitz, A.N. Garroway, A. Pines, Multiple-quantum dynamics in solid state NMR, *J. Chem. Phys.* 83 (1985) 2015–2025.
- [10] O.N. Antzutkin, R. Tycko, High-order multiple quantum excitation in ^{13}C nuclear magnetic resonance spectroscopy of organic solids, *J. Chem. Phys.* 110 (1999) 2749–2752.
- [11] G.R. Goward, M.F.H. Schuster, D. Sebastini, I. Schnell, H.W. Spiess, High-resolution solid-state NMR studies of imidazole-based proton conductors: structural motifs and chemical exchange from ^1H NMR, *J. Phys. Chem. B* 106 (2002) 9322–9344.
- [12] G.R. Goward, D. Sebastini, I. Schnell, H.W. Spiess, H.-D. Kim, H. Ishida, Benzoxazine oligomers: evidence for a helical structure

- from solid-state NMR spectroscopy and DFT-based dynamics and chemical shift calculations, *J. Am. Chem. Soc.* 125 (2003) 5792–5800.
- [13] N.C.N. Nielsen, F. Creuzet, R.G. Griffin, M.H. Levitt, Enhanced double-quantum nuclear magnetic resonance in spinning solids at rotational resonance, *J. Chem. Phys.* 96 (1992) 5668–5677.
- [14] M. Shahat, The crystal and molecular structure of maleic acid, *Acta Crystallogr.* 5 (1952) 763–768.
- [15] M.N.G. James, G.J.B. Williams, A refinement of the crystal structure of maleic acid, *Acta Crystallogr. B* 30 (1974) 1249–1257.
- [16] U. Haeberlen, U. Kohlschütter, Nuclear magnetic shielding anisotropies from proton multiple pulse spectra, *Chem. Phys.* 2 (1973) 76–84.
- [17] R. Grosescu, A.M. Achlama (Chmelnick), U. Haeberlen, H.W. Spiess, Multiple pulse study of the proton shielding in single crystals of maleic acid, *Chem. Phys.* 5 (1974) 119–128.
- [18] R.R. Ernst, G. Bodenhausen, A. Wokaun, *Principles of Nuclear Magnetic Resonance in One and Two Dimensions*, Clarendon Press, Oxford, 1987.
- [19] M.H. Levitt, The signs of frequencies and phases in NMR, *J. Magn. Reson.* 126 (1997) 164–182.
- [20] U. Haeberlen, High resolution NMR in solids. Selective averaging, in: J.S. Waugh (Ed.), *Advances in Magnetic Resonance; Supplement 1*, Academic Press, New York, 1976.
- [21] A.R. Edmonds, *Angular Momentum in Quantum Mechanics*, Princeton University Press, Princeton, NJ, 1974.
- [22] S. Dusold, W. Milius, A. Sebald, Iterative lineshape fitting of MAS NMR spectra: a tool to investigate homonuclear J couplings in isolated spin pairs, *J. Magn. Reson.* 135 (1998) 500–513.
- [23] S. Dusold, H. Maisel, A. Sebald, Magnitudes and orientations of interaction tensors determined from rotational resonance MAS NMR lineshapes of a four- ^{13}C spin system, *J. Magn. Reson.* 141 (1999) 78–90.
- [24] M. Bechmann, X. Helluy, A. Sebald, Double-quantum filtered rotational-resonance MAS NMR in the presence of large chemical shielding anisotropies, *J. Magn. Reson.* 152 (2001) 14–25.
- [25] M. Bak, N.C. Nielsen, REPULSION, a novel approach to efficient powder averaging in solid-state NMR, *J. Magn. Reson.* 125 (1997) 132–139.
- [26] S.A. Smith, T.O. Levante, B.H. Meier, R.R. Ernst, Computer simulations in magnetic resonance. An object oriented programming approach, *J. Magn. Reson. A* 106 (1994) 75–105.
- [27] M. Edén, Y.K. Lee, M.H. Levitt, Efficient simulation of periodic problems in NMR: application to decoupling and rotational resonance, *J. Magn. Reson. A* 120 (1996) 56–71.
- [28] T. Charpentier, C. Fermon, J. Virlet, Efficient time propagation technique for MAS NMR simulation: application to quadrupolar nuclei, *J. Magn. Reson.* 132 (1998) 181–190.
- [29] M. Hohwy, H. Bildsoe, H.J. Jakobsen, N.C. Nielsen, Efficient spectral simulations in NMR of rotating solids. The γ -COMPUTE algorithm, *J. Magn. Reson.* 136 (1999) 6–14.
- [30] M.H. Levitt, M. Edén, Numerical simulation of periodic NMR problems: fast calculation of carousel averages, *Molec. Phys.* 95 (1998) 879–890.
- [31] F. James, M. Roos, MINUIT computer code, Program D-506, CERN, Geneva, 1977.
- [32] M.M. Maricq, J.S. Waugh, NMR in rotating solids, *J. Chem. Phys.* 70 (1979) 3300–3316.
- [33] M. Bechmann, A. Sebald, *J. Magn. Reson.* (2004) in press.
- [34] C.E. Hughes, J. Schmedt auf der Günne, M.H. Levitt, A test for the number of coupled spins $I = 1/2$ in magic-angle-spinning solids: zero-quantum recoupling of multiple-quantum coherences, *Chem. Phys. Chem.* 4 (2003) 457–465.

Danksagung

- Zu allererst möchte ich Angelika Sebald danken. Sie hat durch ihre Persönlichkeit genauso wie durch ihre fachliche Qualifikation eine inspirierende und motivierende Umgebung geschaffen in der es eine Freude ist zu arbeiten.
- Xavier Helluy für die vielen oftmals hitzigen Diskussionen über NMR, Computer und was sonst noch im Leben wichtig ist.
- Stephan Dusold der mich in die Wunderwelt des Fittens einführt hat, mir letzten Endes das root Passwort überließ und dem ich auch sonst viel zu verdanken habe.
- Klaus Hain dessen elektronische Hilfe viele der Experimente erst möglich machte und der es immer wieder schaffte die Spektrometer nach jedem Gewitter auf die Beine zu bringen.
- Hans Förster für die Benutzung der Spektrometer im Bruker Applikationslabor in Rheinstetten: “Irgendwann machen wir auch einmal Experimente von denen man noch nicht alles simulieren kann”.
- Heidi Maisel für die Hilfe bei der Herstellung der Proben ohne die viele der Experimente nicht möglich gewesen wären.
- Dem “Bayerischen Geoinstitut” für die hervorragenden Infrastruktur, die freundliche und internationale Atmosphäre die immer inspirierend und motivierend war.
- Nick Dowell meinem “english fellow” der meine Aufenthalt in Exeter sehr bereichert hat, und der mir half die Dinge mit englischen Augen zu sehen und trotzdem einsehen musste, dass Linux besser ist als Mac OS, aber dennoch keine Körnerbrötchen mag.
- Barbara, Hildegard, Jörg, Josef die hoffentlich wissen was ich ihnen verdanke.
- Allen die ich vergessen habe ohne es zu wollen.

Hiermit erkläre ich, dass ich die vorliegende Arbeit selbstständig verfasst und keine anderen als die von mir angegebenen Quellen und Hilfsmittel verwendet habe.

Ich habe weder diese noch eine gleichartige Doktorprüfung an einer anderen Hochschule endgültig nicht bestanden.

(Matthias Bechmann)